Titre: Title:	Anatomical Modeling of Cerebral Microvascular Structures: Application to Identify Biomarkers of Microstrokes
Auteur: Author:	Rafat Damseh
Date:	2020
Type:	Mémoire ou thèse / Dissertation or Thesis
Référence: Citation:	Damseh, R. (2020). Anatomical Modeling of Cerebral Microvascular Structures: Application to Identify Biomarkers of Microstrokes [Thèse de doctorat, Polytechnique Montréal]. PolyPublie. https://publications.polymtl.ca/5393/

URL de PolyPublie: PolyPublie URL:	https://publications.polymtl.ca/5393/
Directeurs de recherche: Advisors:	Frédéric Lesage, & Farida Cheriet
Programme: Program:	Génie biomédical

POLYTECHNIQUE MONTRÉAL
affiliée à l'Université de Montréal

ANATOMICAL MODELING OF CEREBRAL MICROVASCULAR STRUCTURES: APPLICATION TO IDENTIFY BIOMARKERS OF MICROSTOKES

RAFAT DAMSEH
Institut de génie biomédical

Thèse présentée en vue de l'obtention du diplôme de Philosophiae Doctor

Génie biomédical

Août 2020

POLYTECHNIQUE MONTRÉAL
affiliée à l'Université de Montréal

Cette thèse intitulée :

ANATOMICAL MODELING OF CEREBRAL MICROVASCULAR STRUCTURES: APPLICATION TO IDENTIFY BIOMARKERS OF MICROSTOKES

présentée par **Rafat DAMSEH**
en vue de l'obtention du diplôme de *Philosophiae Doctor*
a été dûment acceptée par le jury d'examen constitué de :

Julien COHEN-ADAD, président

Frédéric LESAGE, membre et directeur de recherche

Farida CHERIET, membre et codirectrice de recherche

Benjamin DE LEENER, membre

Hassan RIVAZ, membre externe

DEDICATION

To my precious parents and my beloved wife,
To my big family and friends . . .

ACKNOWLEDGEMENTS

I would like to express my sincere appreciation to my supervisor and mentor, Frederic Lesage. I consider him a source of inspiration for his unique multidisciplinary knowledge and expertise, combining science and engineering, and I am always impressed about his ability of describing/simplifying complex ideas with few words. I am indebted to him for his continued support and patience, and for spending numerous hours in discussions about my research work, which have vividly contributed to the accomplishment of this thesis. Beside our meetings, I learned much observing his outstanding example of enthusiasm, dedication and punctuality.

I would also like to express my deep gratitude to my co-supervisor and the first person I met at Polytechnique Montreal, Farida Cheriet. I will not forget the time when I passed by Dr Cheriet's office to inquire about potential PhD positions at her laboratory; I still remember her kind words of hospitality and encouragement. I am very thankful for her constant support and invaluable guidance, and I could not imagine my PhD journey without joining her "stress-release" group meetings.

Many thanks go to Philippe Pouliot for helping me to refine my manuscripts, and for the discussions about my research work. I gratefully acknowledge Patrick Delafontaine-Martel, Parikshat Sirpal, Yuankang Lu, Paul Marchand, Xuecong Lu, Christophe Cloutier-Tremblay, Antoine Letourneau, Xavier Bowley, Joel Lefebvre, Samuel Belanger. Thanks for the coffee times and the prosperous conversations!

I am forever thankful to my parents for their countless sacrifices to help me reach this point in my life. Above all, no words can express my unfailing gratitude and love to my soulmate, wife and best friend, Lina, who stood by my side at every moment manifesting unconditional love and patience.

RÉSUMÉ

Les réseaux microvasculaires corticaux sont responsables du transport de l'oxygène et des substrats énergétiques vers les neurones. Ces réseaux réagissent dynamiquement aux demandes énergétiques lors d'une activation neuronale par le biais du couplage neurovasculaire. Afin d'élucider le rôle de la composante microvasculaire dans ce processus de couplage, l'utilisation de la modélisation informatique pourrait se révéler un élément clé. Cependant, la manque de méthodologies de calcul appropriées et entièrement automatisées pour modéliser et caractériser les réseaux microvasculaires reste l'un des principaux obstacles. Le développement d'une solution entièrement automatisée est donc important pour des explorations plus avancées, notamment pour quantifier l'impact des malformations vasculaires associées à de nombreuses maladies cérébrovasculaires. Une observation courante dans l'ensemble des troubles neurovasculaires est la formation de micro-blocages vasculaires cérébraux (mAVC) dans les artérioles pénétrantes de la surface piale. De récents travaux ont démontré l'impact de ces événements microscopiques sur la fonction cérébrale. Par conséquent, il est d'une importance vitale de développer une approche non invasive et comparative pour identifier leur présence dans un cadre clinique.

Dans cette thèse,un pipeline de traitement entièrement automatisé est proposé pour aborder le problème de la modélisation anatomique microvasculaire. La méthode de modélisation consiste en un réseau de neurones entièrement convolutif pour segmenter les capillaires sanguins, un générateur de modèle de surface 3D et un algorithme de contraction de la géométrie pour produire des modèles graphiques vasculaires ne comportant pas de connections multiples. Une amélioration de ce pipeline est développée plus tard pour alléger l'exigence de maillage lors de la phase de représentation graphique. Un nouveau schéma permettant de générer un modèle de graphe est développé avec des exigences d'entrée assouplies et permettant de retenir les informations sur les rayons des vaisseaux. Il est inspiré de graphes géométriques déformants construits en respectant les morphologies vasculaires au lieu de maillages de surface. Un mécanisme pour supprimer la structure initiale du graphe à chaque exécution est implémenté avec un critère de convergence pour arrêter le processus. Une phase de raffinement est introduite pour obtenir des modèles vasculaires finaux. La modélisation informatique développée est ensuite appliquée pour simuler les signatures IRM potentielles de mAVC, combinant le marquage de spin artériel (ASL) et l'imagerie multidirectionnelle pondérée en diffusion (DWI). L'hypothèse est basée sur des observations récentes démontrant une réorientation radiale de la microvascularisation dans la périphérie du mAVC lors de la récupération chez la souris. Des lits capillaires synthétiques, orientés aléatoirement et radialement, et des angiogrammes de tomographie par cohérence optique (OCT), acquis dans le cortex de souris (n = 5) avant et après l'induction d'une photothrombose ciblée, sont analysés. Les graphes vasculaires

informatiques sont exploités dans un simulateur 3D Monte-Carlo pour caractériser la réponse par résonance magnétique (MR), tout en considérant les effets des perturbations du champ magnétique causées par la désoxyhémoglobine, et l'advection et la diffusion des spins nucléaires.

Le pipeline graphique proposé est validé sur des angiographies synthétiques et réelles acquises avec différentes modalités d'imagerie. Comparé à d'autres méthodes effectuées dans le milieu de la recherche, les expériences indiquent que le schéma proposé produit des taux d'erreur géométriques et topologiques amoindris sur divers angiogrammes. L'évaluation confirme également l'efficacité de la méthode proposée en fournissant des modèles représentatifs qui capturent tous les aspects anatomiques des structures vasculaires. Ensuite, afin de trouver des signatures de mAVC basées sur le signal IRM, la modélisation vasculaire proposée est exploitée pour quantifier le rapport de perte de signal intravoxel minimal lors de l'application de plusieurs directions de gradient, à des paramètres de séquence variables avec et sans ASL. Avec l'ASL, les résultats démontrent une différence significative ($p < 0{,}05$) entre le signal calculé avant et 3 semaines après la photothrombose. La puissance statistique a encore augmenté ($p < 0{,}005$) en utilisant des angiogrammes capturés à la semaine suivante. Sans ASL, aucun changement de signal significatif n'est trouvé. Des rapports plus élevés sont obtenus à des intensités de champ magnétique plus faibles (par exemple, B0 = 3) et une lecture TE plus courte (<16 ms). Cette étude suggère que les mAVC pourraient être caractérisés par des séquences ASL-DWI, et fournirait les informations nécessaires pour les validations expérimentales postérieures et les futurs essais comparatifs.

ABSTRACT

Cortical microvascular networks are responsible for carrying the necessary oxygen and energy substrates to our neurons. These networks react to the dynamic energy demands during neuronal activation through the process of neurovascular coupling. A key element in elucidating the role of the microvascular component in the brain is through computational modeling. However, the lack of fully-automated computational frameworks to model and characterize these microvascular networks remains one of the main obstacles. Developing a fully-automated solution is thus substantial for further explorations, especially to quantify the impact of cerebrovascular malformations associated with many cerebrovascular diseases. A common pathogenic outcome in a set of neurovascular disorders is the formation of microstrokes, i.e., micro occlusions in penetrating arterioles descending from the pial surface. Recent experiments have demonstrated the impact of these microscopic events on brain function. Hence, it is of vital importance to develop a non-invasive and translatable approach to identify their presence in a clinical setting.

In this thesis, a fully automatic processing pipeline to address the problem of microvascular anatomical modeling is proposed. The modeling scheme consists of a fully-convolutional neural network to segment microvessels, a 3D surface model generator and a geometry contraction algorithm to produce vascular graphical models with a single connected component. An improvement on this pipeline is developed later to alleviate the requirement of water-tight surface meshes as inputs to the graphing phase. The novel graphing scheme works with relaxed input requirements and intrinsically captures vessel radii information, based on deforming geometric graphs constructed within vascular boundaries instead of surface meshes. A mechanism to decimate the initial graph structure at each run is formulated with a convergence criterion to stop the process. A refinement phase is introduced to obtain final vascular models. The developed computational modeling is then applied to simulate potential MRI signatures of microstrokes, combining arterial spin labeling (ASL) and multi-directional diffusion-weighted imaging (DWI). The hypothesis is driven based on recent observations demonstrating a radial reorientation of microvasculature around the micro-infarction locus during recovery in mice. Synthetic capillary beds, randomly- and radially oriented, and optical coherence tomography (OCT) angiograms, acquired in the barrel cortex of mice (n=5) before and after inducing targeted photothrombosis, are analyzed. The computational vascular graphs are exploited within a 3D Monte-Carlo simulator to characterize the magnetic resonance (MR) response, encompassing the effects of magnetic field perturbations caused by deoxyhemoglobin, and the advection and diffusion of the nuclear spins.

The proposed graphing pipeline is validated on both synthetic and real angiograms acquired with

different imaging modalities. Compared to other efficient and state-of-the-art graphing schemes, the experiments indicate that the proposed scheme produces the lowest geometric and topological error rates on various angiograms. The evaluation also confirms the efficiency of the proposed scheme in providing representative models that capture all anatomical aspects of vascular structures. Next, searching for MRI-based signatures of microstokes, the proposed vascular modeling is exploited to quantify the minimal intravoxel signal loss ratio when applying multiple gradient directions, at varying sequence parameters with and without ASL. With ASL, the results demonstrate a significant difference ($p<0.05$) between the signal-ratios computed at baseline and 3 weeks after photothrombosis. The statistical power further increased ($p<0.005$) using angiograms captured at week 4. Without ASL, no reliable signal change is found. Higher ratios with improved significance are achieved at low magnetic field strengths (e.g., at 3 Tesla) and shorter readout TE (<16 ms). This study suggests that microstrokes might be characterized through ASL-DWI sequences, and provides necessary insights for posterior experimental validations, and ultimately, future translational trials.

TABLE OF CONTENTS

LIST OF TABLES

LIST OF FIGURES

LIST OF SYMBOLS AND ACRONYMS

AD	Alzheimer's disease
ASL	Arterial spin labeling
bSSFP	Balanced steady state free precession
BERT	Bidirectional encoder representations from transformers
BOLD	Blood oxygenation level-dependent
CBF	Cerebral blood flow
CBV	Cerebral blood volume
CMRO2	Cerebral metabolic rate of oxygen
CSF	Cerebrospinal fluid
CoW	Circle of Willis
CTA	Computed-tomography angiography
CNN	Convolutional neural network
DL	Deep learning
DTI	Diffusion tensor imaging
DWI	Diffusion-weighted imaging
DT	Distance transform
DCE	Dynamic contrast enhanced
DSC	Dynamic susceptibility contrast
EPI	Echo-planar imaging
EEG	Electroencephalography
FITC	Fluorescein isothiocyanate
FDOCT	Fourier-domain OCT
FID	Free induction decay
FCNN	Fully convolutional neural networks
fMRI	Functional magnetic resonance imaging
GRU	Gated recurrent unit
GRE	Gradient echo
GNN	Graph neural network
iCNS	Image-based Circulatory Network Synthesis
IVIM	Intravoxel incoherent motion
IVIM	Intravoxel incoherent motion
LFSM	Light-sheet fluorescence microscopy
LSTM	Long short term memory

MR	Magnetic resonance
MRA	Magnetic resonance angiography
MRI	Magnetic resonance imaging
MEG	Magnetoencephalography
MOST	Micro-optical sectioning tomography
MCAO	Middle cerebral artery occlusion
NMR	Nuclear magnetic resonance
OCT	Optical coherence tomography
OMAG	Optical microangiography
SO2	Oxygen saturation
PO2	Partial pressure of oxygen
RF	Radio frequency
RNN	Recurrent neural network
SNR	Signal-to-noise ratios
SDOCT	Spectral-domain OCT
SE	Spin echo
SSOCT	Swept-source OCT
TPM	Two-photon microscopy
VAN	Vascular anatomical network

CHAPTER 1 INTRODUCTION

1.1 Problem Context

Cortical microvascular networks are the carrier of continuous supply of oxygen and energy substrates to neurons, and thus they are responsible for maintaining their healthy state. These networks react dynamically to meet the rapid and substantial increase in energy demands during neuronal activation through the process of neurovascular coupling [1]. Structural deterioration of the cortex microvasculature directly disrupts the regulation of cerebral blood flow and alters the distribution of oxygen and nutrients [2]. Characterization of cerebral microvasculature is thus of vital importance to understand brain physiology, and to evaluate the impact of potential cerebrovascular deteriorations on brain function. A key element in elucidating the role of the cerebrovascular component is through computational modeling. Such analysis opens the door for a detailed understanding of the spatiotemporal nature of the hemodynamic response [3–6], bridging scales and linking the microvascular phenomena with the macroscopic (voxel size) observations found in the blood oxygenation level-dependent (BOLD) response [7, 8], and simulating non-invasive magnetic resonance (MR) signatures, i.e., fingerprinting, to map between the microvascular structural and physiological features and the expected MR response [9, 10]. However, a main challenge that hinders large cohorts and scaled experiments is the lack of fully-automated computational frameworks to model and characterize these microvascular networks. Developing such processing pipelines is substantial for further explorations, including those focusing on studying the impact of cerebrovascular malformations associated with many neurovascular disorders.

1.1.1 Computational Modeling of Cerebrovascular Networks

Computational modeling of cerebrovascular structure and topology is essential in areas ranging from clinical decision support to fundamental research. Non-invasive cerebrovascular imaging techniques including magnetic resonance angiography (MRA) and computed-tomography angiography (CTA) are common practices for both preoperative planning and postoperative surveillance scanning. In experimental studies, optical imaging systems, e.g., two-photon microscopy (TPM) and optical coherence tomography (OCT), have been proposed to provide spatially-resolved measurements of cerebral microvasculature in-vivo. [11–15]. Transforming cerebrovascular structures into interpretable computational models remains problematic. Cerebrovascular images exhibit a high level of intersubject heterogeneity, and contain complex vascular structures. Furthermore, vascular space is submitted to dynamically evolving conditions like acute ischemic strokes. These

obstacles hinder the construction of accurate computational models that encode connectivity and spatial information to be used for further analysis of shape features and hemodynamics properties. In case of TPM, high absorption and scattering of the emitted photons occur with more depth, leading to image degradation and intensity changes. Also, scattering of excited photons by red blood cells degrades their focus and leads to shadows underneath large pial vessels. These deteriorations in the excited and emitted photons yield volumetric image intensity variations, and hence escalate the complexity of processing of TPM angiographies [16]. On the other hand, OCT angiography is a label-free in vivo imaging technique that became popular in many neuroscience fields. Beside its attractiveness, OCT angiograms suffer from an inherent issue related to dynamic scattering of moving erythrocytes within pial vasculature [12, 17]. This induces tail-like artifacts that impose shadows on the capillary vessels, and can result in a misleading interpretation of the angiographic results.

1.1.2 Non-invasive Identification of Cerebrovascular Micro-occlusions

Among pathogenic outcomes in cerebrovascular diseases [2] is the emergence of micro occlusions in penetrating arterioles descending from the pial surface. Recent experiments have provided evidence about the impact of these microscopic events on brain function [18]. Occlusion of a single penetrating vessel was shown to lead into ischemic infarction in the cortex [19] and to have effects on targeted cognitive tasks. Cerebral microinfarcts have emerged as a potential determinant of cognitive decline, as they are one of the most wide-spread forms of tissue infarction in the aging brain [20]. These cortical lesions have been associated with severe deficits in motor output at muscles [21]. It was also shown that microembolism of single cortical arteriole induces cortical spreading depression, a potential trigger and putative cause of migraine with aura [22]. In a separate study, the induction of microvascular lesions in an Alzheimer's mouse model was shown to alter both the deposition and clearance of amyloid-beta plaques [23]. Optical microscopy and photoacoustic imaging are potential techniques for imaging the local architecture of cerebrovascular morphology at micro-scale, however, they remain invasive and not adapted to clinical applications. Given the strong association between these microvascular events and many neurological disorders, it is of vital importance to develop a non-invasive and translatable approach to identify their presence in a clinical setting.

1.2 Objectives and Structure

The initial objective behind this work is to develop a fully-automated processing pipeline to extract useful graphical models of microvascular structures in the brain to facilitate further analysis concerned with simulating hemodynamic response and obtaining better estimation of its underlying

physiological factors. The ultimate goal is to integrate such a scheme in a comprehensive modeling framework that investigates potential biomarkers of cerebrovascular micro-occlusions , i.e., microstokes. The work presented in this thesis has been driven by three specific research objectives that align with the enclosed articles in Chapter 3, 4 and 5.

1.2.1 Objective 1

Graph models of cerebral vasculature derived from TPM angiograms have shown to be relevant to study brain microphysiology. Graphing of their inherited microvascular details remains problematic due to the limitations previously discussed. Therefore, wider and more promising applications of such datasets, especially at scale, requires a fully automatic processing scheme to save time and effort. Developing such an automated pipeline has been the first objective in this thesis. The work conducted to meet this objective forms the body of Chapter 3.

Overview

A fully-automated solution that provides a unique graph-based output for the same TPM input data, in practical computational time has been proposed. The graph extraction scheme consisted of three main stages. A modified version of a recent deep learning model for semantic segmentation [24, 25], employing fully convolutional dense blocks, was utilized to segment potential microvessels [25]. A new in-house labeled TPM dataset has been manually prepared to train the segmentation model. The volumetric output of the segmentation model is processed via 3D morphological filters to omit small isolated segments and to improve the connectivity pattern of microvessels. Second, a surface model generator has been developed to generate polygonal closed-manifold geometries for the microvasculature from its volumetric mask obtained in the first stage. Finally, 3D geometric skeletonization to generate a graph-based representation of microvessel networks, relying on surface mesh contraction [26], was integrated as a final stage to produce final graphs holding the structural and topological features of microvascular networks captured with TPM.

Article: Damseh, R., Pouliot, P., Gagnon, L., Sakadzic, S., Boas, D., Cheriet, F., and Lesage, F. (2018). Automatic graph-based modeling of brain microvessels captured with two-photon microscopy. IEEE journal of biomedical and health informatics, 23(6), 2551-2562.
[DOI:10.1109/JBHI.2018.2884678]

1.2.2 Objective 2

The methodological development carried in accordance with Objective 1 was oriented toward the modeling of high-quality TPM angiograms. Their segmented microvessel maps enjoyed smooth boundaries that simplified the creation of water-tight surface meshes, and hence, enabled the final graphing stage. However, limited applicability has been experienced when processing angiograms of lower quality, particularly those captured with other label-free optical modalities. Indeed, the label-free OCT technique, having images not confounded by dye leakage that can impair those of TPM, formed a cornerstone in the experimental design to study microstrokes in this thesis. Therefore, there has been a need for a graphing scheme that works with relaxed input requirements. Such a scheme should be less restrictive to hardly-encoded inputs (i.e., requiring triangulated watertight surface meshes) or to high quality vascular segmentation, while providing precise topological and structural representations to be used in further vascular analysis. This constitutes the second objective which is addressed in Chapter 4.

Overview

Diverging from the work in [27] and improving on the work presented in [28], a Laplacian framework has been exploited to deform 3D geometric graphs, instead of triangulated meshes, converting them into curve-skeletons as models of vascular structures. Starting with a binary-delineated vascular structure, truncated 3D grid graphs are first constructed within vessel boundaries. A technique to assign affinity weightings to these graphs based on both the binary distance transform and the local geometry of graph compartments has been developed. The weighted graphs are fed into a constrained iterative optimizer to create a Laplacian dynamic flow of graph vertices/nodes toward the centerlines of vascular structures combined with a convergence criterion to stop the iteration process. Finally, a refinement algorithm has been proposed to convert the deformed graph into a final vascular graphed-skeleton model. Interestingly, the new graphing scheme is capable of intrinsically capturing vessel radii information, and thus providing a more comprehensive anatomical features compared to the pipeline introduced in view of Objective 1.

Article: Damseh, R., Delafontaine-Martel, P., Pouliot, P., Cheriet, F., and Lesage, F. (2019). Laplacian Flow Dynamics on Geometric Graphs for Anatomical Modeling of Cerebrovascular Networks. arXiv preprint [arXiv:1912.10003]. (In second-round review with IEEE Transactions in Medical Imaging)

1.2.3 Objective 3

A recent study based on TPM has illustrated that the capillary bed in microvascular networks regenerates into a radially organized structure following a localized photothrombotic infarction [29]. To overcome limitations due to fluorescent dye leakage through the damaged blood-brain barrier, recent work exploiting OCT provided a more thorough exploration of the microvascular angioarchitecture rearrangement at different cortical depths [30] following photo-thrombosis. The latter study confirmed the presence of highly radially organized patterns, at all cortical depths, with a higher degree of structural reorganization in deeper regions. These morphological features could be exploited as clinical signatures of the associated ischemic events. As a third objective in this thesis, the aim has been to provide a proof-of-concept, through simulations, to support the hypothesis that these vascular re-orientations can be detected via magnetic resonance imaging (MRI). This objective is addressed in Chapter 5.

Overview

Diffusion-weighted imaging (DWI), which is an established MRI technique that provide contrast sensitive to the motion of water molecules [31], has been shown to be suitable for identifying cerebral micro occlusions. Computational vascular graphs combined with a 3D Monte-Carlo simulator were used to characterize the MR response, encompassing the effects of magnetic field perturbations caused by deoxyhemoglobin, and the advection and diffusion of the nuclear spins. The minimal intravoxel signal loss ratio, when applying multiple gradient directions, has been quantified at varying sequence parameters with and without arterial spin labeling (ASL). Intravoxel incoherent motion (IVIM) spin echo realistic simulations have been conducted to investigate potential signatures of cerebrovascular micro-occlusions induced in mice brains after targeted photothrombosis. Taking advantage of the radial angiogenesis around the micro-infarction locus after occlusion, a measurable biomarker based on quantifying the ratio of directional signal loss induced when using multiple gradient directions has been introduced. By integrating and excluding ASL in the simulations, parametric simulations have been also performed to evaluate the effect size when using different field strengths, readout times, b-values and gradient duration.

Article: Damseh, R., Lu, Y., Lu, X., Zhang, C., J. Marchand, P., Corbin, D., Pouliot, P., Cheriet, F. and Lesage, F. (2020). A Simulation Study Investigating Potential Diffusion-based MRI Signatures

of Microstrokes. (Submitted to Scientific Reports)

1.3 Contributions / Deliverables

The research work presented in this thesis has been performed under the umbrella of a more inclusive -and multidisciplinary- project to develop a microscopic photo-thrombotic model of micro-infarcts, to characterize and monitor the associated micro-vascular remodeling and to longitudinally investigate MRI biomarkers and microscopic predictions of these lesions. All research activities have been carried out at the Laboratory of Optical and Molecular and Imaging (LIOM), directed by my supervisor, Dr Frederic Lesage. Several original contributions have been established throughout the accomplishment of the current thesis, leading to publication of articles, conferences and computational tools that were essential for the pursuit of the parent research project. The following lists the contributions resulted from the work in this thesis.

1.3.1 JOURNALS

• **Damseh R**, Y Lu, J-Marchand P, X Lu, Pouliot P, Cheriet F and Lesage F, "Diffusion-based MRI Response as a Potential Biomarker of Cerebral Microstrokes." *(Submitted to Scientific Reports)*, 2020.

• Milecki L, Jonathan Porée J, Belgharbi H, Bourquin C, **Damseh R**, Delafontaine-Martel P, Lesage F, Gasse M and Provost J "A Deep Learning Framework for Spatiotemporal Ultrasound Localization Microscopy." *(Submitted to IEEE Transactions in Medical Imaging)*, 2020.

• Tahir W, Zhu J, Kura S, **Damseh R**, Cheng X, Lesage F, Boas D, and Tian L "Anatomical modeling of brain vasculature in two-photon microscopy by generalizable2deep learning." *(Submitted to Science Advances)*, 2020.

• Sirpal P, **Damseh R**, Kassab A, Pouliot P, Nguyen D, Lesage F "Multimodal Autoencoder for Patient-speceific Prediction of Resting State fNIRS from EEG Recordings." *(First-round review with Neuroinformatics)*, 2020

• **Damseh R**, Pouliot P, Delafontaine-Martel P, Cheriet F and Lesage F, " Laplacian Flow Dynamics on Geometric Graphs for Anatomical Modeling of Cerebrovascular Networks." *(arXiv, Second-round review with IEEE Transactions in Medical Imaging)*, 2019.

• X LU, M Moeini, B Li, Y Lu, **Damseh R**, Pouliot P Thorin E and Lesage F "Changes in capillary hemodynamics and its modulation by exercise in the APP-PS1 Alzheimer mouse model." *Frontiers in Neuroscience*, 2019.

• **Damseh R**, Pouliot P. , Gagnon L, Sakadzic S, Boas D, Cheriet F and Lesage F, "Automatic

Graph-based Modeling of Brain Microvessels Captured with Two-Photon Microscopy." *IEEE Journal of Biomedical and Health Informatics (JBHI)*, 2018.

• Moeini M, Lu X, Avti P K, **Damseh, R**, Bélanger S, Picard F. and Lesage F."Compromised microvascular oxygen delivery increases brain tissue vulnerability with age." *Scientific Reports*, 2018.

1.3.2 CONFERENCES

• **Damseh R**, Delafontaine-Martel P, J-Marchand P, Sirpal P, Cheriet F, Lesage F, "Automated Analysis of Brain Microvasculature: From Segmentation to Anatomical Modeling." *Annual International Conference of the IEEE Engineering in Medicine and Biology Society (IEEE EMBC)*, 2020.

• **Damseh R**, Pouliot P, Cheriet F and Lesage F,"Modeling the Topology of Cerebral Microvessels via Geometric Graph Contraction." *IEEE Symposium on Medical Imaging (ISBI)*, 2020.

• Tahir W, ..., **Damseh R**, Lesage F, ..., and Tian L, "A Generalizable Deep-learning Approach to Anatomical Modeling of Brain Vasculature." *Neural Imaging and Sensing, International Society for Optics and Photonics*, 2020.

• Belgharbi H, Porée J, **Damseh R**, Delafontaine-Martel P, Lesage F and Provost J,"Anatomically-Realistic Simulation Framework for Ultrasound Localization Microscopy." *The Journal of the Acoustical Society of America*, 2019

• **Damseh R**, Cheriet F, and Lesage F "Fully Convolutional DenseNets for Segmentation of Microvessels in Two-photon Microscopy." *Proceedings of the Annual International Conference of the IEEE Engineering in Medicine and Biology Society (IEEE EMBC)*, 2018.

• Delafontaine-Martel P, Lefebvre J, **Damseh R**, Castonguay A, Tardif P and Lesage F "Large scale serial two-photon microscopy to investigate local vascular changes in whole rodent brain models of Alzheimer's disease." *Proceedings of Multiphoton Microscopy in the Biomedical Sciences XVIII, International Society for Optics and Photonics*, 2018.

1.3.3 TOOLS and DATASETS

Below are the datasets and tools delivered throughout the research work in this thesis:

• Manually segmented TPM dataset has been prepared based on raw inputs obtained by colleagues working on other projects conducted at LIOM [32, 33]. The dataset comprised about 100 256x256 slices, and was prepared with the help of three intern students in Summer 2017 and Summer 2018.

• A neural network to segment microvessels has been trained, using the dataset mentioned above,

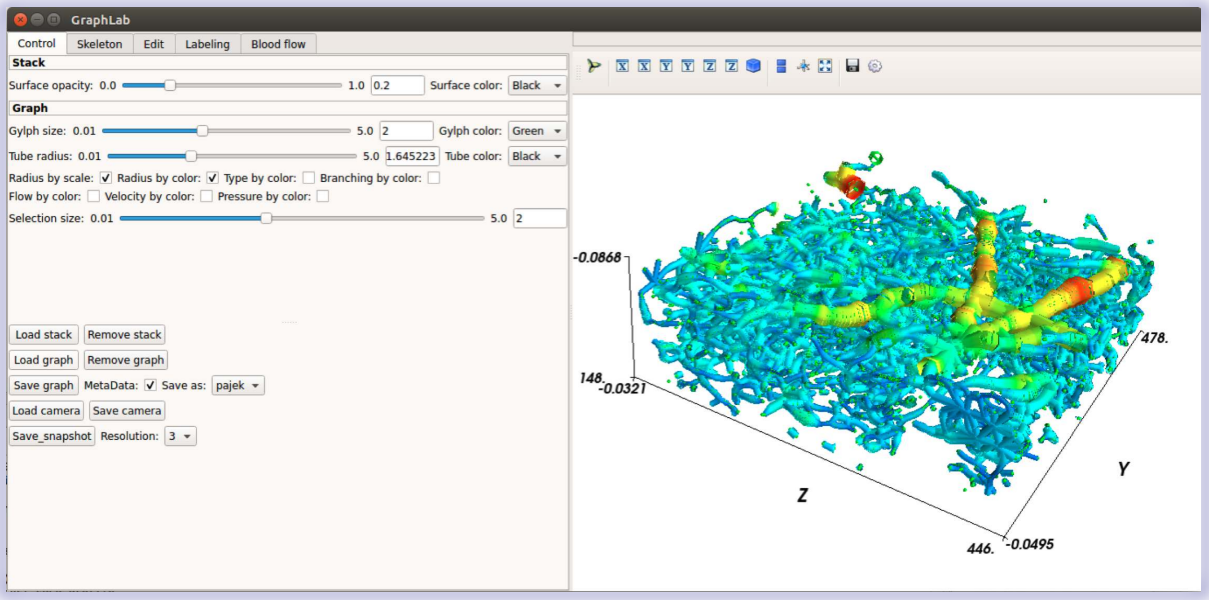

Figure 1.1 A snapshot of the GraphLab GUI built to help visualize and analyze graphed vascular networks. This tool is integrated with the VascGraph Python package that has been developed in the course of this thesis.

and made available on a local server at LIOM; the network is explained in Chapter 3. This network was utilized by other colleagues at LIOM to measure vascular densities in their studies [33–35].

• *VascGraph:* A python package that includes mainly the implementation of the methodological scheme in Chapter 4. It provides extra routines for graph processing, e.g., writing & reading of graph objects, vessel segments clustering, flow propagation. It includes the GraphLab submodule, which is introduced below.

• *GraphLab:* A GUI visualization platform in Python developed based on VTK and MayaVi libraries. It allows for interactive visualization, annotation and modification of graph structures with anatomical and physiological parameters assigned to their nodes. Also, it integrates the routines for skeletonization and flow propagation. The package is made available on `https://github.com/Damseh/VascularGraph`.

• *VirtualMRI:* A Python package developed on top of VascGraph to characterize the intravoxel MRI response through 3D Monte-Carlo simulations of the nuclear spins encompassing the effects of their advection and diffusion. The package will be made available soon!

• *AngioPulse:* A Python package developed on top of VascGraph to simulate the pulsatile haemodynamics at the micro scale. It is still under development!

CHAPTER 2 LITERATURE REVIEW & MATERIALS

The research project conducted in this thesis has a multidisciplinary essence, comprising various aspects, i.e., computational biology and quantitative neuroscience, deep learning and image segmentation, geometry processing and visualization, simulations and medical/optical image acquisition. To help understand the underlying work, this chapter introduces the necessary materials and provide an up-to-date report of the recent literature on each of these aspects.

2.1 Biological Problem

This section is designated to provide the necessary background to better understand the biological side of the project conducted in this thesis.

2.1.1 Brain Microvasculature

The Brain

Our brain is considered as the most complex organ that is still poorly understood. It is responsible for our movement, homeostasis, and sensation. Beside, it provides us with consciousness, memory, and the ability to be self-aware. The brain is protected by several layers: the skull, the pia mater, arachnoid mater, and dura mater (See Figure 2.1). The three mater layers are referred to as the meninges. They are mainly responsible for protecting the brain and central nervous system. The space between the arachnoid and pia mater hosts the circulation of the cerebrospinal fluid (CSF). The brain is divided into three main regions: the brain stem, the cerebellum, and the cerebrum (See Figure 2.1). These regions work in tandem to ensure a healthy brain function. However, studies have suggested that the cerebrum, which is the largest region of the brain, is responsible for most brain functions including all voluntary actions, emotions, hearing, vision, language, and memory [37]. The cerebrum is composed of the cerebral cortex (the outer grey matter) and the underlying white matter (See Figure 2.1). The grey matter contains the cell bodies of our neurons, and has a dense microvascular networks to accommodate the increased energy demands of these neurons [38]. On the other hand, the white matter contains the axonal part of some connecting neurons, and it is given its colour due to the myelinated sheaths of axons which transmit signals across the brain [37].

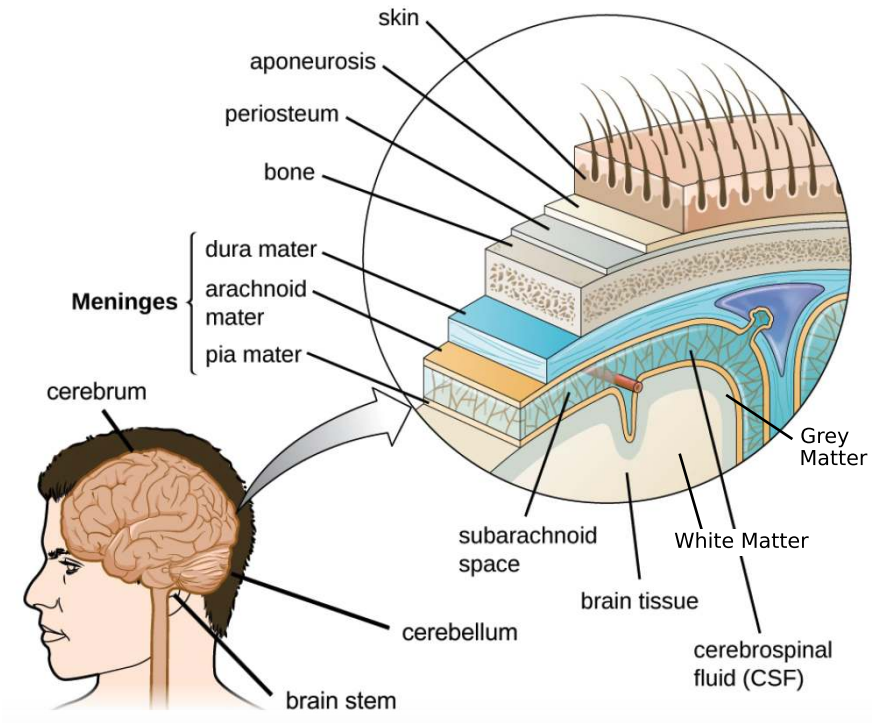

Figure 2.1 Overview of the brain anatomy and its protective layers. (Reproduced from [36])

Cerebral Microvascular Networks

On average, the brain forms only 2% of the body total mass in an adult human; however, it consumes 20% of the oxygen supply [39]. Therefore, our brain requires a continuous supply of blood and oxygen to keep functioning, while a reduction in flow could quickly lead into tissue death. A massive microvascular network provides the necessary distribution of blood and oxygen in our brain; also, it ensures the supply of nutrients and the removal of metabolic waste. The cerebral microcirculation acts as a short-term regulation system, which responds quickly and locally to the metabolic needs of neurons [40], in a process called neurovascular coupling. The cerebral microvascular system includes several architectural components: the pial and penetrating arterioles, the capillaries and the ascending venules (see Figure 2.2). The pial arterioles form a quasi-fractal hierarchy of vessels [41, 42] whose diameter decreases at each successive bifurcation, thus minimizing the time for supplying resources [42]. These vessels feed into the capillary bed, which consists of the smallest vessels in the vasculature with a diameter $\sim 5\mu$m, and forms a dense and 3D interconnected structure. The nature of cerebral capillary structures allows for extremely large surface area facilitating their vital role in nutrient exchange. The volume fraction of the microvasculature volume ranges between 1% and 3% of total brain tissue depending on species type [43]. A good review of the microvasculature of various species is provided in [43].

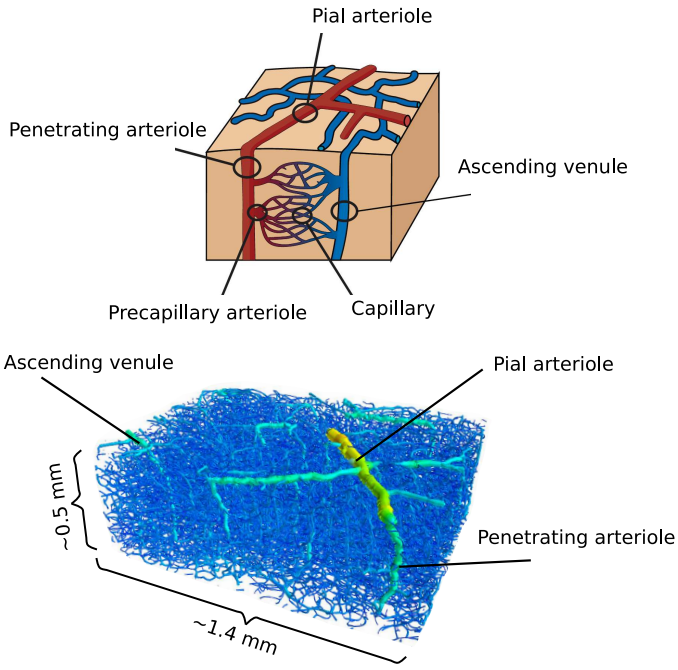

Figure 2.2 The components of a cerebral microvascular unit. (Below) A microvascular unit reconstructed from the mouse cerebral cortex.

Cerebral Microvascular Models

Multi-scale structural characterization of cerebral microvasculature is fundamental for understanding brain physiology and function at various pathological states. These complex networks comprise a high level of heterogeneity in the associated blood flow, transit time and solute transport [44, 45]. Still, capturing the associated anatomical details remains tedious due the inherited structural complexity, limitations in acquisition protocols and the lack of automated reconstruction pipelines. Several attempts have been done to extract computational model of microvascular networks following three main procedures: 1) Approximating their anatomical compartments, while neglecting some geometrical features, to build simplified representations [46]; 2) Synthetic reconstruction of fully resolved representations through biologically-inspired angiogenesis [5]; 3) Casting/reconstruction of 3D computational models from raw structural images captured through microscopic acquisition techniques [47].

Initial models treated the cerebral vascular network as a two-compartment serial pipe with a dilating arteriole and a passively responding venule [48, 49]. However, discrepancies have been reported between the calculations computed with these simplified schemes and the experimental measurements obtained with high temporal resolution optical imaging [50]. More representative three-compartment models [46, 51], composed of an actively dilating arteriole and a passively re-

sponding capillary and venule, was then proposed. A parallel three-compartment vascular anatomical network (VAN) was proposed [46]. Models parameters were driven from physical properties of the vascular network: vessel segment diameters, lengths and viscosity.

Many research works have paved the way for more biologically plausible synthetic circuitries [3–6, 52–55]. A generic model was created using 2D/3D voronoi tessellation in which each edge represents a capillary segment [52, 53]. The method was capable of creating appropriate generic cerebrovascular models with association to each part of the brain cortex based on morphometric parameters extracted from physiological data of the human cortex. Following a similar approach, constrained Voronoi diagrams were applied to generate 3D synthetic cerebral capillary networks that are locally randomized, yet homogeneous at the network-scale. After a careful scale setting, these networks were proved to capture similar properties to the anatomical counterpart. In another work, the authors were able to generate a microvascular geometry through controlling asymmetric conditions of microvascular networks [3]. However, their models were dissimilar to capillary cerebrovascular units. Linninger et al. introduced a detailed three-dimensional anatomically consistent microvascular modeling, where vessel segments are assembled with optimization algorithms emulating angiogenic growth; and aconsequrntly synthetic capillary bed was built with space filling procedures [55]. In a more courageous attempt, as a precursor to the human brain vascular modeling, Linninger et al. presented a computational framework for synthesizing anatomically accurate large-scale microvascular models of the mouse brain [5]. They introduced a new scheme denoted as image-based circulatory network synthesis (iCNS) that combines the critical advantages of image-based models with synthetic vascular growth. Recently, Peyrounette et al. proposed a simplified three-dimensional representation of the capillary networks [6]. Their network segments were composed of elementary patterns of 6- or 3-regular neighborhood constructed from the tessellation of the solution domain into 3D cubic regular grid. Their model proved to have a substantial computational gain over that generated using complex-geometry cerebrovascular modeling.

Other studies relied on image processing techniques to extract computational microvascular models from angiography images. In [57], marmoset brain vasculature were reconstructed from images acquired through 3D synchrotron microtomography. In [47, 58], through TPM angiography, structural images based on FITC-labeled blood plasma were used to construct graphs of the microvascular network of rats. In [59], Computailn micovascular models from homologous sections of the somatosensory cortex in four mice were extracted after imaging with TPM. In [60], three microvascular networks were studied from the mouse parietal cerebral cortex, also after acquiring the networks using TPM. More promising studies tried to reconstruct full scale networks from rodent brains. In [61], a detailed reconstruction of the brainwide vasculature at the capillary level were performed using a novel approach that improves vascular demarcation by combining CLARITY with a vascular staining approach that can fill the entire blood vessel lumen, and imaging with

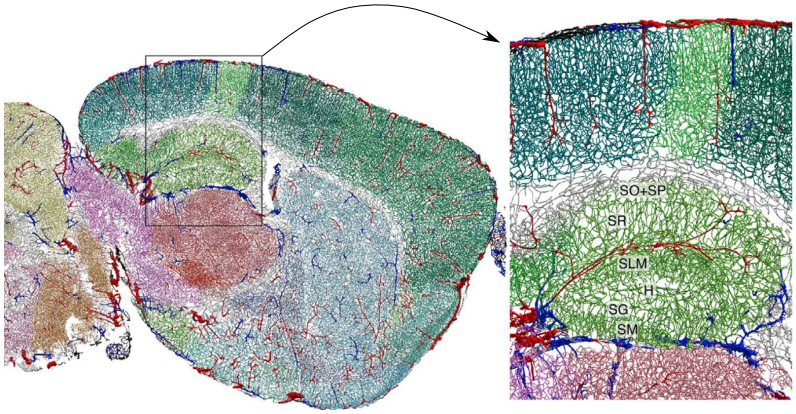

Figure 2.3 Reconstruction of a fine-scaled labeled microvasculature from the hippocampus region in the mouse brain. (Reproduced from [56])

light-sheet fluorescence microscopy (LFSM). In [62], The authors made a precise atlas for cerebral arteries and veins using micro-optical sectioning tomography (MOST) with a modified Nissl staining method. They acquired five mouse brain data sets containing arteries, veins, and microvessels. In [56], a comprehensive work has been done to reconstruct the whole microvascular network in 20 adult mouse brains, using immunolabeling, tissue clearing and LFSM imaging. Their labeled reconstruction enabled the analysis and visualization of vascular graphs composed of over 100 million vessel segments (see Figure 2.3).

Applications of Cerebral Microvascular Modeling

As previously discussed, shape and morphological features of cerebral microvascular networks determine its role in delivering necessary nutrients and meeting metabolic demands of brain tissues[44]. Computational models of microvascular networks have been applied to interpret the macroscopic BOLD response and to understand haemodynamics and cerebral microcirculation. Here, recent potential applications are reviewed.

A study by Gagnon et al. proposed an MR Monte-Carlo simulation framework to understand how oxygen distribution in microvascular compartments contribute to the BOLD signal for specific MR sequence parameters and arbitrary magnetic field strengths [47]. The study takes advantage of TPM combined with an advanced numerical scheme [58] to build a fully resolved geometric representation of microvascular networks with oxygen quantities mapped across vascular compartments at the capillary level. These physiological measurements were then utilized to simulate the BOLD signal from first principles. Interestingly, simulation outputs were also validated against experimental functional magnetic resonance imaging (fMRI) acquisitions with gradient echo (GRE) sequence after a same forepaw stimulus. Gilberto et al. [9] performed a similar study to analyze oxygenation-

related signal alternations in passband balanced steady state free precession (bSSFP), GRE and spin echo (SE) sequences. MR responses were calculated based on both synthetic capillary cylinders and realistic microvascular networks acquired from the mouse parietal cortex through two-photon microscopy scanning. The authors reported an association map between MR signal changes and vessel size, blood volume, and vessel orientation to the main magnetic field. Furthermore, they analyzed the relations between intra- and extravascular, and of micro- and macrovascular contributions to the output MR signal. In contrast to Gagnon et al. trial [47], simplified susceptibility differences between vessel types were used, being one of the main limitations. Hinging on the previous two works, Uhlirova et al. [63] provided a road map for potential clinical identification of cell-type-specific neuronal activity from non-invasive physiological measurements, i.e., fMRI and magnetoencephalography (MEG)/electroencephalography (EEG) observables. They argued that such an approach is feasible upon the identification of the vasoactive role, energetic costs and extracellular electrical potentials associated with activity of specific neuronal cell types through simulations [9, 47] in model organisms studies. Cheng et al. extended the Monte-carlo physiologically-informed MR simulation to analyze the susceptibility effect on the transverse relaxation rate based on realistic microvascular anatomical models. In particular, they aimed at estimating the exponent in the power law that relates the relaxation rate of transverse magnetization to intra-extravascular magnetic susceptibility differences. The value of that exponent was also estimated when introducing contrast agents leading to higher susceptibility concentration than that used for BOLD fMRI calculations. The work has shed the light on the effect of proton diffusion on MR signals associated with cerebral blood volume (CBV) and cerebral metabolic rate of oxygen (CMRO2) measurements. All studies that worked on correlating microscopic measurements with macroscopic fMRI in mice models were relying on acquisitions from anesthetized animals. Since anesthesia can differentially affect blood flow and neurovascular and metabolic coupling, Desjardins et al. [64] provided a protocol feasible for obtaining BOLD fMRI measurements in awake mice that are implanted with long-term glass cranial windows, without any noticeable deterioration of fMRI signal quality. One encouraging application of MR Monte-Carlo simulations based on microscopic vascular anatomical and physiological measurements is fingerprinting the time evolution of the MR signal to retrieve quantitative information about the microvascular network [10, 65, 66]. Christen et al. [66] used a fingerprint defined as the ratio of signals acquired pre- and post-injection of an iron-based contrast agent. Based on gradient echo sampling of the free induction decay and spin echo sequence, they simulated MR responses of virtual voxels, containing blood vessels varying in CBV, mean vessel radius, and blood oxygen saturation (SO2) to obtain a dictionary of all possible signal evolutions. They proved that such fingerprinting enables a high-resolution dictionary mapping between microvascular networks structural and physiological features and the expected MR response. Pouliot et al. [10] elaborated on Christen et al. work through studying the vascular MR fingerprints gen-

erated using realistic models of mouse microvascular networks accompanied with fully-resolved physiological values. They have shown that simulation parameters are fully identifiable with high signal-to-noise ratios (SNR) when a single network model is used for dictionary generation. Large biases in the estimates are observed when the angiograms are different. Nevertheless, their simulations showed that differences in parameters remain estimable. Five dimensional dictionaries were produced, from 6 real angiograms captured from mouse somatosensory cortex, to represent the MR signal profile through GESFIDE sequence.

Several theoretical schemes have been developed in the literature to approximate functional changes in CMRO2 from alterations in cerebrovascular parameters [46, 48–51]. Initial models treated the cerebral vascular network as a two-compartment serial pipe with a dilating arteriole and a passively responding venule [48, 49]. More representative three-compartment model [46, 51], composed of an actively dilating arteriole and a passively responding capillary and venule, was then proposed to accurately predict the oxygenation response as observed in optical imaging data. A more detailed understanding of the spatiotemporal nature of the hemodynamic response and better estimation of its underlying physiological factors was achieved in [46]. Other works aimed at studying cerebral circulation based on biologically plausible synthetic circuitries [4–6, 52–54, 59]. In [52, 53], the hemodynamics and oxygen transport were numerically simulated in the synthetic model, which involves rheological laws in the capillaries, oxygen diffusion, and non-linear binding of oxygen to hemoglobin. Schmid et al. found clear laminar pathways of the RBCs in the flow, shunting between penetrating arterioles and venules, thus indicating a depth dependence on flow and pressure characteristics [60]. Gould et al. found that the wide variation in haemodynamic states in the quasi-random capillary bed was responsible for relatively uniform cortical tissue perfusion and oxygenation [59]. In [6], a new modeling scheme was devised to accurately describe blood flow at large scales.

2.1.2 Ischemic Microinfarctions and Microstrokes

By 2050, dementia will affect 5% of the global population [67], while unfortunately, there is still no cure available with poor knowledge about its evolution. Vascular factors have been recognized in vascular dementia and their relative importance has been furthered with the recognition that all risk factors for Alzheimer's disease (AD) are cardiovascular. Neurovascular coupling describes how local neuronal activity through the coordinated action of smooth muscle cells, endothelial cells, and pericytes, adjusts local cerebral blood flow (CBF) to meet these changing needs. In hypertension [68], Alzheimer's disease [69], age and stroke, documented disruptions in neurovascular coupling suggest that CBF may become uncoupled with the underlying tissue metabolic needs, with potential deleterious consequences on cognition. Aging and vascular diseases are associated with changes

in brain vascular characteristics including thickening of endothelial basement membranes, variable capillary diameters, the presence of lacunas, reduced capillary density, and pericyte loss. These changes are exacerbated in hypertension and Alzheimer's disease with the addition of pericyte degeneration and swelling of the endothelium surrounding astrocytic end-feet. These observations suggest a close association between cerebral vascular dysfunction and the onset and progression of different neurodegenerative diseases. One major issue when clinically analyzing cerebral vascular changes is being invisible at small scales.

The link between major vascular events, such as acute stroke, and their subsequent impact on brain function has long been established. However, the sub-clinical impact of vascular disease on the brain remains poorly understood. In the literature, a correlation has also been established between some cardiovascular risk factors, such as hypertension, elevated cholesterol levels, atherosclerosis, and white matter lesions/cognitive deficits [70, 71]. A major category of these deficits are small infarcts documented to occur both in white matter and in the cortex [72]. Micro-infarcts are defined by small regions of cellular death, invisible to the naked eye, typically of size less than 1mm [19]. In the aging brain, their occurrence ranges from 16% to 46% independent of the cause of death. However, the characterization of their impact remains elusive, even the number of infarcts required to impair cognition is variable. One hypothesis is that this variability can be explained by the more widespread presence of micro-infarcts. Micro-infarcts are invisible except in post-mortem pathological studies using optical microscopy, which do not allow for investigations to be cross-sectional and associative.

Investigating the time course of microinfarcts and identifying measurable biomarkers thus remains a major challenge. Using two-photon phosphorescence lifetime imaging, an age-dependent shift in oxygen delivery between small arterioles and capillaries was observed [33]. For the first time, the presence of sparse pockets of hypoxia in older mice but not in younger and middle-aged ones has been uncovered [33]. It worth mentioning that the investigation of their sparsity and longitudinal formation, along with their effect on brain function, remains a difficult task. It has been shown that inducing micro-occlusions in a penetrating arteriole in the mouse brain leads to tissue infarction [19]. Many other works have relied on inducing photothrombotic clots in single penetrating arterioles as a model of microinfarcts in the mouse cortex [20, 73–76]. In [73], the functional role of arterio-arteriolar anastomosis (AAA) in regulating blood perfusion through penetrating arterioles has been studied. Label-free optical microangiography (OMAG) technique was used to evaluate the changes in vessel lumen diameter and red blood cell velocity among a large number of pial and penetrating arterioles within AAA abundant region overlaying the penumbra in the parietal cortex after a middle cerebral artery occlusion (MCAO). The OMAG technique made it possible to image a large number of vessels in a short period of time without administering exogenous contrast agents during a time-constrained MCAO experiment. In [20], after experimentally creating microinfarcts

in the mouse cortex through induction of photothrombotic clots in penetrating arterioles, hemodynamic changes in tissues surrounding the occluded vessel have been studied using in vivo TPM. A spectrum of infarct volumes resulting from occluding high-flux penetrating arterioles exhibited a radial outgrowth that encompassed unusually large tissue volumes. The gradual expansion of these infarcts was propagated by an evolving insufficiency in capillary flow that encroached on territories of neighboring penetrating arterioles, leading to the stagnation and recruitment of their perfusion domains into the final infarct volume. In [74], the authors showed that small regions of the capillary bed can similarly be occluded to study the ischemic response within the capillary system of the mouse cerebral cortex. The advantage of this approach is that the ischemic zone is restricted to a diameter of approximately 150–250 μ m. This permits better TPM imaging of degenerative processes that are difficult to visualize with models of large-scale stroke, due to excessive photon scattering. In their study, capillary leakage has been quantified by determining the spatial extent and localization of intravenous dye extravasation. In [75], microsphere cerebrovascular occlusions were quantified and changes in cerebral blood flow were measured with laser speckle imaging. Through mesoscopic longitudinal functional connectivity mapping in awake mice, the neurodeficit score in microinfarct mice indicated impairment in motor function. In [76], a photothrombosis stroke model that is capable of targeting a single distal pial branch of the middle cerebral artery with minimal damage to the surrounding parenchyma in awake head-fixed mice was described. Through quantifiable behavior deficits and chronic imaging, the authors showed that their model can be used to study recovery mechanisms or the effects of therapeutics longitudinally.

2.2 Image and Geometry Processing

Here, the topics of deep learning, image segmentation and geometry processing are reviewed.

2.2.1 Deep Learning

Over the past decade, the topic of deep learning (DL) has exponentially overwhelmed the machine learning community, and nowadays it occupies almost all the discussions running along the related academic gatherings, conference proceedings and scientific articles. It induced a quantum leap in the artificial intelligence domain, and it has been commonly regarded as the basis for a third technological/industrial revolution affecting all aspects of life, from cooking, art work and gaming to security, energy, autonomous driving and space discovery. The result is an enormous number of technological startups, massive number of papers, and tons and tons of implementations. Several cutting-edge development frameworks have been introduced by main industrial giants like Facebook (launching PyTorch), and Google (launching TensorFlow). It is nearly impossible to cover all the literature recently introduced in this field. Nevertheless, some of the main cornerstone works

and game-changing articles will be covered below.

Brief Overview

Deep learning is an approach for constructing computational models as artificial neural networks that mimic their biological counterparts; these models consist of multiple processing units/layers to discover representations of data. The term *deep* indicates the aim at producing multiple levels of abstraction for understanding our environment [77]. Deep neural networks are extremely helpful in discovering intricate structures hidden in large data sets, thanks to the algorithm of backpropagation [78] to fit network parameters. Other attempts have been carried out to search for alternatives of backpropagation to enhance the learning process of these networks [79, 80]. Many forms of deep neural networks along with different applications have been introduced [81]. Next, major findings and recent literature found in principle research avenues diverged from the theory of deep neural networks are discussed.

Types of Learning

Learning algorithms of a deep learning model are determined depending on whether to incorporate human manual annotations, the task that the system is designed to tackle and the procedure followed to refine connection weights.

- Supervised learning: The concern here is to build a function that maps inputs to desired outputs, which have been manually prepared. One standard form of supervised learning is the classification problem where a model is trained to categorize an input based on a finite set of classes, by assigning it a probability for each class. One example is the work by Krizhevsky et al. ImageNet classification [82]; the work was a breakthrough that used convolutional nets to almost halve the error rate for image classification, and precipitated the rapid adoption of deep learning by the computer vision community (see Figure 2.4).
- Unsupervised/self-supervised learning: these algorithms deal with unlabeled inputs to perform a variety of tasks including:
  - Clustering: the deep learning model is trained to distinguish between data points and group similar ones together. A survey on clustering via deep learning is provided in [83].
  - Anomaly detection: the detection of fraudulent examples by looking for unusual patterns in them. Similarly, unsupervised learning can be used to flag outliers in a dataset. An example of such an application is found in [84].

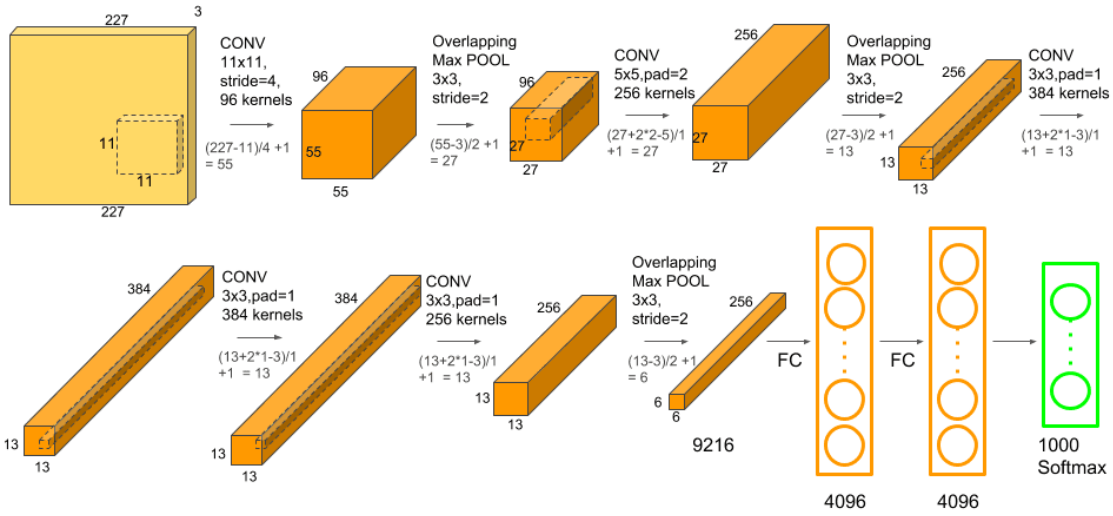

Figure 2.4 AlexNet: a convolutional neural network that made a large impact on the field of deep learning, specifically in the application to machine vision [82]. It famously won the 2012 ImageNet LSVRC-2012 competition by a large margin, 15.3% error rate compared to 26.2% as the second place. (Adapted from https://neurohive.io/)

  - Association: this type of learning is performed to associate certain features of a data sample with other features. By characterizing some key attributes of a data point, an unsupervised learning model can predict other related attributes [85].
  - Autoencoding: an autoencoder takes an input data, compresses it into a code/vector that resides in a latent space, and then tries to recreate the input data from that latent vector. Developing these types of learning models is among the most interesting research directions in deep learning with applications expanded for data compression into data understanding. This topic will be covered, separately, later in this section.

- Semi-supervised learning: these algorithms combine both labeled and unlabeled examples to train a learning model [86, 87]. Since supervised deep learning usually requires large amounts of labeled data, applicability to new problems, e.g., those in the biomedical field [88], is hindered due to scarce labeled samples. Generating manual annotations is always costly and tedious.

- Weakly-supervised Learning: weakly-supervised learning refers to learning methods accepting coarse-grained, incomplete or inaccurate labels. The cost of training through weak supervision is substantially cheaper than preparing fine-grained labels inputs. An example for

a weakly-supervised deep learning architecture for object detection is given in [89].

- Reinforcement learning: this type of learning occupies an expansive space in machine learning research. Briefly, the learning algorithm here actively learns a policy of how an agent acts based on a given observation in real-time scenarios. Every action impacts the environment, and conversely the environment provides feedback that progressively guides the learning process of the agent. Surprising advances in this field have been achieved through the integration of deep learning. The DeepMind team proposed a deep model, denoted as Q-network, that has been successfully trained to learn policies directly from high-dimensional sensory inputs on classic Atari 2600 games, using end-to-end reinforcement learning [90]. It achieved a level comparable to that of a professional human on 49 games. Another two striking works reported by the same team in 2016 and 2017, providing a computer program, called AlphaGo, that for the first time defeated a human professional player in the full-sized game of Go, a feat previously thought to be at least a decade away [91, 92].

- Learning to learn: also referred to as meta-learning, where the model learns its own inductive bias based on previous experience. In other words, the goal is to design learning algorithms that can fit new data more efficiently through faster convergence with less input examples. A famous and recent proposal for model-agnostic meta-learning approach to easily fine-tune deep learning models is presented in [93].

Convolutional Networks

The first introduction of convolutional neural networks (CNN) goes back to the work of LeCun et. al. in 1989 for processing of gridlike topological data, i.e., MNIST data, [94, 95]. CNNs are a type of neural networks that have shown a tremendous success in visual context learning with applications encompassing but not restricted to classification [82, 95–101], segmentation [102–106], object detection [107–111], and image captioning and understanding [112–117]. The topic of deep semantic image segmentation will be covered later in this section. CNNs have also shown impressive performance in exploiting correlation in other types of data, e.g., textual data in natural language processing [118] and graph structured data [119]. A separate part of this section will be designated to discuss graph structured data processing with deep learning using graph neural networks (GNN). The architecture of a typical CNN is composed of a series of processing blocks [120]. A standard block includes convolutional and pooling layers. Units in a convolutional layer are organized in feature maps. A unit is connected to local patches in the feature maps of the previous layer through a set of weights called a filter bank. The output of the local weighted sum is processed through a non-linear operation, e.g. ReLU [121]. The non-linearity generates different patterns of activations for different responses and thus facilitates the learning of semantic features

in images. The output of the non-linear activation function is ideally followed by a pooling layer, i.e., subsampling operation, to help abstracting the convolutional output and making it invariant to geometrical distortions [122]. All units in a feature map share the same filter bank. Different feature maps in a layer use different filter banks. The design of CNNS were inspired by Hubel and Wiesel's work and thus follows the basic structure of the primate's visual cortex [123]. The learning process in CNN has shown resemblance to that in the primate's ventral pathway of the visual cortex [124, 125]. The multilayered and hierarchical structure of deep CNN, emulating the deep and layered structure of the human brain neocortex, is the crucial characteristic that allows for extracting low, mid, and high-level features. The availability of data resources and advancements in hardware capacity are main reasons for the explosive growth in using CNNs. Various improvements on CNN architectures have been proposed to scale for heterogeneous, complex, and multiclass problems. These enhancements became more prevalent after the exemplary performance of AlexNet [82], mentioned previously and shown in Figure 2.4. The layer-wise visualization of CNNc introduced in [126] improved the understanding of feature extraction stages. A new popular architecture denoted as VGG has been introduced in [96]. It contained more convolutional layers than that in [82], and shifted the interest towards the extraction of features at higher abstraction layers. Many new architectures have been built following the principle of simple and homogenous architectural topology, as introduced in VGG. Google AI team introduced an innovative idea of a split, transform and merge of features, codenamed as inception. The concept of inception allowed for the abstraction of features at different spatial scales [97]. More deep convolutional networks became achievable through the concept of residual skip connections introduced in [98]; the corresponding architectures referred to as ResNets. Residual connections was then employed by most of the succeeding enhanced networks, such as Inception-ResNet and ResNeXt [127, 128]. Densely connected architecture, or DenseNets, has been proposed in [99] relying on concatenation blocks rather than residual connections for information flow. More efficient architectural designs and implementations have been recently proposed to both decrease the number of parameters and improve the performance [100, 101], helping to scale the use of these networks even on low-capacity hardware setups.

Recurrent Networks

Recurrent neural networks (RNNs) are a family of artificial neural networks that have a long history of modelling sequential data for various applications ranging from natural language processing to stock prediction [130–132]. The structure of RNNs serve to include memory modeling where a hidden layer within the network at a time is conditioned on its previous states [132]. This structure of RNNs enables the processing of complex signals monitored for long time periods. RNNs can map an arbitrary input sequence to an arbitrary output sequence (see Figure 2.5). Compared to other

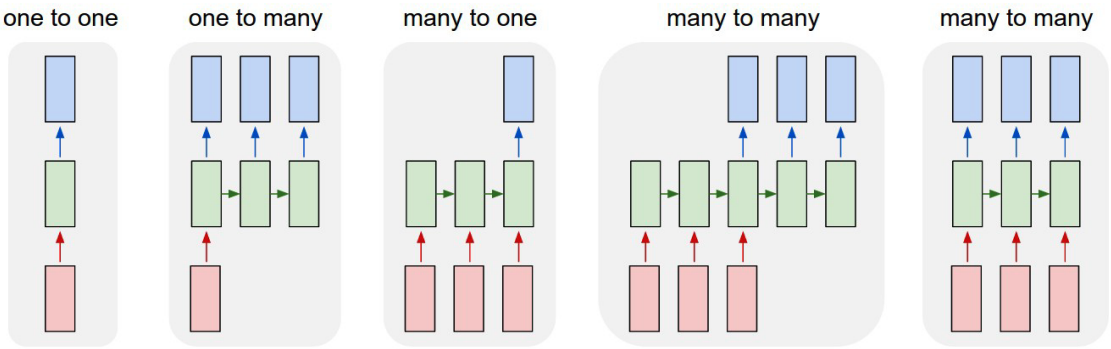

Figure 2.5 Various forms of RNNs used in different applications. (Adapted from [129])

forms of feed forward neural networks, RNNS are more difficult to train due to the problem of vanishing gradients [130]. One of the most notable variants, and most widely used, are the long short term memory (LSTM) networks [133], which can in principle store and retrieve information over long sequences with explicit gating mechanisms and a built-in constant error carousel. Recently, there has been renewed interest in further improvement on the RNNS basic architectures. Examples of resulting works are the gated recurrent units (GRUs) [134] and incorporating content-based soft attention mechanisms [135]. One recent and major work in recurrent data processing, specially applied to language processing tasks, is the bidirectional encoder representations from transformers (BERT) proposed by Google AI team [136]. BERT is designed to pretrain deep bidirectional representations, single-direction models, from unlabeled text by jointly conditioning on both left and right context in all layers. The proposal is based on the concepts attention and transformers [137], which is currently gaining a tremendous interest in the machine learning community. As a result, the BERT model can be finetuned with just one additional output layer showing state-of-the-art results tasks like question answering and language inference, without substantial task specific modifications. Successful application of BERT has been done on biomedical textual datasets [138].

Graph Networks

While most successful deep learning models have been proposed to particularly deal with datasets embodied within an Euclidean structure i.e., structured grids, there has been an escalating interest toward learning from non-Euclidean geometric data, e.g., graphs, [139]. These types of data arise in numerous applications, such as social networks [140], functional structures of the brain [141], and molecular biology and pharmacology [142]. Non-Euclidean representations do not have the familiar properties such as global parameterization, common system of coordinates or shift-invariance. Consequently, conventional operations in the Euclidean case like convolutions, do not have a straightforward translation on non-Euclidean domains. Many works have been proposed to

extend deep learning approaches for graph-based datasets [139]. One of the main and first works is presented in [140]. A scalable approach for semi-supervised learning approach operating directly on graphs, based on an efficient variant of convolutional neural networks, is proposed. First-order approximation of spectral graph convolutions have been used. Other works based on deep learning and applied to extract graph embeddings are recently proposed [143, 144]. An interesting work leveraged the concept of attention to address the shortcomings of prior methods based on graph convolutions and their approximations [145]. In that work, several key challenges of spectral-based graph neural networks have been tackled, and the presented model made readily applicable to inductive as well as transductive problems. In another work, convolution operations in neural networks have been reformulated to deal with point clouds, a flexible geometric representation suitable for countless applications in computer graphics [146]. A promising application of deep graph learning in medicine is the modeling polypharmacy side effects [142]. The authors processed a multimodal graph, with a large number of edge types, of protein–protein interactions, drug–protein target interactions and polypharmacy side effects, which were represented as drug–drug interactions. At the time of writing this thesis, humanity is struggling to face the overwhelming COVID-19 pandemic. This demands a rapid identification of drug-repurposing candidates. In [147], a predictive model has been proposed, based on deep graph learning, to study host-pathogen interactions, unveil the molecular mechanisms of the infection, identify comorbidities as well as rapidly detect drug repurposing candidates.

Generative Models

Deep generative models have resulted as one of the most astonishing outcomes of the deep learning research [81]. Rather than learning for discriminative tasks, the primary interest here is to learn the distribution that summarizes all the information about a certain dataset. These models could be then applied to generate new fake but realistic samples from the learned distribution. These Generative models can be categorized into those learning implicit [148] and explicit distributions [149]. Large number of papers have been produced in this domain in the past five years. Some recent developments with state-of-the-art performance for generative modeling in computer vision are presented in [150, 151].

Regularization

One of the most important characteristics of a successful deep learning model is its ability to generalize for new inputs not seen during the training process. Many strategies have been designed to reduce the test error, i.e., regularization of the trained model. The most common techniques for regularisation are Dropout [152], L2 and L1 regularization, data augmentation and early stopping

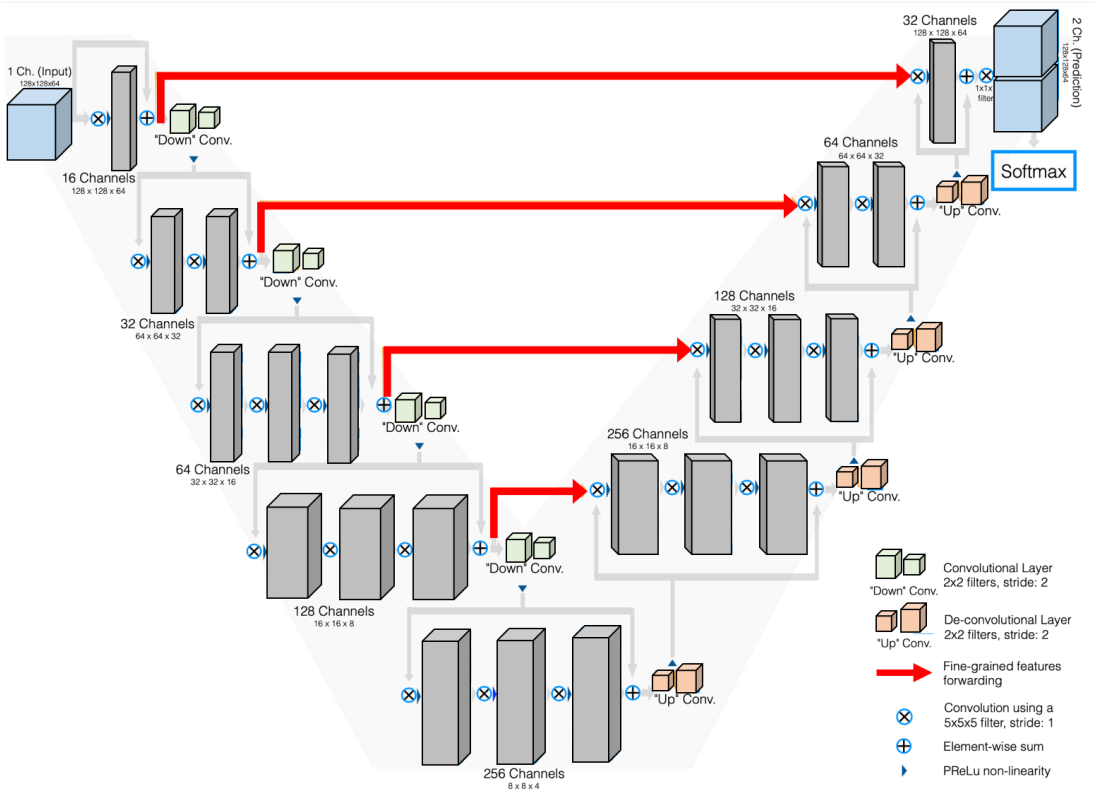

Figure 2.6 The architecture of V-Net [154], which was proposed for 3D segmentation of biomedical images. (Adapted from [153])

[81].

2.2.2 Deep Segmentation

In this section, recent advances in image segmentation based on DL architectures will be covered. More focus and orientation will be toward methods applied into medical images. A recent survey on this topic is given in [153]. Separately, a discussion on deep vascular segmentation will be also provided.

Deep Image Segmentation

CNNs were the main cornerstone in developing DL segmentation models for natural and medical images. Early proposals relied on pixel-wise predictions [153, 155]. However, since the introduction of the famous fully convolutional neural networks (FCNN), all efforts have been redirected toward end-to-end architectures [102, 103]. The concept of deconvolution layers, i.e., upsampling layers, was introduced in [102]. To avoid loss of contextual spatial information, outputs from shal-

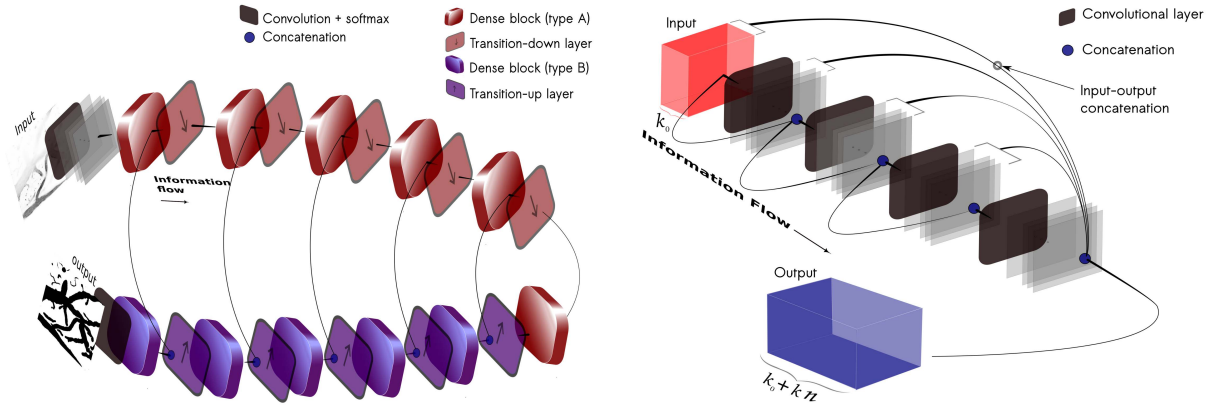

(a) (b)

Figure 2.7 The architecture of densely connected FCNN used for segmentation of TPM angiographic stacks in Chapter 3. (a) Full architecture. (b) Components of a single dense block. The block is referred to as dense block (type A) if the input-output concatenation is maintained, and as dense block (type B) if this concatenation is omitted.

lower layers were fused to reconstruct the final output. On the other hand, in [103], a contracting path (composed of convolutions and pooling operations) and a symmetric expanding path (composed of deconvolution operations) were proposed with skip connections between them to attain the contextual integrity. The architecture is currently very-well known as U-Net. A new similar proposal for an architecture referred to as V-Net has been also proposed in [154]. The difference is the ability to process 3D inputs, integration of residual connections inspired by the work in [98], and the selection of Dice metric as the loss function (see Figure 2.6). After, in [106], U-Net-like segmentation architecture, containing up to one hundred convolutional layers, has been proposed through incorporation of dense blocks [99] instead of residual ones. An example of this densly-connected FCNN model is captured in figure 2.7 [27, 156], where the task was to segment 2D TPM angiographic stacks. This architecture is used in the work presented in Chapter 3. Currently, the state-of-the-art performance for semantic segmentation on the popular PASCAL and Cityscapes datasets is achieved by the model proposed in [157], which referred to as DeepLabV3+. The architecture leveraged both dilated convolutions and feature pyramid pooling [158].

Many works adapted general FCNN architectures proposed for processing of natural images after inducing necessary modifications to fit medical images [159–161]. In [159], input images were normalized using a simple CNN prior and a residual-based U-Net was utilized for liver and prostate segmentations from CT, and MRI images, respectively. In [160] a dilated convolution block close to the network's bottleneck was used to save contextual information. Interestingly in [161], a new rewiring of skip connections has been proposed in a framework of U-Net to segment chest in low-

dose CT scans, nuclei in microscopy images, liver structure in CT scans, and polyp in colonoscopy videos. On the other hand, several improvements have been proposed to refine the performance of FCNN when applied to medical image segmentation. To scale these models to larger and high-resolution images and accelerate the processing to fit in real-time settings, model compression approaches were used [162, 163]. In [162], a reduced architecture is obtained through searching for a most efficient U-Net model to segment tumors and organs from CT and MRI images. In [163], group normalization and leaky ReLU activations were used to make the network more memory 3D medical image segmentation. The concept of attention has been incorporated in many works to enhance the segmentation output from medical images [164, 165]. Some methods used adversarial training to improve the generalization and enhance the segmentation performance [166]. Lastly, RNNs also found their place in other works of medical image segmentation; examples are in [167].

Deep Vascular Segmentation

Vascular segmentation has been thoroughly studied in the literature [168], [169], and applied on angiograms captured in MRI, CT and fundus fluorescein imaging modalities. Vascular segmentation schemes have exploited various image properties including the Hessian matrix [170], moments of inertia [171], gradient vector flow [172] or geometrical flux flow [173]. Schemes have explored a wealth of segmentation strategies, e.g., vessel-like prior modeling [170], classical machine learning [174], morphological processing [175], tracing [176], evolution of deformable models [173]. A recent review of general techniques and methodologies followed to segment vessels in medical images is given in [177].

Recent developments of vascular segmentations were inspired by the success of DL, and have tackled both macroscopic and new microscopic datasets, which contain more complex 2D/3D vessel structures, [27, 155, 156, 178–190]. Some methods were applied to segment vascular structures from MRA and CTA. In [178], the authors improved the HED method [191] to extract 3D vascular boundaries from MRA angiograms. In [179], A specialized deep learning U-Net method is used to replace manual annotations. The labeled training dataset was gathered from 66 patients with cerebrovascular disease. In [180], a novel encoder–decoder deep network was developed to segment 2D vessels from CTA angiograms. The method exploits 2D+t sequential images in a sliding window centered at the frame to be segmented. In [192], a large dataset from 1018 subjects was used to train a densely connected U-Net to generate 3D aortic segmentations from 4D-flow MRI data. Tremendous amounts of papers have been proposed to deal with retinal vessel segmentation, due to the less-challenging 2D nature and the open-source availability of many datasets. In [181], the task of segmentation is formulated as a problem of cross-modality data transformation. A patch-wise neural network was proposed to model the transformation and produce the segmentation. In

[193], a pixel-wise feed forward network was utilized to segment vessels from fundus imaging. Later, various improvements were introduced to include geometric priors and consider the connectivity and topological features of vascular maps. In [183], GNN module was employed within a CNN architecture to exploit the strong relationship that exists between vessel neighborhoods. In [184], the connectivity of the segmented maps have been improved through the incorporation of a dense dilated network within the U-Net framework. In [185], a deformable U-Net (DUNet), which exploits the retinal vessels' local features, was proposed. Interesting works have been presented recently leveraging DL techniques in microscopic cerebrovascular segmentation. In [155], pixel-wise networks were used through integrating some 3D convolutional blocks to automatically annotated vessels in TPM stacks. Other schemes used varying U-Net structures to address the same task [27, 156, 186–188]. In citedamseh2018automatic, a densely-connected U-Net module has been used. In [188], the U-Net performance has been enhanced through the integration of an untrainable block that induces the total variation measures within the total loss while training. In [189], a novel deep learning method was presented for unsupervised segmentation of blood vessels. The method is inspired by the field of active contours. Interestingly in [190], a deep-learning based pipeline was developed to segment and analyze the global vascular structure at various scales from full 3D brain images after registering them to the Allen mouse brain atlas.

2.2.3 Laplacian Geometry Processing

In this section, a necessary material related the domain of discrete differential geometry is presented. This discussion forms the basis for a part of the methodological procedures proposed in Chapter 3 and 4.

Fourier analysis stood out for a very long time as a pivotal tool for processing and decomposition of signals situated within structured and uniform grids. Such signals can be decomposed into orthogonal subspaces associated with different frequencies; low frequencies are regarded as subjacent information, whether the high frequency component as noise. For the case of discrete structures, e.g., graphs, and representations on unstructured grids, e.g., surface meshes, spectral analysis is translated through studying the properties of eigenvalues and eigenvectors associated with the Laplacian operator defined on these domains. Let $\mathcal{G} = (V, E)$ be a graph with vertices $v_i \in \{v_1, v_2 \ldots, v_n\}$ and edges $\{(v_i, v_j), \forall v_i \in V$ and $v_j \in N(v_i)\}$, where $N(v_i) : E \rightarrow \mathbb{R}$ gives the set of neighboring vertices connected to v_i. Let $\phi : V \rightarrow \mathbb{R}$ be a function of graph vertices. Then, the corresponding discrete Laplacian acting on ϕ is defined as

$$\Delta_\phi(v_i) = \sum_{v_j \in N(v_i)} w_{i,j}[\phi(i) - \phi(j)] \tag{2.1}$$

where $w_{i,j} \in \mathbb{R}$, and $\sum_{(i,j)\in E} w_{i,j} = 0$, is the weight between the two vertices v_i and v_j. Laplacian-based analysis on graphs and geometric representations has been applied to address many problems related to smoothing, compression or watermarking of surface geometries [194–196]. Also it forms the basis of spectral-based clustering algorithms [197, 198]. It has been applied to image denoising [199]. An important application that is relevant to the work conducted in this thesis is skeletonization [200–202]. A separate discussion on various skeletonization techniques and their applications for vascular modeling is given in the next section. When the Laplacian is applied to all vertices in $\mathcal{G}$, the formula in 2.1 can be rewritten in the matrix form:

$$\Delta_\phi(v_i) = \begin{bmatrix} \delta_\phi(v_1) \\ \delta_\phi(v_2) \\ \vdots \\ \delta_\phi(v_{n-1}) \\ \delta_\phi(v_n) \end{bmatrix} = L \times \begin{bmatrix} \phi(v_1) \\ \phi(v_2) \\ \vdots \\ \phi(v_{n-1}) \\ \phi(v_n) \end{bmatrix} \tag{2.2}$$

where L is the Laplacian matrix. There are many forms of this matrix; the general normalized form can be defined as

$$L_{i,j} = \begin{cases} 1, \text{if } i = j \\ -w_{i,j}, \text{if } i \neq j \text{ and } (i,j) \in E \\ 0, \text{otherwise} \end{cases} \tag{2.3}$$

where $w_{i,j}$ is obtained as follows

$$w_{i,j} = \frac{\omega_{i,j}}{\sum_{(i,k)\in E} \omega_{i,k}} \tag{2.4}$$

Let us consider the simple path graph depicted in Figure 2.8. It is to be noted that this is a geometric graph, where each vertex has a determined position in the 3D space. If one aims at smoothing the original structure of the graph, a simple procedure would be to repeatedly connect the midpoints of successive contour segments, which is called midpoint smoothing, see Figure 2.8 (a). Specifically, if ϕ assigns the position to graph vertices: $\phi_i = \phi(v_i) = (x_i, y_i)$, then, the new vertex position $(\hat{x}_i, \hat{y}_i)$ calculated after two steps of midpoint smoothing is given by the local averaging:

$$\hat{\phi}_i = \frac{1}{2}\left[\frac{1}{2}(\phi_{i-1} + \phi_i)\right] + \frac{1}{2}\left[\frac{1}{2}(\phi_i + \phi_{i+1})\right] = \frac{1}{4}\phi_{i-1} + \frac{1}{2}\phi_i + \frac{1}{4}\phi_{i+1} \tag{2.5}$$

If graph edges have uniform unit weights, $\omega_{i,j} = 1$, the spatial shift from the position of v_i to that of $\hat{v}_i$ is defined as the 1D Laplacian operator at v_i, as plotted in Figure 2.8, given by

$$\delta_\phi(v_i) = \frac{1}{2}(\phi_{i-1} + \phi_{i+1}) - \phi_i \tag{2.6}$$

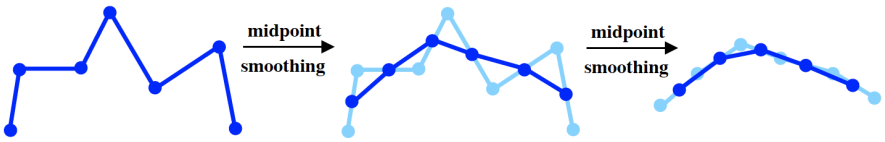

(a) Two steps of midpoint smoothing.

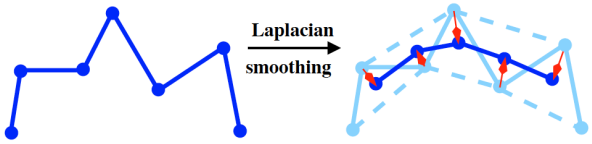

(b) Laplacian smoothing.

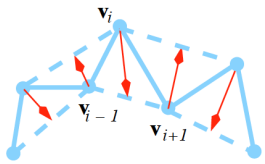

(c) 1D Laplacians (red).

Figure 2.8 A simple example on the use of 1D Laplacians for smoothing of a geometric graph structure. One step of Laplacian smoothing is equivalent to two steps of midpoint smoothing.(Adapted from [196])

To show how one can perform smoothing using the Laplacian operator, let us consider the circular path in Figure 2.9. With ϕ returning the x coordinate of a vertix v, i.e., $\phi_i = x_i$, the Laplacian operator can be represented in the matrix form as

$$\Delta_\phi(v) = L \begin{bmatrix} x_1 \\ x_2 \\ \vdots \\ x_{n-1} \\ x_n \end{bmatrix} = \begin{bmatrix} 1 & -\frac{1}{2} & 0 & \cdots & \cdots & 0 & -\frac{1}{2} \\ -\frac{1}{2} & 1 & -\frac{1}{2} & 0 & \cdots & \cdots & 0 \\ \vdots & \vdots & \vdots & \vdots & \vdots & \vdots & \vdots \\ 0 & \cdots & \cdots & 0 & -\frac{1}{2} & 1 & -\frac{1}{2} \\ -\frac{1}{2} & 0 & \cdots & \cdots & 0 & -\frac{1}{2} & 1 \end{bmatrix} X \tag{2.7}$$

Hence, the new coordinates after applying the smoothing operator, S, can be calculated as

$$\hat{X} = \begin{bmatrix} \hat{x}_1 \\ \hat{x}_2 \\ \vdots \\ \hat{x}_{n-1} \\ \hat{x}_n \end{bmatrix} = \begin{bmatrix} \frac{1}{2} & \frac{1}{4} & 0 & \cdots & \cdots & 0 & \frac{1}{4} \\ \frac{1}{4} & \frac{1}{2} & \frac{1}{4} & 0 & \cdots & \cdots & 0 \\ \vdots & \vdots & \vdots & \vdots & \vdots & \vdots & \vdots \\ 0 & \cdots & \cdots & 0 & \frac{1}{4} & \frac{1}{2} & \frac{1}{4} \\ \frac{1}{4} & 0 & \cdots & \cdots & 0 & \frac{1}{4} & \frac{1}{2} \end{bmatrix} \begin{bmatrix} x_1 \\ x_2 \\ \vdots \\ x_{n-1} \\ x_n \end{bmatrix} = SX \tag{2.8}$$

The smoothing operator S is defined in terms of the Laplacian matrix L as

$$S = I - \frac{1}{2}L \tag{2.9}$$

Above, an example on how the Laplacian operator can be employed to solve a simple smooth-

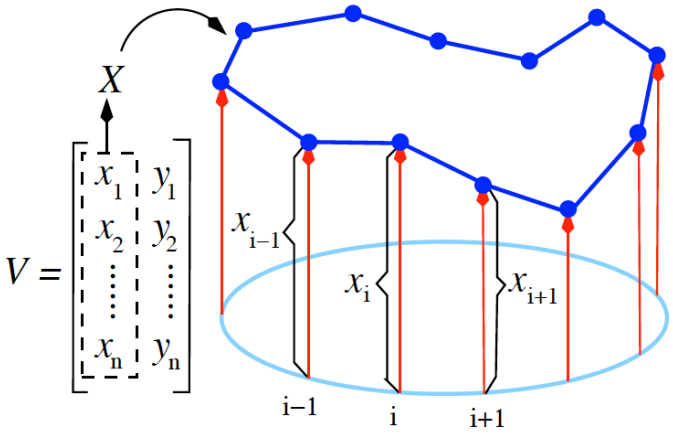

Figure 2.9 Laplacian smoothing operator on circular geometric graph based on x coordinates of its vertices.(Reproduced from [196])

ing problem, i.e, eliminating of higher frequency components in geometric structures, was provided. This is a subcategory of various spectral-based methodologies than can be applied to analyze unstructured geometric representations, such as compression, decomposition and clustering/partitioning. Previous works extended the notion of Fourier analysis to manifold or surface setting, in particular to 2-D triangulated meshes [194, 203–205]. In [203, 204], an appropriate definition and approximation of the discrete Laplacian operator, namely, the Laplacian-Beltrami operator, for triangulated meshes has been given. Such an operator is related to the calculation of the discrete mean curvature on mesh surfaces. The mean curvature on 2D triangulated meshes can be calculated as [204]

$$K(v_i) = \frac{1}{2A(v_i)} \sum_{(i,j)\in E} (cot(\alpha_{ij}) + cot(\beta_{ij}))(\phi_i - \phi_j) \tag{2.10}$$

where ϕ returns the position at v_i and A is the Voronoi region area computed from the 1-ring neighborhood of v_i, see the blue-bounded region in Figure 2.10 (b). Considering the scaling by the Voronoi area, the mean curvature is related to the cotangent Laplacian operator, which can be obtained after resetting the weights in 2.4:

$$\omega_{i,j} = cot(\alpha_{ij}) + cot(\beta_{ij}) \tag{2.11}$$

In [194], the cotangent Laplacian is applied within an iterative optimization scheme to obtain a triangulated mesh smoothing that preserves contextual details (see Figure 2.11). A similar optimization framework is utilized in Chapter 3 and 4 to decimate triangulated mesh and graph geometries,

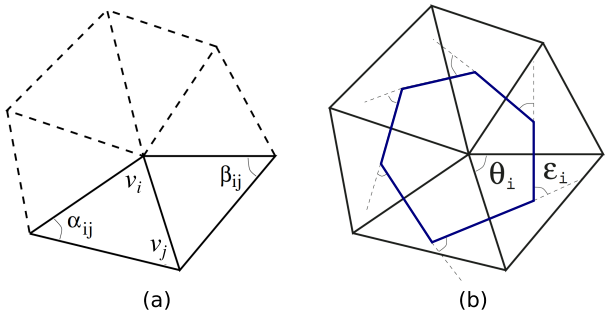

Figure 2.10 The 1-ring neighborhood of a vertex on a 2D triangulated mesh.

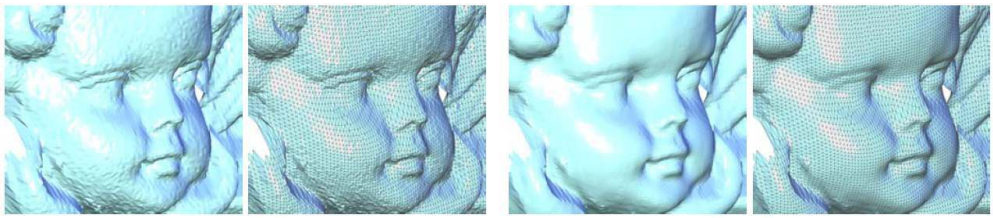

Figure 2.11 Triangulated mesh smoothing through the cotangent Laplacian operator. (Reproduced from [194])

respectively, to form graph-based representations of vascular structures.

2.2.4 Skeletonization

There has been numerous literature on techniques addressing the problem of skeletonization, which is a process of abstracting object shapes in compact forms that can yet describe the original features. With variations in the corresponding theoretical definitions and formulations, these compact outputs are referred to as medial axes, skeletons, curve skeletons, centerlines or graphs. State-of-art reports on the various skeletonization schemes have been provided in [202, 206–208]. Skeletonization methods were employed for a variety of applications extending from shape recognition and retrieval [209], shape decomposition, animation and motion tracking [210], to various medical imaging applications [28, 211–216]. Skeletonization schemes have been applied to process 2D and 3D objects; also, they vary in the type of skeletonization output, e.g., centerlines, curve skeletons and medial surfaces, [202]. The various procedures followed in the literature to acquire object skeletons can be classified into three main categories. 1) Geometrically formulated skeletons, e.g., based on Voronoi diagrams [217], geometric deformation [200, 201, 218] and shrinking balls[219]. This category ecomapsses methods that have demonstrated state-of-the-art performances in terms of acceptable computational effort, and topologically-correct and smooth outputs (see Figure 2.12).

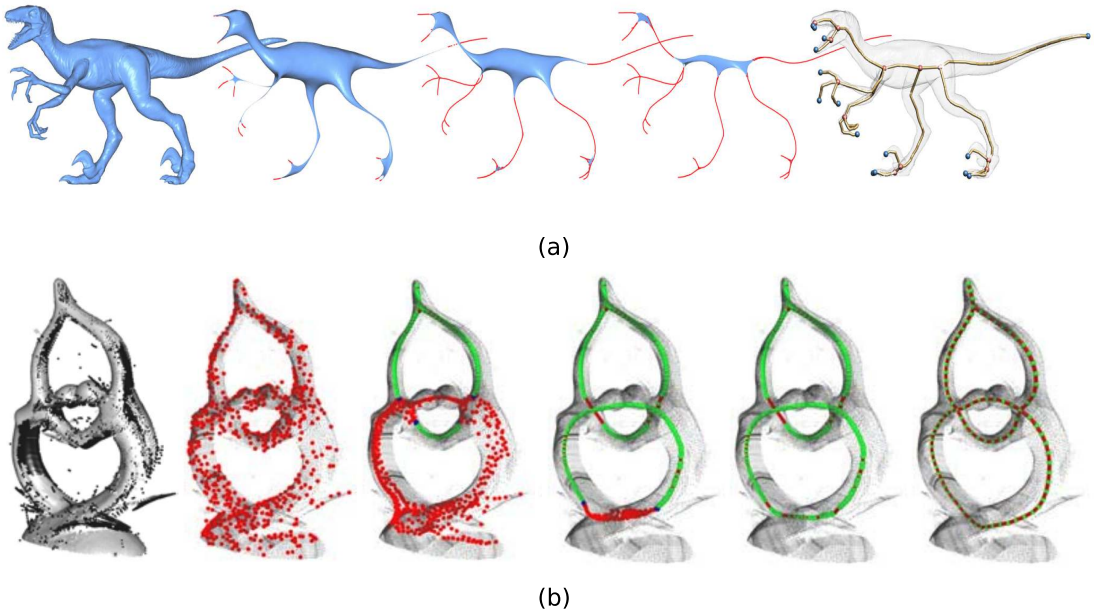

Figure 2.12 Skeletons obtained through geometric deformation of (a) triangulated meshes [200] and (b) point clouds [218].(Reproduced from [200, 218])

2) Methods based on continuous curve evolution where skeletons are formed at the locations of singularities (mathematically referred to as *shocks*) in specifically designed fields, e.g., Hamiltonian field [220] and gradient vector field [221]. 3) Image-based algorithms based on the principle of digital morphological erosion/thinning [222] or location of singularities on a digital distance transform (DT) field [223].

As recent application examples in the biomedical field, in [215], an automated method for anatomical labeling of the Circle of Willis (CoW), by detecting its main bifurcations, was proposed. Graphed skeletons of the CoW were extracted, with bifurcations as its vertices. By training on a set of pre-labeled examples, their global method learnt to distinguish the variability of local bifurcation features as well as the variability in the topology across different samples. In [213], separation and classification of pulmonary arteries and veins were performed from CT images. After, given the segmented vessels, geometric graphs were constructed to model the topology and the spatial distribution. In [214], An automatic approach for saccular intracranial aneurysm isolation was proposed based on extracting vascular curve skeletons using the method in [221]. In [212], a modified version of the technique in [201] was proposed for extracting and decomposition of vascular skeletons applied to computer-assisted diagnosis and analysis. In [216], retinal arteriovenous nicking, a marker that has been strongly suggested to be associated with eye disease, was assessed after extracting the vascular network through a multiscale line detection method. In [211], A method for

providing graphed skeletons of macroscopic cerebrovascular networks that embodies quantitative topological features has been provided. Geodesic vascular minimum spanning trees were extracted from angiographic data by solving a connectivity-optimized anisotropic level-set over a voxel-wise tensor field representing the orientation of the underlying vasculature. More specific review of various methods used for vascular modeling is given in Chapter 3 and 4. In Chapter 3, the method in [201] is integrated within a fully-automated pipeline to model microvascular structures from scalable TPM angiograms. Motivated by the shortcomings experienced from the work conducted in Chapter 3, a novel and yet robust technique that deals with low-quality angiograms acquired at varying scales is presented in Chapter 4.

2.2.5 Gabor Filters

This section provides a review on Gabor filters, which have been employed in Chapter 5 to reconstruct final OCT angiograms from images acquired at different depth setups. Gabor filters were introduced for the first time by Dennis Gabor in 1946. These filters have been utilized in many image processing tasks, especially those concerned with extracting texture-related features. Simple visual receptive fields in some mammals' cortex were shown to have a strong correspondence with a class of linear spatial filters analogous to 2D Gabor filters [224]. Gabor filters can be seen as band pass filters, i.e., they allow a certain *band* of frequencies while rejecting the others. Their mathematical formulation is based on defining a sinusoidal signal, of a particular frequency and orientation, modulated by a Gaussian wave. For the 2D case, a Gabor filter, with both real g_r and imaginary g_i parts, can be defined as

$$g_r = \frac{1}{2\pi\sigma^2} e^{-\frac{1}{2}(\frac{x^2+y^2}{\sigma^2})} \cos(2\pi\omega(x\cos\theta + y\sin\theta)) \tag{2.12}$$

$$g_r = \frac{1}{2\pi\sigma^2} e^{-\frac{1}{2}(\frac{x^2+y^2}{\sigma^2})} \sin(2\pi\omega(x\cos\theta + y\sin\theta)) \tag{2.13}$$

where ω defines the frequency being looked when analysing a 2D image. By varying θ, one can look for texture oriented in a particular direction. The parameter σ is responsible for the Gaussian envelop width, i.e., the size of local image region to be analyzed. Examples of 2D Gabor kernels obtained with different values of ω, θ and σ are depicted in Figure 2.13.

2.2.6 Image Entropy

This section discusses the calculation of local image entropies, which forms a portion of the technical content in Chapter 5. In information theory, one can quantify the amount of information, i.e., uncertainty or entropy, of a discrete random variable X following the probability distribution $p(x)$

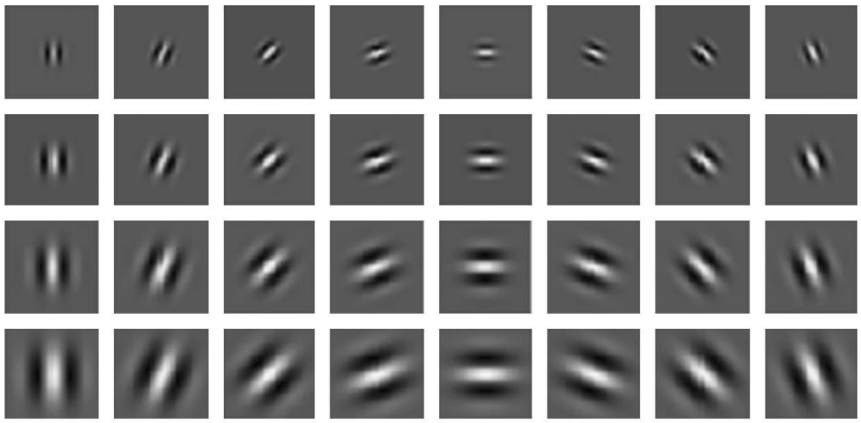

Figure 2.13 A set of Gabor filters. (Reproduced from [225])

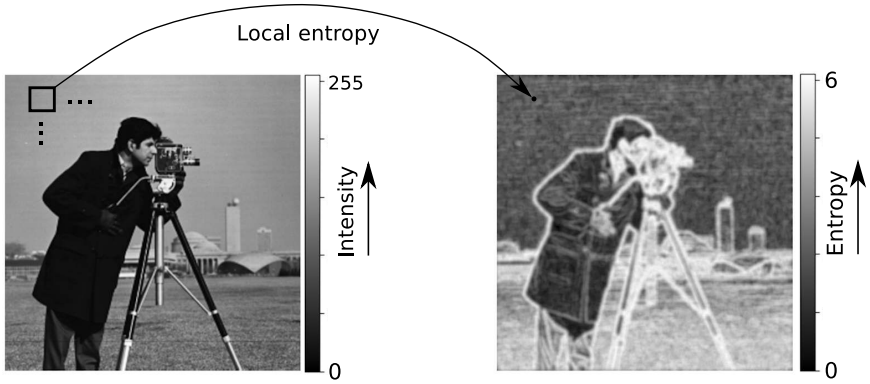

Figure 2.14 Calculation of the local entropy of 2D images.

using Shannon entropy formulation as

$$H(X) = -\sum p(x) \log p(x) \tag{2.14}$$

where $-\log(p(x))$ quantifies the information associated with a single event x. The unit of information is referred to as a *bit*. It is realized from the above formula that the entropy measure is always positive. Zero probabilities do not add to the entropy, i.e., 0 log 0 = 0. The value of the entropy indicates the number of bits on average required to describe X. The higher the entropy, the more information our random variable contains. One can notice that H is a concave function, reaching its maximum if and only if $p(x)$ is equal for all x, i.e., when having uniform probability distribution. Shannon entropy has been applied in the field of image processing to indicate how much information is contained in an image. This is done after approximating the probability distribution of pixel values based on their histogram. A straightforward procedure is performed by normalizing the

frequency of each histogram bin, i.e., range of pixel values, as the probability $p(x)$. Interestingly, the application of this idea could be done kernel-wise through translating over the image domain. Local regions containing a larger collection pixel values, i.e., ridgy structures and rich textures, would result in high entropy measure, whereas for smooth and flat pixel values the entropy will be smaller. An example of this local entropy over a test image is captured in Figure 2.14. It is clear that, at edges and rich texture details, the entropy is higher. We exploited this idea in Chapter 5 to reconstruct an OCT angiogram from different depth-dependent acquisitions.

2.2.7 Random Forests

Here, a popular machine learning model for regression [226], called random forests, is reviewed. This model is used in Chapter 5 to approximate Partial pressure of O2 (PO2) and blood flow values in realistic OCT angiograms.

Individual Decision Trees

Decision trees have become one of the most powerful and popular approaches in data science. A decision tree is a predictive model that works through recursively partitioning the features space into subspaces that constitute a basis for producing the output. Feature subspaces are obtained by axis parallel splitting that straightforwardly generalises to dimensions greater than two. For a covariate/feature space $\mathbf{x} = (x_1, x_2, \cdots, x_p), \mathbf{x} \in \mathbb{R}^p$, one can express a decision tree model in the following form

$$f(\mathbf{x}) = \mathbb{E}(y|\mathbf{x}) = \sum_{m=1}^{M} w_m \sqcap_{(\mathbf{x} \in \mathbb{R}^p_m)} = \sum_{m=1}^{M} w_m \phi(\mathbf{x}; \mathbf{v}_m) \tag{2.15}$$

where w_m is the mean response, obtained from observed data, in the region $\mathbb{R}^p_m$ and $\sqcap_{(\mathbf{x})}$ is the *boxcar* function, with a value of one for $\mathbf{x}$ and 0 otherwise. The parametric set $\mathbf{v}_m$ encodes the choice of variables to split on, and the threshold value, on the path from the root to the mth leaf. It is clear that the above model is not but an adaptive basis-function model, where the basis functions define the regions, and the weights specify the response value in each region. In order to build a regression tree, a recursive binary splitting can be used to grow a large tree on the training data, stopping only when each terminal node has fewer than some minimum number of observations. Recursive binary splitting is a greedy and top-down algorithm that works through minimizing the residual sum of squares at each split in the partitioned feature space as

$$error = \sum_{m=1}^{M} \sum_{\mathbf{x} \in \mathbb{R}^p_m} (\hat{y} - f(\mathbf{x}))^2 \tag{2.16}$$

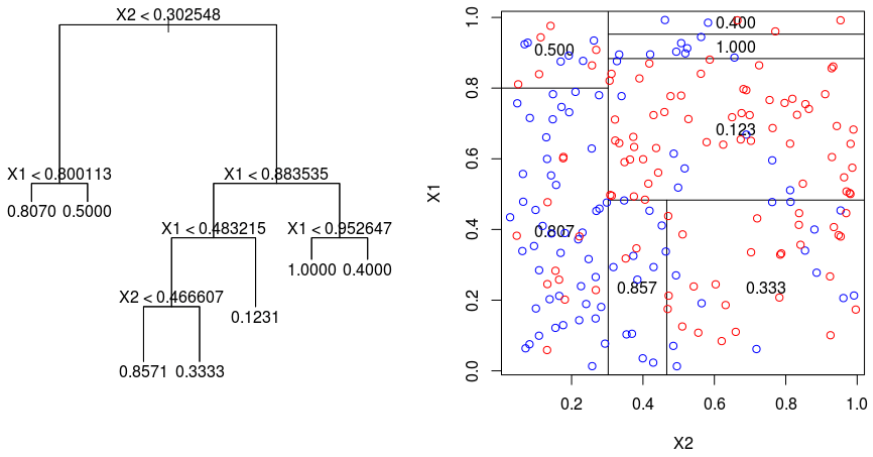

Figure 2.15 Building a regression decision tree from a 2D feature space, with randomly generated samples, through binary greedy splitting. Blue samples have values > 0.5, whereas that of red samples are < 0.5.

where $\hat{y}$ is the observation at $\mathbf{x}$. An example that illustrates the partitioning of a feature space of 2 dimensions, i.e., $\mathbf{x} = (x_1, x_2)$ with randomly generated samples is shown in Figure 2.15.

Regression Random Forests

Random forests are a type of ensemble models built using a collection of decision trees [227]. Their most common version follows a technique known as bagging (also referred to as bootstrap aggregation) to enhance the prediction power [228]. In particular, a random forest takes advantage of multiple decision trees, each modeled based on a subset of the original dataset, and combines their outputs to produce the result. Incorporating different decision trees could lead into a higher variance in the final prediction, i.e., after splitting the dataset into several parts, fitting a different decision tree on each part produces variations in trees' outputs. Bagging or bootstrap aggregation is a simple procedure to reduce the variance by combining the result of multiple trees fitted on random sub-samples, with replacement, from the original dataset. The final output after bagging is represented as

$$f_{bag}(x) = \frac{1}{B}\sum_{b=1}^{B} f_b(x) \tag{2.17}$$

In which B is the number of trees fitted on the different bootstrapped training datasets and $f_b(\cdot)$ is the model of the bth tree. To construct better versions of random forests, especially when numeric features are involved, other techniques differing from the bagging method have been proposed. For example, instead of using all the samples to determine the best splitting threshold for each numeric feature, a sub-sampling from these samples/instances has been used [229]. This technique

can result in reduced variance across predictions from different trees. Another method is called adaptive boosting [230]. The method iteratively invokes a decision tree by training on a part of the dataset that is taken from various distributions. In contrast to the bootstrapping method, instead of randomly sampling the instances in each iteration, boosting ensures the most useful sample to be picked for fitting a single tree. A more recent method for enhancing random forests is based on extremely randomized trees [231]. It is to be noted that a classical random forest deterministically picks the best splitting attribute and its corresponding cut-point, certainly based on a random subset of features. To have a better performance, the method in [231] induces more randomness in building a tree through randomizing both the attribute used to decide the split and its corresponding cut-point. The method of rotation forests has been also proposed to provide better predictions [232]. The idea is to achieve diversity among the individual decision trees by consistently training on the whole dataset, but in a rotated feature space at each iteration.

2.3 Image Acquisition

A number of noninvasive/minimally-invasive in vivo imaging modalities have been applied to investigate brain functions in neuroscience. Many noninvasive MR imaging modalities, e.g., fMRI, DWI and IVIM, have been employed in experimental and translational studies to map neural activity and structure at macroscopic scale. However, these techniques cannot resolve the changes at microscopic scale, making it difficult to understand complex neural models. Alternatively, other minimally-invasive in vivo techniques, e.g. OCT and TPM allow for detailed examination of neural activities in rodent models. In this section, some angiographic/microscopic and MR imaging techniques, which are associated with the methodological schemes proposed in this thesis, are reviewed.

2.3.1 OCT Angiography

Optical coherence tomography (OCT) is a noninvasive method for 3D imaging of biological tissues at high resolution (<10 μm), yet without a need for contrast agents as compared to the TPM technique [12]. OCT imaging can reach a depth of several millimeters with a speed (line scan rate) up to 1.6 MH_z. The core principle behind OCT imaging systems is light interference. In a typical OCT configuration (See Figure [233]), the light from a low-coherence source is split into two paths by a coupler/splitter directing it along two different arms of an interferometer. One arm is referred to as the reference arm, while the other is the sample arm. When the light is transmitted along the fiber to the end of either arm, it is shaped by various optical components to adjust the beam shape shape, depth of focus and the intensity distribution of the light. In the reference arm, the light is back-reflected by a reference mirror and it returns into the interference system. The same process

occurs with the light in the sample arm. In a tissue sample, different structures will have different indices of refraction, and thus the light will be backscattered each time it encounters structures of different refractive index. The returning light from both arms recombine at the splitter producing an interference pattern that is recorded by the detector. The light transmitted in the reference arm forms an interference pattern only with light that traveled the same optical distance along the sample arm. Therefore, when the position of the reference mirror is altered, the interference pattern will change reflecting the corresponding depth within the sample. In this way, A dependence of the reflection potential based on depth is acquired. The OCT signal recorded during a complete travel of the reference mirror is called a depth scan or an A-scan. The sample beam is translated across the sample surface capturing consecutive A-scans to form an OCT image or otherwise called a B-scan. Next, various configurations are discussed including that which do not require the translation of the reference mirror.

For in vivo rodent brain imaging, many OCT-based schemes have been proposed to provide high-resolution volumetric images at high speed covering a large field of view. There are two main types of OCT implementations, namely, time-domain OCT [234] and Fourier-domain OCT (FDOCT) [235]. Introducing FDOCT triggered many promising applications in several fields, e.g., ophthalmology, dermatology and neuroscience. It has been shown that FDOCT systems have larger sensitivity advantage and higher imaging speed as compared to its time domain counterpart, even in situations with low light levels and high speed detection [236]. One of the main applications of FDOCT systems, due to its speed, is the investigation physiological parameters related to in vivo blood flow information [237]. The inherent contrast for FDOCT blood flow imaging comes from the endogenous light scattering of moving blood cells, indicating its merit of not requiring exogenous agents for imaging. The FDOCT technique exploits the relationship between the signal autocorrelation and its spectral power density, i.e., the Fourier transform of the backscattered wave is computed to resolve the axial distribution of the object scattering potential. The advantage of FDOCT over time-domain OCT is that the reflection potionel is represented as a function of depth, i.e, A-line scan, and is obtained in without a need to move the reference mirror, which results in enhanced sensitivity substantially faster imaging. Furthermore, due to its speed, this technique for a reduced light power to be used when imaging living tissue. The FDOCT method has two main variants, spectral-domain OCT (SDOCT) and swept-source OCT (SSOCT). In the SDOCT protocol, frequency components are simultaneously captured using a dispersive element and a linear array detector e.g., line scan camera. A typical implementation of an SDOCT system is captured in Figure 2.16. On the other hand, the SSOCT technique captures the optical frequency components using a single detector, e.g., photodiode, in a time-encoded sequence by sweeping the frequency of the laser source. It is to be noted that this technique suffers from high phase noise, which is introduced due to the cycle-to-cycle tuning and timing variability.

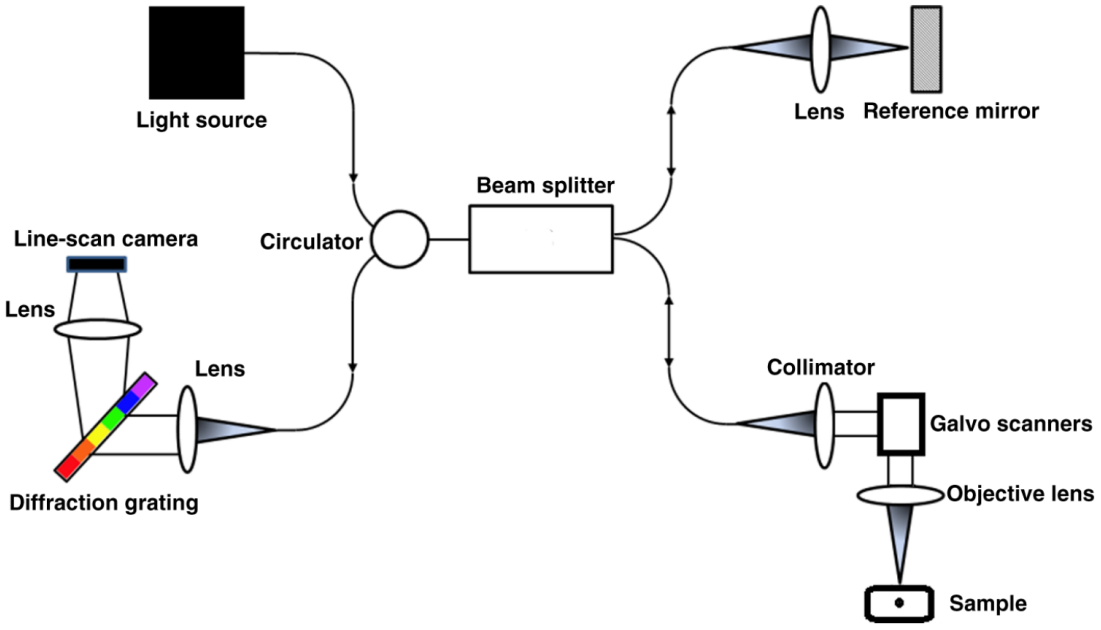

Figure 2.16 A typical implementation of an FDOCT system. (Adapted from [12])

The temporal and spatial profile of the OCT signal encompasses information about the motion of the imaged particles. Signals belonging to regions with moving particles experience a larger variance compared to that of a static tissue. Thus, to extract vascular related parameters due to moving blood cells, one can analyze the phase and/or intensity of OCT signals. Many angiography techniques have been developed based on FDOCT: phase-based methods that are sensitive to the axial flow component only [238]; intensity-based methods that are sensitive to the dynamic speckle induced by the moving blood cells [239]; complex signal–based methods [240], which are sensitive to both the axial flow and the dynamic speckle generated from blood cells moving in all directions; and other methods directed to measure capillary-level parameters [241]. Phase-based methods evaluate the axial velocity of flowing particles within by utilizing the Doppler effect. This is performed through analyzing the phase difference between adjacent A-lines. The techniques based on the intensity of OCT signals take advantage of the strong speckle effect in the vicinity of vascular regions compared to non-flow regions. The complex signal-based methods analyze the A-lines that are acquired at the same location over some time period.

2.3.2 TPM Angiography

Two-photon fluorescence microscopy or TPM is one of the most important technologies that enables minimally invasive 3D imaging of biological tissues with submicrometer resolution. First two-photon fluorescence microscopy system that initialized a revolutionary progress in the 3D

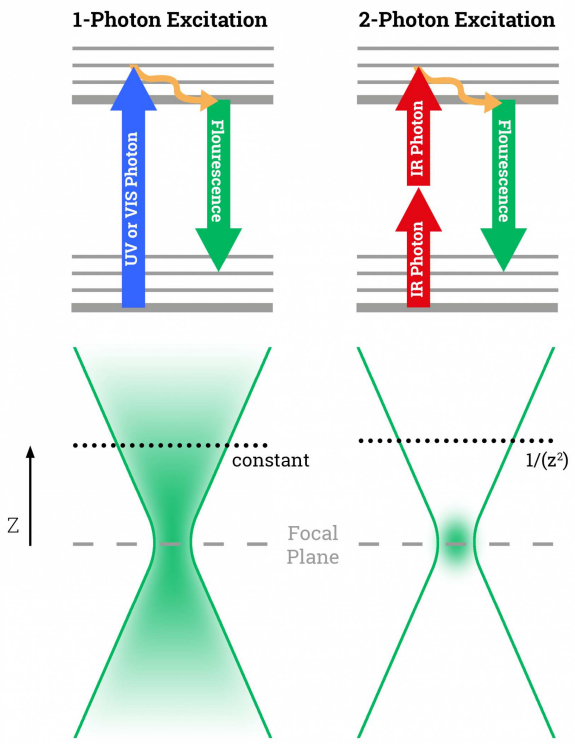

Figure 2.17 A simplified Jablonski diagram showing that two-photon excitation depends on the simultaneous absorption of two photons. (Adapted from [242])

imaging of cells and tissue in vivo was introduced by Denk et al. in 1990 [243]. Compared to precedent optical techniques, a TPM system can image living specimens because of the reduced photodamage caused by a laser source. It incorporates a larger wavelength of the light, usually between 700 and 1000 nm allowing for deeper penetration, and thus deeper imaging. Also, compared with confocal and single-photon microscopy, TPM technique provides higher sensitivity imaging. The principle of TPM excitation is elegantly simple: a fluorophore molecule is excited by a nearly simultaneous absorption (within 10–18 s) of two photons, each about twice the wavelength (half the energy) required for single-photon excitation (see Figure 2.17). The imaging technique enabled imaging of the function and structure of specific cell types (e.g. neurons, microglia, and astrocytes) in the brain, through the use of specific fluorescent probes [244]. The properties of brightness and photostability of different probes continue to improve [245]. TPM has been applied in many biological problems, e.g., to study calcium passage, neuronal and cellular changes [246–248]. Another important application is the imaging of structural and functional vascular changes in the rodent brain [47, 249, 250]. For angiography applications, the fluorescein isothiocyanate (FITC) -labeled Dextran, emitting a green fluorescence, has been commonly used as the fluorophore injected in the bloodstream.

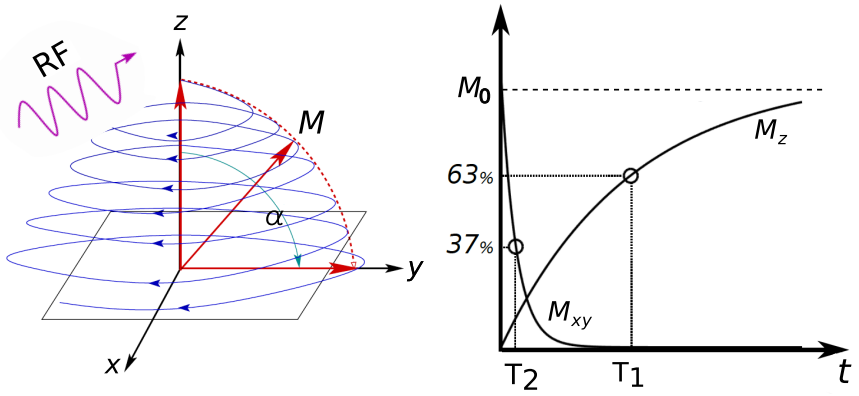

(a) (b)

Figure 2.18 The excitation, (a), and relaxation, (b), processes with their effect on the net magnetization M.

2.3.3 MRI Imaging

MRI is one of the most prominent imaging techniques used for medical diagnosis in clinics. It is based on the principle of nuclear magnetic resonance (NMR), for medical diagnosis. Originally, NMR was introduced to perform NMR spectroscopy, ie. to study the atomic composition of a given sample, and was simultaneously described by Felix Bloch [251] Edward Mills Purcell [252] in 1946. In 1952, they both received the Nobel Prize in Physics for their discovery. The basic concept behind NMR is that, after aligning a magnetic nucleus, e.g., hydrogen-1 using a high-strength magnetic field, its response to a perturbation of the alignment, by an external electromagnetic field, is characteristic. MRI is based on the response of the hydrogen-1 atoms, which represents 99.89% of the naturally found hydrogen atoms and are a main component in biological systems. When dealing with biological samples, the response of these nuclei (*spins*), vary across different types of tissue, exhibiting different T1 and T2 relaxation times after the excitation induced through the external electromagnetic field. In [253], Paul Lauterbur proposed a method based on gradients of magnetic fields to build 2D MR images. Later, a famous technique for a faster acquisition, known as the echo-planar technique, has been proposed [254]. Currently, MRI allows for obtaining non-invasively 3D images at high spatial resolution. Current MRI scanners include various acquisition protocols that address a wide range of problems in medicine, e.g., structural MRI, fMRI, DWI, perfusion MRI and MR angiography.

Principles

The nucleus of an atom consists of neutrons, with no charge, and protons, with positive charge and rotates around itself. If the sum of protons and neutrons is odd, like in the case of hydrogen-1 isotope, the nucleus possesses an intrinsic magnetic angular moment or a spin, inducing a tiny magnetic field. Within an ensemble of spins, the resulting moment is zero because they are randomly oriented. However, applying a powerful magnetic field B_0 imposes a mechanical moment on each spin that depends on the gyromagnetic ratio γ of the type of nucleus. For the hydrogen-1 isotope, $\gamma = 267.513 \times 10^6 rad/sT$. The mechanical moment induces *precession*, i.e. a motion of the spins within a circular path about the field's direction, at angular speed w_0 determined by the Larmor's law

$$w_0 = \gamma \|B_0\| \tag{2.18}$$

Under the effect of B_0, the energy state of a spin is determined by two eigen-states based on their alignment with B_0, If the alignment of an individual spin is towards the direction of the field, it has a parallel direction associated to a low energy level. Otherwise, it has a high energy state associated with the anti-parallel direction. For an ensemble of spins, the difference between the parallel and the anti-parallel precessions defines the amount of net magnetization M resulting as the sum of all the elementary moments. Indeed, at $\|B_0\| = 1Tesla$ and temperature of $300Kelvin$, about 3 spins per million contribute to have a positive net magnetization. At equilibrium, the magnetization M is aligned with B_0, having the component $M_z \neq 0$ that is parallel to B_0, and the component $M_{xy} = 0$ that is perpendicular to it. M_z is referred to as the longitudinal magnetization, whereas M_{xy} is called the transverse magnetization. The Equilibrium can be perturbed, or excited, by the mean of another magnetic field B_1, which can be of a lower strength than B_0 but pulsates at a radio frequency (RF) of w_0 to cause the nuclear magnetic resonance. The duration of the RF pulse determines the nautation angle, α, at which the net magnetization M is flipped (see Figure 2.18). To apply a $90°$ RF, i.e., $\alpha = \pi/2$, the duration of the pulse is computed as

$$\tau_{90\circ} = \frac{\pi}{2\gamma \|B_1\|} \tag{2.19}$$

After the $90°$ RF excitation, we will have $M_z = 0$ and $M_{xy} \neq 0$. The NMR analysis is based on characterizing the restoration of the equilibrium, i.e., relaxation, after it has been perturbed. Two types of relaxation occur in a counterintuitive fashion, and are described by exponential laws with different time rates, T1 and T2 [251]. In the case of the $90°$ RF, the formulas of these relaxations

can be described as

$$M_z = M_0 \left[1 - e^{-t/\mathrm{T1}}\right] \tag{2.20}$$

$$M_{xy} = M_0 \, e^{-t/\mathrm{T2}} \tag{2.21}$$

where M_0 is the magnitude of longitudinal magnetization before excitation. The longitudinal relaxation associated with T1, called spin-lattice relaxation, occurs due to the energy exchange between spins with the surrounding molecules. On the other hand, the transverse relaxation, called spin-spin relaxation, happens due local interactions between spins without necessarily involving energy exchange. The RF signal received during the relaxation process from the fluctuating transverse magnetization is called the free induction decay (FID). Indeed, this signal is the basis of all MRI acquisitions. It is to be noted that quantifying the parameter T2 is not trivial. In a real case scenario, an ensemble of spins could experience minor differences in the B_0 strength, i.e., field inhomogeneity, due to the environment setup. This implies a variation in their precession rates which leads into a loss of phase coherence, and hence more signal loss. Therefore, signal decay is normally expressed by the time rate 1/T2* that is always larger than 1/T2 according to

$$\frac{1}{\mathrm{T2*}} = \frac{1}{\mathrm{T2}} + \gamma \, \Delta \, \|B_0\| \tag{2.22}$$

where the second term in the right side indicates the contribution from the local variations/perturbations in the static magnetic field. Characterizing these perturbations is the focus for many MRI modalities, e.g., fMRI and DWI.

The envelope of the FID represents the loss of transversal magnetization based on the T2* constant. In fact, the FID signal has not been fully destroyed; it has merely become disorganized because the individual spins lost their phase coherence due to static field inhomogeneity. A technique proposed by Hahn in [255] showed that applying another RF pulse of 180° after the FID refocuses the dephased spins, and thus regenerates the symmetrically reversible portion of the FID signal (see Figure 2.19). This rebirth of the FID signal is referred to as spin echo (SE). Since M is the sum of spin moments, if spins rotate coherently (no phase offsets) at the same speed w_0 about the z axis, then the magnitude of the net magnetization is preserved. However, if the spins have variable speeds around the ideal w_0, a loss of phase coherence occurs leading to a destructive effect on the net magnetization over time. By flipping the spins at 180° in the xy plane, the moments of the spins that were faster than w_0 will change location to be behind the moments of the spins that were slower. Eventually, faster spins will catch up with the slower ones, causing a refocusing of the spins, or reestablishing of the phase coherence.

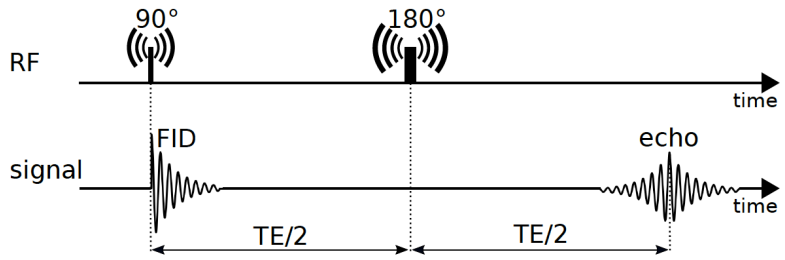

Figure 2.19 The spin echo technique proposed by Hahn [255]. (Reproduced from [256])

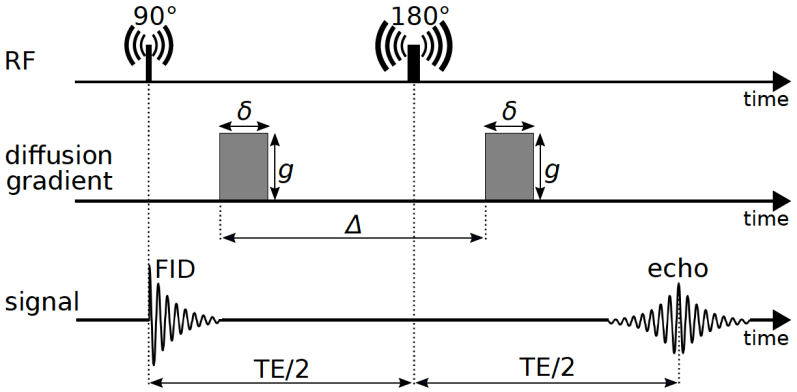

Figure 2.20 The pulsed gradient spin echo sequence proposed by Stejskal and Tanner in [257] to quantify molecular diffusion using NMR. (Reproduced from [256])

Diffusion MRI

Water molecules in our tissues freely move and collide with each other according to Brownian motion; this yields into a diffusion process observed at the macroscopic scale. In an isotropic medium, the diffusion can be characterized by the coefficient D introduced by Einstein [258]. The diffusion coefficient D quantifies molecular mobility in an isotropic environment depending on the molecular type and medium properties. However, in anisotropic tissue environment, water molecules diffuse but with constraints imposed by surrounding structures, i.e., different amounts of diffusion is experienced in various directions. Interestingly, NMR can be used to measure water molecules diffusion in a given direction through the well-known Stejskal-Tanner imaging sequence [257] depicted in Figure 2.20. The idea is to apply a magnetic gradient in a certain direction, referred to as the diffusion gradient, before the $180°$ to force spins that are moving along that direction to precess at different speeds about w_0. After a short period of time, these spins will accumulate phase incoherence based on the amount of displacement, thus reducing the total amount of transverse magnetization that can be measured. A magnetic gradient, similar to the first one, is

then applied but in the opposite direction to compensate for the signal loss imposed by stationary spins with respect to the gradient direction. To this end, the signal loss will be accumulated by only the moving spins that had a displacement component along the gradient direction. Signal decay in presence of diffusion gradients can be expressed as

$$S(b) = S_0\, e^{-bD} \tag{2.23}$$

Where S_0 is the signal acquired without the diffusion gradient, and

$$b = \gamma^2 \delta^2 g^2 (\Delta - \frac{\delta}{3}) \tag{2.24}$$

is the b-value determining the diffusion weighting. In the above formula, g is the strength of diffusion gradients, δ and Δ define the duration of and the separation between the two diffusion gradients (see Figure 2.20).

One of the first clinical applications to leverage DWI was done in 1984 by Le Bihan et al. trying to differentiate liver tumors from angiomas [259]. Initial experience with a $0.5T$ scanner was disappointing due to slow acquisition and sensitivity to motion artifacts due to respiration. When the echo-planar imaging (EPI) became available in the early 1990s, DWI started to show promising applicability in the clinical domain [260]. Now, DWI is used in a wide variety of clinical applications, e.g., to study white matter disease [261] and brain development [262]. Moseley et al. [263] observed that contrast on diffusion images changes according to the spatial direction of the diffusion encoding gradients. In [264], this concept was used to color-map water diffusion in white matter fibers. With the use of a tensor formalism, Basser et al. [265] developed an algorithm to generate 3D representations of fibre bundles in the white matter paving the way for the modern diffusion tensor imaging (DTI) and the field of *tractography*. DWI is also the modality of choice to study brain ischemia and stroke [266]. The DWI technique was integrated in perfusion MRI techniques, which is covered in the next section, to estimate several perfusion parameters, such as cerebral blood volume (CBV), cerebral blood flow (CBF).

Perfusion MRI

The term *perfusion* refers to the biophysical phenomenon of blood circulation in the parenchyma. The level of perfusion is associated with the metabolic demand of the parenchyma based on its activity. The blood coming from an artery goes through the capillary bed, where the exchange of oxygen for carbon dioxide happens. Red blood cells are transported through a venous blood vessel until they reach the lungs, where the respiration process takes place. One of the main indicators of perfusion in tissues is the blood flow. The level of blood flow in different types of tissues

might change in the presence of pathology, and hence perfusion MRI could play a key role in diagnosis and treatment. Many techniques for quantification of perfusion are built by means of tracers, which are substances that are not metabolized by the tissue but can circulate with the blood stream, and can be detected separately from the blood with NMR. Two main categories are the dynamic susceptibility contrast MRI (DSC-MRI) and the dynamic contrast enhanced MRI (DCE-MRI) [267]. The DSC-MRI technique exploits the decrease of T2/T2* signal intensity, i.e. related to the transverse magnetization, in the presence of a paramagnetic contrast agent. The passage of contrast agent through the tissue is monitored by a series of T2- or T2*-weighted MR images. The susceptibility effect induced by the paramagnetic contrast agent results in a loss of intensity in the time profile of the received signal. The principles of the *indicator dilution* theory is then used to perform voxel-wise approximation of many perfusion parameters, such as CBV and CBF. On the other hand, DCE-MRI is based on the acquisition of T1-weighted images under the administration of extracellular contrast agents. The resulting intensity–time curve reflects a composite of tissue perfusion, vessel permeability, and extravascular-extracellular space, and thus provides more tissue-related physiological characteristics at the microvascular level [268].

Another technique used for mapping of perfusion parameters is the arterial spin labeling (ASL) technique, which does not rely on an injected contrast agent. Instead, this technique infers perfusion from the signal attenuation observed in an imaging slice caused by inflowing spins arriving from outside the imaging slice. Many ASL schemes have been proposed [269]. The simplest ASL scheme requires two image types, referred to as the *label*, or *tag*, and *control* images. The tag is applied with an 180° pulse to alter the longitudinal magnetization of protons in the arterial blood before it enters the imaging slice; after a delay time, an image from that slice is constructed. The control image is acquired at the same delay time without tagging. It is clear that the only difference between the control and label images is the inverted magnetization of the inflowing spins. Thus, a simple subtraction of the label from the control image yields a perfusion-weighted image.

One diffusion-based technique that has demonstrated its applicability in the domain perfusion imagine is the intravoxel incoherent motion (IVIM). This method was introduced by Le Bihan et al. in [270] to quantitatively assess all the microscopic translational motions, e.g, microcirculation of blood, that could contribute to the DWI signal. In his model, biological tissue contains two distinct types of diffusion: tissue-related, i.e., *true diffusion* and capillary flow, i.e., *perfusion*. The water molecules flowing in capillaries at the voxel level resembles a random walk motion with no net coherent flow, and thus, is called *pseudo-diffusion*. The IVIM signal decay model can be seen as an extension of the mono-exponential diffusion model into a bi-exponential model described as

$$S(b) = S_0 \left[f\, e^{-b\, D^*} + (1 - f)\, e^{-b\, D} \right] \tag{2.25}$$

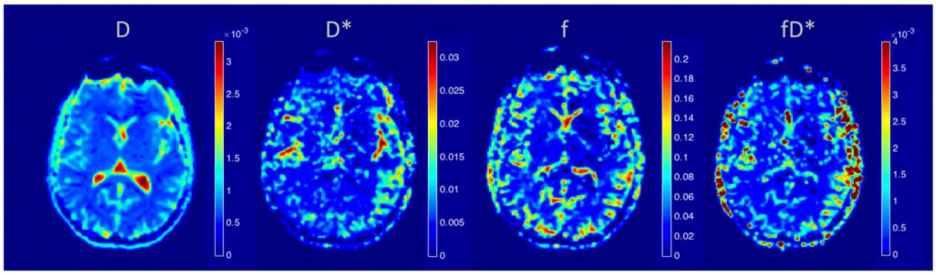

Figure 2.21 Quantifying the perfusion parameters related the IVIM scheme. (Reproduced from [271])

where D^* stands for the pseudo-diffusion coefficient and f for the perfusion fraction, e.g., could be the fraction of the microvascular component in a voxel if other sources of perfusion are neglected. An example on the estimation of the perfusion parameters associated with the IVIM model is depicted in Figure 2.21. A recent review about the in vivo measurement of perfusion using IVIM is presented in [271].

CHAPTER 3 ARTICLE 1: AUTOMATIC GRAPH-BASED MODELING OF BRAIN MICROVESSELS CAPTURED WITH TWO-PHOTON MICROSCOPY

Authors: Rafat Damseh[1], Philippe Pouliot[2,3], Louis Gagnon[4], Sava Sakadzic[5], David Boas[6], Farida Cheriet[7] and Frederic Lesage[1,2,3]

[1] Institute of Biomedical Engineering, École Polytechnique de Montréal, Montreal, QC, Canada;

[2] Department of Electrical Engineering, École Polytechnique de Montréal, Montreal, QC, Canada;

[3] Research Centre, Montreal Heart Institute, Montreal, QC, Canada;

[4] Physics Department, Université Laval, Quebec, QC, Canada;

[5] Athinoula A. Martinos Center for Biomedical Imaging, Department of Radiology, Massachusetts General Hospital, Harvard Medical School, Charlestown, MA, USA;

[6] Neurophotonics Center, Department of Biomedical Engineering, Boston University, Boston, MA, USA;

[7] Department of Computer and Software Engineering, École Polytechnique de Montréal, Montreal, QC, Canada.

This article has been published in IEEE Journal of Biomedical and Health Informatics (IEEE JBHI).

Abstract: Graph models of cerebral vasculature derived from 2-photon microscopy have been shown to be relevant to study brain microphysiology. Automatic graphing of these microvessels remain problematic due to the vascular network complexity and 2-photon sensitivity limitations with depth. In this work, we propose a fully automatic processing pipeline to address this issue. The modeling scheme consists of a fully-convolutional neural network to segment microvessels, a 3D surface model generator and a geometry contraction algorithm to produce graphical models with a single connected component. Quantitative assessment using NetMets metrics, at a tolerance of 60 μm, false negative and false positive geometric error rates are 3.8% and 4.2%, respectively, whereas false negative and false positive topological error rates are 6.1% and 4.5%, respectively. Our qualitative evaluation confirms the efficiency of our scheme in generating useful and accurate graphical models.

Key words: Cerebral microvasculature, deep learning, convolutional neural networks, segmentation, graph, two-photon microscopy.

3.1 Introduction

With the emergence of two-photon microscopy (2PM), it has become feasible to obtain microscopic measurements of the cerebral vascular geometry and, more recently, of associated oxygen distributions [1, 2]. Such investigations of cerebral microvasculature is essential to understand brain neurovascular coupling and neuro-metabolic activity [3]. It can also help in underpinning neurological pathologies associated with microvascular ischemic changes [4]. Furthermore, microscopic studies can be scaled: quantitative analysis of cerebral microvasculature has recently been used to establish a link between the microscopic vascular phenomena and the macroscopic (voxel size) observations found in the blood oxygenation level-dependent (BOLD) response [5, 6]. A key problem encountered in the efforts of [5] and [6] to model cerebral microvasculature is the construction of a sufficiently complete and detailed vascular network from noisy 2PM data. Physiological simulations were based on vascular connectivity which in turn required extensive manual annotations to reconstruct the microvascular topology of each dataset. This human interaction limits the applicability of such simulation frameworks in further neurological studies that would require scaling to large datasets.

Imaging brain tissue using 2PM is associated with high absorption and scattering of the emitted photons with depth leading to image degradation and intensity changes as laser power and detector gains are dynamically adjusted with depth. Also, scattering of excited photons by red blood cells degrades their focus and leads to shadows underneath large pial vessels. These deteriorations in the excited and emitted photons yields volumetric image intensity variations such that automatic processing of two-photon microscopic data is tedious and even problematic [1]. Modeling of angiographic information from 2PM includes segmentation of captured microvessels [7, 8], computation of the microvasculature network shape and topology [9, 10] and anatomical labeling of the extracted components (e.g. arterioles, venules and capillaries). Until recently, some work has been done to automate the processing of these microscopic datasets. However, the developed techniques were not sufficient to avoid significant manual corrections. With the emergence of sophisticated microvascular modeling, the design of a fully-automated scheme that is capable of generating topological models for vasculature in microscopy data is required to scale previous studies. This is the goal of this research work.

Numerous schemes for vascular segmentation have been proposed in the literature exploiting various image properties, such as the Hessian matrix [11, 12], moments of inertia [13], geometrical flux flow [14] and image gradient flux [15]. These schemes also vary in their segmentation strategies, e.g., vessel-like prior modeling [11, 12, 15], tracing [16], evolution of deformable models [14] and deep learning [7, 17–19]. Applications to automatically segment microvessels captured with 2PM are further limited due to the very large number of segments, uneven intensities associated with

optical imaging and shadowing effects. Previous studies have heavily relied on manual interactions to obtain satisfactory segmentations [5]. In recent works, models inspired by the success of ConvNets have been proposed to provide very good vascular segmentation [7, 17–19] with some applied to segmentation of microvessels in 2PM [7, 18]. In [7], the authors implemented a recursive architecture composed of 3D convolution blocks. However, their shallow model provides poor pixel-wise segmentation and is computationally demanding. In [18], the proposed scheme was not targeted to label the vascular space, but rather to provide a skeleton-like version of it. Other recent work, based on FC-ConvNets [20], performed end-to-end vessel segmentation using images from volumetric magnetic resonance angiography [19]. However, the proposed scheme is patch-based, which makes it hard to apply when there is significant variation in local features as observed in 2PM.

Automated representations of data topology has been of importance in many research disciplines: aerial remote sensing [21, 22], neuroinformatics [23–26], and vascular imaging [9, 27, 28]. Some techniques [24–26] target the reconstruction of tree-like structures, by first generating seed points based on probabilistic measurements to then apply algorithms, such as Shortest Path Tree [24], Minimum Spanning Tree (MST) [25] or kMST [24], to extract an optimal graph. On the other hand, modeling loopy curvilinear structures has been investigated in [9, 21–23, 28]. The problem we aim to solve in this paper resembles that investigated in the latter work since 2PM angiograms capture capillaries connecting the arteries to the veins which together also form a topology that is not tree-like. In [21], intensities in road images are clustered into superpixels. The shortest path algorithm is then used to assign connections between superpixels based on road likelihood. Optimal subsets of the connections are finally processed in a framework of conditional random fields. In [22], a thinned version of segmented road maps is simplified and then passed through a shortest path algorithm [22] to generate an undirected graph for road networks. The works in [21, 22], are designed only for two dimensional natural images that have low scale variability and semi-constant luminosity, and which have few disconnected components. In [27], automatic topological annotation of macroscopic cerebral arteries forming the circle of Willis was achieved. However, the task was performed with a predefined knowledge about the topological structure of the annotated object. In [9, 23, 28] different schemes have been developed to extract graphs from more complex three dimensional images (microscopy data) by optimizing a designed objective function. These schemes first attempt at building an overcomplete weighted connections between seed points, which are detected based on tabularity [9] or bifurcation [23, 28] measures. They then search for optimal subgraph representations by solving a linear integer programming (LIP) problem with specific constraints.

In [9, 23, 28], pre-processing steps to provide preliminary weighted graphs, forming the basis of a LIP solution, are designed for less-noisy datasets containing tubular structures of high size unifor-

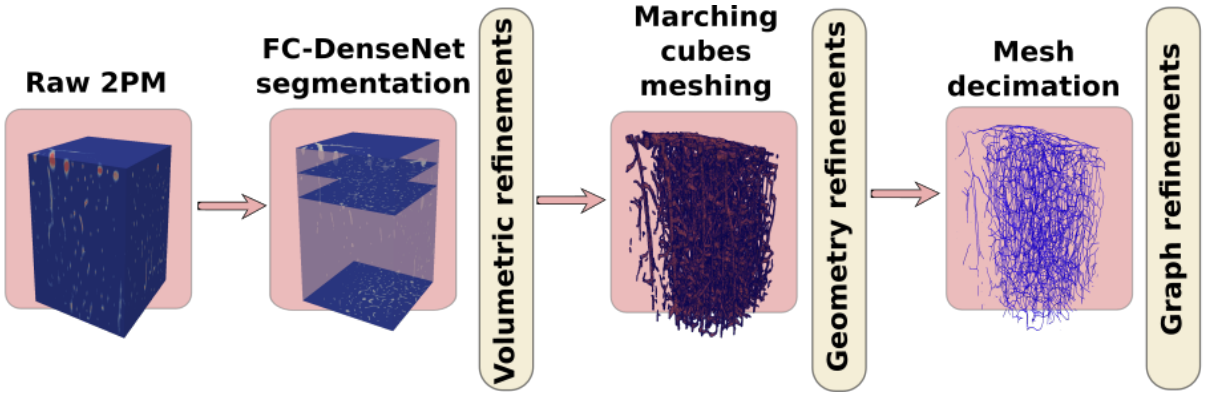

Figure 3.1 A schematic diagram describing the proposed multi-stage graph extraction scheme.

mity. High noise level and variation in tubular sizes are exhibited across microscopic angiograms acquired with two-photon fluorescence scanning. Moreover, despite the cautious problem formulation in the mentioned works designed to approach a near-optimal solution, LIP is theoretically a non-deterministic polynomial-time hard (NP-hard) problem. The hardness of the problem increases for applications on scalable datasets, which results in more decision variables. Lastly, practical solutions of LIP do not necessarily provide consistent output at different runs.

Our work below addresses the issue of extracting topological models from scalable and complex datasets, i.e. 2PM angiograms. We propose a fully-automated solution that provides a unique output for the same input data, in practical computational time. The proposed graph extraction scheme consists of 3 main stages, described in Figure 3.1. First, we take advantage of a recent development in deep learning semantic segmentation [20, 29] employing a fully convolution (FC) network based on the DenseNet architecture to segment potential microvessels [29]. A new well-labeled 2PM dataset is manually prepared to train our segmentation model. The volumetric output of the segmentation model is processed by 3D morphological filters to omit small isolated segments and improve the connectivity pattern of microvessels. Second, we propose a data processing flow to generate a polygonal closed-manifold geometry for the microvasculature from its volumetric mask obtained in the first stage. Finally, we exploite the 3D geometric skeletonization [30] to generate a direct representation of the microvessel network.

The paper is organized as follows. In the Methods Sections 3.2-3.4, we describe each phase of the graph extraction scheme: Section 3.2 details the proposed deep learning architecture for microvessels segmentation and explains the subsequent morphological refinements, Section 3.3 describes the techniques used to generate and post-process the polygonal mesh to represent the shape of the microvasculature, and Section 3.4 provides the formalism of the 3D skeletonization to produce a final graph-based model of the microvascular network. The Results Section 3.5 demonstrates the

validity of the proposed modeling scheme. A discussion and concluding remarks are provided in Section 3.6.

3.2 Deep Segmentation of Microvessels

In this section, various versions of the recently developed FC-DenseNets [29] are employed to address the problem of microvessel segmentation in large-scale 2PM images. Our use of the FC-DenseNets architectures is inspired by their success in achieving the state-of-the-art performance in semantic segmentation in natural images. We prove that applying this data-driven solution to segment microvessels in 2PM volumes can induce a substantially improved performance compared to that of other hand-crafted schemes. Below we discuss the architectures of the neural networks that were devised, data preparation and training procedure. Let $\mathcal{I} : P \rightarrow \mathbb{R} \mid P \subset \mathbb{R}^3$ be the 3D image representing the observed microscopic measurements. The aim is to create a binary mask $\mathcal{I}_{mask} : P \rightarrow \{1, 0\} \mid \mathcal{I}_{mask}(p) = 1 \quad \forall p \in \mathcal{O}$ and $\mathcal{I}_{mask}(p) = 0$ otherwise, where $\mathcal{O} \subset \mathbb{R}^3$ is the object that represents the vasculature.

3.2.1 Networks Architecture

Generally, in a neural network with layers l_n, $n = 0, 1, 2, ...,$ N, each layer l_n performs a non-linear transformation $H_n(\cdot)$ that might include several operations, e.g. batch normalization, rectified linear units (ReLUs), convolutions or pooling. Let x_n denote the output of the layer l_n. In DenseNets [31], consisting of building units called dense blocks, the output x_n of the layer l_n is connected to its previous layers contained in the same dense block [31] by cascading operations. The layer transition is therefore described by the following formula:

$$x_n = H_n([x_{n-m-1}, ..., x_{n-2}, x_{n-1}]) \tag{3.1}$$

where $[\cdot]$ operation denotes the concatenation process and m denotes the number subsequent layers contained in a dense block.

DenseNets are extended to a fully convolution scheme [29], analogous to that proposed in [20], comprising down- and up-sampling paths. The down-sampling pattern is composed of dense blocks and transition-down (T-down) layers, where T-down layers consist of three operations: batch normalization, convolution and max-pooling. Alongside the down-sampling path, the up-sampling path is inserted to recover the input spatial resolution. It is composed of dense blocks, transition-up (T-up) layers and skip connections where T-up layers are built of transposed convolution operations. To avoid the increase in the number of feature-maps in the up-sampling path, the input of dense blocks in this path is not concatenated with its output. Henceforth, we refer to dense blocks

in the down-sampling path as *type A*, and that of the up-sampling path as *type B*. As in typical fully convolution networks [20], skip connections – from the down-sampling path to the up-sampling one – have been introduced to allow the network to compensate for the loss of information due to the pooling operations in the T-down layers.

In this work, to perform the segmentation task, we investigate three different architectures of FC-DenseNets varying in their deepness, namely, Net71, Net97 and Net127 . Our architectures consist of 71, 97 and 127 convolution layers, respectively, with an input size of 256x256x1 for each. The detailed specifications for implemented convolution and pooling layers, with their number of feature-maps, in each architecture are listed in Table 3.1. The down-sampling and up-sampling paths have 36 convolution layers each, whereas the networks bottlenecks have 11, 13 and 15, respectively. The down-sampling path is composed of dense blocks *type A*, that have input-output concatenation. This concatenation is omitted in the dense blocks *type B* forming the up-sampling path. Each T-down block is composed of one convolution layer followed by dropout [32] with p =0.2 and non-overlapping max-pooling. Each T-up block is a transposed-convolution layer with $stride$ =2. The growth rate of feature maps in each dense block is set to k =18 and a dropout of p =0.2 is applied in all contained layers. In each architecture, one convolution layer is applied on the input and another is placed before the last (softmax) layer that provides the bi-class predictions.

3.2.2 Data Collection

To train our segmentation networks, manual annotations were performed to create a ground truth labeling of mice cerebral microvessels captured using our custom-built two-photon laser scanning microscope. To image microvessels, 200 μL 2MDa dextran-FITC (50 mg/ml in saline, Sigma) was injected through the tail vein of mice. Due to the injected fluorescent dye, the plasma appeared bright in the images while red blood cells (RBCs) appeared as dark shadows. Acquisition was performed using 820 nm, 80 MHz, 150 fs pulses from MaiTai-BB laser oscillator (Newport corporation, USA) through an electro-optic modulator (ConOptics, USA) to adjust the gain. The optical beam was scanned in the x-y plane by galvanometric mirrors (Thorlabs, USA). Reflected light was collected by a 20X objective (Olympus XLUMPLFLN-W, NA=1). Fluorescent photons were separated by dichroic mirrors, passed through a filter centered at 520 nm and relayed to a photomultiplier tube (PMT, R3896, Hamamatsu Photonics, Japan) for detection of the dextran-FITC. Manual annotations from the 3D microscopic measurements were done slice-by-slice. The annotation process was carried out with the assistance of MayaVi visualization tool to consider the final 3D structure of the microvessel network. Eight angiograms were labeled to produce a training dataset of images $\mathbf{T} = \left\{(\mathbf{I}^{(q)}, \mathbf{I}^{(q)}_{mask}) \mid q \in Q = [1, 2, 3, ..., 396]\right\}$, each of size 256×256. Next we omit the superscript q for notational simplicity.

3.2.3 Networks Objective & Training

Let $p_x, p_y, p_z \in \mathbb{R}$ define the dimensions of one of our networks output $F(\mathbf{I}; \theta_F)$, where θ_F is vector containing the model parameters. The model was trained to minimize the following cross-entropy loss function [33]:

$$\begin{aligned} \Psi(F) = -[\Sigma_{p_x,p_y} \mathbf{I}_{mask} \log(F(\mathbf{I}; \theta_F) \mid p_z = 0) \\ + \Sigma_{p_x,p_y}(1 - \mathbf{I}_{mask}) \log(F(\mathbf{I}; \theta_F) \mid p_z = 1)]. \end{aligned} \tag{3.2}$$

The stochastic RMSprop gradient descend algorithm was employed to solve our model parameters based on backpropagation [33]. Given an initial learning rate ρ and a decay parameter γ, model parameters were updated as follows:

$$\begin{aligned} \theta_{F_{(t+1)}} = \theta_{F_{(t)}} - \frac{\rho}{\sqrt{\zeta_{(t)}}} \nabla_{\theta_F} \Psi(F(\mathbf{I}; \theta_F)), \text{ where} \\ \zeta_{(t)} = (1 - \gamma)[\nabla_{\theta_F} \Psi(F(\mathbf{I}; \theta_F))]^2 + \gamma \zeta_{(t-1)}. \end{aligned} \tag{3.3}$$

Algorithm 1 Training of the Segmentation Model with Stochastic Gradient Descent

Require: $\mathbf{I}$, Weights Initialization
  for *maximum number of epochs* **do**
    if *patience period*$<\lambda$ **then**
      for *number of mini-batches* **do**
        Recall mini-batch [33]: $\mathbf{b} = \{(\mathbf{I}, \mathbf{I}_{mask})\} \subset \mathbf{T}$
        Compute $F(\mathbf{I}; \theta_F)$
        Update θ_F as described in (3.3)
      end for
    else
      Exit training
    end if
  end for

The training procedure is described in Algorithm 1. In each training iteration, a set of samples from our dataset ("mini-batch") was processed by the network models with their current parameters. Then, the gradient of the loss function Ψ was computed with respect to θ_F and parameters were updated by stepping in the descending direction of the gradient as stated in (3.3). In the algorithm, the training process was early-stopped if no minimization of the loss function Ψ was achieved after a certain number of consecutive training epochs, denoted as the patience period λ.

3.2.4 Morphological Post-Processing

The trained segmentation models can accept a 2D input $\mathbf{I}$ of an arbitrary size and produce an output $F(\mathbf{I})$ of the same size. To segment microvessels in a 3D two-photon angiogram and obtain I_{mask}, we first stacked the outputs of the trained neural networks applied to each slice in the z-direction. Morphological 3D closing and opening filtering was then applied on the resultant image stack with a spherical shape filter of radius=8 to refine the stacked segmentation outputs. It has been found that by applying this 3D morphological processing to obtain I_{mask}, a reduction in false positive structures emerging after the 2D segmentation is achieved.

3.3 Surface Modeling

This section describes the process used to construct a triangulated mesh $\mathcal{M} = (\mathbf{V}, \mathbf{C})$ representing the shape of microvasculature, where $\mathbf{V} = \left[\mathbf{v}_1^T, \mathbf{v}_2^T, ..., \mathbf{v}_d^T\right]^T$ are the vertices positions, $\mathbf{v} \in \mathbb{R}^3$, and $\mathbf{C} = \{\mathbf{c}_i\}_{i=1,...,l}$, $\mathbf{c} \in \mathbf{v} \times \mathbf{v}$, are the edges connecting the vertices of the mesh. The extracted mesh should form a 2D manifold to allow successful geometrical contraction and convergence towards a curve skeleton formulation. Many computational paradigms have been proposed to provide isosurface representations of the binary output $\mathcal{I}_{mask}$ obtained in the previous section. Examples are those based on the concepts of Marching Cubes (MC) [34–36], dual contouring [37] and advancing-front construction [38]. The MC algorithm [34] is arguably the most widely used due to its robustness and speed, however it has an ambiguity problem in its classical formulation due to lookup table redundancy. MC with asymptotic decider [35] was proposed to give better, topologically consistent, surface models. In [36], an interior ambiguity test was added to the scheme of [35] to achieve even higher topological correctness. A modified version of [36], introduced by Liener et. al.[39], was utilized to generate an initial triangulated mesh model for the microvessels surface.

The output from the MC algorithm is a polygonal mesh with a high level of triangulation redundancy. The algorithm produces a large number of small coplanar triangles resulting in a big size model. Direct processing of this raw 3D model to generate a curve skeleton abstraction would be computationally expensive. Also, the MC process introduces excessive roughness with stair-step effects that need to be removed. We applied a polygonal simplification procedure to circumvent these concerns. Many mesh simplification approaches have been developed in the literature [40–44] with varied characteristics: topological invariance, view-dependency – based on objects location, illumination and motion in the scene – and the polygonal removal mechanism. The vertex clustering technique in [40] works by superimposing a grid with a pre-determined resolution to the cells resulting after clustering the original meshes vertices. The resampling technique [41] is based on performing low-pass filtering of the original volumetric data. These approaches are topology in-

sensitive and provide a drastic reduction in the number of elements of the original geometry. Other simplification approaches [42, 43] have been developed to ensure appearance/rendering quality in complex scenes that hinder the rendering process by assuming different levels of detail for the discovered objects. The vertex merging technique proposed by Garland et al. [44] gives an accurate geometry for the simplified model and works on non-manifold inputs that could result from the MC process [39]. We used these features of the vertex merging technique [45] to simplify our surface model.

The process undertaken to create a surface model is not guaranteed to be a manifold and even less a closed manifold [46]. Further processing was used to eliminate possible non-manifold local defects such as self-intersections based on the work done in [47]. Lastly, the hole filling algorithm illustrated in [48] was used to ensure a watertight surface model that can be further used in the next stage of our modeling pipeline.

3.4 Graph Extraction

Various definitions have been suggested as a basis to compute formal skeletons (also called medial axes) [49]. These definitions emerged from conceptualizing the skeleton based on maximally-inscribed balls, Grassfire Analogy, Maxwell Set or Symmetry Set [50]. Let $\mathcal{S} = d\mathcal{O}$ be the 2D-manifold surface of the 3D-manifold volume $\mathcal{O}$ of interest. The idea of maximally-inscribed balls defines the skeleton of $\mathcal{O}$ to be the locus of the centers of maximally inscribed balls in $\mathcal{O}$. Extension to the Medial Axis transform is done by associating the radii of these balls to their center locations. The Grassfire analogy defines the skeleton as the locations inside $\mathcal{O}$ where quenching happens if we let the surface $\mathcal{S}$ propagate isotropically toward the interior of $\mathcal{O}$. The Maxwell Set definition captures the curve skeleton as an extension of the Voronoi diagram by encoding the loci that are equidistant from at least two points on the surface $\mathcal{S}$. In the Symmetry Set definition, a curve skeleton is regarded as the infinitesimal symmetry axes generated by first linking each pair-point on the surface to calculate their symmetry centers and then combine these centers to form a curvilinear infinitesimal axis. In all definitions, skeletonization depends only on the shape of $\mathcal{O}$ rather than its position or size in its embedding space.

In this study, the target is to generate a graphed form of 1D curve skeletons that capture the topology of the microvasculature. In general, the medial axes for 3D objects are 2D [49]. Therefore, two main solutions have been proposed, following the procedures to either simplify the 2D medial axes [51, 52] or to calculate the curve skeletons directly from 3D objects [30, 53, 54]. The techniques in [51, 52] are computationally expensive and very dependent on the quality of the associated surface skeletonization. From a geometric perspective, the techniques that are based on shape contraction [30, 54] are proven to be the most successful in extracting accurate and yet smooth curve skeletons

from a variety of different shapes. Moreover, such techniques provide skeletonization embedded in the geometrical space, and thus it coincides with our goal in generating a graph-based representation of microvessel networks. Therefore, we adapt the work proposed in [30] to perform graph extraction in our last stage of the designed pipeline.

3.4.1 Geometric Contraction

Based on the triangulated mesh $\mathcal{M} = (\mathbf{V}, \mathbf{C})$ generated in the previous section, our goal is to extract a geometric graph $\mathcal{G}$ with node positions $\mathbf{N} = \left[\mathbf{n}_1^T, \mathbf{n}_2^T, ..., \mathbf{n}_m^T\right]^T$, $\mathbf{n} \in \mathbb{R}^3$, and edges (connections) $\mathbf{E} = \{\mathbf{e}_i\}_{i=1,...,h}$, $\mathbf{e} \in \mathbf{n} \times \mathbf{n}$. We follow the geometrical contraction technique in [30] to achieve our goal by iteratively moving the vertices of $\mathcal{M}$ along the corresponding curvature normal directions. At iteration t, we minimize the constrained energy function:

$$\begin{aligned}\mathcal{E} = &\parallel \mathbf{W}_S \mathbf{L} \mathbf{V}^{t+1} \parallel^2 + \\ &\sum_{i=1}^{d} \mathbf{W}_{V,i}^2 \parallel \mathbf{v}_i^{t+1} - \mathbf{v}_i^t \parallel^2 + \\ &\sum_{i=1}^{d} \mathbf{W}_{M,i}^2 \parallel \mathbf{v}_i^{t+1} - \xi(\mathbf{v}_i) \parallel^2 \end{aligned} \tag{3.4}$$

where $\mathbf{W}_S$, $\mathbf{W}_V$ and $\mathbf{W}_M$ are diagonal matrices of size $d \times d$ that impose constraints on the geometrical contraction process, such that for the ith diagonal element: $\mathbf{W}_{S,i} = w_S$, $\mathbf{W}_{V,i} = w_V$ and $\mathbf{W}_{M,i} = w_M$. w_S, w_V and w_M serve as tuning parameters to control the smoothness, velocity and mediality of the contraction process at each iteration. In (3.4), the function $\xi(\cdot)$ maps the vertex $\mathbf{v}_i$ to the corresponding Voronoi pole calculated before the iteration process [30], and $\mathbf{L}$ is the $d \times d$ curvature-flow Laplace operator with its elements obtained as:

$$\mathbf{L}_{ij} = \begin{cases} w_{ij} = \cot(\alpha_{ij}) + \cot(\beta_{ij}) & i, j \in \mathbf{C} \\ -\sum_{(i,k)\in\mathbf{C}}^{k} w_{i,k} & i = j \\ 0 & otherwise, \end{cases} \tag{3.5}$$

where α_{ij} and β_{ij} are the angles opposite to the edge (i, j) in the two triangles which have this edge in common [55].

3.4.2 Geometric Decimation

At each iteration step in the geometric contraction process, higher levels of local anisotropy is introduced in the processed mesh. We follow the procedure described in [54] to reduce the mesh at each contraction step maintaining a water-tight manifold structure. After completing the iteration process, the degenerated surface mesh is reduced to form a graph model by applying a series of shortest edge-collapses [54] until all mesh faces have been removed. Lastly, to ensure that the output of our modeling framework is valid for running physiological simulations, we extract the largest single connected component (LSCC) of the resulting graph to be our final graphical model.

3.5 Validation Experiments

In this section, we carry out various experimentations to evaluate the designed pipeline in producing graph-based representation for microvessels captured with 2PM. First, we describe the parametric settings used to train the segmentation model, extract 3D surface models and generate final geometric graphs. We illustrate the manual procedure followed to prepare a graph-based ground truth baseline. Next, we discuss the validation mechanism and the metrics used to study the performance of the designed pipeline. Lastly, based on these metrics, we present a comprehensive evaluation of our proposed modeling scheme.

3.5.1 Baseline, Parameters and Implementation

Here we discuss the issue of finding a baseline performance for the purpose of validation and the parametric setup of the model used to generate results. Also we describe implementation details.

Baseline

To study the segmentation performance of the our deep segmentation models before and after applying the 3D morphological processing (3DM). Segmentation results were compared with that of manual segmentation (gold-standard), optimally oriented flux method [15] (OOF) and the hessian-based method in [12], which are state-of-the techniques used in 3D vascular segmentation.

To our knowledge, this work is the first fully automatic scheme designed to extract graph-based representation from sizable 3D 2PM datasets. Other baseline methods in the literature applicable to similar datasets rely on human interaction. Hence, in order to validate the correctness of our graphing scheme, we compare our results with manually prepared graphs recently utilized in [5, 56]. To create the manually-graphed datasets in [5, 56], manual annotations were performed on contrast-enhanced structural images of the cortical vasculature which were then skeletonized

using erosion. Ensuing graphs were hand-corrected and verified by visual inspection to generate a single connected component. Datasets of six graphs (from six different mice) were prepared from angiograms with $1.2 \times 1.2 \times 2.0$ μm voxel sizes acquired with a $20X$ Olympus objective (NA= 0.95). To illustrate our choice of the surface modeling and mesh contraction processes in the proposed pipeline, we compare our graph outputs with that resulting from applying the widely used 3D Thinning method [57] on the same binary masks.

Training the Segmentation Model

Implementation of the deep-learning portion of the pipeline was done in Python under the Theano framework. We ran the experiments on two 12GB NVIDIA TITAN X GPUs. The model was initialized using the HeUniform method as in [29]. The training was performed by setting $\rho = 10^{-3}$ and $\gamma = 0.995$ in (3.3) for all epochs of training. To monitor the training process, we randomly selected 25% of the training data as a validation set. The selection of the validation set was performed by randomly picking several 2D slices after grouping all the slices forming the 2PM stacks in one pile. The validation set was used to early-stop the training based on the acquired accuracy, with a patience of 25 epochs. The model was regularized with a weight decay of 10^{-5}.

3D Modeling and Contraction Process

We have followed a brute-force selection of parameters used in the processes of creating 3D surface and carrying out geometric contraction, based on the quality of the generated graphs. To reduce the 3D model using the vertex merging technique in [44], we set the target number of faces in the reduced model to be half of that of the original one. Our code for generating and processing the 3D surface model was based on the VTK Python library. The parameters w_S, w_V and w_M were set to 1, 20 and 35, with $\epsilon_{vol} = 10^{-6}$. We built Python bindings using SWIG to call the C++ API, CGAL, containing the implementation of the geometric contraction algorithm.

3.5.2 Metrics

To quantify the performance of the various segmentation methods, the metrics of sensitivity $= TN/(TN + FP)$, specificity$= TP/(TP + FN)$, accuracy $= (TP + TN)/(FP + FN)$ and Intersection Over Union (IoU) $= TP/(TP+FP+FN)$, were used. The terms TP and FP denote respectively the positive predictions (vessel) with true and false ground truth, whereas TN and FN denote respectively the negative predictions (not vessel) with true and false ground truth. It is to be noted that to generate binary masks using the methods in [15] and [12], empirical thresholding is performed to achieve the highest IOU value.

For the quantification and visualization of errors incurred by our graphing scheme, we used the NetMets metrics proposed in [58]: four measures were computed to compare both the geometry and connectivity between two interconnected graphs. Namely, the Graph False Negative/Positive Rate metrics GFNR and GFPR reflected the false negative rate and the false positive rate, respectively, in the geometry of the extracted graph while the metrics CFNR and CFPR provided measures about the false negative rate and the false positive rate in the topology of the graph.

Let us define $\mathcal{G}_r$ and $\mathcal{G}_e$ as the ground truth and experimentally generated graphs. In the validation process using NetMets, we first performed a two-way matching between the junction nodes in both graphs. These nodes, denoted as $\mathbf{J}_r$ and $\mathbf{J}_e$ for $\mathcal{G}_r$ and $\mathcal{G}_e$, respectively, were those representing bifurcations in the vascular network or terminals of vessel pathways. Graph paths between junction nodes were referred to as graph branches $\mathcal{B}$. Junction node mappings $\mathbf{J}_r$ to $\mathbf{J}_e$ were denoted as $\mathbf{J}_r \rightarrow \mathbf{J}_e$, whereas $\mathbf{J}_e \rightarrow \mathbf{J}_r$ denoted the opposite matching processes. In the matching process, we assigned each junction node in the first graph with one in the second graph based on the shortest Euclidean distance measured. GFNR was computed as $1/n_{\mathbf{J}_r} \sum_{i \in \mathbf{J}_r} 1 - e^{D(i,\mathcal{G}_e)^2/2\delta^2}$ and that of GFPR as $1/n_{\mathbf{J}_e} \sum_{i \in \mathbf{J}_r} 1 - e^{D(i,\mathcal{G}_r)^2/2\delta^2}$, where $n_{\mathbf{J}_r}$ and $n_{\mathbf{J}_e}$ are the number of junction nodes in $\mathcal{G}_r$ and $\mathcal{G}_e$, respectively, $D(i, \mathcal{G})$ is the Euclidean distance between a node i and its matched node in $\mathcal{G}$, and δ is a sensitivity parameter.

Now, to compute CFNR and CFPR as described in [58], core graphs $\check{\mathcal{G}}_r$ and $\check{\mathcal{G}}_e$ were extracted from $\mathcal{G}_r$ and $\mathcal{G}_e$. Core graphs were obtained by first reducing both graphs, $\mathcal{G}_r$ and $\mathcal{G}_e$, by eliminating each junction node and its immediate branches if the distance D from the corresponding nodes was greater than δ. Then, in the reduced graphs of $\mathcal{G}_r$ and $\mathcal{G}_e$, we further eliminated junction nodes, and their corresponding branches, that did not form the same matching pair in the two-way matching process. Lastly, we compared the reduced $\check{\mathcal{G}}_r$ and $\check{\mathcal{G}}_e$ to calculate the following: $\mathcal{B}_{TP}$ = number of graph branches in $\check{\mathcal{G}}_r$ or $\check{\mathcal{G}}_e$; $\mathcal{B}_{FN}$ = number of graph branches in $\mathcal{G}_r$ but not in $\check{\mathcal{G}}_r$; $\mathcal{B}_{FP}$ = number of graph branches in $\mathcal{G}_e$ but not in $\check{\mathcal{G}}_e$. CFNR and CFPR were calculated as $\mathcal{B}_{FN}/(\mathcal{B}_{FN} + \mathcal{B}_{TP})$, and $\mathcal{B}_{FP}/(\mathcal{B}_{FP} + \mathcal{B}_{TP})$, respectively.

3.5.3 Results

Microvessels Segmentation

In this section, we study the performances of the various segmentation schemes used to generate microvessels binary masks. Table 3.2 provides the averaged quantitative results obtained after applying the various segmentation schemes on the 2PM slices in our validation set. From the table, despite the slight degradation in sensitivity scores, one can notice that carrying out the 3DM post-processing on the FC-DenseNets outputs substantially improves the measures of accuracy,

specificity and IOU. The table obviously shows that the method in [15] is not a suitable choice for extracting microvessel maps. The highest sensitivity value of $98.9\% \pm 0.01$ was achieved by the Net71 architecture but at the expense of very poor specificity. The method in [12] achieved the highest specificity value of $57.33\% \pm 2.20$. However, it produces vessel masks with poor IOU scores. The table proves that the Net97+3DM architecture achieves the best accuracy and IOU values, $92.3\% \pm 0.1$ and $41.1\% \pm 0.4$, respectively, with comparable values of sensitivity and specificity corresponding to the schemes of Net97 and that in [12], respectively.

To qualitatively assess the segmentation performances, Fig. 3.2 depicts two raw 2PM slices, obtained from our validation set, with their binary masks counterparts generated by applying the various segmentation schemes. It is clearly seen that the scheme in [15] and those of Net71, Net71+3DM, Net127 and Net127+3DM, produce microvessel mappings that suffer from over-segmentation. On the other hand, the scheme in [12] is highly specific in a way that generates outputs with large portion of false negatives, thus missing important vesselness structures. This observation coincides the low IOU measure of this scheme reported in Table 3.2. From the figure, one can see that the schemes of Net97, Net97+3DM exhibit better segmentation results with superiority of the Net97+3DM scheme in providing less over-segmentation. Hence, based on the previous experimental demonstration, in our study, we choose the scheme Net97+3DM to generate binary maps needed for extracting graph-based models of microvessels.

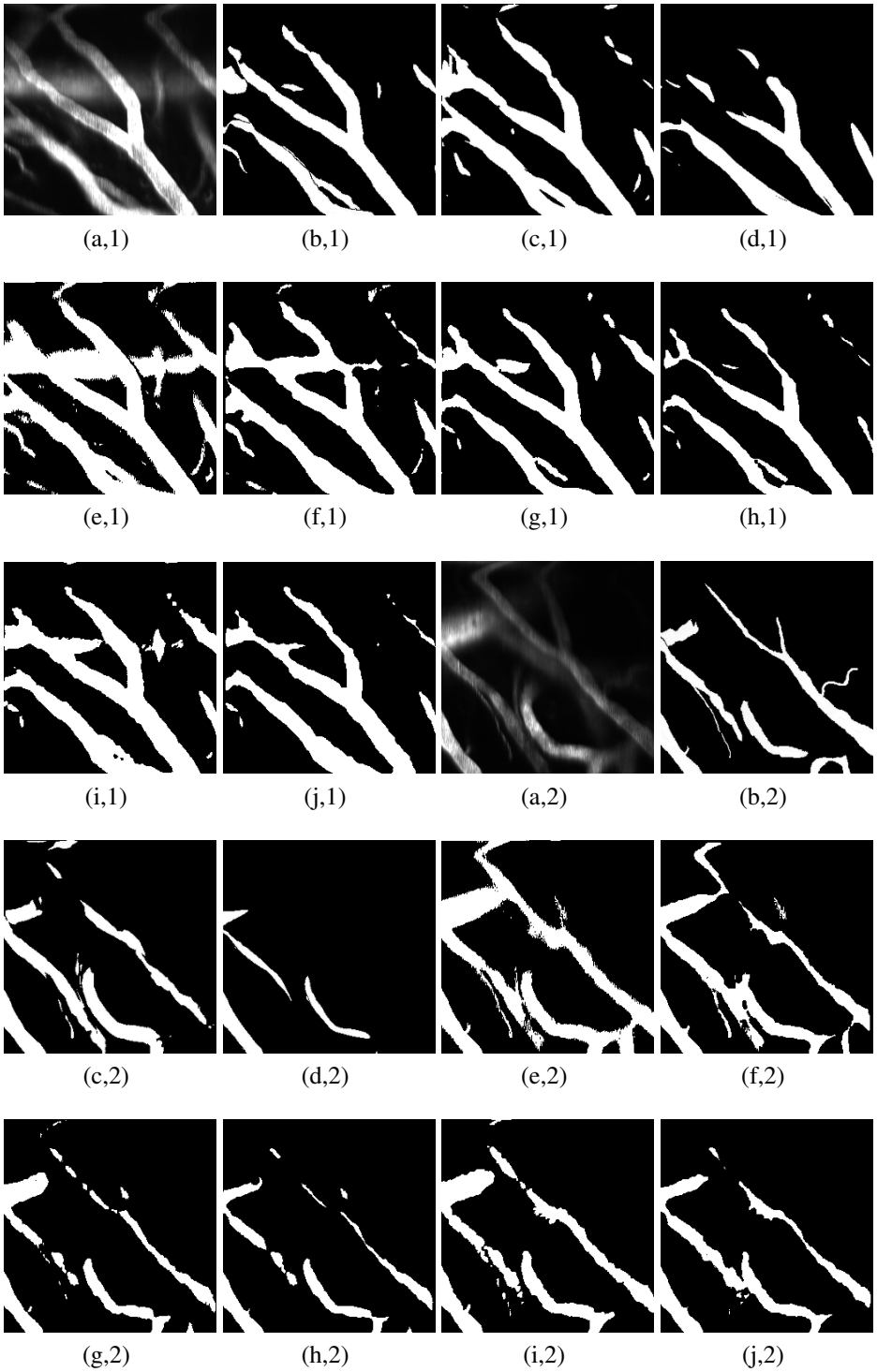

Figure 3.2 Examples of microvessel masks obtained after applying the various segmentation schemes: (a,1-2) Raw 2PM, (b,1-2) true label, (c,1-2) OOF method [15], (d,1-2) Hessian-based method [12], (e,1-2) Net71, (f,1-2) net71+3DM , (g,1-2) Net97, (h,1-2) Net97+3DM, (i,1-2) Net127 and (j,1-2) Net127+3DM.

Table 3.1 The various FC-DenseNet architectures tested to perform the segmentation task. At each component, we report the number of convolution layers followed by the number of feature maps.

Component	Architecture		
	Net71	Net97	Net127
Input	-; 1	-; 1	-; 1
3X3 Convolution	1; 48	1; 48	1; 48
Dense block *type A*	4; 120	4; 120	4; 120
T-down layer	1; 120	1; 120	1; 120
Dense block *type A*	5; 210	5; 210	5; 210
T-down layer	1; 210	1; 210	1; 210
Dense block *type A*	7; 336	7; 336	7; 336
T-down layer	1; 336	1; 336	1; 336
Dense block *type A*	9; 498	9; 498	9; 498
T-down layer	1; 498	1; 498	1; 498
Dense block *type A*	-	11; 696	11; 696
T-down layer	-	1; 696	1; 696
Dense block *type A*	-	-	13; 930
T-down layer	-	-	1; 930
Bottleneck	11; 198	13; 234	15; 270
T-up layer + concatenation	-	-	1; 1200
Dense block *type B*	-	-	13; 234
T-up layer + concatenation	-	1; 930	1; 930
Dense block *type B*	-	11; 198	11; 198
T-up layer + concatenation	1; 696	1; 696	1; 696
Dense block *type B*	9; 162	9; 162	9; 162
T-up layer + concatenation	1; 498	1; 498	1; 498
Dense block *type B*	7; 126	7; 126	7; 126
T-up layer + concatenation	1; 336	1; 336	1; 336
Dense block *type B*	5; 90	5; 90	5; 90
T-up layer + concatenation	1; 210	1; 210	1; 210
Dense block *type B*	4; 72	4; 72	4; 72
1X1 Convolution	1; 2	1; 2	1; 2
Softmax	-; 2	-; 2	-; 2

Convolution layer	Transition-down layer (T-down)	Transition-up layer (T-up)
Batch Normalization	Batch Normalization	3X3 Transposed convolution, stride = 2
ReLu	ReLu	
3X3 Convolution	1X1 Convolution	
Dropout $p = 0.2$	Dropout $p = 0.2$	
	2X2 Max-pooling	

Table 3.2 Quantitative performance evaluation of the various segmentation schemes.

	Method in [15]	Method in [12]	Net71	Net71+3DM	Net97	Net97+3DM	Net127	Net127+3DM
Accuracy(%)	85.3 ± 0.6	92.1 ± 0.1	82.7 ± 0.3	88.3 ± 0.2	90.3 ± 0.1	$\mathbf{92.3 \pm 0.1}$	88.8 ± 0.3	91.1 ± 0.1
Sensitivity(%)	95.1 ± 0.1	94.64 ± 0.1	$\mathbf{98.9 \pm 0.01}$	97.1 ± 0.06	97.7 ± 0.1	96.74 ± 0.1	98.7 ± 0.1	97.17 ± 0.2
Specificity(%)	31.0 ± 2.3	$\mathbf{57.33 \pm 2.20}$	31.2 ± 0.9	36.2 ± 1.3	51.3 ± 1.9	56.5 ± 2.1	46.8 ± 1.6	50.8 ± 1.8
IOU(%)	28.9 ± 0.4	34.4 ± 0.4	30.9 ± 0.4	34.2 ± 0.3	40.2 ± 0.4	$\mathbf{41.1 \pm 0.4}$	38.9 ± 0.4	40.2 ± 0.4

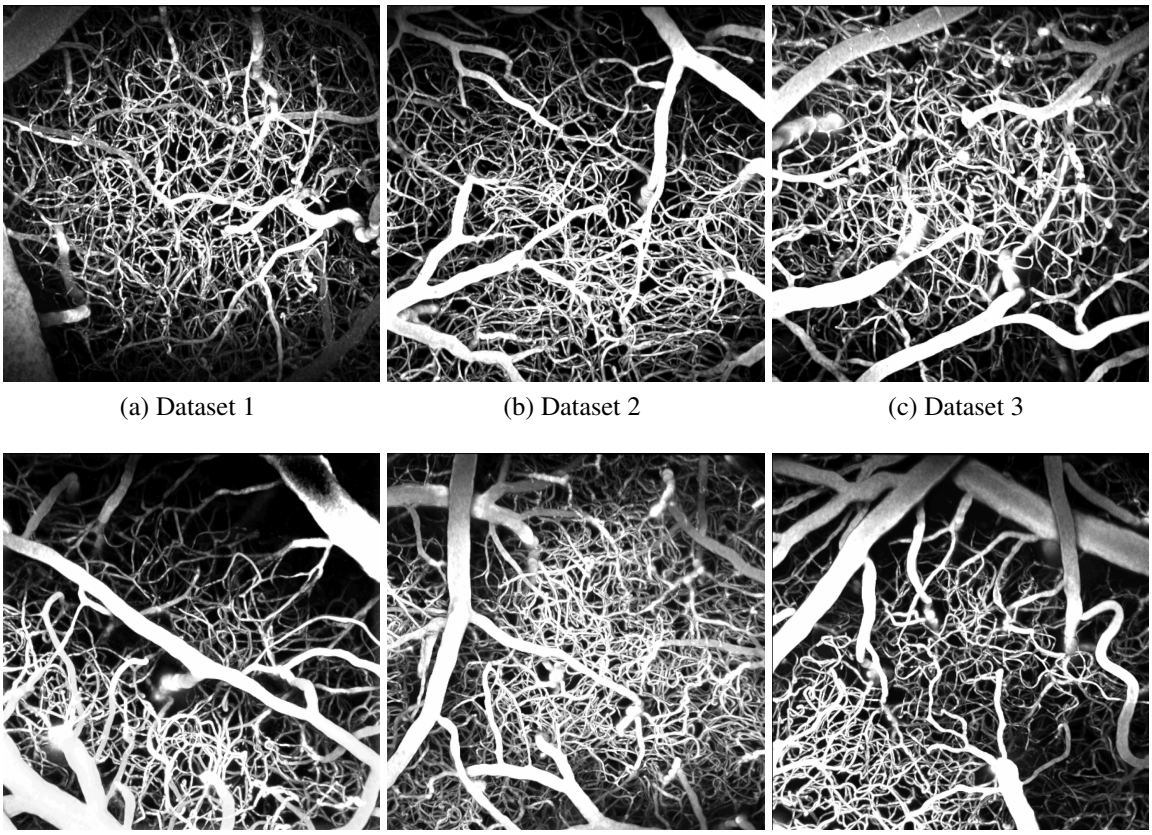

(a) Dataset 1 (b) Dataset 2 (c) Dataset 3

(d) Dataset 4 (e) Dataset 5 (f) Dataset 6

Figure 3.3 Maximum intensity projections of raw angiograms used to validate the proposed graph extraction scheme.

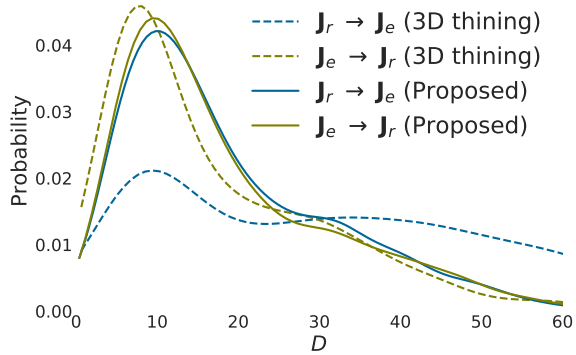

Figure 3.6 Experimental probability distributions of mapping distances D for the two-way matchings between the ground-truth and experimental graphs.

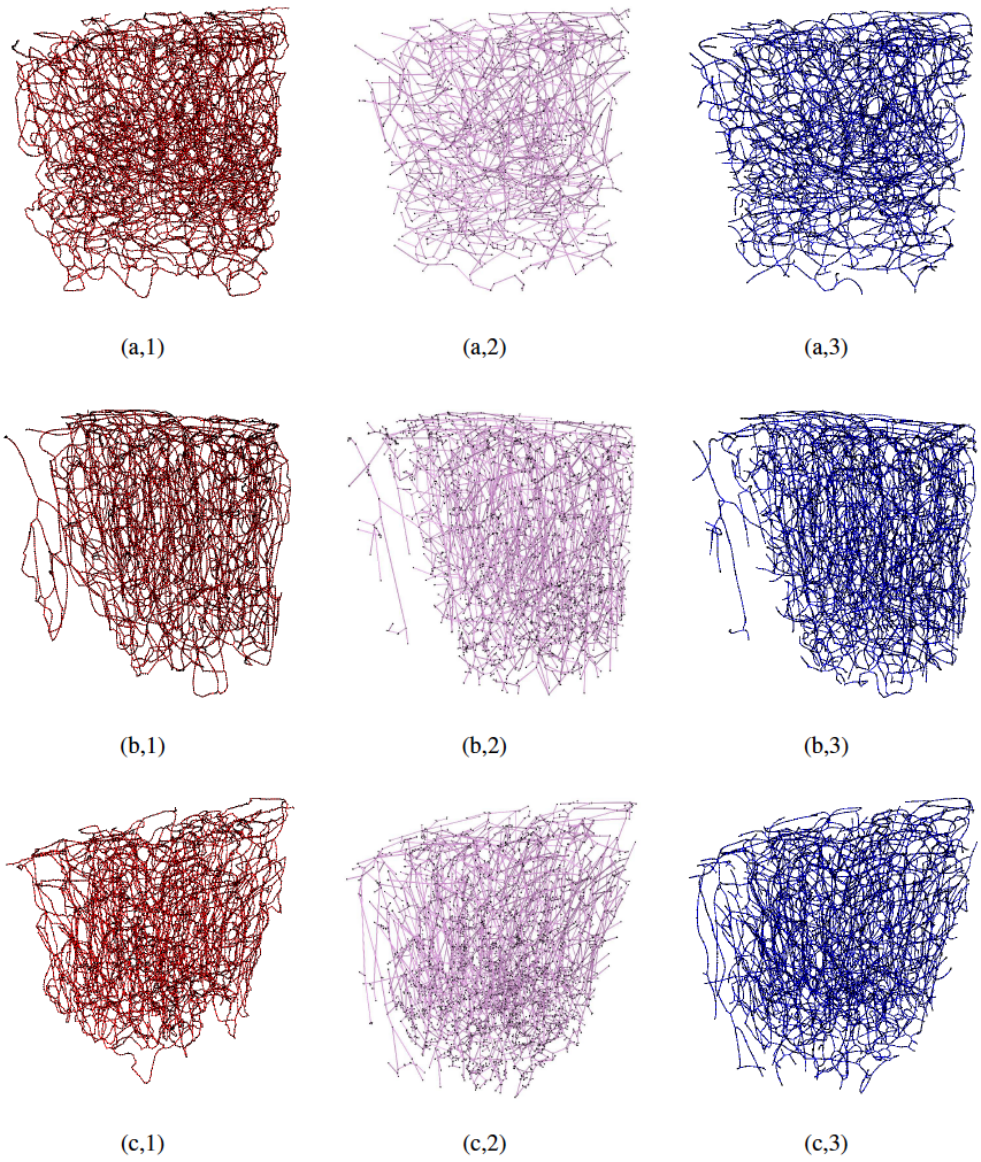

Figure 3.4 (Continued in the next page).

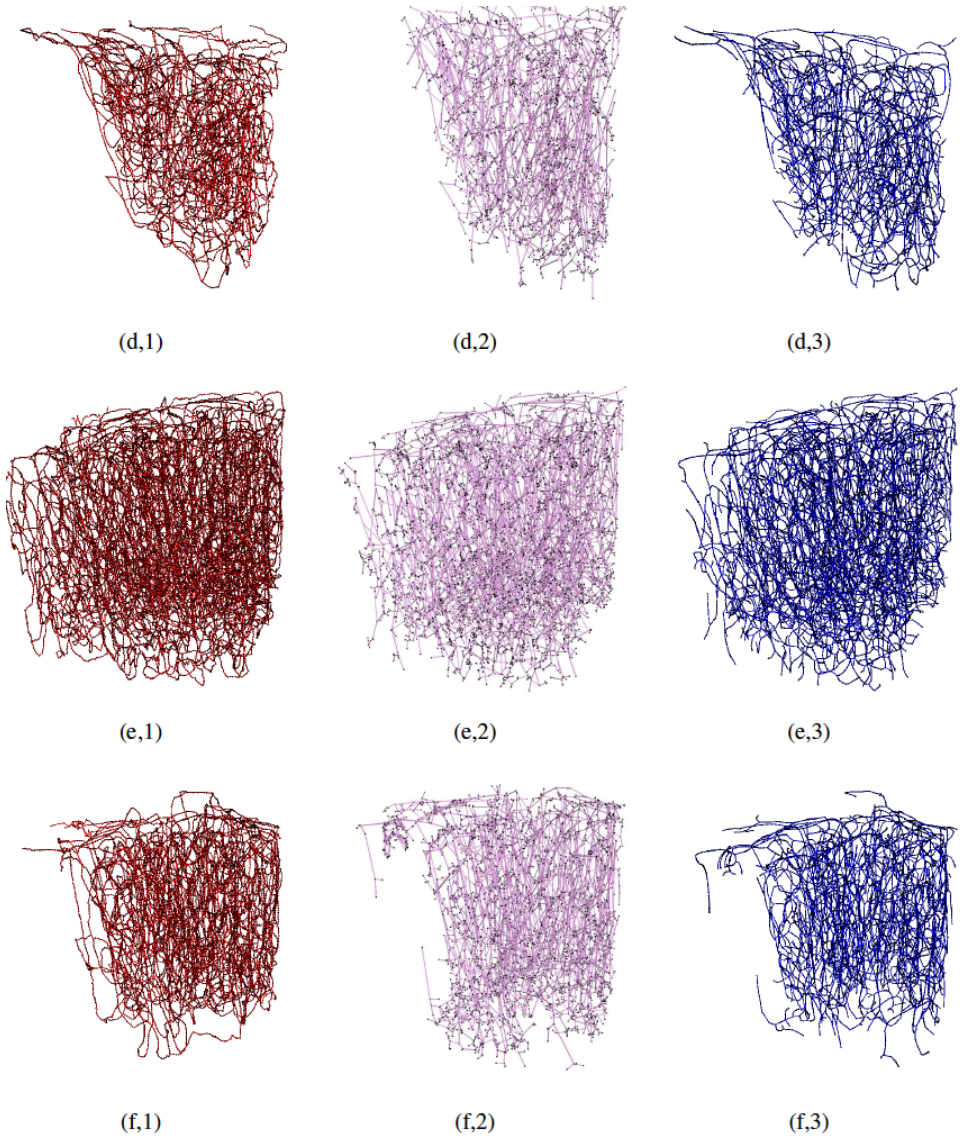

Figure 3.5 Visual assessment of our graph modeling scheme applied on the six raw 2PM datasets. For all datasets (1-6), manually processed graphs (ground-truth) are depicted in the left column (a-f,1); the graphs generated based on 3D Thinning are depicted in the middle column (a-f,2); the graphs generated using our scheme are depicted in the right column.

Table 3.3 Number of nodes in the ground-truth graphs and in those generated by the 3D Thinning method and the proposed scheme. The generated graphs are obtained after extracting the LSCC from their original version.

	Ratio of LSCC to origional models		Number of all nodes			Number of junction nodes		
	$\mathcal{G}_e$ (3D thining)	$\mathcal{G}_e$ (Proposed)	$\mathcal{G}_r$	$\mathcal{G}_e$ (3D thining)	$\mathcal{G}_e$ (Proposed)	$\mathcal{G}_r$	$\mathcal{G}_e$ (3D thining)	$\mathcal{G}_e$ (Proposed)
Dataset 1	95.5%	99.5%	18624	1670	15902	1496	1371	1289
Dataset 2	86.6%	99.0%	16122	3292	17524	827	1890	906
Dataset 3	91.6%	99.0%	12301	4989	16843	782	2638	876
Dataset 4	87.4%	98.5%	9678	3239	10127	640	1668	718
Dataset 5	89.3%	99.0%	27745	6619	23307	1843	3615	1783
Dataset 6	87.2%	97.5%	13723	4527	11871	841	2377	894

Table 3.4 Computational times (in seconds) required by each processing stage in our modeling pipeline.

	Dataset					
	1	2	3	4	5	6
Segmentation/ morphology	1053/ 37	1183/ 43	1059/ 42	1111/ 44	1262/ 43	1113/ 40
Surface Modeling	177	206	204	250	291	195
Graph Extraction	1981	2463	2210	1524	2930	1860

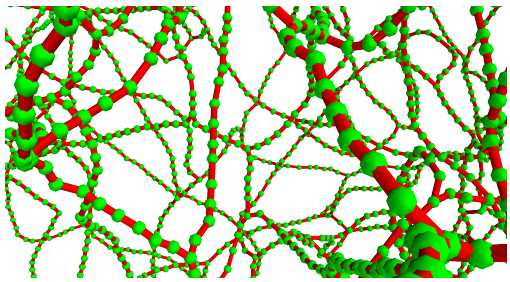

(a)

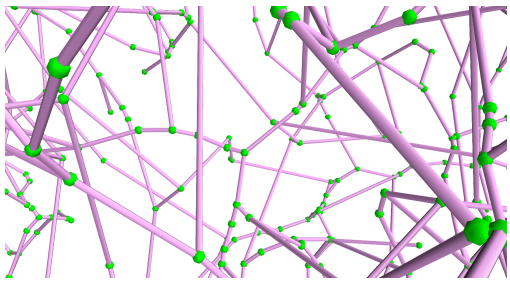

(b)

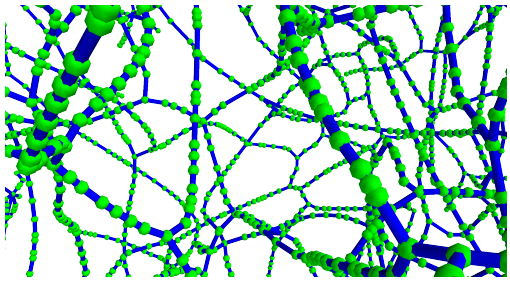

(b)

Figure 3.7 Magnified perspective view of Fig. 3.5 (a,1): (a), Fig. 3.5 (a,2): (b) and Fig. 3.5 (a,3): (c) with enlarged and recolored graph nodes.

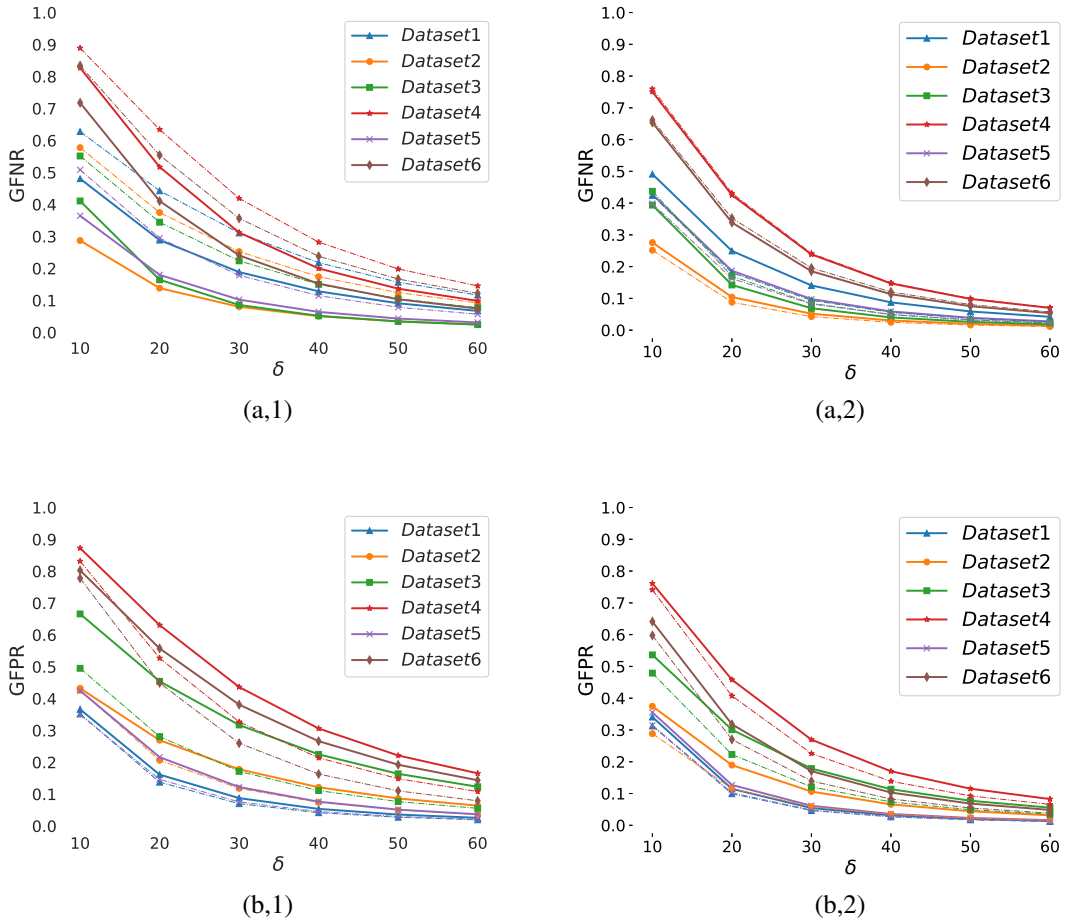

Figure 3.8 (Continued in the next page).

Graph Modeling

The six ground-truth graph datasets were carefully annotated, ensuring a fully interconnected topology for the captured microvessel networks. Each graph provides a model for descending arterioles, capillary bed, and then ascending venules. These graphical models have been employed in [5] to simulate oxygen-dependent quantities across the network, and then generate synthetic MRI signals based on these measurements. Fig. 3.3 shows the six maximum intensity projections of the raw cerebral microvascular spaces captured with 2PM, with their corresponding ground truth and experimental graphical modelings depicted in Fig. 3.5. The reader is also referred to Supplemental Fig. 1 in the supplementary material for assessing the proposed graph models based on visualizing only thin slices (10-30 μm thick) of the stack in Fig. 1 (a,1) at various depth levels. Empirical visual inspection shows that the outputs of our graph modeling scheme are significantly superior to that of the 3D Thinning method and are globally comparable to the ground-truth annotations. However,

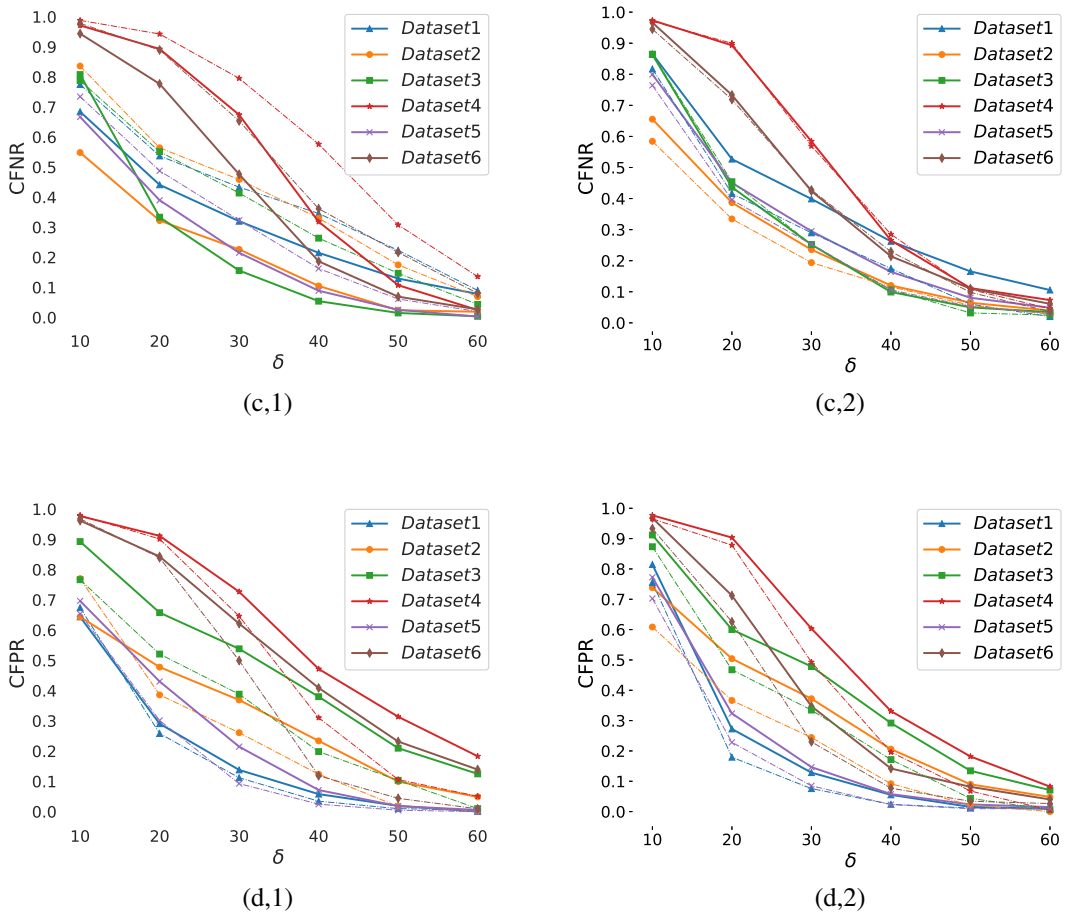

Figure 3.9 Quantitative assessment of the 3D Thinning method (a-d, 1) and the proposed graphing scheme (a-d,2), as a function of the δ parameter based on (a,1-2) GFNR, (b,1-2) GFPR, (c,1-2) CFNR and (d,1-2) CFPR metrics. Dashed lines quantify the performance excluding the graphs boundary parts from the assessment process.

some defects are present for some boundary parts of the vascular networks, especially the capillary bed where one can observe that microvessel terminals are present for the experimentally generated models but not in the manually prepared ones. It is to be noted that the experimental models in Fig. 3.5 are fully interconnected graphs obtained after attaining the LSCC from the raw graph outputs. The ratio of these LSCCs to the original models generated from the first-sixth 2PM datasets, respectively, are listed in Table 3.3. The table demonstrate that the proposed scheme generates less disconnected components compared to that produced by the 3D Thinning method.

As previously mentioned, in order to quantify the performance of the modeling schemes, we performed a two-way matching, based on the shortest Euclidean distance, between junction nodes in the ground truth graphs and those in the generated ones. Fig. 3.6 plots the estimated probability

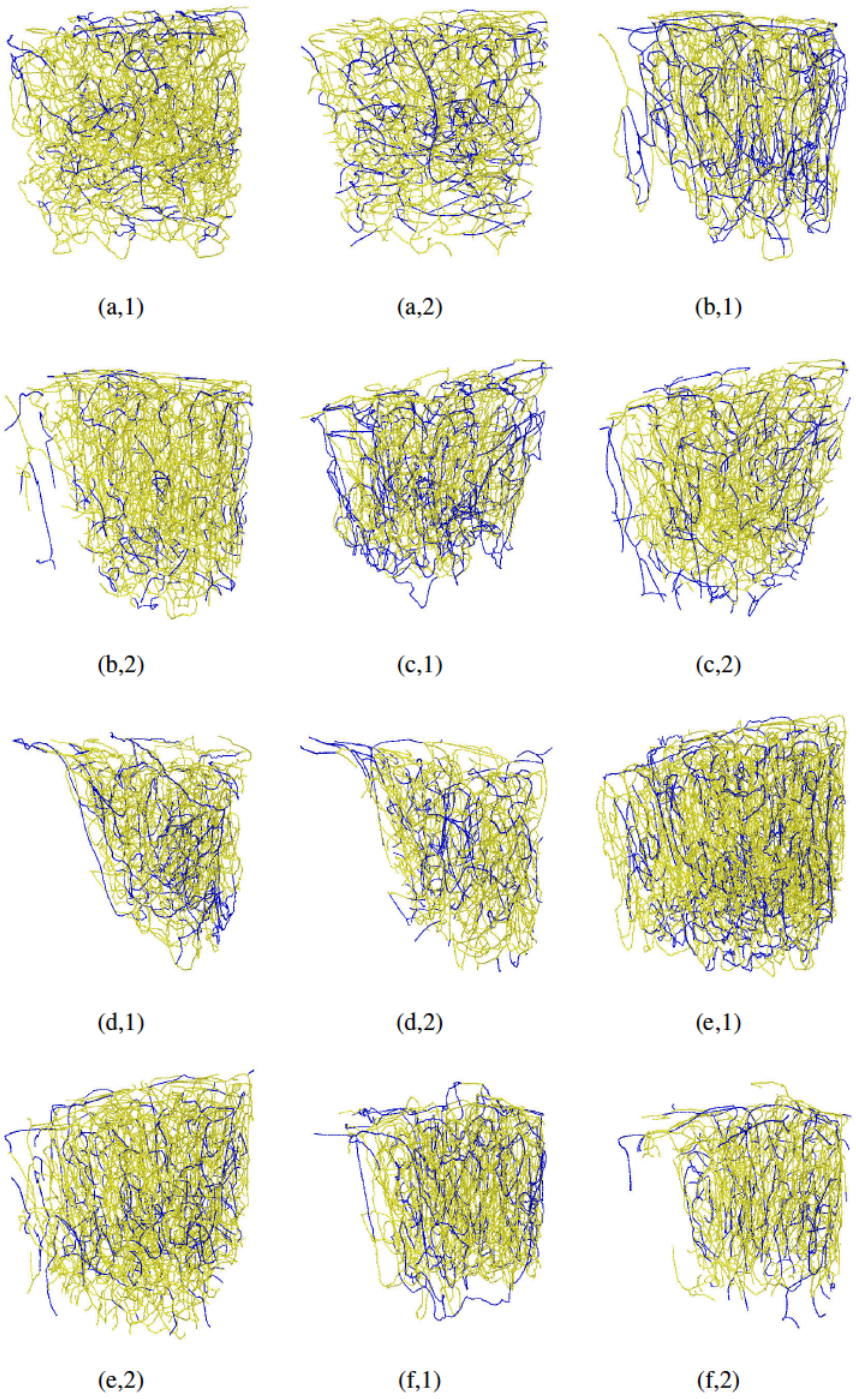

Figure 3.10 Visual illustration of mismodeled edges (blue-colored) for all datasets: false negative edges in (a-f,1); false positive edges in (a-f,2).

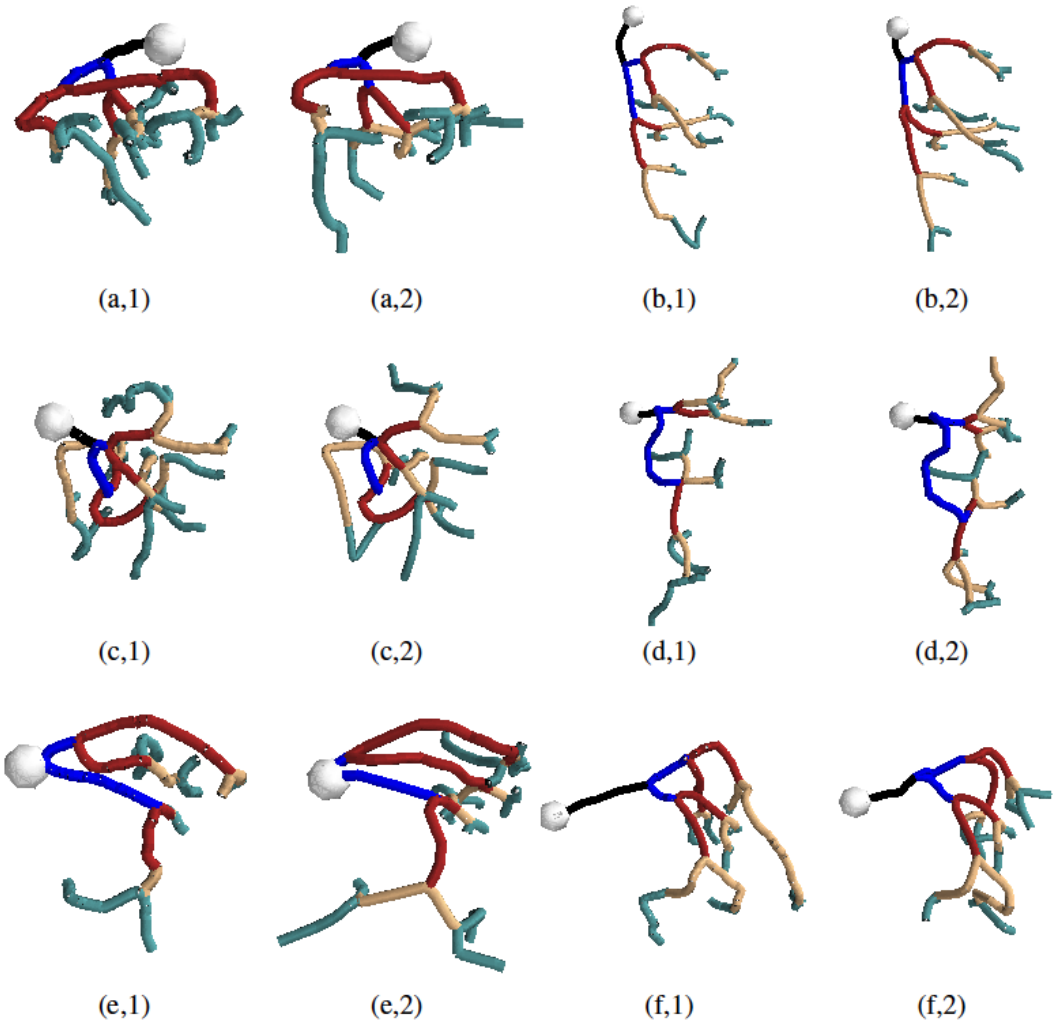

Figure 3.11 Propagating through the various microvessel networks for five consecutive branching levels beginning at the start of a penetrating arteriole (represented by white spheres), ground-truth (a-f,1) and automatically modeled (a-f,2). Each branching level is assigned a different colour.

distribution, using a Gaussian kernel, of the mapping distances D obtained after performing the matching process. It is seen that, in the case of the proposed graph modeling, the $\mathbf{J}_e \rightarrow \mathbf{J}_r$ matching process produced D mappings similar to that resulting from the $\mathbf{J}_e \rightarrow \mathbf{J}_r$ process. This implies that the localization of junction nodes coincides in both manual and experimental modelings, thus resulting a negligible difference between the statistics obtained from the two matching processes. On the other hand, the figure shows a big statistical difference between $\mathbf{J}_e \rightarrow \mathbf{J}_r$ and $\mathbf{J}_e \rightarrow \mathbf{J}_r$ calculated based on the graphs extracted by the 3D Thinning method.

Table 3.3 shows the number of nodes in the graphs generated manually, by the 3D Thinning method

and by our automatic processing. It is seen from the table that, in all cases, the 3D Thinning method produces sparser models having dramatically fewer nodes than that in the ground truth ones. Our modeling scheme produces fewer nodes in some cases (datasets 1, 5 and 6), whereas the opposite was observed in the other cases. To interpret this, Fig. 3.7 depicts magnified versions of the dataset 1 graph. It is clearly seen that manually processed graphs are composed of nodes with almost uniform Euclidean distances between all nodes and their neighboring ones. This is due to regraphing procedures [56]. In contrast, our automatic graphing results in non-regularized placement of nodes due to the dependency of the geometric contraction process on the complexity and tortuosity of the surface modeling for microvessels. However, the figure explains the superiority of the proposed modeling scheme compared to the 3D Thinning method in extracting more accurate graphs. Also from Table 3.3, one can note a variation in the number of junction nodes observed in the ground-truth and the experimental models generated by the proposed scheme. Hence, our modeling produces either denser or sparser interconnections than that of the manually processed graphs when applied to different raw 2PM angiographies.

Fig. 3.9 plots the measurements of the GFNR, GFPR, CFNR, CFPR metrics obtained for the various datasets at different tolerance values δ. It is noted that these measurements are bounded between zero and one; the lower the value the better the performance. The figure illustrates that in all cases, the proposed modeling achieves lower geometrical and topological error rates than that of the 3D Thinning method. At the highest tolerance, $\delta = 60$, our scheme achieves an average of $3.8 \pm 2.1\%$ and $4.2 \pm 2.6\%$ of false negative and false positive error rates, respectively, in modeling the geometry of the vascular networks. These error rates decrease to $3.5 \pm 2.6\%$ and $3.0 \pm 1.9\%$ respectively, when excluding boundary microvessels (≈ 25 % of the angiograms) from our assessment. At the same value of δ, our scheme is able to capture the topology of the vascular networks with an average false negative and false positive error rates of $6.1 \pm 2.6\%$ and $4.5 \pm 2.9\%$, respectively. When excluding the boundary microvessels, the average error rates decrease to $4.4 \pm 2.8\%$ and $1.5 \pm 0.9\%$, respectively. It is to be noted the 3D Thinning method achieves even higher false negative rates when excluding the boundary microvessles, thus proving that this method is poor in capturing the geometrical and topological details from the segmented angiograms. We provide a visual illustration in Fig. 3.10 to interpret the improved performance when excluding the boundary vascular structures in the experimental graphs generated by the proposed scheme. The figure shows the false positive and false negative edges obtained at $\delta = 60$ to compute the corresponding CFNR, CFPR values. One can inspect that a large portion of the mismodeled edges are those located at the boundary of the angiograms. As a result, a better performance of our modeling is achieved at the center of the angiograms, due to 2-photon sensitivity limitations. One goal of our proposed scheme is to generate topological models of microvessel networks that can be used for calculating physiological quantities. Towards that goal, we study the propagation of microvessels in the modeled

networks. Fig. 3.11 depicts examples of ground-truth and experimental sub-graphs generated by propagating through the microvessel networks, beginning with nodes at the start pf a penetrating arteriole and ending with bifurcation nodes after 5 levels of consecutive branching. Despite some few mismodeled network branches, propagation through our experimental networks is very similar to that achieved in ground-truth ones.

Computational Complexity

To provide a comprehensive performance evaluation of the proposed graphing scheme, analysis of its complexity in terms of computational time is necessary. We have run the experiments on a 3.0 GHz Rayzen AMD processor (8 cores, 16 threads in each) with 64 GB of RAM. Segmentation of microvessels has been carried out on a 12GB NVIDIA TITAN X GPU. The times required to perform the computations in each stage of our modeling pipeline are reported in Table 3.4. It is noted that most of the computation times ($\approx 91.8\%$) is used for segmenting microvessels and contracting the generated mesh-based models. From the table, the averaged calculation time for processing one 2PM angiogram, begining with the segmentation of microvessels and ending with the extraction of their graphed networks, reaches 53 minutes. Hence, our fully automatic scheme is proved to provide a very reliable solution when applied to study cerebral microvasculature in large cohorts and can save weeks of manual labor.

3.6 Conclusion and Future Work

In this work, we have proposed a novel fully-automatic processing pipeline to produce graphical models for cerebral microvasculature captured with 2-photon microscopy. Our scheme is composed of three main processing blocks. First, a 3D binary mapping of microvasculature is obtained using a fully-convolution deep learning model. Then, a surface mesh is computed using a variant of the marching cube algorithm. Lastly, a reduced version of the generated surface model is contracted toward the 1D medial axis of the enclosed vasculature. The contracted mesh is post-processed to generate a final graphical model with a single connected component. We used a set of manually processed graphing of 6 angiograms to validate our graphs. From the quantitative validation based on NetMet measures, our model was able to produce accurate graphs with low geometrical and topological error rates, especially at a tolerance $> 30\mu m$. Further qualitative assessment has shown that automatic processing generates realistic models of the underlying microvascular networks having accurate propagation through the modeled vessels. One important issue that could be addressed in a future work is related to the difficulty in generating watertight surface models. The employed contraction algorithm is not applicable to surfaces lacking such characteristics. Introducing a geometric contraction not restricted to such conditions on the obtained surface model

could be an area of further investigation.

3.7 References

[1] Fritjof Helmchen and Winfried Denk. “Deep tissue two-photon microscopy”. In: *Nature methods* 2.12 (2005), pp. 932–940.

[2] Alexandre Parpaleix, Yannick Goulam Houssen, and Serge Charpak. “Imaging local neuronal activity by monitoring PO2 transients in capillaries”. In: *Nature medicine* 19.2 (2013), pp. 241–246.

[3] Louis Gagnon et al. “Modeling of cerebral oxygen transport based on in vivo microscopic imaging of microvascular network structure, blood flow, and oxygenation”. In: *Frontiers in computational neuroscience* 10 (2016).

[4] Roy O. Weller, Delphine Boche, and James A. R. Nicoll. “Microvasculature changes and cerebral amyloid angiopathy in Alzheimer’s disease and their potential impact on therapy”. In: *Acta Neuropathologica* 118.1 (2009), p. 87.

[5] Louis Gagnon et al. “Quantifying the microvascular origin of BOLD-fMRI from first principles with two-photon microscopy and an oxygen-sensitive nanoprobe”. In: *Journal of Neuroscience* 35.8 (2015), pp. 3663–3675.

[6] Mario Gilberto Báez-Yánez et al. “The impact of vessel size, orientation and intravascular contribution on the neurovascular fingerprint of BOLD bSSFP fMRI”. In: *NeuroImage* 163 (2017), pp. 13–23.

[7] Petteri Teikari et al. “Deep learning convolutional networks for multiphoton microscopy vasculature segmentation”. In: *arXiv preprint arXiv:1606.02382* (2016).

[8] Russell Bates et al. “Segmentation of Vasculature from Fluorescently Labeled Endothelial Cells in Multi-Photon Microscopy Images”. In: *IEEE transactions on medical imaging* (2017).

[9] Engin Türetken et al. “Reconstructing curvilinear networks using path classifiers and integer programming”. In: *IEEE transactions on pattern analysis and machine intelligence* 38.12 (2016), pp. 2515–2530.

[10] Russell Bates et al. “Extracting 3D Vascular Structures from Microscopy Images using Convolutional Recurrent Networks”. In: *arXiv preprint arXiv:1705.09597* (2017).

[11] Alejandro F Frangi et al. “Multiscale vessel enhancement filtering”. In: *International Conference on Medical Image Computing and Computer-Assisted Intervention*. Springer. 1998, pp. 130–137.

[12] Tim Jerman et al. “Enhancement of vascular structures in 3D and 2D angiographic images”. In: *IEEE transactions on medical imaging* 35.9 (2016), pp. 2107–2118.

[13] Marcela Hernández Hoyos et al. “Vascular centerline extraction in 3D MR angiograms for phase contrast MRI blood flow measurement”. In: *International Journal of Computer Assisted Radiology and Surgery* 1.1 (2006), pp. 51–61.

[14] Alexander Vasilevskiy and Kaleem Siddiqi. “Flux maximizing geometric flows”. In: *IEEE transactions on pattern analysis and machine intelligence* 24.12 (2002), pp. 1565–1578.

[15] Max WK Law and Albert CS Chung. “Three dimensional curvilinear structure detection using optimally oriented flux”. In: *European conference on computer vision*. Springer. 2008, pp. 368–382.

[16] Kelvin Poon, Ghassan Hamarneh, and Rafeef Abugharbieh. “Live-vessel: Extending livewire for simultaneous extraction of optimal medial and boundary paths in vascular images”. In: *Medical Image Computing and Computer-Assisted Intervention–MICCAI 2007* (2007), pp. 444–451.

[17] Kevis-Kokitsi Maninis et al. “Deep retinal image understanding”. In: *International Conference on Medical Image Computing and Computer-Assisted Intervention*. Springer. 2016, pp. 140–148.

[18] Russell Bates et al. “Extracting 3D Vascular Structures from Microscopy Images using Convolutional Recurrent Networks”. In: *arXiv preprint arXiv:1705.09597* (2017).

[19] Jameson Merkow et al. “Dense volume-to-volume vascular boundary detection”. In: *International Conference on Medical Image Computing and Computer-Assisted Intervention*. Springer. 2016, pp. 371–379.

[20] Jonathan Long, Evan Shelhamer, and Trevor Darrell. “Fully convolutional networks for semantic segmentation”. In: *Proceedings of the IEEE Conference on Computer Vision and Pattern Recognition*. 2015, pp. 3431–3440.

[21] Jan Dirk Wegner, Javier Alexander Montoya-Zegarra, and Konrad Schindler. “Road networks as collections of minimum cost paths”. In: *ISPRS Journal of Photogrammetry and Remote Sensing* 108 (2015), pp. 128–137.

[22] Gellért Máttyus, Wenjie Luo, and Raquel Urtasun. “DeepRoadMapper: Extracting Road Topology From Aerial Images”. In: *Proceedings of the IEEE Conference on Computer Vision and Pattern Recognition*. 2017, pp. 3438–3446.

[23] Engin Turetken et al. “Reconstructing loopy curvilinear structures using integer programming”. In: *Proceedings of the IEEE Conference on Computer Vision and Pattern Recognition*. 2013, pp. 1822–1829.

[24] Hanchuan Peng, Fuhui Long, and Gene Myers. “Automatic 3D neuron tracing using all-path pruning”. In: *Bioinformatics* 27.13 (2011), pp. i239–i247.

[25] Yu Wang, Arunachalam Narayanaswamy, and Badrinath Roysam. “Novel 4-D open-curve active contour and curve completion approach for automated tree structure extraction”. In: *Computer Vision and Pattern Recognition (CVPR), 2011 IEEE Conference on*. IEEE. 2011, pp. 1105–1112.

[26] Engin Türetken, Fethallah Benmansour, and Pascal Fua. “Automated reconstruction of tree structures using path classifiers and mixed integer programming”. In: *Computer Vision and Pattern Recognition (CVPR), 2012 IEEE Conference on*. IEEE. 2012, pp. 566–573.

[27] Hrvoje Bogunović et al. “Anatomical labeling of the circle of willis using maximum a posteriori probability estimation”. In: *IEEE transactions on medical imaging* 32.9 (2013), pp. 1587–1599.

[28] Sepideh Almasi et al. “A novel method for identifying a graph-based representation of 3-D microvascular networks from fluorescence microscopy image stacks”. In: *Medical image analysis* 20.1 (2015), pp. 208–223.

[29] Simon Jégou et al. “The one hundred layers tiramisu: Fully convolutional DenseNets for semantic segmentation”. In: *arXiv preprint arXiv:1611.09326* (2016).

[30] Oscar Kin-Chung Au et al. “Skeleton extraction by mesh contraction”. In: *ACM Transactions on Graphics (TOG)* 27.3 (2008), p. 44.

[31] Gao Huang et al. “Densely connected convolutional networks”. In: *arXiv preprint arXiv:1608.06993* (2016).

[32] Nitish Srivastava et al. “Dropout: a simple way to prevent neural networks from overfitting.” In: *Journal of machine learning research* 15.1 (2014), pp. 1929–1958.

[33] Ian Goodfellow et al. *Deep learning*. Vol. 1. MIT press Cambridge, 2016.

[34] William E Lorensen and Harvey E Cline. “Marching cubes: A high resolution 3D surface construction algorithm”. In: *ACM siggraph computer graphics*. Vol. 21. 4. ACM. 1987, pp. 163–169.

[35] Gregory M Nielson and Bernd Hamann. “The asymptotic decider: resolving the ambiguity in marching cubes”. In: *Proceedings of the 2nd conference on Visualization’91*. IEEE Computer Society Press. 1991, pp. 83–91.

[36] Evgeni Chernyaev. *Marching cubes 33: Construction of topologically correct isosurfaces*. Tech. rep. 1995.

[37] Tao Ju et al. “Dual contouring of hermite data”. In: *ACM transactions on graphics (TOG)*. Vol. 21. 3. ACM. 2002, pp. 339–346.

[38] Joseph R Tristano, Steven J Owen, and Scott A Canann. “Advancing Front Surface Mesh Generation in Parametric Space Using a Riemannian Surface Definition.” In: *IMR*. 1998, pp. 429–445.

[39] Thomas Lewiner et al. “Efficient implementation of marching cubes’ cases with topological guarantees”. In: *Journal of graphics tools* 8.2 (2003), pp. 1–15.

[40] Kok-Lim Low and Tiow-Seng Tan. “Model simplification using vertex-clustering”. In: *Proceedings of the 1997 symposium on Interactive 3D graphics*. ACM. 1997, 75–ff.

[41] Fakir S. Nooruddin and Greg Turk. “Simplification and repair of polygonal models using volumetric techniques”. In: *IEEE Transactions on Visualization and Computer Graphics* 9.2 (2003), pp. 191–205.

[42] Jonathan Cohen et al. “Simplification envelopes”. In: *Proceedings of the 23rd annual conference on Computer graphics and interactive techniques*. ACM. 1996, pp. 119–128.

[43] David Luebke and Carl Erikson. “View-dependent simplification of arbitrary polygonal environments”. In: *Proceedings of the 24th annual conference on Computer graphics and interactive techniques*. ACM Press/Addison-Wesley Publishing Co. 1997, pp. 199–208.

[44] Michael Garland and Paul S Heckbert. “Surface simplification using quadric error metrics”. In: *Proceedings of the 24th annual conference on Computer graphics and interactive techniques*. ACM Press/Addison-Wesley Publishing Co. 1997, pp. 209–216.

[45] David P Luebke. “A developer’s survey of polygonal simplification algorithms”. In: *IEEE Computer Graphics and Applications* 21.3 (2001), pp. 24–35.

[46] Elena Ovreiu. “Accurate 3D mesh simplification”. PhD thesis. INSA de Lyon, 2012.

[47] André Guéziec et al. “Cutting and stitching: Converting sets of polygons to manifold surfaces”. In: *IEEE Transactions on Visualization and Computer Graphics* 7.2 (2001), pp. 136–151.

[48] Peter Liepa. “Filling holes in meshes”. In: *Proceedings of the 2003 Eurographics/ACM SIGGRAPH symposium on Geometry processing*. Eurographics Association. 2003, pp. 200–205.

[49] Andrea Tagliasacchi et al. “3D Skeletons: A State-of-the-Art Report”. In: *Computer Graphics Forum*. Vol. 35. 2. Wiley Online Library. 2016, pp. 573–597.

[50] Kaleem Siddiqi and Stephen Pizer. *Medial representations: mathematics, algorithms and applications*. Vol. 37. Springer Science & Business Media, 2008.

[51] Tamal K Dey and Jian Sun. “Defining and computing curve-skeletons with medial geodesic function”. In: *Symposium on geometry processing*. Vol. 6. 2006, pp. 143–152.

[52] Andrei C Jalba, Jacek Kustra, and Alexandru C Telea. “Surface and curve skeletonization of large 3D models on the GPU”. In: *IEEE transactions on pattern analysis and machine intelligence* 35.6 (2013), pp. 1495–1508.

[53] Antoine Manzanera et al. “Medial faces from a concise 3D thinning algorithm”. In: *Computer Vision, 1999. The Proceedings of the Seventh IEEE International Conference on*. Vol. 1. IEEE. 1999, pp. 337–343.

[54] Andrea Tagliasacchi et al. “Mean curvature skeletons”. In: *Computer Graphics Forum*. Vol. 31. 5. Wiley Online Library. 2012, pp. 1735–1744.

[55] Mathieu Desbrun et al. “Implicit fairing of irregular meshes using diffusion and curvature flow”. In: *Proceedings of the 26th annual conference on Computer graphics and interactive techniques*. ACM Press/Addison-Wesley Publishing Co. 1999, pp. 317–324.

[56] Sava Sakadžić et al. “Large arteriolar component of oxygen delivery implies a safe margin of oxygen supply to cerebral tissue”. In: *Nature communications* 5 (2014), p. 5734.

[57] Hanno Homann. “Implementation of a 3D thinning algorithm”. In: (2007).

[58] David Mayerich et al. “NetMets: software for quantifying and visualizing errors in biological network segmentation”. In: *BMC bioinformatics* 13.8 (2012), S7.

CHAPTER 4 ARTICLE 2: LAPLACIAN FLOW DYNAMICS ON GEOMETRIC GRAPHS FOR ANATOMICAL MODELING OF CEREBROVASCULAR NETWORKS

Authors: Rafat Damseh[1], Patrick Delafontaine-Martel[2], Philippe Pouliot[2,3], Farida Cheriet[4] and Frederic Lesage[1,2,3]

[1] Institute of Biomedical Engineering, École Polytechnique de Montréal, Montreal, QC, Canada;

[2] Department of Electrical Engineering, École Polytechnique de Montréal, Montreal, QC, Canada;

[3] Research Centre, Montreal Heart Institute, Montreal, QC, Canada;

[4] Department of Computer and Software Engineering, École Polytechnique de Montréal, Montreal, QC, Canada.

This article is under review with IEEE Transactions on Medical Imaging (IEEE TMI).

Abstract: Generating computational anatomical models of cerebrovascular networks is vital for improving clinical practice and understanding brain oxygen transport. This is achieved by extracting graph-based representations based on pre-mapping of vascular structures. Recent graphing methods can provide smooth vessels trajectories and well-connected vascular topology. However, they require water-tight surface meshes as inputs. Furthermore, adding vessels radii information on their graph compartments restricts their alignment along vascular centerlines. Here, we propose a novel graphing scheme that works with relaxed input requirements and intrinsically captures vessel radii information. The proposed approach is based on deforming geometric graphs constructed within vascular boundaries. Under a laplacian optimization framework, we assign affinity weights on the initial geometry that drives its iterative contraction toward vessels centerlines. We present a mechanism to decimate graph structure at each run and a convergence criterion to stop the process. A refinement technique is then introduced to obtain final vascular models. Our implementation is available on `https://github.com/Damseh/VascularGraph`. We benchmarked our results with that obtained using other efficient and state-of-the-art graphing schemes, validating on both synthetic and real angiograms acquired with different imaging modalities. The experiments indicate that the proposed scheme produces the lowest geometric and topological error rates on various angiograms. Furthermore, it surpasses other techniques in providing representative models that capture all anatomical aspects of vascular structures.

Key words: Brain microvessels, segmentation, network, geometry contraction, graph, two-photon microscopy.

4.1 Introduction

Modeling of cerebrovascular structures is essential in areas ranging from clinical decision support to fundamental research. Topological and structural representations of cerebrovascular networks substantially facilitate guided surgical procedures involving intracranial electrode placement [1], catheter motion planning [2] and endovascular aneurysm repair [3]. Computational modeling of cerebrovascular networks can also allow for better intersubject assessment of vascular features [4]. Beyond macro-scaled clinical images, studying cerebral microvasculature is vital for understanding brain neurovascular coupling and neuro-metabolic activity [5]. It is also important to investigate neuropathologies associated with a deterioration in cerebral oxygen transport [6, 7].

Clinically, non-invasive cerebrovascular imaging techniques including magnetic resonance angiography (MRA) and computed-tomography angiography (CTA) are common practices for both preoperative planning and postoperative surveillance scanning. In experimental studies, optical imaging systems have been recently proposed to provide spatially-resolved measurements of cerebral microvasculature in-vivo. [8]. Transforming the cerebrovascular structure represented within a quantized spatial grid into an interpretable computational model is problematic. Cerebrovascular images exhibit a high level of intersubject heterogeneity, and contain complex vascular structures. Furthermore, vascular space is submitted to dynamically evolving conditions like acute ischemic strokes. These obstacles hinder the construction of accurate computational models that encode connectivity and spatial information to be used for further analysis of shape features and hemodynamics properties.

4.2 Related Work

Automatic graph extraction schemes have generated interest in many fields spanning from urban planning to neuroinformatics [9–25]. For the use of topological and geometrical features in medical imaging applications, the reader is referred to [25]. Some graphing techniques [14–16] aim to reconstruct tree-like structures, whereas others target the modeling of loopy curvilinear structures [19–24].

4.2.1 Models Accepting Raw Inputs

In terms of the format of input data to be processed, some modeling techniques rely directly on raw inputs [16, 19–23]. The work in [20] assumes a predefined topological knowledge about the object to be modeled while other solutions have been proposed in the framework of linear integer programming [19, 21, 22]. After building overcomplete connections between automatically identified nodes, optimal subgraphs are extracted. These techniques are based on solving a theoretically non-deterministic polynomial-time hard (NP-hard) problem with increased complexity in case of scalable inputs. In [23], a graph representation was generated by first initializing multiple short parametric curves along intensity ridges of the image. These open contours are iteratively deformed by internal stretching forces and external image forces until saturation. Geometrical post-processing is then performed to connect the deformed contours and build a final graphical model. In [16], after calculating a Riemann vesselness potential, based on convolving the image with a steerable Laplacian of Gaussian filter banks, exhaustive search for geodesic connecting paths is performed to construct an over-connected graph. Then, a final minimum spanning tree is calculated. Methods accepting raw inputs are susceptible to other elongated structures in angiographic datasets and cannot ensure an alignment of the extracted graphs with vessels centerlines. Also, they can introduce over- or reduced-connectivity patterns, thus resulting in false topological interpretations.

4.2.2 Models Accepting Voxel-based Mappings

Graphing solutions have also been proposed requiring pre-mapping of the object structure to be modeled [9–13, 24, 26, 27]. Various techniques are surveyed in [28]. Here, we discuss those relying on voxel-based binary pre-mapping. Methods in [9, 10, 26] produce image-based curve-skeletons following homotopic thinning. In [9], topological models for blood vessels are generated from 3D power doppler ultrasound images to differentiate changes in benign and malignant tumors. In [26], improved thinning performance is achieved by first shrinking the input volumetric binary mask through an iterative least squares optimization. Other image-based skeletonization techniques are based on calculating the singularities of distance-related fields [11]. Hybrid distance-based skeletonization is employed to provide a 3D path planning for virtual bronchoscopy in multidetector computed tomography. Thinning and distance-based skeletonization techniques are fast and easy to implement, however, they produce less-smooth skeletons with disconnected-compartments, that need extensive pruning and re-graphing.

4.2.3 Models Accepting Geometry-based Mappings

The pre-mapping of vascular structures can also be a triangulated surface model or a point cloud. Geometric mapping of objects structure can yield graphical models with improved quality [12, 13, 24, 27]. Methods to extract curve-skeletons from incomplete point clouds are proposed in [13, 29]. In [29], the authors proposed an improved cloud-based graphing scheme exploiting piecewise cylindrical segmentations of the vascular structure. As reported in the corresponding papers, cloud-based schemes suffer from incorrect centeredness of the obtained models, especially in the case of irregular/non-sufficient sampling of the object structure. In [12], a mesh contraction scheme is introduced using differential geometry to decimate a surface model into a curve-skeleton. In [24], mesh contraction is combined with a segmentation network and a surface mesh generator to model cerebral microvessels from raw two-photon microscopy (TPM). Geometry-based skeletonization techniques require exhaustive efforts in preparing suitable surface model inputs, which is a major obstacle when working with complex and scalable cerebrovascular structures.

4.2.4 Our Contribution

There is a need for vascular graphing schemes that are less restrictive to either hardly-encoded inputs or to high-quality vascular labeling while providing precise topological and structural representations to be used in further vascular analysis. Here, to address this issue, we propose a novel vascular graphing scheme inspired by the Laplacian flow formulation. Diverging from the work in [24] and improving on the work presented in [27], we exploit the Laplacian framework to deform 3D geometric graphs, instead of triangulated meshes, converting them into curve-skeletons as models of vascular structures. Starting with a binary-delineated vascular structure, truncated 3D grid graphs are first constructed within vessels boundary. We develop a technique to assign affinity weightings to these graphs based on both the binary distance transform and the local geometry of graph compartments. The weighted graphs are fed into a constrained iterative optimizer to create a Laplacian dynamic flow of graph vertices/nodes toward the centerlines of vascular structures combined with a convergence criterion to stop the iteration process. Finally, a refinement algorithm is proposed to convert the deformed graph into a final vascular graphed-skeleton model. The proposed scheme can provide smooth and well-connected graph models regardless of the quality of image vascular pre-mapping, and yet does not require complex input representations, such as water-tight surface meshes. Our modeling is shown to provide improved vessel radii estimates, which are performed intrinsically during the geometric deformation process. This property is vital for biophysical studies that heavily rely on structural information encoded in vascular models. Furthermore, with simple hyper parameterization, the proposed scheme provides control over the calculation speed and the smoothness and centeredness properties of the generated graphs. The

proposed scheme can be extended to process scalable vascular images at reasonable computational effort.

In the following, we present the formulation of the modeling scheme. We describe its parameter sensitivity and study performance on synthetic and real datasets acquired using different imaging modalities. Results are compared with that produced by other efficient and recent state-of-the-art graphing techniques. A brief conclusion follows.

4.3 Method

In this section, we describe a novel computational geometry scheme to generate graph-based anatomical models of cerebrovascular networks based on their binary maps.

4.3.1 Initial Geometry

We first construct an initial geometric graph enclosed within the boundary of the masked microvascular structure. We then aim at building a reduced grid graph with its nodes emerging from the true-valued voxels of the vascular mask. For $\mathcal{O} \subset P \subset \mathbb{R}^3$ being the object that represents the microvasculature in the image domain P, the corresponding 3D binary mapping is defined as $\mathcal{I} : P \rightarrow \{1, 0\} \mid \mathcal{I}(\mathbf{p}) = 1 \quad \forall \mathbf{p} \in \mathcal{O}$ and $\mathcal{I}(\mathbf{p}) = 0$ otherwise. Furthermore, we define $\mathcal{D} : P \rightarrow \mathbb{R}$ to be the Euclidean distance transform obtained for $\mathcal{I}$. Now, one could define a reduced grid graph $\mathcal{G} = (\mathbf{V}, \mathbf{E})$, with $\mathbf{V} : \{1, 2, 3, \ldots, k\}$, where k is equal to the number of voxels in $\mathcal{O}$. The labeling function ϕ_p assigns voxel coordinates $\mathbf{P} = [\mathbf{p}_1, \mathbf{p}_2, \mathbf{p}_3, \ldots, \mathbf{p}_k]^T, \mathbf{p}_i = [p_{xi}, p_{yi}, p_{zi}] \in \mathbb{R}^3$, to $\mathbf{V}$. Likewise, the function $\phi_r : \mathbf{V} \rightarrow \mathbf{R}$ maps graph nodes to $\mathbf{R} = [r_1, r_2, r_3, \ldots, r_k]^T, r_i = \mathcal{D}(\mathbf{p}_i)$. We construct the edges $\mathbf{E} : \{\{i, j\}, \ \forall i \in \mathbf{V}$ and $j \in \mathcal{N}(i)\}$, where $\mathcal{N}(i)$ is the set of nodes emerging from the voxels forming the 6-connectivity neighbors of the voxel associated with the node i. For an arbitrary voxel in 3D space, its 6-connectivity neighbors are the voxels sharing one of their surfaces with it. Employing other connectivity patterns for the construction of $\mathcal{G}$ is achievable, however, the 6-neighborhood pattern utilized in our scheme ensures a consistent performance at a lower computational burden.

4.3.2 Geometric Flow and Graph Contraction

We follow the paradigm of Laplacian optimization to derive a geometric flow for the nodes of $\mathcal{G}$. One crucial characteristic sought for the dynamics of this flow is the inward contraction of $\mathbf{V}$. Precisely, the flow should ensure a convergence of node positions toward the centerline of the object $\mathcal{O}$. Now, let us consider $\mathcal{G}$ as a weighted graph with affinity matrix $\mathbf{W}$. We define $\delta_{i,\mathbf{W}}$ as the Laplacian operator applied on the ith node of $\mathcal{G}$ and acting on the labeling function ϕ_p:

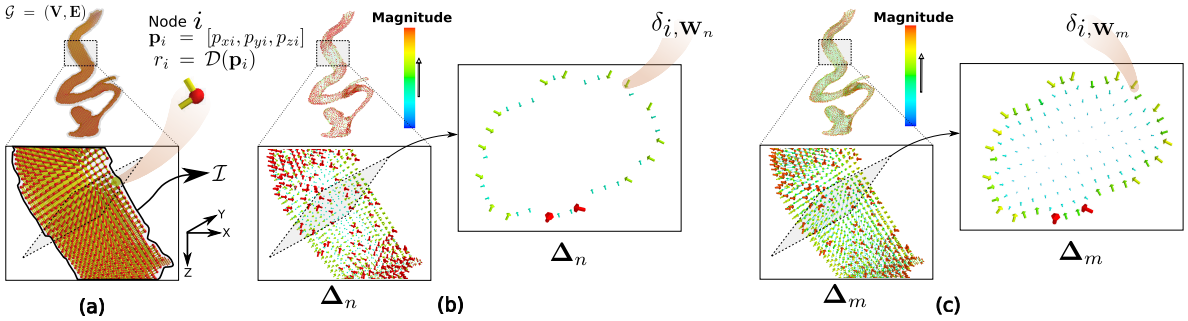

Figure 4.1 Visualization of the $\mathbf{\Delta}_n$ and $\mathbf{\Delta}_m$ vector fields, depicted in (b) and (c), and calculated using (4.5) and (4.6), respectively. The two fields result from applying the proposed Laplacian operators on a geometric graph enclosed within vascular space, shown in (a). Vectors colors and scales reflect their magnitudes, which are bounded between 0 and 1.

$$\delta_{i,\mathbf{W}} = \left[\sum_{j \forall \{i,j\} \in \mathbf{E}} \mathbf{W}^{ij} \phi_p(j) \right] - \phi_p(i) \,, \tag{4.1}$$

where $\sum_{j \forall \{i,j\} \in \mathbf{E}} \mathbf{W}^{ij} = 1$. To establish a geometric flow dynamics bearing the features discussed above, we propose a combined use of two different normalized affinity weightings on $\mathcal{G}$ defined as

$$\mathbf{W}_n^{ij} = \frac{\|\mathbf{p}_i - \mathbf{p}_j\|_2}{\sum_{k \forall \{i,k\} \in \mathbf{E}} \|\mathbf{p}_i - \mathbf{p}_k\|_2} \tag{4.2}$$

$$\mathbf{W}_m^{ij} = \frac{|r_i - r_j|}{\sum_{k \forall \{i,k\} \in \mathbf{E}} |r_i - r_k|} \,. \tag{4.3}$$

Henceforth, we will refer to $\mathbf{W}_n^{ij}$ and $\mathbf{W}_m^{ij}$ as $l2$-norm and medial affinity matrices, respectively, and the associated $\delta_{\mathbf{W}_n}$ and $\delta_{\mathbf{W}_m}$ as $l2$-norm and medial Laplacians. Based on a normalized affinity matrix $\mathbf{W}$ for $\mathcal{G}$, one can compute the Laplacians for the entire graph using the Laplacian matrix, i.e.,

$$\mathbf{L}_{ij} = \begin{cases} -1 & i = j \\ \mathbf{W}^{ij} & \{i,j\} \in \mathbf{E} \\ 0 & otherwise \,. \end{cases} \tag{4.4}$$

We denote the Laplacian matrices associated with the l-norm and medial weights as $\mathbf{L}_n$ and $\mathbf{L}_m$, respectively. Consequently, the $l2$-norm and medial Laplacians of the entire graph are given by

$$\mathbf{\Delta}_n = [\delta_{1,\mathbf{W}_n}, \delta_{2,\mathbf{W}_n}, \ldots \delta_{k,\mathbf{W}_n}]^T = \mathbf{L}_n \mathbf{P} \,, \tag{4.5}$$

$$\mathbf{\Delta}_m = [\delta_{1,\mathbf{W}_m}, \delta_{2,\mathbf{W}_m}, \ldots \delta_{k,\mathbf{W}_m}]^T = \mathbf{L}_m \mathbf{P} \,. \tag{4.6}$$

Interestingly, in the formulas above, each of the elements $\delta_{k,\mathbf{W}_n}$ and $\delta_{k,\mathbf{W}_m}$, corresponding to a node k in the graph, represents a local vector pointing toward a non-uniformly weighted centroid of its 6-connectivity neighbors. The vector fields, $\mathbf{\Delta}_n$ and $\mathbf{\Delta}_m$, calculated based on a geometric grid graph generated from a labeled angiogram, are depicted in Fig. 4.1. Both fields comprise vectors that have different magnitudes and directed toward the centerline of the vessel tree. The field $\mathbf{\Delta}_n$ is zero within vessel boundaries due to the equal spacing of grid graph nodes. Based on (4.1) and (4.2), this results into a zero net-vector. It is worth mentioning that if the grid graph loses its isotropic property due to any deformation of its node positions, $\mathbf{\Delta}_n$ will develop non-zero components within vessel boundaries. On the other hand, $\mathbf{\Delta}_m$ has non-zero magnitude even inside vessels body, since its calculated based on the Euclidean distance transform mapping.

Now, if graph nodes are further moved inward, both $\mathbf{\Delta}_n$ and $\mathbf{\Delta}_m$ will have smaller magnitudes (≥ 0) in directions perpendicular to the centerline. Hence, contracting graph geometry toward vessels centerlines can be obtained by implicitly solving

$$\begin{bmatrix} \mathbf{L}_n \\ \mathbf{L}_m \end{bmatrix} \widehat{\mathbf{P}} = \mathbf{0} \,, \tag{4.7}$$

where $\widehat{\mathbf{P}}$ are the new positions of graph nodes. Since both matrices $\mathbf{L}_n$ and $\mathbf{L}_m$ are singular, this sparse system admits the trivial solution $\widehat{\mathbf{P}} = \mathbf{0}$. To address this issue, a regularized version of the system can be solved as

$$\begin{bmatrix} \mathbf{W}_\alpha \mathbf{L}_n \\ \mathbf{W}_\beta \mathbf{L}_m \\ \mathbf{W}_\gamma \end{bmatrix} \widehat{\mathbf{P}} = \begin{bmatrix} \mathbf{0} \\ \mathbf{W}_\gamma \mathbf{P} \end{bmatrix} \,. \tag{4.8}$$

Above, $\mathbf{W}_\alpha$, $\mathbf{W}_\beta$ and $\mathbf{W}_\gamma$ are diagonal matrices such that $\mathbf{W}_\alpha^i = \alpha$, $\mathbf{W}_\beta^i = \beta$ and $\mathbf{W}_\gamma^i = \gamma$, respectively. The elements in $\mathbf{W}_\gamma^i = \gamma$ constrain all graph nodes to their current positions. Those in $\mathbf{W}_\alpha$, $\mathbf{W}_\beta$ determine the dependence of the solution on either the $l2$-norm or the medial Laplacians, respectively.

4.3.3 Contraction Flow Dynamics

Solving (4.8) iteratively generates a geometric flow for graph nodes by moving them along the direction of their $l2$-norm or the medial Laplacians. This flow dynamics will serve as the core of the proposed skeletonization scheme. The nature of the flow is controlled by varying the weights α, β and γ. Several iterations, and proper weights, are required for the process to converge towards the centerline of vascular structures. The proposed model creates a dual-mechanism to guide the dy-

namics of graph nodes by exploiting both, their connectivity-encoded geometry and distance transform mapping. This duality is vital to ensure a better convergence of graph geometry. Using only the weights from $\mathbf{L}_n$ could lead to unwanted straightening of the graph geometry, and integrating $\mathbf{L}_m$ weights in the dynamics will restrict flow dynamics toward singularities/ridges emerging in the distance transform field. On the other hand, relying only on distance field weightings does not guarantee a convergence into a curve-skeleton with centeredness property [30]. Despite a less-complex computation, the distance transform has the shortcoming of forming medial surfaces rather than medial curves in the case of 3D objects. Thus, combining $\mathbf{L}_n$ weights in (4.8) provides additional constraints on the flow dynamics to impose further shrinking of graph geometry. At each iteration, the solution of the over-determined system in (4.8) is obtained by least-squares minimization. The parameters $\alpha \in [0, 1]$ and $\beta \in [0, 1]$ were chosen to have a partition of unity property, and thus only one of the two needs to be specified. The speed of flow is thus tuned by altering the value of $\gamma \in [0, 1]$. Lower values of γ accelerate the contraction process at the expense of over-deformed graph geometry. Conversely, higher values of γ decelerate the geometric evolution of graph nodes but can result in slow convergence. The final concern is to define a criterion to stop the contraction process when converged. In principle, the volumetric space that the graph geometry can occupy is of zero volume if the graph is perfectly situated at vessel centerlines. Zero-volume graph geometry indicates that polygons formed by its nodes/vertices have areas equal to zero. At an iteration t, we calculate the areas of polygons derived from the cycle basis of the graph [31]. Then, we retain the cumulative sum of areas, denoted as A_t, for polygons containing a number of nodes less than ϵ_n. The iteration stops when the ratio of A_t and A_0 is smaller than a threshold, referred to as ϵ_A. Choosing a relative quantity (A_t/A_0) makes the convergence more independent of the size and scale of the initial geometry. In the following, the values of ϵ_n and ϵ_A were set empirically to 10 and 10^{-3}, respectively.

4.3.4 Adaptive Flow Dynamics

Throughout the contraction process, an initial graph geometry will keep evolving toward vessel centerlines. Some regions of graph geometry, falling within smaller vessel zones, will achieve a faster convergence than that belonging to larger vessels. The nodes forming graph regions that have well converged into their local vessel centerlines are referred to as skeletal-like nodes (see Fig. 4.2(a)). Further contraction of these nodes in next iteration steps, will introduce over-deformation that negatively affects the quality of our final output. Here, we propose a technique to alleviate the dynamics of these nodes in following time steps. The technique calculates the angles that are formed between any pair of edges arising from a node i. If the absolute cosine of these angles is close to one, that node is more-likely to be a skeletal-like node. For a node i to undergo a reduced

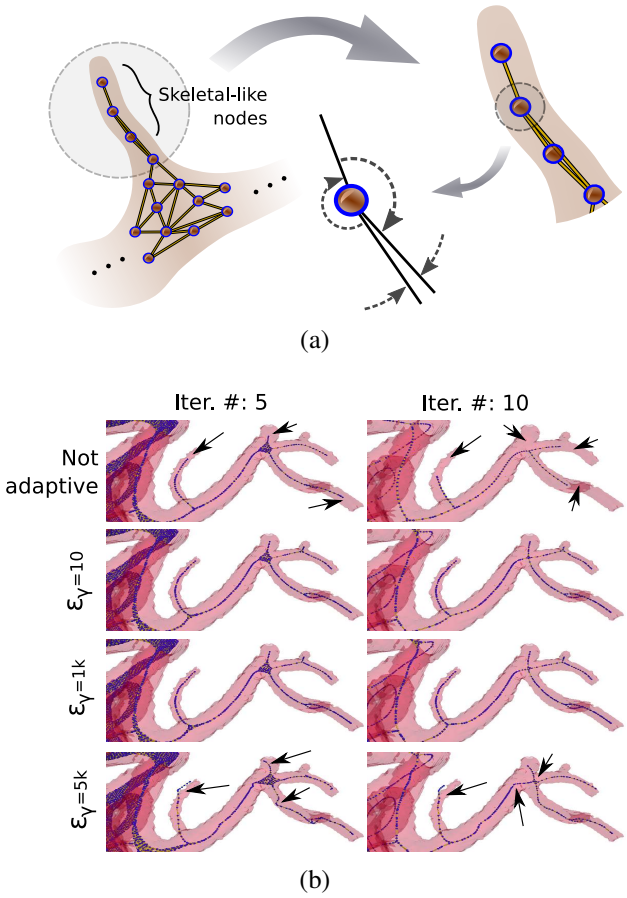

Figure 4.2 Illustration of the adaptive technique integrated in the proposed graphing scheme. (a) The condition used to identify a skeletal-like node is based on the absolute cosines of the angles formed between its edges; computed absolute cosines must satisfy the inequality in (4.9). (b) The effect of omitting the condition in (4.9) or choosing very large values of ϵ_γ. The arrows indicate inappropriate localization of graph nodes after the 5th and 10th iterations of contraction.

contraction force in the next time step, it has to satisfy the condition:

$$|\cos(\pi - \angle\left[\overrightarrow{\mathbf{p}_i\ \mathbf{a}}, \overrightarrow{\mathbf{p}_i\ \mathbf{b}}\right])|, \quad \mathbf{a}, \mathbf{b} \in \mathcal{N}(\mathbf{p}_i), \quad \geq 0.9 \ . \tag{4.9}$$

When a node i passes the above condition, its corresponding element in $\mathbf{W}_\gamma$ is altered to $\mathbf{W}_\gamma^i = \epsilon_\gamma * \gamma$. The value of the factor ϵ_γ (>1) should be chosen carefully. Larger values of ϵ_γ (>1k) can disrupt the row/column scaling in the system, thus hindering its convergence. On the other hand, smaller values are not helpful in restraining skeletal-like nodes. Based on experimentations, setting ϵ_γ to 10 was a good choice for the modeling done below. Our choice was based on visually assessing the quality of the converged graphs extracted from a set of synthetic angiograms used in our work (see Section 4.4), by setting ϵ_γ to $5, 10, 50$ or 100. We aimed at picking the lowest value

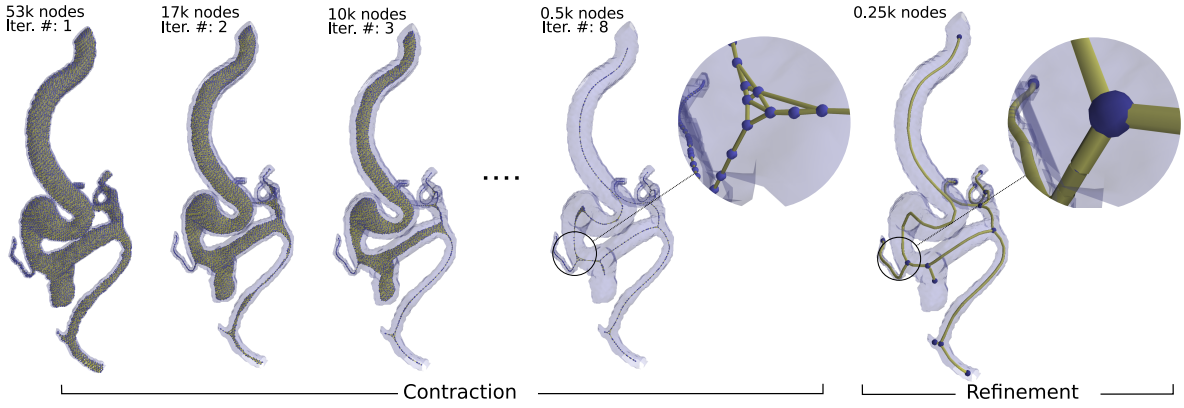

Figure 4.3 Visual example of the contraction and refinement processes integrated in the proposed scheme to produce a final graphed-skeleton from a binary-labeled vascular structure. In the contraction phase from left to right, the initial geometric graph evolves toward vessels centerline with further structural reduction at each iteration. The refinement phase accounts for fixing over-connectivity patterns on the contacted graph, converting it into a graphed curve-skeleton.

that can achieve a desirable performance. Fig. 4.2 demonstrates the benefit of using the proposed adaptive procedure and interpret our value selection of the factor ϵ_γ.

4.3.5 Geometric Graph Decimation

Following contraction, graph nodes are squeezed after each iteration forming a denser geometry while shifting closer to the object centerline in each step. Yet, the topology of the graph, remains the same. To address this, we take advantage of the collapsed geometry to adjust graph structure. The structural surgery includes a reduction of the graph and a modification of its topology after each iteration. This decimation process helps in deforming the graph to approach that of a curve-skeleton. Also, it delivers a reduced model that will require less computational effort when processed in the next iteration. Consequently, the overall contraction time will be minimized. First, the Euclidean space is tessellated into a 3D regular grid with equally-spaced cubic cells of size c^3. Practically, we used a cell size equal to the size of a voxel in the 3D input image. Graph nodes situated within a cell are then grouped as one cluster. After generating the clusters, $\mathcal{C} : \{\mathbf{C}_1, \mathbf{C}_2, \mathbf{C}_3, \ldots, \mathbf{C}_k\}$, their centroids, $\mathbf{S} : \{\mathbf{s}_1, \mathbf{s}_2, \mathbf{s}_3, \ldots, \mathbf{s}_k\}$, are calculated and integrated as new nodes in the graph. Then, new edges are assigned for the newly created nodes and an edge between a pair of centroid nodes is created if there is any connection between their corresponding samples. Finally, we remove graph nodes used in clustering, and only the new ones, with their constructed edges, are maintained. The structural surgery described above is depicted in figure 4.4.

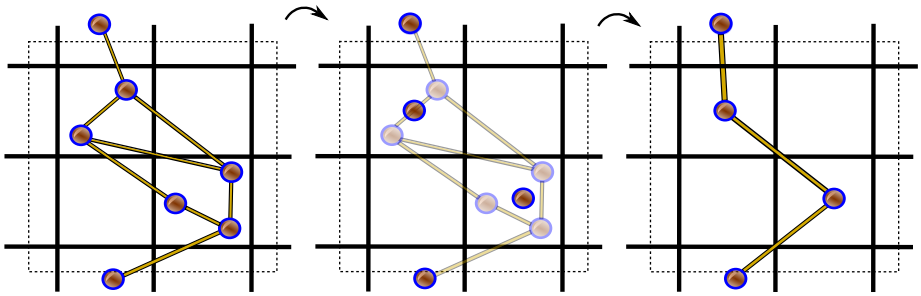

Figure 4.4 An illustration of the proposed clustering technique used for decimation of the evolving geometric graph at each iteration.

4.3.6 Transferable Radius Attributes

Values at the ridges formed by the distance transform provides a good estimation of the radii of tubular objects along the trace of their centerlines. As previously discussed, a graph node i has the attribute r_i representing the closest Euclidean distance of the node from the object boundary. If the node is located at the medial curve of the object, the value of r_i can serve as a measure of the object radius at that point. Based on the proposed contraction scheme, existing graph nodes are replaced at each time step with those newly created through our structural operation. When applying the structural surgery, a new node i, emerging as the centroid of the cluster $\mathbf{C}_i$, will be assigned an attribute r_i computed as the maximum of those associated with the nodes in $\mathbf{C}_i$. Using this technique, the graphed skeleton will not only model objects topology, but also their shapes, an essential input to cerebrovascular models in wider biophysical applications.

An example that illustrates the proposed contraction process is depicted in Figure 4.3 (contraction phase). It shows how a decimated version of the graph $\mathcal{G}$ is moved towards the object medial line at each iteration. The algorithmic pipeline for the contraction scheme is summarized in Algorithm 2.

Algorithm 2 Structural processing of $\mathcal{G}$ in the contraction phase.

Require: $\mathcal{G}$, α or β, γ
1: Compute A_0; $A_t \leftarrow A_0$.
2: **while** $\frac{A_t}{A_0} < 10^{-3}$ **do**
3: Compute $\mathbf{L}_n$, $\mathbf{L}_m$ based on (2), (3) and (4). (Section 4.3.2)
4: Obtain $\mathbf{W}_\gamma$ after imposing each $\mathbf{p}_i \in \mathbf{P}$ to (4.9). (Section 4.3.4)
5: Solve (4.8). (Section 4.3.2)
6: Create $\mathcal{C}$ and apply graph decimation. (Section 4.3.5)
7: Calculate radii attributes. (Section 4.3.6)
8: Update A_t. (Section 4.3.3)
9: **end while**

4.3.7 Geometric Graph Refinement

The output graph resulting from the contraction scheme is converged to the centerline of the object $\mathcal{O}$ but does not have the skeleton structure properties required for modeling. In this section, we propose a refinement operation to convert the geometric graph $\mathcal{G}$ resulting from Algorithm 2 into a curve-skeleton. The procedure is based on eliminating small polygons formed in $\mathcal{G}$. One need to set a threshold for the smallest cycles to be cleaned. In fact, some polygons could represent a real cycles in the original angiogram, and thus need to be kept. In our study, we picked a threshold of $10c^2$ after investigating the areas of the smallest cycles $\sim 75c^2$ found in our two-photon microscopy datasets, since they are the only ones that contain cyclic structures. Our choice was found to provide a correct refinement without missing any cyclic compartments. The cycle basis of $\mathcal{G}$ is computed and the set of cycles $\mathcal{X}$ with edges $\mathbf{E}_{\mathbf{X}_i}$ in the ith cycle, is retained as follows:

$$\mathcal{X} = \left\{ \mathbf{X}_i, \ \text{if} \ \frac{1}{2} \left\| \sum_{(\mathbf{a},\mathbf{b}) \in \mathbf{E}_{\mathbf{X}_i}} [\overrightarrow{O\mathbf{a}} \times \overrightarrow{O\mathbf{b}}] \right\| < 10 \right\} , \tag{4.10}$$

where O is the origin. Nodes in the cycle $\mathbf{X}_i$ are contracted towards their centroid $\mathbf{s}_i$:

$$\mathbf{p} \leftarrow (\mathbf{p} + \mathbf{s}_i)/2, \ \ \forall \mathbf{p} \in \mathbf{X}_i \ . \tag{4.11}$$

If a node belongs to multiple cycles, it is randomly processed within one of these cycle. After adjusting nodes geometry, we carry out the same structural surgery presented in the contraction stage. We repeat the steps discussed above until we reach a state where the number of elements in $\mathcal{X}$ is equal to zero. Figure 4.3 visualizes how the proposed refinement technique transforms a decimated graph resulting from the contraction process into a graph-based skeleton.

4.4 Validation and Discussion

In this section, we evaluate the performance of the proposed modeling scheme through various experiments conducted on synthetic and real cerebrovascular datasets. The data includes both tree-like and loopy vascular structures. Fist, we present the evaluation metrics, the different datasets and baselines utilized for performance evaluation. We study the sensitivity of our modeling to its tunable parameters. Finally, We compare our results with that obtained by other standard and state-of-the-art skeletonization approaches [12, 16, 23, 32, 33] when applied to the same datasets.

4.4.1 Experimental Setup and Datasets

We compared the performance of our modeling scheme with other efficient methods used to generate graphed skeletons for tubular or vessel-like structures. These methods are: the classical 3D-thinning (Voxel-based) [9][1], mesh-based mean-curvature skeletonization (Mesh-based) [12][2], 3D points-cloud contraction (PC-based) [13][3], multiple stretching of open active contours (SOAX-based) [23][4] and geodesic minimum spanning trees extraction (VTrails-based) [16][5]. For quantitative assessments of the structural errors produced by the various skeletonization methods, we use the DIADEM metric [34][6]. This metric provides a value $\in [0, 1]$, with 1 indicating a perfect model match. It is to be noted the DIADEM metric is used for evaluating only tree vascular structures and is not applicable for acyclic vascular networks. The NetMets measures [35] are also exploited to assess the quality of both tree-like and loopy vascular structures. These measures are employed to provide detailed quantification of the geometrical and topological errors incurred by the different schemes. A code for generating these measures is available online [7]. The associated measures contain four metrics. Two metrics, namely GFNR and GFPR, are used to evaluate the geometric false negative and false positive errors, respectively. The other two metrics, namely, CFNR and CFPR, quantify the false negative and false positive topological errors, respectively. The sensitivity of NetMets measures is controlled by one parameter denoted by τ. For more details on these metrics, the reader is referred to [35].

We based our evaluation on both synthetic and real cerebrovascular structures captured in in-vivo studies using different acquisition modalities. We used the VascuSynth toolbox [36] to prepare 3 sets of synthetic vascular trees, with 30 samples in each, D^{nl}, considering different levels of surface noise $nl = low, medium$ and $high$. Each set contains samples with three different branching levels (10 samples for each level), namely, $16, 32$ and 64. Surface noise was created by adding bubbles on vessel boundaries. The higher the noise level, the higher is the number and size of these bubbles. The clinical validation set is composed of x-ray cerebral aneurysm angiograms (RAA) [37] and magnetic resonance angiograms (MRA) [38]. We also assessed the algorithm on in-vivo TPM stacks obtained from [39]. Ground truth annotations from the various datasets were provided as spatial centerlines. In-detail explanation on the preparation and pre-processing of our realistic datasets, to fit as inputs to the benchmarked methods, is provided in the supplementary material (Section I). After generating an output graph using any of the methods used in our comparison, radii

[1]Implementation: *https://github.com/InsightSoftwareConsortium/ ITKThickness3D*
[2]Implementation: *https://github.com/CGAL/cgal*
[3]Implementation: *http://www.shihaowu.net*
[4]Code: *https://github.com/tix209/SOAX*
[5]*https://github.com/VTrails/VTrailsToolkit*
[6]*http://diademchallenge.org/metric.html*
[7]*https://git.stim.ee.uh.edu/segmentation/netmets*

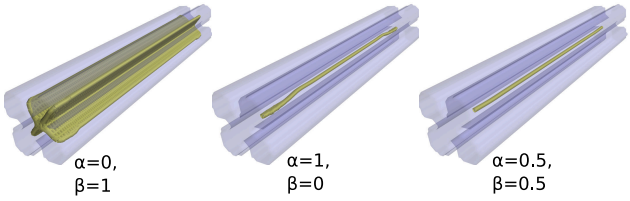

(a)

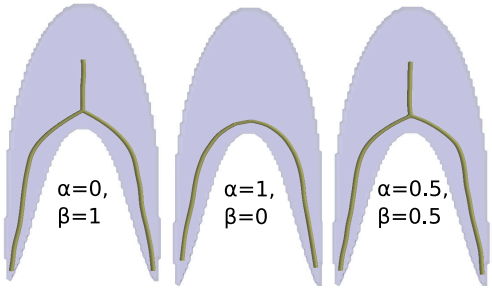

(b)

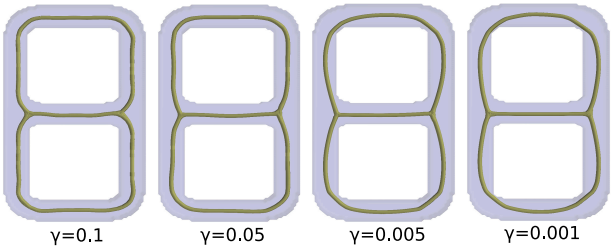

(c)

Figure 4.5 The response of the proposed scheme when modeling various structures using different parametric settings. In (a) and (b), the skeletonization output is robust to variations in the input structure when using a combined setting of α and β. Varying the value of γ impacts the quality of the output graph as seen in (c).

values are assigned to its nodes. Vascular radius at each graph node is quantified as the intensity of the Euclidean distance transform at the coordinate of that node. We assess the correctness of radius mappings on the generated graph by measuring the mean absolute percentage error (MAP) between the estimated and true radii values. To compute MAP scores, we first match the nodes of the experimental model with that of the ground truth as explained in [24].

4.4.2 Parametric setting

The parameters that need to be tuned in our methodology are α, β and γ. This section provides insights on the behavior of the algorithm when varying these parameters. Synthetic objects, depicted in Figure 4.5, were skeletonized at different values of α, β and γ. The upper row displays a tubular

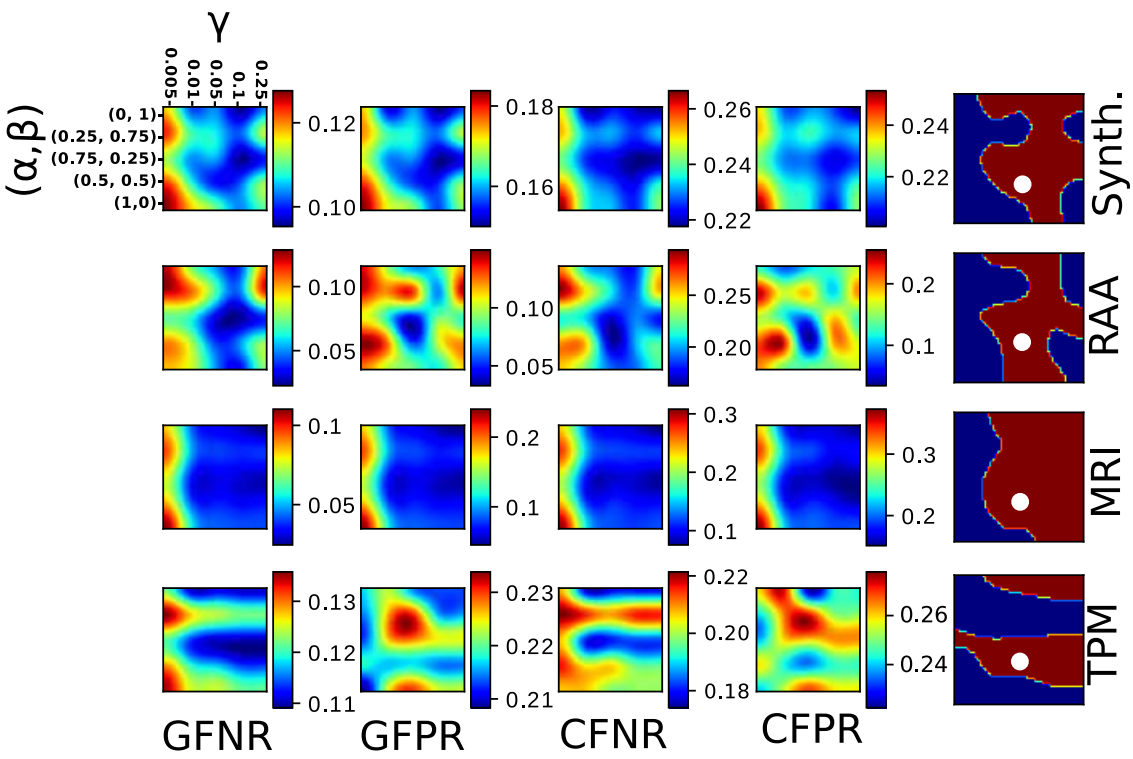

Figure 4.6 Identifying the best parametric setting of α, β and γ in our modeling. (left-four columns) Heatmaps generated based on the averaged NetMets errors (GFNR, GFPR, CFNR and CFPR), each row shows that obtained for one of the datasets. (right column) Best regions in the parameters space projected from NetMets heatmaps. The white dot represents the point at $\alpha = 0.5$, $\beta = 0.5$ and $\gamma = 0.05$ used in our experiments.

object with large boundary perturbations, i.e., less-informative distance transform mapping about the tubular structure. In the upper row, after solving (4.8) for 10 iterations, it is clearly seen that enforcing the contraction process to rely only on medial Laplacians, $\mathbf{L}_m$ hinders the convergence toward object centerline. The deformed model remains on object medial surfaces. On the other hand, when increasing the effect of the $l2$-norm Laplacians by increasing the value of α, better convergence and centerline modeling is achieved. In the middle row of the figure, a bent tubular structure inflated at its center is used in the modeling process. When cancelling medial Laplacians $\mathbf{L}_m$ by setting β to zero, the output graph is abstract and fails in capturing the full information about the object. Nevertheless, adding $\mathbf{L}_m$ in the optimization problem creates better modeling. Here, we conclude by stating that solving (4.8) with a combined setting of both α and β can provide smooth, and yet, well-detailed graph models. As previously mentioned, the speed of the contraction process can be controlled by γ. In the bottom row of the figure, from left to right, an 8-shape object is modeled with decreasing values of γ, namely, $0.1, 0.05, 0.005, 0.001$. The number of iterations required to converge were $34, 17, 9$ and 5, respectively. It is observed that the lower the value of

γ, fewer iterations are needed, but at the expense of more abstract graphical representation. It is also seen that abstracted graphs suffer from poor alignment of their compartments along the object centerline. To have a more comprehensive understanding about the behaviour of the proposed algorithm, we studied the effect of varying our parametric setting on its performance when modeling the various realistic datasets used in our experimentations. Fig. 4.6 plots the averaged NetMets errors, calculated after applying our scheme on each of RAA, MRA and TPM datasets, using different points in a subspace of the α, β and γ parameters. In particular, the figure depicts NetMets error heatmaps accompanied annotations of the best regions to be used in selecting a suitable parametric setting. Delineating best regions in the parametric space was done though thresholding at the mean error value plus one standard deviation. We picked the parametric setting $\alpha = 0.5$, $\beta = 0.5$ and $\gamma = 0.05$, which is shown to be appropriate in all dataset cases, to produce our results in the following sections. More discussion and visual illustrations on the sensitivity of the proposed scheme, based on the topological NetMets errors, are provided in Section III in the supplementary material.

4.4.3 Synthetic Vascular Trees

Table 4.1 lists the error measures based on the metrics used for each graphing scheme on synthetic angiograms. For each metric, the top-three scores are color-labeled, while the top-score is green-labeled. The arrow next to each metric name indicates if a high (up-arrow) or low (down-arrow) score is better. When assessing the extracted geometry based on GFNR and GFPR metrics, one can note that at low level of boundary noise, the voxel-based method provides the lowest false negative and positive rates. However, with increased noise level, it fails by introducing large geometric errors. The voxel-based method exhibits variable robustness against different levels of boundary noise. The SOAX-based method provides low false positive errors but at the expense of very high false negative rates. This observation indicates that it misses substantial geometric details of the vascular structures. Overall, our algorithm performs better against other schemes in providing more robust graph models at high noise levels, with, overall, the lowest false negative and false positive rates. Analysing the topological CFNR and CFPR errors, the voxel-based method gives low false negative scores but at the expense of a degradation in false positive rates. This reflects a deterioration of the original topology with a large amount of over-connectivity. The Vtrails-based method provides balanced, yet weak false negative and positive rates. The mesh-based technique shows a similar trend with some improvements. When considering both CFNR and CFPR scores, the proposed work stands again as the best scheme to provide the best error-less topological representations. We then analysed the tree-like correctness of the graphs generated by the various schemes based on the DIADEM metric. The mesh based scheme provides comparable results to ours in some cases. Yet, the proposed method shows superior performance over all other methods in most of the cases. Finally the MAP metric is of vital importance for validating the various techniques at

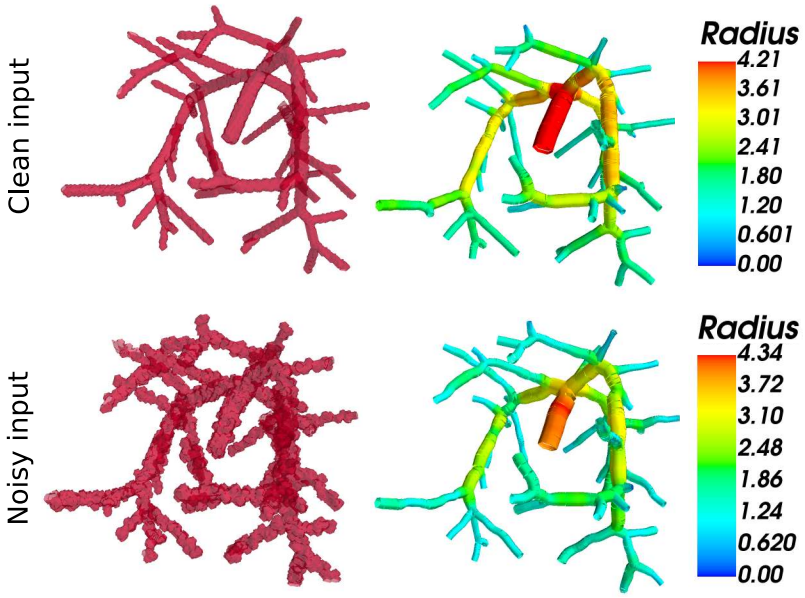

Figure 4.7 Robustness of the proposed modeling to perturbations/ridges in vascular boundaries.

providing comprehensive anatomical models of the vascular structure. It is very clear from the table that, in all cases, the method described here was the best at capturing of anatomical information. A visual example supporting our quantitative conclusion above is provided in Fig. 4.7. We depicted two output models generated from one of our synthetic samples based on zero and high-level (D^2) surface perturbations. Our method was robust at capturing the vascular anatomy even in presence of highly-deteriorated vascular surfaces.

Table 4.1 Error scores calculated after applying the different graphing schemes on the synthetic vascular dataset. Colored cells indicate the best 3 scores while a green cell indicates the best score.

GFNR ↓

	Voxel-based	Mesh-based	PC-based	SOAX-based	Vtrails-based	Proposed
D^0	**0.15±0.01**	0.27±0.03	0.23±0.04	0.35±0.05	0.32±0.03	0.22±0.03
D^1	0.27±0.03	0.28±0.04	0.32±0.07	0.40±0.05	0.37±0.05	**0.20±0.02**
D^2	0.41±0.09	0.34±0.04	0.35±0.09	0.44±0.06	0.42±0.06	**0.26±0.03**

GFPR ↓

	Voxel-based	Mesh-based	PC-based	SOAX-based	Vtrails-based	Proposed
D^0	**0.11±0.02**	0.14±0.02	0.33±0.04	0.15±0.03	0.20±0.03	0.12±0.02
D^1	0.28±0.05	0.19±0.04	0.31±0.07	**0.16±0.02**	0.23±0.05	**0.16±0.03**
D^2	0.33±0.06	0.24±0.04	0.25±0.04	0.19±0.03	0.23±0.05	**0.17±0.03**

CFNR ↓

	Voxel-based	Mesh-based	PC-based	SOAX-based	Vtrails-based	Proposed
D^0	0.27±0.05	0.37±0.04	0.49±0.11	0.56±0.09	0.52±0.06	**0.23±0.06**
D^1	**0.24±0.05**	0.41±0.11	0.54±0.08	0.62±0.16	0.57±0.09	0.28±0.07
D^2	**0.17±0.03**	0.34±0.07	0.51±0.11	0.67±0.14	0.53±0.13	0.26±0.05

CFPR ↓

	Voxel-based	Mesh-based	PC-based	SOAX-based	Vtrails-based	Proposed
D^0	**0.07±0.03**	0.12±0.04	0.25±0.05	0.13±0.05	0.11±0.03	0.08±0.02
D^1	0.27±0.06	0.17±0.07	0.31±0.05	0.13±0.04	0.19±0.08	**0.11±0.04**
D^2	0.57±0.11	0.32±0.06	0.37±0.08	0.16±0.04	0.21±0.05	**0.10±0.03**

DIADEM(%) ↑

	Voxel-based	Mesh-based	PC-based	SOAX-based	Vtrails-based	Proposed
D^0	65.1±8.22	72.54±9.8	63.2±12.1	66.9±6.44	58.4±8.82	**74.8±7.29**
D^1	54.1±13.5	69.3±8.2	51.1±14.0	56.5±10.4	55.9±7.35	**71.7±6.42**
D^2	42.4±7.06	64.4±9.45	44.5±13.8	49.3±9.91	56.2±9.3	**67.1±8.15**

MAP(%) ↓

	Voxel-based	Mesh-based	PC-based	SOAX-based	Vtrails-based	Proposed
D^0	13.4±0.84	14.5±1.44	21.7±2.13	18.2±1.59	18.4±1.46	**11.3±1.67**
D^1	14.1±1.34	16.8±2.13	19.2±1.97	18.4±2.07	20.8±3.07	**12.1±1.87**
D^2	14.8±1.84	16.4±2.39	22.6±1.70	19.2±1.37	19.6±2.19	**12.7±1.43**

4.4.4 Clinical Vascular Trees

Figure 4.8 (a) and (b) depicts the NetMets measures when testing the graphing schemes on RAA and MRA datasets, respectively, at different tolerance levels τ. Again, the proposed scheme was capable of providing superior models in all cases. SOAX-based and VTrails-based methods provide graph models with disparate topological false negative and false positive rates, hence indicating under- or over-connected graph models. This is confirmed qualitatively later in the discussion. The remaining schemes, including ours, are proven to deliver better geometrical/topological models. In most cases of RAA and MRA datasets, the proposed modeling scheme outperformed all other methods. We also studied the correctness of the tree-like structures obtained by running the minimum spanning tree algorithm on the graphs extracted. Arterial trees were constructed from MRA models based on the root branching from the Circle of Willis. The root arteries in RAA graphs were identified based on the vessel size and shape. Table 4.2 lists the DIADEM errors calculated from mapping the MRA and RAA trees to their corresponding ground truths. It is clear from the table that the proposed scheme performed substantially better in providing accurate minimum spanning trees of vascular structures with about 90% of ground truth similarity. The anatomical structure of the extracted trees were also assessed based on the MAP metric. Again, the proposed scheme outperformed other schemes in correctly mapping radius information, reflecting a more acurate anatomy. For visual assessment, examples of tree-like graphs, generated using the various schemes to model RAA and MRA angiograms, are depicted in Figure 4.9. The branching level along the tree is coded in color while radius information is mapped as the scale of cylinders (their diameters) capturing vessel segments. As shown in the figure, PC-based , SOAX-based and VTrails methods produce poorly connected graphs with degraded radius mapping and errors in their tree-like representations. The voxel-based method produce less-smooth graphs with many discontinuities. The mesh-based method is providing improved smoothness and inter-connectivity but with poor anatomical mapping. Nevertheless, in all cases, the proposed method is clearly shown to provide accurate, and yet smooth tree-like graphs with substantial improvement on the anatomical modeling aspect based on radius information.

4.4.5 In-vivo Microvascular Networks

We then studied more complex microscopic angiographies acquired with TPM. It is to be noted that tree-like models cannot be extracted from these angiograms since they include loopy structures. Thus assessments are based on NetMets and MAP metrics. NetMets measures are depicted in Figure 4.8 (c). It is seen from the figure that the proposed method produces models having the lowest geometric and topological errors compared to all other methods. It is also seen that the PC-based and SOAX-based methods are not suitable for modeling such complex angiograms. It should

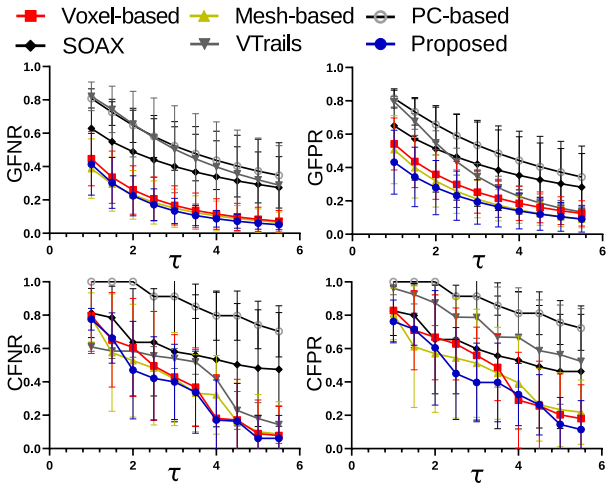

(a) RAA dataset

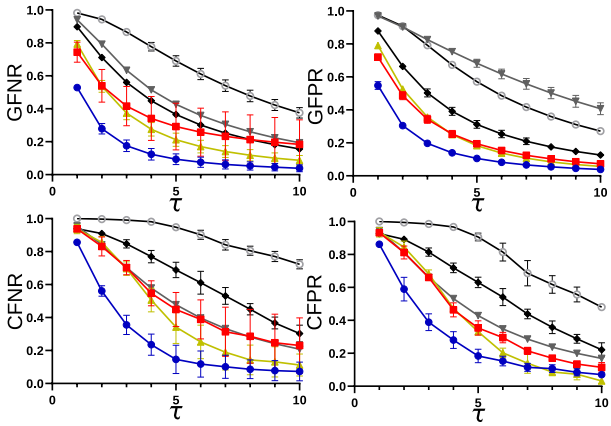

(b) MRA dataset

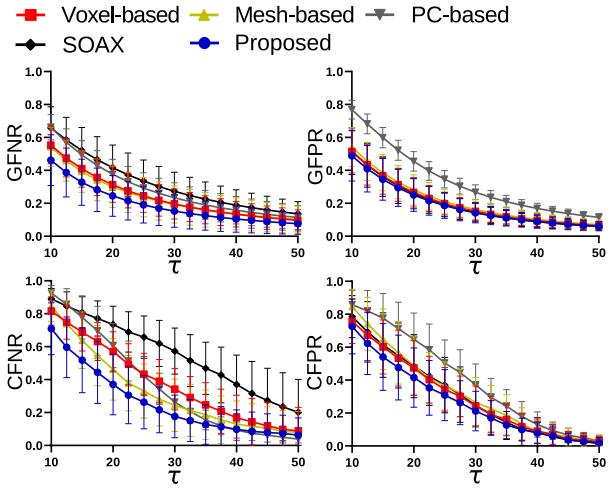

(c) TPM dataset

Figure 4.8 NetMets measures obtained at different tolerance levels τ after applying the various schemes on real datasets.

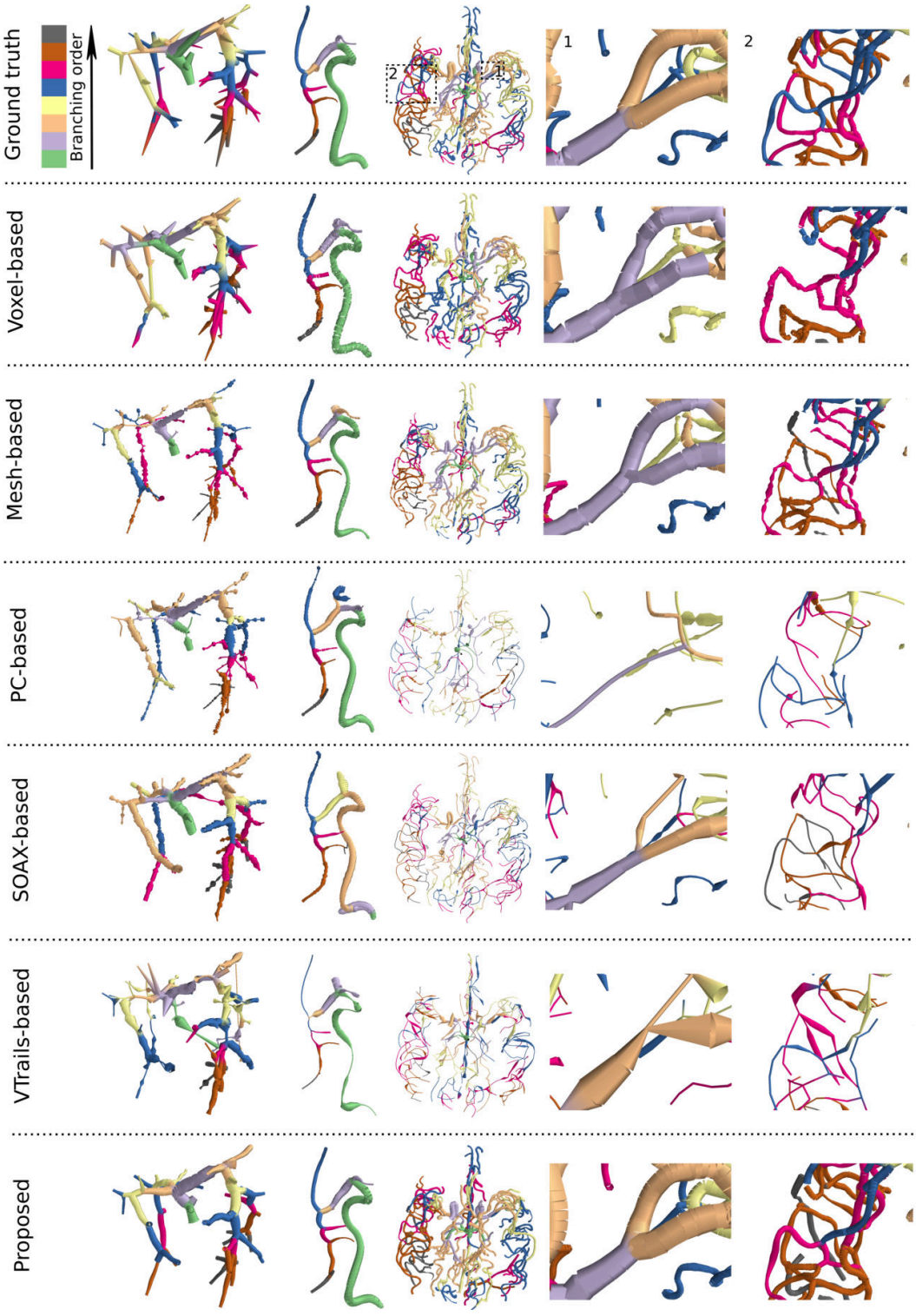

Figure 4.9 3D rendering of the vascular tree models obtained using the various schemes when applied to samples from synthetic (left column), RAA (second-left column) and MRA (middle column) datasets. The last two right columns depict magnified regions from the MRA models.

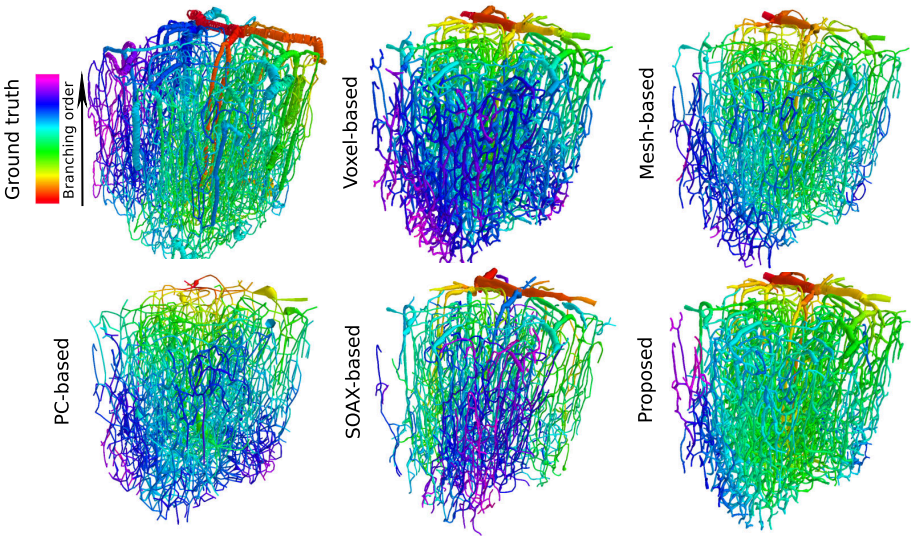

(a)

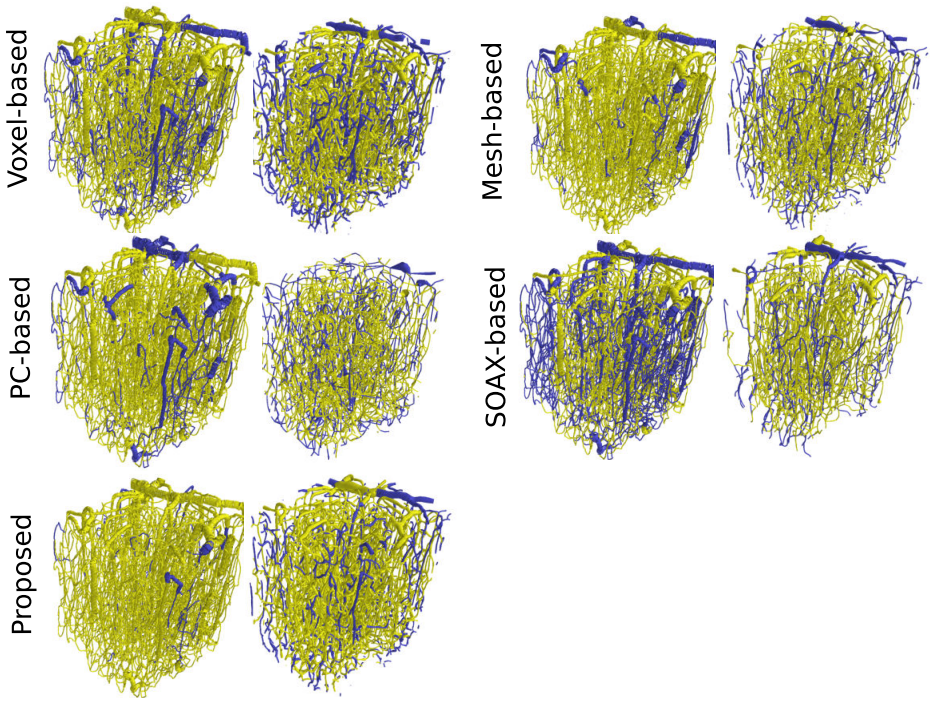

(b)

Figure 4.10 (a) Graph models generated for one of the TPM angiograms using the various skeletonization schemes. (b) For each method, we visualize the topological errors, namely, CFNR (left) and CFPR (right). Errors are blue-coded.

Table 4.2 DIADEM and MAP measurements obtained after applying the various graphing schemes on the RAA and MRA datasets. MAP metric is also used to assess the performance on the TPM dataset.

DIADEM(%) ↑						
	Voxel-based	Mesh-based	PC-based	SOAX-based	Vtrails-based	Proposed
RAA	81.6±9.05	83.6±8.64	54.5±12.9	75.8±12.0	78.4±6.93	**89.5±7.38**
MRA	85.5±6.19	90.4±3.61	69.6±5.07	78.5±9.40	77.1±8.85	**92.8±4.29**
MAP(%) ↓						
	Voxel-based	Mesh-based	PC-based	SOAX-based	Vtrails-based	Proposed
RAA	8.08±1.88	8.22±1.81	18.9±5.28	10.6±1.75	11.7±2.60	**6.03±1.73**
MRA	11.5±3.88	10.8±2.39	14.9±0.24	15.1±0.97	15.8±1.36	**4.77±0.23**
TPM	7.73±2.36	8.93±3.44	14.1±4.65	10.5±3.58	–n/a–	**6.37±2.35**

be noted that the Vtrails-based method is not applicable in this case since it is specific to tree-like structures. The voxel-based method tends to create graphs missing many topological details, as seen in the CFNR plot. Mesh-based technique can provide acceptable graph models, however, its requirement of hardly-encoded surface models as inputs can hinder its applicability, especially in case of unclean TMP data. Figure 4.10 (a) shows the 3D rendering of one TMP graph produced using the different methods. The figure depicts the propagation across the branches in the microvascular network by manually selecting a descending arterial as a source branch. These directed graphs are produced following a search from the source branch. Again, the figure illustrates the good performance of the Mesh-based and the proposed schemes in providing proper models compared to that of other schemes. Yet, our methodology is superior when considering the anatomical structures represented in vessels radii. Figure 4.10 (b) visualizes the topological errors, namely, CFNR and CFPR, incurred in the graphs presented in Figure 4.10 (a). Compared to all other methods, the proposed scheme is capable of generating TPM vascular models having less false negative and false positive topological errors. This coincides the results obtained in Figure 4.8 (c).

4.5 Computational time

All of our experiments were executed on a 3.0 GHz Ryzen AMD processor (8 cores, 16 threads in each) with 64 GB of RAM. For a comprehensive assessment of the various graphing schemes, we plot in Figure 4.12 their average computation time needed to process the angiograms in the RAA, MRA and TPM datasets. The computational time of the proposed scheme was calculated as the sum of times required through our model generation and contraction and refinement phases. It is to

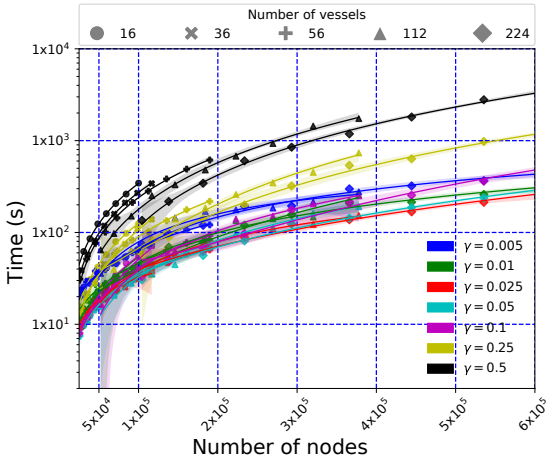

(a)

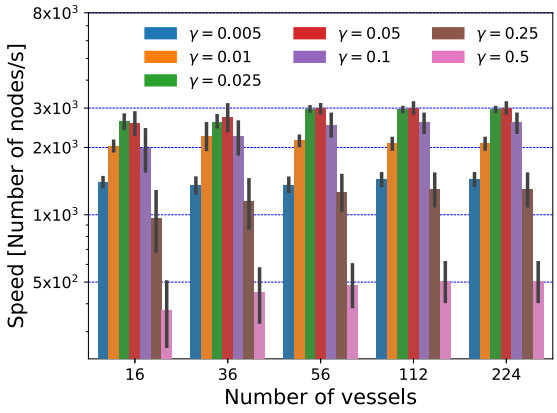

(b)

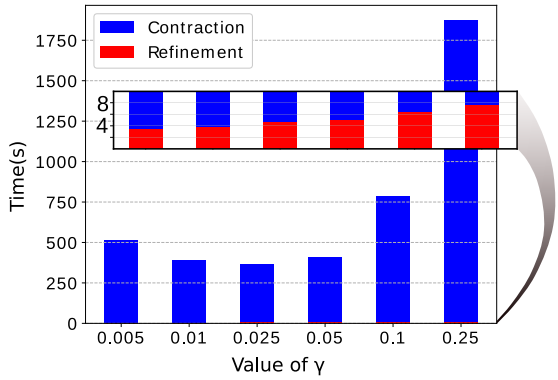

(c)

Figure 4.11 (a)-(b) Systematic analysis of the computational time required when applying the proposed scheme on a set of synthetic vascular trees with varying vessel radii and number of vessel segments. (c) A comparison between the times required for the contraction and refinement phases. We considered different values of our deformation speed parameter γ.

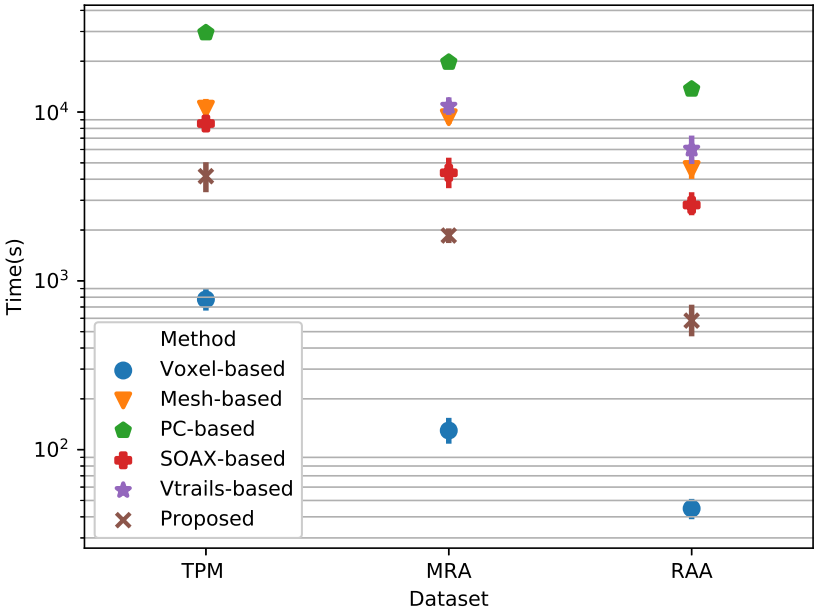

Figure 4.12 Computation times (plotted as average and standard deviation) required by the various graphing schemes when applied to different datasets.

be also noted that the calculated times was independent of the the stopping criterion presented in Section 4.3.3, since it was identical, with the same setting mentioned in that section, in all of our executions. Hence, measured computational times of the proposed methods were subjected only to the variations in the vascular structure in the binary input images. Only one execution on each input was performed to produce the results in Figure 4.12. As seen from the figure, the Voxel-based technique scores the lowest computational effort. However, this speed improvement comes at the expense of unreliable topological results, that suffer from false negative connectivity patterns as previously shown from the CFNR measures in Figure 4.8 and disconnected components as shown in Figures 4.9. Comparing with other schemes, apart for the voxel-based method, the proposed scheme reduces the computational time by a large margin. Based on its improved modeling results at a lower demand of computational power, our scheme stands as a suitable alternative to the currently available graphing techniques for processing binary-labeled angiographic datasets.

Next, we provide a systematic analysis focused on understanding the complexity of the proposed scheme when applied to inputs with differences in the inherited vascular structures. To perform such analysis, we created a set of synthetic angiograms using the VascuSynth toolbox [36] varying in the number of vascular branches and vessel radii. Our procedure for assembling this synthetic dataset is described in the supplementary material, Section IV. Fig. 4.11 (a) shows a scatter plot

of the computational times (in seconds) calculated after modeling of all vascular inputs in our synthetic inputs. The times are the sum of that required for running the contraction and refinements phases. We also plotted the calculation times resulting when using different values of the γ parameter, which is responsible for controlling the speed of graph deformation. We fitted a curve of the second order, on each set of data points that refer to angiograms comprising a similar number of vascular segments and processed using an identical setting of γ. This fitting was employed to understand the complexity of our modeling when applied to vascular inputs varying in their vascular volumes, due to only the differences in vessel radii, but not other factors. One can conclude from this plot that the complexity of the proposed scheme is greatly affected by the choice of γ parameter and the values of vessel radii. However, varying the number of vascular segments, for inputs having similar radii values, has little effect on the computational time, especially at lower values γ (meaning a faster convergence). Fig. 4.11 (b) plots the time complexity in terms of the number of nodes processed per second for each set of inputs consisting of the same number of vessel segments at different values of γ. It is again depicted that alterations in time complexity are more associated with model sizes due to enlarged vessel radii rather than to the number of vessel segments. Also, it is interestingly noticed that excessively decreasing the γ value, to obtain a faster graph deformation, will not necessarily ensure faster solutions. Over-deformations hinders the convergence of our contraction process, and thus leads to higher computational times. The values of 0.01, 0.025 and 0.05 for γ provided the best computational times. Finally in Fig. 4.11 (c), we separately plot the computational times required by the contraction and refinements phases when modeling one of the angiograms (having 224 vessels with the largest radii values) using the different settings of γ. This plot shows that the modeling time is majorly occupied by the contraction process. This is obvious since our refinement is applied on a converged geometry, which is in principle extremely smaller than that initially digested by our contraction scheme.

4.6 Discussion, Limitations and Future Directions

The ultimate goal behind this study is to provide vascular modeling outcomes suitable for exploring further research avenues concerned with hemodynamic simulations and understanding of biophysical phenomena occurring at various scales [6, 40–43]. Our validations show that techniques accepting pre-mapped vascular structures, when compared to that dealing with raw inputs, can provide enhanced anatomical models. Raw-input-based techniques are still advantageous in avoiding extra pre-processing steps associated with vascular delineation, and can be applied to some types of studies, e.g., that focus on investigating topology-based biomarkers [16, 44, 45]. Among all validated methods, the proposed work superiorly approaches the anticipated vascular models that hold comprehensive anatomical details. A challenging future direction could be related to improving the

proposed algorithm to process raw inputs. Indeed, such direction becomes more intractable when dealing with inputs that are scalable, of low-quality, or containing highly-variable vessel scales, e.g., TPM angiograms. One limitation to be mentioned about the proposed method is its sensitivity to gaps that could be found in the binary vascular inputs. Hence, such artifacts should be fixed in advance. Another aspect that could be a topic of further investigations is the formulation of our initial geometries. As previously discussed, larger vessels lead the production of sizable initial grid graphs, which in turn impose higher computational burdens. Uniformly increasing the size of grid cells, to produce less number of nodes, precipitate losses in smaller vessel structures. Thus, introducing an adaptive construction of grid/3D-mesh graphs, with variable cell sizes according to local changes in radius scales, can substantially improve the performance. It is clear that the proposed method is not designed to extract useful information related vascular pathologies. The integration of the proposed scheme in an extended problem formulation to explore structural phenotyping associated with diseased and degenerated vasculature, e.ganeurysmal dilatation or thrombosis, could of regarded as an interesting research direction.

4.7 Conclusion

Overcoming current challenges in vascular graph-based modeling using available and state-of-the-art methods, which produce less-accurate connectivity patterns and under-complete anatomical features, a novel graphing approach has been proposed. The proposed scheme works on binary maps of vascular structures regardless of its quality, and is not restricted to hard-coded inputs like water-tight surface models. The proposed work is inspired by the Laplacian flow formulation used for mesh processing in the field of differential geometry. First, an initial geometric graph, in the form of a truncated 3D grid graph, is created filling the vascular space. A procedure for assigning affinity weights on the initial graph has been described. Based on these weights, we derived the Laplacian optimization problem to be solved iteratively, thus generating a dynamic evolution of the initial geometry toward vascular centerlines. We have designed a full algorithmic scheme to stop the iterative process when converged and apply a refinement surgery to convert the evolved geometry into a graphed skeleton. Our scheme integrates a local and intrinsic vessels radii calculations during the evolution and refinement stages. We validated the proposed scheme on synthetic and real angiographies and compared our results with those extracted by other efficient and state-of-the-art graphing schemes. The results support that the proposed algorithm provides

more accurate vascular models holding better anatomical features.

4.8 References

[1] Kuo Li et al. “Stereoelectroencephalography electrode placement: Detection of blood vessel conflicts”. In: *Epilepsia* (2019).

[2] Wenqiang Chi et al. “Learning-based endovascular navigation through the use of non-rigid registration for collaborative robotic catheterization”. In: *International journal of computer assisted radiology and surgery* 13.6 (2018), pp. 855–864.

[3] Junjie Zhao et al. “Current treatment strategies for intracranial aneurysms: An overview”. In: *Angiology* 69.1 (2018), pp. 17–30.

[4] Stefano Moriconi et al. “Elastic registration of geodesic vascular graphs”. In: *International Conference on Medical Image Computing and Computer-Assisted Intervention*. Springer. 2018, pp. 810–818.

[5] Sava Sakadžić et al. “Large arteriolar component of oxygen delivery implies a safe margin of oxygen supply to cerebral tissue”. In: *Nature communications* 5 (2014), p. 5734.

[6] Philippe Pouliot et al. “Magnetic resonance fingerprinting based on realistic vasculature in mice”. In: *NeuroImage* 149 (2017), pp. 436–445.

[7] Mohammad Moeini et al. “Compromised microvascular oxygen delivery increases brain tissue vulnerability with age”. In: *Scientific reports* 8.1 (2018), p. 8219.

[8] Nicholas G Horton et al. “In vivo three-photon microscopy of subcortical structures within an intact mouse brain”. In: *Nature photonics* 7.3 (2013), p. 205.

[9] Kálmán Palágyi and Attila Kuba. “A parallel 3D 12-subiteration thinning algorithm”. In: *Graphical Models and Image Processing* 61.4 (1999), pp. 199–221.

[10] Sheng-Fang Huang et al. “Analysis of tumor vascularity using three-dimensional power Doppler ultrasound images”. In: *IEEE transactions on medical imaging* 27.3 (2008), pp. 320–330.

[11] Atilla P Kiraly et al. “Three-dimensional path planning for virtual bronchoscopy”. In: *IEEE Transactions on Medical Imaging* 23.11 (2004), pp. 1365–1379.

[12] Andrea Tagliasacchi et al. “Mean curvature skeletons”. In: *Computer Graphics Forum*. Vol. 31. 5. Wiley Online Library. 2012, pp. 1735–1744.

[13] Hui Huang et al. “L1-medial skeleton of point cloud.” In: *ACM Trans. Graph.* 32.4 (2013), pp. 65–1.

[14] Hanchuan Peng, Fuhui Long, and Gene Myers. “Automatic 3D neuron tracing using all-path pruning”. In: *Bioinformatics* 27.13 (2011), pp. i239–i247.

[15] Engin Türetken, Fethallah Benmansour, and Pascal Fua. “Automated reconstruction of tree structures using path classifiers and mixed integer programming”. In: *Computer Vision and Pattern Recognition (CVPR), 2012 IEEE Conference on*. IEEE. 2012, pp. 566–573.

[16] Stefano Moriconi et al. “Inference of Cerebrovascular Topology With Geodesic Minimum Spanning Trees”. In: *IEEE transactions on medical imaging* 38.1 (2018), pp. 225–239.

[17] Jan Dirk Wegner, Javier Alexander Montoya-Zegarra, and Konrad Schindler. “Road networks as collections of minimum cost paths”. In: *ISPRS Journal of Photogrammetry and Remote Sensing* 108 (2015), pp. 128–137.

[18] Gellért Máttyus, Wenjie Luo, and Raquel Urtasun. “DeepRoadMapper: Extracting Road Topology From Aerial Images”. In: *Proceedings of the IEEE Conference on Computer Vision and Pattern Recognition*. 2017, pp. 3438–3446.

[19] Engin Turetken et al. “Reconstructing loopy curvilinear structures using integer programming”. In: *Proceedings of the IEEE Conference on Computer Vision and Pattern Recognition*. 2013, pp. 1822–1829.

[20] Hrvoje Bogunović et al. “Anatomical labeling of the circle of willis using maximum a posteriori probability estimation”. In: *IEEE transactions on medical imaging* 32.9 (2013), pp. 1587–1599.

[21] Engin Türetken et al. “Reconstructing curvilinear networks using path classifiers and integer programming”. In: *IEEE transactions on pattern analysis and machine intelligence* 38.12 (2016), pp. 2515–2530.

[22] Sepideh Almasi et al. “A novel method for identifying a graph-based representation of 3-D microvascular networks from fluorescence microscopy image stacks”. In: *Medical image analysis* 20.1 (2015), pp. 208–223.

[23] Ting Xu et al. “Automated Tracking of Biopolymer Growth and Network Deformation with TSOAX”. In: *Scientific reports* 9.1 (2019), p. 1717.

[24] Rafat Damseh et al. “Automatic Graph-Based Modeling of Brain Microvessels Captured With Two-Photon Microscopy”. In: *IEEE journal of biomedical and health informatics* 23.6 (2018), pp. 2551–2562.

[25] Punam K Saha, Robin Strand, and Gunilla Borgefors. “Digital topology and geometry in medical imaging: a survey”. In: *IEEE transactions on medical imaging* 34.9 (2015), pp. 1940–1964.

[26] Yu-Shuen Wang and Tong-Yee Lee. “Curve-skeleton extraction using iterative least squares optimization”. In: *IEEE Transactions on Visualization and Computer Graphics* 14.4 (2008), pp. 926–936.

[27] R. Damseh, F. Cheriet, and F. Lesage. “Modeling the Topology of Cerebral Microvessels Via Geometric Graph Contraction”. In: *2020 IEEE 17th International Symposium on Biomedical Imaging (ISBI)*. 2020, pp. 1004–1008.

[28] Andrea Tagliasacchi et al. “3d skeletons: A state-of-the-art report”. In: *Computer Graphics Forum*. Vol. 35. 2. Wiley Online Library. 2016, pp. 573–597.

[29] Mingqiang Wei et al. “Centerline extraction of vasculature mesh”. In: *IEEE access* 6 (2018), pp. 10257–10268.

[30] Andrea Tagliasacchi et al. “3D Skeletons: A State-of-the-Art Report”. In: *Computer Graphics Forum*. Vol. 35. 2. Wiley Online Library. 2016, pp. 573–597.

[31] Keith Paton. “An algorithm for finding a fundamental set of cycles of a graph”. In: *Communications of the ACM* 12.9 (1969), pp. 514–518.

[32] Ta-Chih Lee, Rangasami L Kashyap, and Chong-Nam Chu. “Building skeleton models via 3-D medial surface axis thinning algorithms”. In: *CVGIP: Graphical Models and Image Processing* 56.6 (1994), pp. 462–478.

[33] Junjie Cao et al. “Point Cloud Skeletons via Laplacian-Based Contraction”. In: *Proc. of IEEE Conf. on Shape Modeling and Applications*. 2015.

[34] Todd A Gillette, Kerry M Brown, and Giorgio A Ascoli. “The DIADEM metric: comparing multiple reconstructions of the same neuron”. In: *Neuroinformatics* 9.2-3 (2011), p. 233.

[35] David Mayerich et al. “NetMets: software for quantifying and visualizing errors in biological network segmentation”. In: *BMC bioinformatics* 13.8 (2012), S7.

[36] Ghassan Hamarneh and Preet Jassi. “VascuSynth: Simulating vascular trees for generating volumetric image data with ground-truth segmentation and tree analysis”. In: *Computerized medical imaging and graphics* 34.8 (2010), pp. 605–616.

[37] L. Antiga et al. *AneuriskWeb*. 2011. URL: `http://ecm2.mathcs.emory.edu/aneuriskweb/index`.

[38] E. Bullitt. *Healthy MR database: Designed database of MR brain images of healthy volunteers*. 2007. URL: `https://data.kitware.com/#collection/`.

[39] Seong-Gi Kim and Seiji Ogawa. “Biophysical and physiological origins of blood oxygenation level-dependent fMRI signals”. In: *Journal of Cerebral Blood Flow & Metabolism* 32.7 (2012), pp. 1188–1206.

[40] Louis Gagnon et al. “Quantifying the microvascular origin of BOLD-fMRI from first principles with two-photon microscopy and an oxygen-sensitive nanoprobe”. In: *Journal of Neuroscience* 35.8 (2015), pp. 3663–3675.

[41] Michèle Desjardins et al. “Awake Mouse Imaging: From Two-Photon Microscopy to Blood Oxygen Level–Dependent Functional Magnetic Resonance Imaging”. In: *Biological Psychiatry: Cognitive Neuroscience and Neuroimaging* 4.6 (2019), pp. 533–542.

[42] Grant Hartung et al. “Simulations of blood as a suspension predicts a depth dependent hematocrit in the circulation throughout the cerebral cortex”. In: *PLoS computational biology* 14.11 (2018), e1006549.

[43] Andreas Linninger et al. “Mathematical synthesis of the cortical circulation for the whole mouse brain-part I. theory and image integration”. In: *Computers in biology and medicine* 110 (2019), pp. 265–275.

[44] Stefano Moriconi et al. “Towards Quantifying Neurovascular Resilience”. In: *Machine Learning and Medical Engineering for Cardiovascular Health and Intravascular Imaging and Computer Assisted Stenting*. Springer, 2019, pp. 149–157.

[45] Stefano Moriconi. “Inferring geodesic cerebrovascular graphs: image processing, topological alignment and biomarkers extraction”. PhD thesis. UCL (University College London), 2020.

CHAPTER 5 ARTICLE 3: A SIMULATION STUDY INVESTIGATING POTENTIAL DIFFUSION-BASED MRI SIGNATURES OF MICROSTROKES

Authors: Rafat Damseh[1,2], Yuankang Lu[1,2], Xuecong Lu[1,2], Cong Zhang[2,3], Paul J. Marchand[1,2], Denis Corbin[1], Philippe Pouliot[1,2], Farida Cheriet[4] and Frédéric Lesage[1,2]

[1] Laboratoire d'Imagerie optique et moléculaire, École Polytechnique de Montréal, 2900 Edouard Montpetit Blvd, Montréal (Québec), Canada, H3T 1J4;

[2] Institut de Cardiologie de Montréal, 5000 Rue Bélanger, Montréal (Québec), Canada, H1T 1C8;

[3] Université de Montreal, 2900 Edouard Montpetit Blvd, Montréal (Québec), Canada, H3T 1J4;

[4] Département de génie informatique et génie logiciel, École Polytechnique de Montréal, 2900 Edouard Montpetit Blvd, Montréal (Québec), Canada, H3T 1J4.

This article has been submitted to Scientific Reports.

Abstract: Recent studies suggested that cerebrovascular micro-occlusions , i.e. microstokes, could lead to ischemic tissue infarctions and cognitive deficits. Due to their small size, identifying measurable biomarkers of these microvascular lesions remains a major challenge. This work aims to simulate potential MRI signatures combining arterial spin labeling (ASL) and multi-directional diffusion-weighted imaging (DWI). Driving our hypothesis are recent observations demonstrating a radial reorientation of microvasculature around the micro-infarction locus during recovery in mice. Synthetic capillary beds, randomly- and radially- oriented, and optical coherence tomography (OCT) angiograms, acquired in the barrel cortex of mice (n=5) before and after inducing targeted photothrombosis, were analyzed. Computational vascular graphs combined with a 3D Monte-Carlo simulator were used to characterize the magnetic resonance (MR) response, encompassing the effects of magnetic field perturbations caused by deoxyhemoglobin, and the advection and diffusion of the nuclear spins. We quantified the minimal intravoxel signal loss ratio when applying multiple gradient directions, at varying sequence parameters with and without ASL. With ASL, our results demonstrate a significant difference ($p<0.05$) between the signal-ratios computed at baseline and 3 weeks after photothrombosis. The statistical power further increased ($p<0.005$) using angiograms measured at week 4. Without ASL, no reliable signal change was found. We found that higher ratios, and accordingly improved significance, were achieved at lower magnetic field strengths (e.g., B0=3) and shorter readout TE (<16 ms).

Our simulations suggest that microstrokes might be characterized through ASL-DWI sequence, providing necessary insights for posterior experimental validations, and ultimately, future translational trials.

5.1 Introduction

Cortical microvascular networks are the carrier of continuous supply of oxygen and energy substrates to neurons, and thus they are responsible for maintaining their healthy state. These networks react dynamically to meet the rapid and substantial increases in energy demands during neuronal activation through the process of neurovascular coupling [1]. Structural deterioration of the cortex microvasculature directly disrupts the regulation of cerebral blood flow and alters the distribution of oxygen and nutrients. Among pathogenic outcomes in cerebrovascular diseases [2] is the emergence of micro occlusions in penetrating arterioles descending from the pial surface. Recent experiments have provided evidence about the impact of these microscopic events on brain function [3]. Occlusion of a single penetrating vessel was shown to lead to ischemic infarction in the cortex [4] and to have effects on targeted cognitive tasks. Cerebral microinfarcts have emerged as a potential determinant of cognitive decline, as they are one of the most wide-spread forms of tissue infarction in the aging brain [5]. These cortical lesions have been associated to severe deficits in motor output at muscles [6]. It was also shown that a microembolism of a single cortical arteriole induces cortical spreading depression, a potential trigger and putative cause of migraine with aura [7]. In a separate study, the induction of microvascular lesions in an Alzheimer's mouse model was shown to alter both the deposition and clearance of amyloid-beta plaques. Optical microscopy and photoacoustic imaging are potential techniques for imaging the local architecture of cerebrovascular morphology at micro-scale, however, they remain invasive and are currently limited to preclinical studies. Given the strong association between these microvascular events and many neurological disorders, developing non-invasive and translatable approaches is of vital importance to identify their presence in clinical settings.

A recent study based on 2-photon microscopy has illustrated that the capillary bed in microvascular networks regenerates into a radially organized structure following a localized photothrombotic infarction [8]. To overcome limitations due to fluorescent dye leakage through the damaged blood-brain barrier, recent work exploiting optical coherence tomography (OCT) provided a detailed exploration of the microvascular angio-architecture rearrangement at different cortical depths [9] following photo-thrombosis. This latter study confirmed the presence of highly radially organized patterns, at all cortical depths, with a higher degree of structural reorganization in deeper regions. These morphological features could be exploited as clinical signatures of the associated ischemic events.

In this study, we hypothesize that these vascular re-orientations can be detected through magnetic

resonance imaging (MRI), and we provide a proof-of-concept through simulations. Our assumption is based on diffusion-weighted imaging (DWI), which is an established MRI technique that provide contrast sensitive to the motion of water molecules [10]. DWI is widely applied to capture white matter tracts [11], through the use of arbitrarily selected directions of the diffusion gradient to measure the directional bias of molecular movements. A sub-type of DWI is the intra-voxel incoherent motion (IVIM) technique, used to detect the high pseudo-diffusion coefficient that is attributed to the vascular component of the tissue [12]. Pseudo-diffusion measurements were used to quantify changes in cerebral perfusion [13]. Previous studies have shown that a hybrid scheme, combining IVIM and multi-direction DWI, could allow for a measurable effect size caused by microcirculation architecture [14–16]. Phantom-based simulations and realistic measurements of calf muscle were performed to characterize capillary anisotropy of skeletal muscle microvasculature [14]. A further in-vivo study used the same approach to characterize microvascular renal flow anisotropy [15]. Arterial spin labeling (ASL) was combined with an IVIM model to show that such technique is able to capture the dominant directionality of cerebral microvasculature in the rat brain [16]. Here, we conduct IVIM spin echo realistic simulations, to investigate potential signatures of cerebrovascular micro-occlusions induced in mice brains after targeted photothrombosis. Taking advantage of the radial angiogenesis around the micro-infarction locus after occlusion, we propose a measurable biomarker based on quantifying the ratio of directional signal loss induced when using multiple gradient directions. By integrating and excluding ASL, we performed parametric simulations using different field strengths, readout times, b-values and gradient duration. This study provides meaningful insights about the effect size as a function of parameters, which could be of great benefit for guiding further experimental investigations.

5.2 Results

5.2.1 Differences between diffusion MRI responses due to altered vascular orientations

Exploiting Monte-Carlo MRI simulations, on synthetically approximated capillary beds, we show that orientations of vascular geometry lead to different profiles of the diffusion MRI signal. We constructed two sets (30 samples each), see Figure 5.3 (B), of synthetic microvessel tubes, with distinct orientional structures. We aimed at mimicking the dissimilarity between healthy and post-stroke angiogenesis occurring before and after the induction of thrombotic occlusions on a penetrating artery within a microvascular unit. The first synthetic set contained randomly oriented vascular segments, which one would expect in healthy microvascular networks. On the other hand, samples in the second set were designed to follow radial orientations observed from realistic post-occlusion OCT acquisitions (see Figure 5.1 (D)). Random vessel radii ranging from 2-4 μm and arbitrary flow directions were assigned to capillary segments in our synthetic data. We approximated flow and

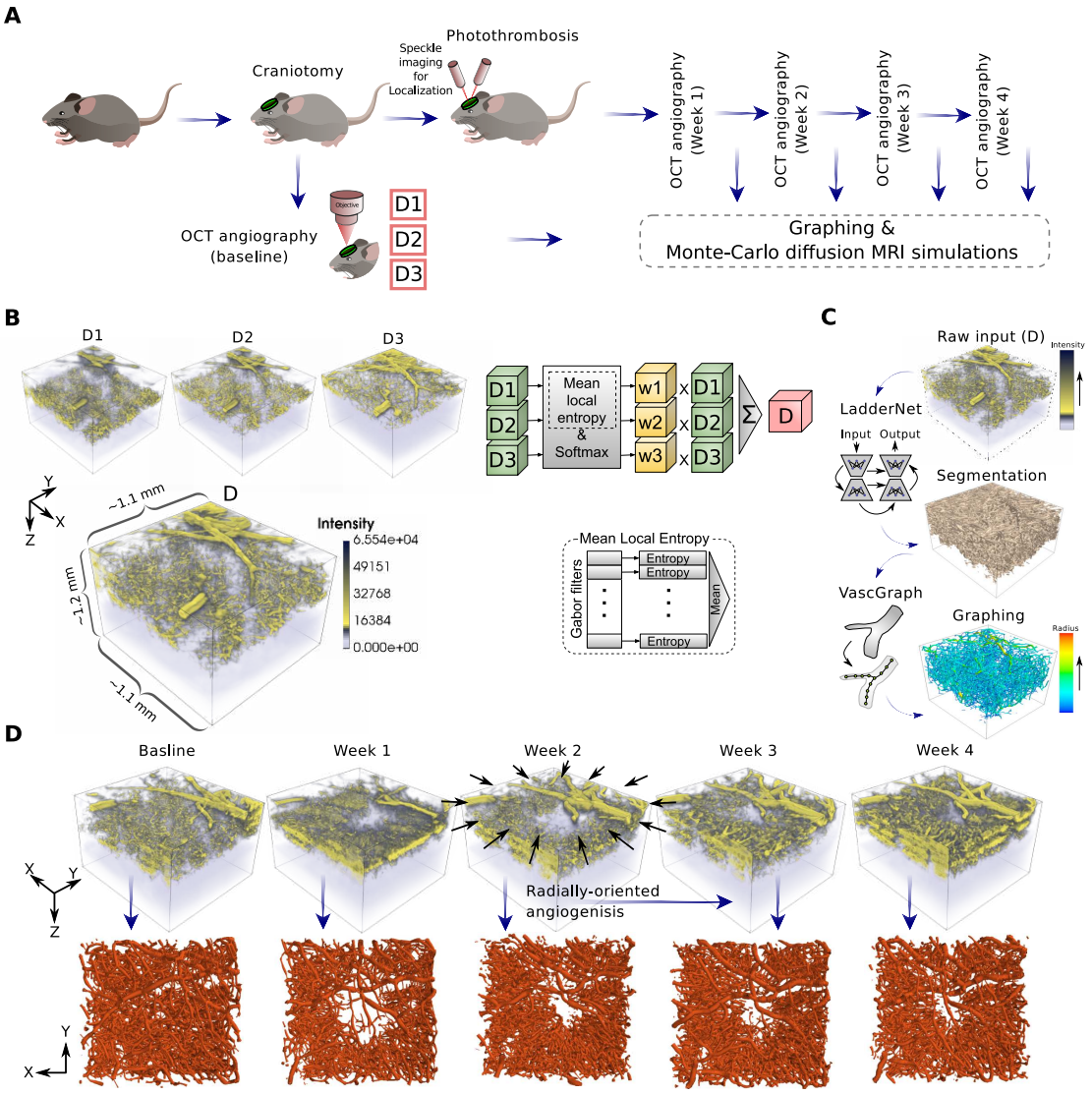

Figure 5.1 (A) Our experimental procedure for inducing and monitoring of micro-occlusions. Depth-dependant Pre- and post-lesion OCT angiographic acquisitions were preformed to capture vascular degeneration. The OCT stacks acquired at different time points are fed to our computational pipeline to study differences in their diffusion MRI response. (B) Our technique for reconstructing a final 3D OCT angiogram from the three depth-dependent images. We computed their mean local entropy after processing with a set of Gabor filters; a patch with richer vascular structures contributes more to the weighted sum. (C) Our image processing pipeline used to extract useful structural/topological models of vascular networks. These models are essential to perform Monte-Carlo MRI simulations. The Segmentation is based on a customly trained LadderNet architecture. We used The VascGraph toolbox [17] to obtain graph-based vascular skeletons that can approximate the needed anatomical information. (D) 3D rending of the vascular structure before and after creating a photothrombotic lesion. A noticeable radial-wise orientation is observed after-lesion especially following Week 2.

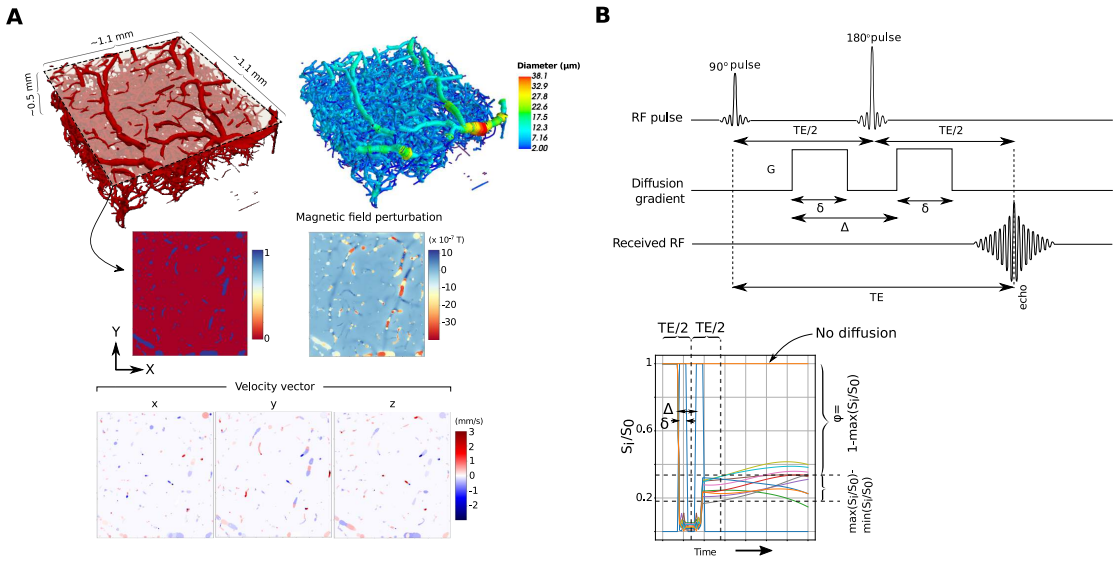

Figure 5.2 The simulation framework used to compute the MRI response through the diffusion and advection of nuclear spins within the cerebral microvasculature. (A) The computation of alterations in the main magnetic field due to the distribution of deoxyhemoglobin in the blood. These perturbations are calculated based on the PO2 values approximated using our random forest model (see Figure 5.3). Following the same machine learning approach, we estimated the velocity field that drives the advection of the spins. (B) The quantification of signal variations after simulating the diffusion MRI responses of a vascular unit using different gradient directions; above is the DWI sequence used for each gradient direction.

intravascular PO2 as described in the Methods section (see Figure 5.3 (C)). We extracted an MRI response simulating several gradient directions uniformly distributed in space by varying $\theta 1$ and $\theta 2$ as depicted in Figure 5.3 (A). Our simulations show variations in signal behavior as a result of changing gradients associated with different vascular orientations. An example of simulated output from both randomly- and radially-oriented samples is shown in Figure 5.3 (A). It is clear that after the second diffusion gradient following the 180° pulse, signals recover at different rates depending on gradient directions. When the direction is perpendicular to the vascular flow, advection of spins had no contribution on signal loss. On the other hand, diffusion gradients that had components aligned with flow direction introduced a noticeable loss in signal intensity. This observation suggests that a quantification of the differences between signal readouts at TE time point can uncover useful information about vascular orientation, and thus be used as a signature of angioarchitecture changes associated with microthrombosis.

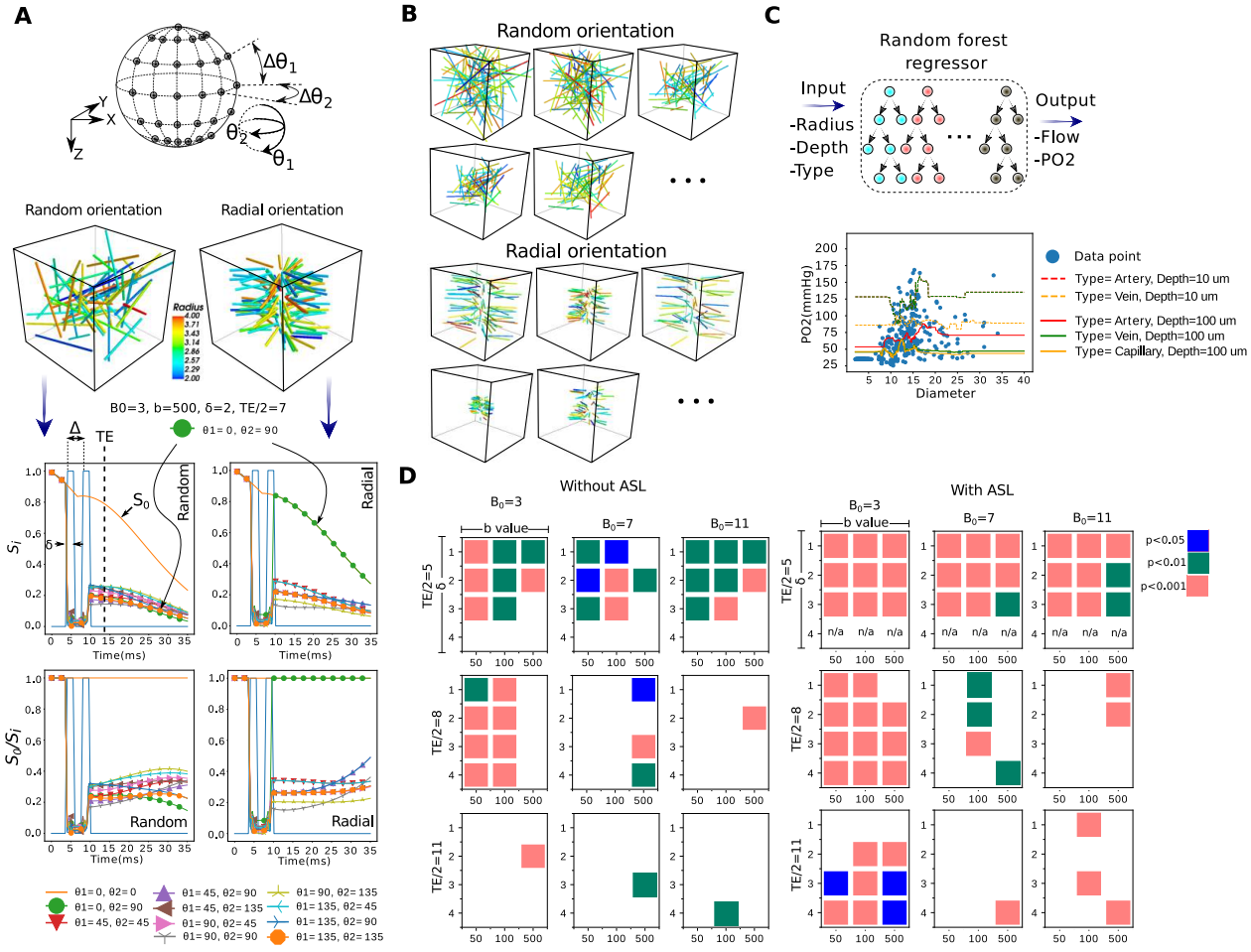

Figure 5.3 (A) A plot describing the difference between two diffusion-based MRI responses simulated -using a Monte-Carlo framework- from synthetic randomly- and radially-oriented capillary structures. For each sample, we simulate signals resulting from using different gradient directions controlled by the angles $\theta 1$ and $\theta 2$. (B) Examples from the two groups in our synthetic dataset. (C) A description of the random forest regression model used to approximate Flow and PO2 across the all branches/segments in our vascular models. The model predicts these values for a vascular element based on its annotated radius, depth and vessel type information. (D) Using a subspace of parameters that determine our diffusion MRI sequence, we plot the corresponding statistical p-values computed between our two synthetic groups based on their simulated ϕ values.

5.2.2 Effect size using different MRI parameters

To investigate the statistical significance between the randomly- and radially-oriented synthetic samples based on their diffusion-based MRI responses, we quantified the sample-wise maximum difference of signal loss at readout, $max(S_i/S_0) - min(S_i/s_0)$, (see the Methods section and Figure 5.2 (B)). Larger differences imply more anisotropic orientations (i.e., radially structured in our case). We used a non-parametric Mann-Whitney test to examine the statistical significance between ϕ values associated with the two synthetic sets. We retained the set of p-values calculated after using a subspace of B0, TE, δ and b (see Figure 5.3 (D)). We repeated the experiment with and without eliminating signal contributions of spins in the extravascular space, i.e., using ASL. As anticipated, we observed larger effect sizes, in general, when using ASL. The selection of the TE value had a key role in increasing the difference between the two set of measurements. The lower the TE value, the greater the statistical significance. A comparable effect was observed of the field strength B0: a higher B0 reduced the difference between the two configurations. Furthermore, an increased effect size was observed when using longer gradient time δ. Conversely, the effect associated with the various b-values on effect size was unnoticeable.

5.2.3 Diffusion-based MRI signatures of microstrokes using realistic simulations

Exploiting acquisitions of the angioarchitecture acquired longitudinally following photo-thrombosis, we then investigated the capability of the above sequences at detecting a longitudinal change in microvasculature that reflects in vivo conditions. Here, we report the statistical differences, in terms of the measured ϕ values (see Figure 5.2 (B)), between healthy (baseline) and after-lesion (at week 1, 2, 3 and 4) acquisitions. We performed our experiments with and without involving ASL, using different sequence parameters, by varying the field strength B0 and the b-value while setting TE, δ and Δ to 16 ms, 3 ms and 6 ms, respectively. To quantify the values of ϕ from each sample, we simulated uniformly distributed gradient directions with $\delta\theta = 30^\circ$ (see Figure 5.3 (A)). From Figure 5.4, it is observed that no reliable difference was achieved when excluding ASL from our simulations. On the other hand, the use of ASL suggests that the proposed marker, ϕ, is effective in differentiating between samples at baseline and after the 3rd and 4th weeks of occlusion. For example, at B0=3 and b=500, $\phi = 0.1533 \pm 0.0083$, whereas it is 0.06978 ± 0.01890 and 0.06148 ± 0.01187 at week 3 and 4, respectively. Noticeably, the scaling of ϕ increases with lower B0 field strengths and higher b-values.

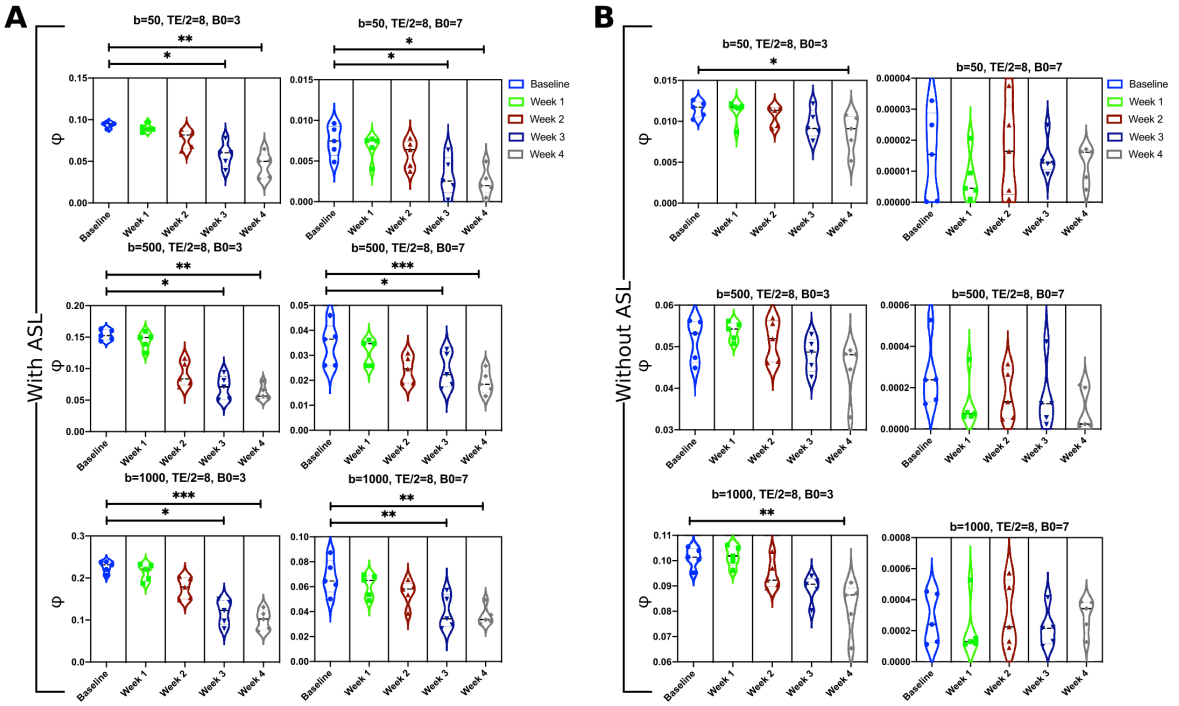

Figure 5.4 The ratio of minimal signal loss ϕ ($\times 100\%$) simulated from our OCT angiograms per (or before) and after occlusion through a the multi-directional IVIM scheme (see Figure 5.2 (B)). We used a set of uniformly distributed gradient directions ($\Delta\theta = 30°$, see Figure 5.3 (A)). We propose this measurement as signature distinguishing healthy from lesioned samples. We carried out the Friedman's test followed by post-hoc comparisons to study the statistical significance between the ratio obtained at the baseline and that calculated at the following 4 weeks after occlusion. Our analysis was performed with and without involving ASL (A) and (B), respectively.

5.3 Discussion

We leveraged OCT microscopic imaging and Monte-Carlo simulations to study potential diffusion MRI signatures of microvascular architecture after experimentally inducing photothrombosis. Our results support the hypothesis that such biomarkers are achievable, under certain assumptions, by exploiting the radial arrangement of microvascular capillary compartments post-lesion. Thus this work suggests that quantifying the differences in signal readouts arising from utilizing multiple gradient directions can characterize such vascular orientations. Simulation outputs provided useful insights about the prospective experimental implications. The use of ASL is of critical importance when characterizing microvascular occlusions based on the associated disruption in vascular geometry. In the mouse cerebral cortex, microvascular density sums to less than 0.05 mm^3 of a tissue volume of $1mm$; this ratio decreases with depth [18]. Eliminating the MRI signal contributed from the extravascular space is thus necessary. ASL approaches have already shown promising applications in measuring regional cerebral blood flow (rCBF) or perfusion [19–21], and in assessing vascular disorders [20, 22, 23]. Our simulation outcomes justify the selection of ASL-coupled multi-directional diffusion MRI used by Well et al. [16] to annotate flow patterns in the mouse cerebral cortex. We observed a noticeable drop in statistical significance between the responses of healthy and lesioned vasculature at longer echo time TE. This is due to the dominant T2/T2* shortening caused by deoxyhemoglobin distribution, opposed to that rising from diffusion gradients. A similar conclusion of reduced statistical differences was obtained when examining the responses at higher B0 values. Ultra-high field strengths, despite improving signal-to-noise (SNR) ratio, translate into shorter T2* and T2 [24, 25]. In other words, The increased B0 inhomogeneity at higher B0 leads to more signal loss, especially with longer echo times, which offset the advantage of its higher SNR. A straightforward approach would employ shorter echo time to mitigate the adverse effect of stronger fields [26, 27].

No clear association has been found between the b-value and the statistical difference used to distinguish normal from lesioned samples. More comprehensive investigations are conditioned on further improvements of our simulation framework. We employed a machine learning approach to predict SO2 and blood flow distributions across our vascular networks to enable this study. These measurements can be improved through oxygen transport modeling based on more adequate vascular computational graphs. It is to be mentioned that such modeling remains challenging since it requires tedious manual efforts and can be infeasible at scale [28]. It is known that larger microstrokes impose T2 changes in tissue. The proposed modeling could be improved through the incorporation of measured T2 tissue changes to understand their impact with a more realistic simulation. Another aspect of improvement is related to integrating a model of the restricted diffusion in tissue, instead of assuming a constant extravascular T2 field. An improved framework could en-

compass the magnetic perturbations induced by susceptibility interfaces between vessels and cells, and the permeability of the vessel wall [29].

5.4 Methods

5.4.1 Animals

All procedures were approved by the Animal Research Ethics Committee of the Montreal Heart Institute. Animal experiments were performed complying with the Canadian Council on Animal Care recommendations. Five C57BL/6J male mice of age 3-6 months were used. Cranial window implantation was carried out for each mouse over its left barrel cortex (0.5mm posterior to bregma, 3.5mm lateral to the midline) to perform OCT imaging. Following scalp retraction, a craniotomy with a diameter of 3 mm was done using a micro-drill and the dura was kept intact. We covered the exposed brain surface with a stacked four-layer glass cover slip (3x3mm, 1x5mm diameter) and sealed it with dental acrylic cement to prevent potential infection. A fixation bar was glued to the skull using the dental acrylic. During surgery, physiological parameters, including electrocardiogram, respiration, heart rate and oxygen saturation of the isoflurane-anesthetized mouse were continuously monitored by a small animal physiological monitoring system (Labeo Technologies Inc. Canada), whose heated platform module also maintained the mouse body temperature at 37 °C. OCT acquisitions were performed on awake resting mice to avoid the modulation of vascular and neural physiology [30, 31] by anesthetics. During image acquisition, the mice were placed on a free treadmill wheel with their head fixed on a metal frame by the surgically attached bar. It is to be mentioned that OCT-angiography is phase-sensitive and that even sub-pixel motions can dramatically diminish signal to noise ratio (SNR), and hence it is important that the mice stay still during imaging sessions. Accordingly, we trained the mice for head restraint prior to OCT measurements to habituate them to head fixation and reduce their stress. After a week of training on the treadmill wheel, the mice were able to reach a resting state within five minutes after being fixed onto the setup. They were able to stay calm and still for periods of minutes separated by short bouts of locomotion. After the initial baseline measurement, the mice were still trained every day between imaging sessions to maintain their habituation to head restraint throughout the study. The mice were closely monitored for locomotion during image acquisitions.

5.4.2 Ischemic stroke model

The stroke model exploited a localized photo-thrombosis procedure which is based on a photochemical reaction introduced by Watson et al. [32]. Mice were first intraperitoneally administered Rose Bengal (15 mg/mL, 0.2 ml), a photosensitive dye. A selected cortical region, free of large

vessels, was irradiated by a focused green laser beam, since large-vessel thrombosis could lead to a less predictable and less controlled outcome. In addition, avoiding regions with large pial vessels could also minimize the effect of tail artifacts in OCT angiography images [33]. Green light illumination enforces Rose Bengal to produce free radicals that lead to a damage in the endothelium of the microvasculature, thereby triggering discoid platelet aggregation that eventually leads into thrombotic occlusions. The whole process of photo-thrombosis was managed and monitored using a home-built laser speckle imaging system.

5.4.3 OCT Acquisition system

Imaging of cortical structure and vasculature was performed with a home-build spectral-domain OCT. A broadband light source centered at 1310 nm from a superluminescent diode (SLD) (LS2000C, Thorlabs, USA) was split between the sample arm and the reference arm by a 90:10 fiber optic coupler (TW1300R2A2, Thorlabs, USA). A long working distance objective (M Plan Apo NIR 10X, Mitutoyo, Japan) was installed at the end of the sample arm to focus the collimated light beam into the tissue sample. The spectral interferogram was registered by a spectrometer (Cobra 1300-[1235-1385 nm], Wasatch Photonics, USA) and then digitized by a frame grabber (PCIe-1433, National Instruments, USA). Dispersion mismatch between the two arms was first carefully compensated with N-SF11 compensation glass (Edmund Optics, USA), and the small residual mismatch was then finely corrected with a numerical compensation technique [34]. The axial resolution was measured to be about 4.15 μm in biological tissues. The lateral resolution in tissue was about 2.3 μm. In the sample arm, a dichroic filter was placed to transmit the infrared light used by the OCT system and deflect the visible light for wide-field imaging. The wide-field imaging helped locate the region of interest (ROI) to be scanned by OCT. The sample arm consisted of a galvanometer scanner, a beam expander and an objective lens. The arm was mounted on a motorized vertical translation stage (MLJ150/M, Thorlabs, USA). Adjusting the depth of the imaging focal point can be performed by elevating or lowering the vertical stage. The treadmill wheel onto which the mouse was attached was fixed on a motorized XY linear translation stage (T-LSR, Zaber Technologies, Canada) for fine adjustment of the relative lateral position of the cranial window with respect to the light beam. The 3-axis motion control was integrated into our acquisition software.

5.4.4 OCT angiographies

We scanned a 1 mm x 1 mm region with the photo-thrombosis-induced lesion located in the center. Our Volumetric scans of the cortex contained 450 B-frames, each of which was composed of 500 A-lines. First, raw spectra were resampled in k-space and then multiplied by a Hanning window. Then, inverse Fourier transform (IFT) was applied to obtain 3D complex-valued OCT structural im-

ages. B-scans were repeated twice at each position along the slow axis. Global phase fluctuations (GPF) caused by sub-pixel motion within repeated B-frames were corrected based on the assumption that dynamic tissue only accounts for a very small percentage of brain tissue and that phase and intensity of light reflected from static tissue remain constant [35]. In principle, light reflected by moving red blood cells (RBC) experiences a large phase shift and/or a big intensity change. Thus, we obtain a vascular image by taking the phase and intensity difference between GPF-corrected repeated B-frame [36]. The resulting 3D angiograms were filtered with a 3D Gaussian smoothing kernel with a standard deviation equal to 1 pixel in all three dimensions. A fast axis scan rate of 90 Hz was used, which resulted in an acquisition time of 10 seconds per volumetric scan. In order to extract more comprehensive information of the capillary network in the cortex, three time-resolved OCT-angiographies were performed in the same ROI with light beam being focused at three different cortical depths, namely 250 μm, 400 μm and 550 μm beneath the cortical surface. To achieve a shift of the axial focus in the tissue, we preformed a vertical translation of the objective lens in the sample arm mounted on the vertical translation stage. After, OCT stacks for each animal that were taken considering three different depth-dependent setups, are recombined to form one stack. To obtain the final desired stack, we followed a procedure based on measuring the mean of local entropies computed from each stack after normalizing and convolving it with a set of Gabor filters. Mean entropy measures for all the stacks are then normalized with a softmax function imposed on the axis representing the index of each stack. Voxel intensities in each stack are then weighted by the corresponding normalized local entropies. Finally, we take the sum of the weighted intensities from all the stacks to reconstruct the output stack. In our procedure, we used 18 two-dimensional Gabor filters built with orientations $\in 0, \pi/6, \pi/3, \pi/2, 2\pi/3, \pi$, phase offset $\in 2.5, 5, 7.5$ and a wavelength = 0.01. The kernel used for calculating the local entropy is of size (15, 15). We ran slice-wise calculations to quantify the entropy of each stack. In our chronic microstroke study, we performed 6 OCT imaging sessions over 28 days. The baseline measurement was taken one day before photo-thrombosis. The second imaging session took place 3 days after the thrombotic lesion was induced in the mouse brain, and the following 4 measurements were made 8 days, 14 days, 21 days and 28 days respectively after the ischemic stroke event.

5.4.5 Vascular Segmentation and Graphing

Many works on vessel segmentation have been presented in the literature. The best recent schemes were based on U-Net neural networks [37] with their convolutional architecture that accepts images of arbitrary sizes. In this work, we used the LadderNet architecture employed in [38], which is inspired from the U-Net one but with more interconnected information paths. This architecture can be seen as multiple stacked U-Nets with more pathways. Compared to the conventional U-Net scheme, the shared-weights structure in the LadderNet allows horizontal propagation through the

stacked U-Nets which forces the learning process to be made in earlier layers, and thus provides better results [39]. We trained and evaluated our network on an in-house prepared and annotated dataset from Two-photon microscopy angiograms. Our dataset consisted of 59 8-bits 2D grayscale images of 256x256 pixels which were then split into 70%, 15% and 15% portions for training, validation and testing, respectively. Images were standardized by subtracting the mean and dividing by the standard deviation. Contrast limited adaptive histogram equalization was then applied to correct light imbalance. Images were adjusted with a gamma value of 1.2. Training, testing and validation processes were done patch-wise (patch size of 32x32) after augmentation with random rotations. Each of the down and up streams paths in the network had 4 convolutional layers. A leaning rate of 0.001 was used. We applied the trained network on each slice in our 3D OCT angiograms to obtain the corresponding delineated vascular structures. After segmentation, we employed a graphing method, proposed recently by Damseh et al. [17], to transform our binarized inputs into a fully-connected graph-based skeletons. The method initiates geometric grid graphs encapsulated within vascular boundaries and iteratively deforms them toward vessel centerlines. Converged geometries are then refined and converted into graph-based skeletons. The output graph models consisted of nodes distributed along vessel centerlines to capture the geometry and edges connecting these nodes to represent the inherited topology. The method assigns vessel radii to graph nodes with unique identifiers to each set of them located at a certain vascular branch/segment. We used the VascGraph toolbox associated with that work, available on *https://github.com/Damseh/VascularGraph*, to generate and visualize the anatomical graphs.

5.4.6 Flow and PO2 Regression

To prepare the generated anatomical model to undergo MRI simulation experiments, we had to assign biophysical quantities across vascular compartments, namely flow and PO2 values, necessary for reconstructing the T2* field. Resolving these values through biophysical simulations is tedious due to the low-quality nature of OCT inputs, which hinders the formulation of a correct geometric domain suitable for such computations. In other words, such computations are extremely sensitive to topological errors that can easily disrupt the final solution. Here, instead, we followed a machine-learning based approach that utilizes an ensemble of random decision trees, i.e, random forests, fitted on experimental data collected from mice models in a previous work performed by Moeini et al. [40]. The data consisted of > 300 measurements of PO2 and Flow values of cerebral microvascular segments having different sizes, types and located at different cortical depths. We built two separate random forest models that accept radius, type and depth information for a vascular segment and output the corresponding flow and PO2 values. Types of vessel segments were determined after thresholding on the radius value of 3 μm [40]. Vascular segments with radii above the threshold were randomly set to be either arteries or veins, whereas the rest were set as

capillaries. Following this procedure, we only needed an approximation of the vascular geometry to capture the anatomical features required by the random forest model, and avoided the dependency on the biophysical modeling that requires accurate annotations and is highly prone to any topological error induced in the vascular model. Each of the two random forests consisted of 100 decision trees with 10 maximum depth. The architecture of our regression forests was selected after assessing the mean square error (MSE) resulting from using different architectural setups. The same measure of MSE was used to determine the quality of a split in the single decision trees that compose the forest model. The minimum number of samples required to split in each decision tree has been set to 2. Bootstrapping was used to reduce the variance resulting from the outputs of multiple trees fitted on random sub-samples, with replacement, from the original training set [41].

5.4.7 MRI simulations

We implemented a Monte-Carlo MRI simulation code in Python following the same routines of previous protocols [28, 42], which was built using Matlab. Simulation principles in these works were originally based on descriptions detailed in [43]. The previous implementations were performed to tackle the Blood-oxygen-level-dependent (BOLD) MRI response. Here, to align with our study goals, we developed new functionalities to create multi-directional spin echo DW sequence simulations. In our numerical MRI trails (coinciding with the aforementioned studies), it was assumed that the MRI response in the mouse brain could be approximated by probing the behavior of a large number of hydrogen water protons moving in background due to free diffusion and constrained advection processes. Practically, our assumption incorporated the following in-detail descriptions: the domain enjoys a spatially constant T1 relaxation; T2 value in tissue regions is fixed but varies within the vascular space; T2* effect has spatial variations subjected to the level of deoxyhemoglobin within the vasculature (see Figure 5.2 (A)). As suggested in previous works designed for studying vascular-based MRI responses [28, 42, 44, 45], we neglected a set of factors that have insignificant effect on the extracted signal: hydrogen atoms not bound to water, additional iron presence in basal ganglia and some other brain parts, external B0 and B1 fields inhomogeneities, gradient nonlinearity, hematocrit variability. Also, to enable our analysis, we excluded the macroscopic magnetic field destruction occurring due to imperfect shimming or the microscopic field differences emerging from the applied gradients. In our Monte-Carlo simulations, we measured the voxel-wise response based on summing the accumulated complex phase from 1×10^{-6} spins, after initiating their positions at $t = 0$ using a uniform probability distribution that covers the spatial domain, and then updating their location every 0.05 ms. The protons were let to diffuse isotropically with a diffusivity constant of 0.8 μm^2/ms [46]. With the assumptions mentioned above, among the relaxation constants necessary for our computations is that attributed to the local magnetic field inhomogeneities, affecting T2*, due to the presence of deoxyhemoglobin in

the vasculature. We followed the numerical method described in [47] to compute the perturbations in the magnetic field by convolving the susceptibility shift volume, which is calculated depending on the level of PO2, with an ellipsoidal kernel oriented with the field B0. Another important relaxation factor affecting T2 is that related to the spin-spin coupling, where it is computed based on the fitted models illustrated in [48]. In the extravascular space, T2 is fixed and obtained in seconds as

$$\mathrm{T2}_{tissue} = [1.74 * \mathrm{B0} + 7.77]^{-1} \tag{5.1}$$

On the other hand, this parameter spatially varies in the vasculature depending on the oxygen saturation level (SO2):

$$T2_{vessel} = \Big[12.67 * \mathrm{B0}^2 * (1 - \mathrm{SO2})^2 + 2.74 * \mathrm{B0} - 0.6\Big]^{-1} \tag{5.2}$$

The SO2 values were calculated from their PO2 counterparts based on the Hill conversion equation with coefficients specific for C57BL/6 mice (h=2.59 and P50=40.2) [49]. The relaxation effect due to T1 was included as an exponential decay with T1 =1590 ms [50]. Hematocrit values necessary to compute the field susceptibility as described in [47] were assumed to be 0.44 in arterioles and venules, and 0.33 in capillaries [51]. Based on the mappings of anatomical features and biophysical quantities computed from OCT angiographies, we computed their MRI response following a combined design of IVIM and multi-direction DWI sequence. The simulated MRI signal is constructed from the contributions of intravascular (IV) and extravascular (EV) spins. Assuming a negligible exchange between the IV and EV components during the echo time [16], the total DW voxel signal captured at a gradient i, with its direction $\mathbf{u}_i \in \mathbf{U} = \{\mathbf{u}_1, \mathbf{u}_2, ...\mathbf{u}_n\}$, could be expressed as:

$$S_i = S_0[fe^{-b_i D_i^*} + (1 - f)e^{-b_i D_i}] \tag{5.3}$$

where S_0 is the response at zero diffusion gradient, f is the fraction of vasculature in the voxel, and b_i(mm^2/s) is a parameter that characterizes the diffusion gradient i. The term D_i is the apparent diffusion coefficient (ADC) influenced by the Gaussian diffusion in tissue, whereas D_i^* is the pseudo-diffusion coefficient (PDC) representing the perfusion of spins in the microvascular network. A diffusion gradient consists of two short pulses of duration δ, with amplitude G, separated by a short amount of time Δ. The corresponding b-value can be obtained as:

$$b = \gamma^2 G^2 \delta^2 (\Delta - \frac{\delta}{3}) \tag{5.4}$$

where γ is the proton gyromagnetic ratio of Hydrogen. Reflecting this on our task of finding a signature about the deterioration in the microvascular architecture occurring due ischemic throm-

botic events, our interest is the set of ratios $R = \{r_i = \frac{S_i}{S_0}, i \in \{1, 2, ..., n\}\}$, calculated through applying n gradients with directions equally sampled from all possible choices in the 3D space. As discussed in the Introduction section, previous works [8, 9] reported that voxels with thrombotic ischemia exhibit a highly radial orientation of microvessels in the lateral plane around the lesion core. This implies that a higher perfusion rate, i.e., an increased loss in MRI signal, would be observed when a gradient field is parallel to the lateral plane compared to that occurring when it is perpendicular to it. In general, healthy voxels beneath the pial surface are assumed to be composed of randomly oriented capillary segments, and thus would result in comparable MRI signal loss regardless to the direction of the selected gradient. Hence, the ratio $\phi = 1 - max(R)$ could be regarded as a biological marker distinguishing healthy voxels from those having a thrombotic lesion (see Figure 5.2 (B)). Beside computing ϕ through probing spins behavior in an entire voxel or ROI, we also studied the response when neglecting the extravascular spins, thus omitting the diffusion term in (5.3). Such procedure could be practically translated with ASL. Based on the mappings of anatomical features and biophysical quantities computed from OCT angiographies, we computed their MRI response following a combined design of IVIM and multi-direction DWI sequence. Simulated MRI signal is constructed from the contributions of intravascular (IV) and extravascular (EV) spins. Assuming a negligible exchange between the IV and EV components during the echo time.

5.5 Acknowledgements

This study was funded by a Canadian Institutes of Health Research (CIHR, 299166) operating grant and a Natural Sciences and Engineering Research Council of Canada (NSERC, 239876-2011) discovery grant to F. Lesage.

Author contributions statement

R.D. and F.L devised the main conceptual ideas and proof outline. R.D. wrote the manuscript and developed the codes for all the computational blocks in the study, from vascular graphing to MRI simulations, and analyzed the data. Y.L. built the OCT system and performed acquisitions. X.L and Y. L. and C. Z. conducted the craniotomy, the cover glass implantation, and the induction of photo-thrombotic lesions. P. M. did the post-processing of the OCT acquisitions. D. C. prepared

the LadderNet segmentation code. All authors reviewed the manuscript.

Competing interests

Te authors declare no competing interests.

Additional information

Correspondence and requests for materials should be addressed to R.D.

5.6 References

[1] Elizabeth MC Hillman. “Coupling mechanism and significance of the BOLD signal: a status report”. In: *Annual review of neuroscience* 37 (2014), pp. 161–181.

[2] Leonardo Pantoni. “Cerebral small vessel disease: from pathogenesis and clinical characteristics to therapeutic challenges”. In: *The Lancet Neurology* 9.7 (2010), pp. 689–701.

[3] Philipp M Summers et al. “Functional deficits induced by cortical microinfarcts”. In: *Journal of Cerebral Blood Flow & Metabolism* 37.11 (2017), pp. 3599–3614.

[4] Andy Y Shih et al. “The smallest stroke: occlusion of one penetrating vessel leads to infarction and a cognitive deficit”. In: *Nature neuroscience* 16.1 (2013), pp. 55–63.

[5] Zachary J Taylor et al. “Microvascular basis for growth of small infarcts following occlusion of single penetrating arterioles in mouse cortex”. In: *Journal of Cerebral Blood Flow & Metabolism* 36.8 (2016), pp. 1357–1373.

[6] Eitan Anenberg et al. “Ministrokes in channelrhodopsin-2 transgenic mice reveal widespread deficits in motor output despite maintenance of cortical neuronal excitability”. In: *Journal of Neuroscience* 34.4 (2014), pp. 1094–1104.

[7] Buket Dönmez-Demir et al. “Microembolism of single cortical arterioles can induce spreading depression and ischemic injury; a potential trigger for migraine and related MRI lesions”. In: *Brain research* 1679 (2018), pp. 84–90.

[8] Christian J Schrandt et al. “Chronic monitoring of vascular progression after ischemic stroke using multiexposure speckle imaging and two-photon fluorescence microscopy”. In: *Journal of Cerebral Blood Flow & Metabolism* 35.6 (2015), pp. 933–942.

[9] Yuankang Lu et al. “Longitudinal optical coherence tomography imaging of tissue repair and microvasculature regeneration and function after targeted cerebral ischemia”. In: *Journal of Biomedical Optics* 25.4 (2020), p. 046002.

[10] Derek K Jones. *Diffusion mri*. Oxford University Press, 2010.

[11] Andrew L Alexander et al. “Diffusion tensor imaging of the brain”. In: *Neurotherapeutics* 4.3 (2007), pp. 316–329.

[12] Denis Le Bihan. “Intravoxel incoherent motion perfusion MR imaging: a wake-up call”. In: *Radiology* 249.3 (2008), pp. 748–752.

[13] Christian Federau et al. “Quantitative measurement of brain perfusion with intravoxel incoherent motion MR imaging”. In: *Radiology* 265.3 (2012), pp. 874–881.

[14] Dimitrios C Karampinos et al. “Intravoxel partially coherent motion technique: characterization of the anisotropy of skeletal muscle microvasculature”. In: *Journal of Magnetic Resonance Imaging: An Official Journal of the International Society for Magnetic Resonance in Medicine* 31.4 (2010), pp. 942–953.

[15] Mike Notohamiprodjo et al. “Combined intravoxel incoherent motion and diffusion tensor imaging of renal diffusion and flow anisotropy”. In: *Magnetic resonance in medicine* 73.4 (2015), pp. 1526–1532.

[16] JA Wells et al. “MRI of cerebral micro-vascular flow patterns: A multi-direction diffusion-weighted ASL approach”. In: *Journal of Cerebral Blood Flow & Metabolism* 37.6 (2017), pp. 2076–2083.

[17] Rafat Damseh et al. “Laplacian Flow Dynamics on Geometric Graphs for Anatomical Modeling of Cerebrovascular Networks”. In: *arXiv preprint arXiv:1912.10003* (2019).

[18] Philbert S Tsai et al. “Correlations of neuronal and microvascular densities in murine cortex revealed by direct counting and colocalization of nuclei and vessels”. In: *Journal of Neuroscience* 29.46 (2009), pp. 14553–14570.

[19] Yang Wang et al. “Regional reproducibility of pulsed arterial spin labeling perfusion imaging at 3T”. In: *Neuroimage* 54.2 (2011), pp. 1188–1195.

[20] Nicholas A Telischak, John A Detre, and Greg Zaharchuk. “Arterial spin labeling MRI: clinical applications in the brain”. In: *Journal of Magnetic Resonance Imaging* 41.5 (2015), pp. 1165–1180.

[21] Pan Su et al. “Multiparametric estimation of brain hemodynamics with MR fingerprinting ASL”. In: *Magnetic resonance in medicine* 78.5 (2017), pp. 1812–1823.

[22] Greg Zaharchuk et al. “Arterial spin-labeling MRI can identify the presence and intensity of collateral perfusion in patients with moyamoya disease”. In: *Stroke* 42.9 (2011), pp. 2485–2491.

[23] Jeroen Hendrikse, Esben Thade Petersen, and Xavier Golay. “Vascular disorders: insights from arterial spin labeling”. In: *Neuroimaging Clinics* 22.2 (2012), pp. 259–269.

[24] Seongjin Choi et al. “DTI at 7 and 3 T: systematic comparison of SNR and its influence on quantitative metrics”. In: *Magnetic resonance imaging* 29.6 (2011), pp. 739–751.

[25] Cornelius von Morze et al. “Reduced field-of-view diffusion-weighted imaging of the brain at 7 T”. In: *Magnetic resonance imaging* 28.10 (2010), pp. 1541–1545.

[26] Liang Zhan et al. “Magnetic resonance field strength effects on diffusion measures and brain connectivity networks”. In: *Brain connectivity* 3.1 (2013), pp. 72–86.

[27] Daniel Gallichan. “Diffusion MRI of the human brain at ultra-high field (UHF): A review”. In: *NeuroImage* 168 (2018), pp. 172–180.

[28] Louis Gagnon et al. “Quantifying the microvascular origin of BOLD-fMRI from first principles with two-photon microscopy and an oxygen-sensitive nanoprobe”. In: *Journal of Neuroscience* 35.8 (2015), pp. 3663–3675.

[29] Nicolas Adrien Pannetier et al. “A simulation tool for dynamic contrast enhanced MRI”. In: *PloS one* 8.3 (2013), e57636.

[30] Ben JA Janssen et al. “Effects of anesthetics on systemic hemodynamics in mice”. In: *American Journal of Physiology-Heart and Circulatory Physiology* 287.4 (2004), H1618–H1624.

[31] Kazuto Masamoto and Iwao Kanno. “Anesthesia and the quantitative evaluation of neurovascular coupling”. In: *Journal of Cerebral Blood Flow & Metabolism* 32.7 (2012), pp. 1233–1247.

[32] Brant D Watson et al. “Induction of reproducible brain infarction by photochemically initiated thrombosis”. In: *Annals of Neurology: Official Journal of the American Neurological Association and the Child Neurology Society* 17.5 (1985), pp. 497–504.

[33] Utku Baran et al. “Tail artifact removal in OCT angiography images of rodent cortex”. In: *Journal of biophotonics* 10.11 (2017), pp. 1421–1429.

[34] Maciej Szkulmowski, Szymon Tamborski, and Maciej Wojtkowski. “Spectrometer calibration for spectroscopic Fourier domain optical coherence tomography”. In: *Biomedical optics express* 7.12 (2016), pp. 5042–5054.

[35] Jonghwan Lee et al. “Motion correction for phase-resolved dynamic optical coherence tomography imaging of rodent cerebral cortex”. In: *Optics express* 19.22 (2011), pp. 21258–21270.

[36] Anqi Zhang et al. “Methods and algorithms for optical coherence tomography-based angiography: a review and comparison”. In: *Journal of biomedical optics* 20.10 (2015), p. 100901.

[37] Olaf Ronneberger, Philipp Fischer, and Thomas Brox. “U-net: Convolutional networks for biomedical image segmentation”. In: *International Conference on Medical image computing and computer-assisted intervention*. Springer. 2015, pp. 234–241.

[38] Olaf Ronneberger, Philipp Fischer, and Thomas Brox. *U-Net: Convolutional Networks for Biomedical Image Segmentation*. 2015. arXiv: 1505.04597 [cs.CV].

[39] Juntang Zhuang. *LadderNet: Multi-path networks based on U-Net for medical image segmentation*. 2018. arXiv: 1810.07810 [cs.CV].

[40] Mohammad Moeini et al. “Compromised microvascular oxygen delivery increases brain tissue vulnerability with age”. In: *Scientific reports* 8.1 (2018), pp. 1–17.

[41] Gilles Louppe. “Understanding random forests: From theory to practice”. In: *arXiv preprint arXiv:1407.7502* (2014).

[42] Philippe Pouliot et al. “Magnetic resonance fingerprinting based on realistic vasculature in mice”. In: *Neuroimage* 149 (2017), pp. 436–445.

[43] Xiang He and Dmitriy A Yablonskiy. “Quantitative BOLD: mapping of human cerebral deoxygenated blood volume and oxygen extraction fraction: default state”. In: *Magnetic Resonance in Medicine: An Official Journal of the International Society for Magnetic Resonance in Medicine* 57.1 (2007), pp. 115–126.

[44] Bing Yao et al. “Susceptibility contrast in high field MRI of human brain as a function of tissue iron content”. In: *Neuroimage* 44.4 (2009), pp. 1259–1266.

[45] Michèle Desjardins et al. “Aging-related differences in cerebral capillary blood flow in anesthetized rats”. In: *Neurobiology of aging* 35.8 (2014), pp. 1947–1955.

[46] Denis Le Bihan. *Apparent diffusion coefficient and beyond: what diffusion MR imaging can tell us about tissue structure*. 2013.

[47] JP Marques and R Bowtell. “Application of a Fourier-based method for rapid calculation of field inhomogeneity due to spatial variation of magnetic susceptibility”. In: *Concepts in Magnetic Resonance Part B: Magnetic Resonance Engineering: An Educational Journal* 25.1 (2005), pp. 65–78.

[48] Kâmil Uludağ, Bernd Müller-Bierl, and Kâmil Uğurbil. “An integrative model for neuronal activity-induced signal changes for gradient and spin echo functional imaging”. In: *Neuroimage* 48.1 (2009), pp. 150–165.

[49] Kou Uchida, Michael P Reilly, and Toshio Asakura. “Molecular stability and function of mouse hemoglobins”. In: *Zoological Science* 15.5 (1998), pp. 703–706.

[50] Brige Paul Chugh et al. “Robust method for 3D arterial spin labeling in mice”. In: *Magnetic resonance in medicine* 68.1 (2012), pp. 98–106.

[51] Valerie EM Griffeth and Richard B Buxton. “A theoretical framework for estimating cerebral oxygen metabolism changes using the calibrated-BOLD method: modeling the effects of blood volume distribution, hematocrit, oxygen extraction fraction, and tissue signal properties on the BOLD signal”. In: *Neuroimage* 58.1 (2011), pp. 198–212.

CHAPTER 6 GENERAL DISCUSSION

6.1 Summary of Works

This thesis presented three distinct contributions aligned with the objectives that have been set in the Introduction section. A summary of each contribution is given below.

In Chapter 3, a novel fully-automatic processing pipeline to produce graphical models for cerebral microvasculature captured with TPM has been presented. The proposed modular scheme encompasses three main stages. First, 3D segmentations of the microvasculature were obtained using a Densely connected U-net architecture. In-house labeled angiograms have been prepared to train the model, after employing data augmentation. Second, a surface model generator has been designed, relying on a marching cube algorithm, to extract water-tight 2-manifold triangulated meshes of the vascular structures. In the last stage, a Laplacian-based mesh contraction scheme has been exploited to transform the generated surface models into 1D medial axes, or graphed-curve skeletons, that serve computational/anatomical representations of the microvasculature. The proposed pipeline has been validated using a set of manually annotated graphs of 6 TPM angiograms of size $\sim 512 \times 512 \times 512$. The proposed modeling was able to produce accurate graphs with low geometrical and topological error rates, especially at a tolerance $> 30\mu$m. Qualitative assessments have shown that proposed automatic processing generates realistic models having accurate propagation through the modeled vessels.

In Chapter 4, a novel geometry contraction scheme has been proposed to replace the second stage of the pipeline developed in Chapter 3. The new algorithmic solution is less restrictive to either water-tight surface inputs or to high-quality vascular labeling, and yet provides precise topological and structural representations of the vasculature. The method works on binary inputs regardless of their quality, by initially creating geometric graphs, in the form of truncated 3D grids filling the vascular space. A procedure for assigning affinity weights on the initial graph has been described. Based on these weights, a Laplacian optimization problem has been derived to be solved iteratively, thus generating a dynamic evolution of the initial geometry toward vascular centerlines. A convergence criterion has been developed to stop the iterative process; and a refinement surgery has been proposed to convert the evolved geometry into a graphed skeleton. The new graph-based contraction scheme integrates local and intrinsic vessel radii information during the evolution and refinement stages. Validity of the model outputs has been demonstrated on synthetic and real angiographies acquired using different modalities. Compared to the initial development in Chapter 3, the results have shown that the new algorithm provides more accurate vascular models holding

better anatomical features.

In Chapter 5, a simulation study has been presented to evaluate a potential MRI identification of microstrokes, incorporating the vascular modeling pipeline developed in Chapter 3 and 4. MRI signatures have been assessed through combining the ASL and multi-directional DWI techniques. The main hypothesis was driven based on recent observations demonstrating a radial reorientation of microvasculature around the micro-infarction locus during recovery in mice [29]. The effect size has been systematically evaluated based on synthetic capillary beds following random and radial orientations. Realistic simulations were then performed based on OCT angiograms acquired in the barrel cortex of mice (n$= 5$) before and after inducing targeted photothrombosis. A 3D Monte-Carlo simulator was developed to quantify the MR response from the vascular models extracted from these angiograms. The MR response was characterized encompassing the effects of magnetic field perturbations caused by deoxyhemoglobin, and the advection and diffusion of the nuclear spins. The minimal intravoxel signal loss ratio was studied when applying multiple gradient directions, using different sequence parameters with and without ASL. It has been demonstrated that a significant difference (p< 0.05) is obtained between the signal-ratios computed at baseline and 3 weeks after photothrombosis. The statistical power further increased (p< 0.005) using angiograms measured at week 4. No reliable signal change was found without integrating ASL in the analysis. Furthermore, it has been shown that higher significance was achieved at lower magnetic field strengths (e.g., B0$= 3$) and shorter readout TE (< 16 ms). The study suggested that microstrokes might be characterized through ASL-DWI sequence, providing necessary insights for posterior experimental validations, and ultimately, future translational trials.

6.2 Limitations & Future Work

One main concern that has been addressed in one part of the thesis, namely in Chapter 3 and 4, is related to developing a fully automated framework capable of extracting useful anatomical models of microvascular structures from raw angiographic inputs. Building these computational/geometrical models is crucial for multi-scale characterization of cerebral haemodynamics and for understanding brain physiology and function at various pathological states [44, 47]. In the literature, some attempts have focused on extracting computational models of cerebral microvasculature through either approximation of their anatomical compartments to build simplified representations [46], or reconstructing them based on through biologically-inspired angiogenesis [5]. In general, these models have less applicability when studying pathological vascular states, and are not guaranteed to reflect all anatomical details necessary to understand the physiological and structural components of the neurovascular phenomena. Therefore, in Chapter 3 and 4, a fully automated solution has been developed to generate such microvascular models through casting/reconstruction from raw angio-

graphic images, which can be captured through microscopic acquisition techniques such as TPM or OCT. Through comparing with other available casting/graphing algorithms, the presented validations showed that techniques accepting pre-mapped vascular structures, when compared to those dealing with raw inputs, can provide enhanced anatomical models. Raw-input-based techniques are still advantageous in avoiding extra pre-processing steps associated with vascular delineation, and can be applied to some types of studies, e.g., that focus on investigating topology-based biomarkers [211, 272, 273]. Among all validated methods, the proposed work superiorly approaches the anticipated vascular models that hold comprehensive anatomical details. An interesting future direction could be related to the following.

- The pipeline proposed in Chapter 3 is composed of three phases; the first one focused on generating binary vascular masks from raw inputs. Other types of representations could be generated to enhance the outputs of the following stages concerned with geometry processing as described in Chapter 3 and 4. For instance, as proposed in [274], a well-trained deep learning model can provide precise distance transforms of tubular structures to be used for further vascular modeling. It is to be mentioned that additional effort is needed to mitigate the difficulty of processing scalable inputs of low-quality and containing highly-variable vessel scales, e.g., as in TPM angiograms.

- Improved segmentation schemes could be integrated in phase one of the graphing pipeline in Chapter 3 to provide enhanced generalizability and multiscale segmentation performance. A total variation term in the training process [275] or extending the deep network to include better skip connections and information pathways [276] could be potential options.

- One limitation to be mentioned about the proposed graphing schemes in Chapter 3 and 4 is the sensitivity to gaps and touching vessels that could be found in the binary vascular inputs. Hence, additional processing blocks could be added to the scheme to deal with these cases.

- The methodological schemes in Chapter 3 and 4 are not designed to extract representative features related to some non-regular vascular details, e.g. cerebral aneurysm. The integration of the proposed scheme in an extended problem formulation to explore structural phenotyping associated with some types of diseased vasculature, e.g., aneurysmal dilatation [277], could be regarded as an interesting research direction.

- Another aspect that could be a topic of further investigations is the formulation of initial gird graph geometries in Chapter 4. In the proposed method, larger vessels lead sizable initial grid graphs, and thus to higher computational burdens. Uniformly increasing the size of grid cells, to produce less number of nodes, precipitate losses in smaller vessel structures.

Thus, introducing an adaptive construction of grid/3D-mesh graphs, with variable cell sizes according to local changes in radius scales, can substantially improve the performance.

In the second part of the thesis, namely, in Chapter 5, OCT microscopic imaging and Monte-Carlo simulations have been employed to study potential diffusion MRI signatures of microvascular architecture after experimentally inducing photothrombosis. The work suggests that quantifying the differences in signal readouts arising from utilizing multiple gradient directions can characterize such microvascular orientations. Simulation outputs provided useful insights about the prospective experimental implications. Future directions on the experimental and clinical sides could be related to the following.

- The use of ASL has been shown to be of critical importance when characterizing microvascular occlusions based on the associated disruption in vascular geometry. In the mouse cerebral cortex, microvascular density sums to less than 5% of a tissue volume of 1 mm^3; this ratio decreases with depth [278]. Eliminating the MRI signal contributed from the extravascular space is thus necessary. ASL approaches have already shown promising applications in measuring regional cerebral blood flow (rCBF) or perfusion [279–281], and in assessing vascular disorders [280, 282, 283].

- The simulation outcomes in Chapter 5 justify the selection of ASL-coupled multi-directional diffusion MRI used by Well et al. [284] as the modality of choice to annotate flow patterns in the mouse cerebral cortex.

- It has been observed that a noticeable drop in statistical significance between the responses of healthy and lesioned vasculature at longer echo time TE. This observation is associated with the dominant T2/T2* shortening caused by deoxyhemoglobin distribution, opposed to that rising from diffusion gradients.

- Reduced statistical differences have been also observed when examining the responses at higher B0 values. Ultra-high field strengths, despite improving Signal-to-noise (SNR) ratio, translate into shorter T2* and T2 [285, 286]. In other words, The increased B0 inhomogeneity at higher B0 leads to more signal loss, especially with longer echo times, which offset the advantage of its higher SNR. A straightforward approach would employ shorter echo time to mitigate the adverse effect of stronger fields [287, 288].

Some useful directions to furtherly improve the proposed simulation framework could be summarized as follows.

- A machine learning approach has been employed to predict SO2 and blood flow distributions across our vascular networks to enable the study in this thesis. Oxygen transport modeling, based on more representative vascular graphs, can be used to improve these measurements. However, such modeling remains challenging since it requires tedious manual efforts and can be infeasible at scale [47].
- One aspect of improvement relates to integrating a model of the restricted diffusion in tissue, instead of assuming a constant extravascular T2 field. An improved framework could encompass the magnetic perturbations induced by susceptibility interfaces between vessels and cells, and the permeability of the vessel wall [289].
- It is known that larger microstrokes impose T2 changes in tissue. The proposed modeling could be improved through the incorporation of measured T2 tissue changes to understand their impact with a more realistic simulation.

When considering the global experimental design and research scheme, stronger longitudinal investigations of the time course characteristics and the evolution of microstokes can be achieved through improving upon the following aspects:

- Larger cohort studies could be involved to increase the statistical power and to provide stronger proof of concept with respect to the MRI simulations. Such direction is important to provide more definitive information about further experimental implications.
- One improvement could be related to the animal model designed for creating ischemic lesions. Instead of focusing on occluding pial vessels located nearly in the same cortical region across different animals, creating microstrokes that vary in their size and location could be considered. However, such direction is inapplicable given the current craniotomy procedure and the corresponding occlusion principles. It is impractical to perform multiple craniotomy at different regions of the skull in the same animal, whereas photothrombotically occluding larger vessels leads into tail artifacts in OCT angiography images and into less predictable outcomes. Thus, imposing improvements in such direction requires the development of a novel microstoke model.
- OCT imaging was used to assess the outcomes of cerebrovascular micro-occlusions, to avoid image degeneration and artifacts that could result from dye leakage in case of other label-based imaging techniques, e.g., TPM angiography. However, it is known that OCT angiography suffers from low-resolution outputs that complicate the process of vascular modeling. Therefore, improvements in the image acquisition part could enhance the modeling of the microvasculature and consequently help to obtain better MRI simulations.

CHAPTER 7 CONCLUSION

In this thesis, the initial objective has focused on developing a fully-automated processing pipeline to extract useful graphical models of cerebral microvascular structures to facilitate further analysis of its underlying physiological factors. A fully-automated solution that provides a unique graph-based output based on raw TPM inputs has been proposed in Chapter 3. The solution comprises a fully-convolutional neural network to segment microvessels, a water-tight triangulated mesh generator to model vessel boundaries, and a mesh contraction algorithm to produce graph-based vascular models. An improvement of this pipeline is proposed in Chapter 4. In particular, a novel framework has been presented to deform 3D geometric graphs, instead of triangulated meshes, converting them into graphed curve-skeletons. Truncated 3D grid graphs are first constructed within vessel boundaries. A method is proposed to assign weights on these graphs, and a constrained iterative optimizer is developed to decimate them toward vessel centerlines. A refinement algorithm has been illustrated to convert a deformed graph into a final vascular graphed-skeleton model. The new graphing scheme showed more generalizability with less restriction on the quality of binary inputs. The ultimate goal of the work in this thesis has been to integrate such modeling scheme to investigate potential non-invasive biomarkers of cerebrovascular micro-occlusions , i.e., microstokes. In Chapter 5, based on the developed computational modeling, potential MRI signatures of microstrokes have been simulated combining ASL and DWI techniques. The hypothesis has been driven based on recent observations demonstrating a radial reorientation of microvasculature around the micro-infarction locus during recovery in mice. Synthetic and realistic computational vascular models have been exploited within a 3D Monte-Carlo simulator to characterize the MR response, encompassing the effects of magnetic field perturbations caused by deoxyhemoglobin, and the advection and diffusion of the nuclear spins.

REFERENCES

[1] Elizabeth MC Hillman. “Coupling mechanism and significance of the BOLD signal: a status report”. In: *Annual review of neuroscience* 37 (2014), pp. 161–181.

[2] Leonardo Pantoni. “Cerebral small vessel disease: from pathogenesis and clinical characteristics to therapeutic challenges”. In: *The Lancet Neurology* 9.7 (2010), pp. 689–701.

[3] Tae-Rin Lee et al. “A computational modeling of blood flow in asymmetrically bifurcating microvessels and its experimental validation”. In: *International journal for numerical methods in biomedical engineering* 34.6 (2018), e2981.

[4] Amy F Smith et al. “Brain capillary networks across species: a few simple organizational requirements are sufficient to reproduce both structure and function”. In: *Frontiers in physiology* 10 (2019), p. 233.

[5] Andreas Linninger et al. “Mathematical synthesis of the cortical circulation for the whole mouse brain-part I. theory and image integration”. In: *Computers in biology and medicine* 110 (2019), pp. 265–275.

[6] Myriam Peyrounette et al. “Multiscale modelling of blood flow in cerebral microcirculation: Details at capillary scale control accuracy at the level of the cortex”. In: *PloS one* 13.1 (2018).

[7] Louis Gagnon et al. “Quantifying the microvascular origin of BOLD-fMRI from first principles with two-photon microscopy and an oxygen-sensitive nanoprobe”. In: *Journal of Neuroscience* 35.8 (2015), pp. 3663–3675.

[8] Louis Gagnon et al. “Modeling of cerebral oxygen transport based on in vivo microscopic imaging of microvascular network structure, blood flow, and oxygenation”. In: *Frontiers in computational neuroscience* 10 (2016).

[9] Mario Gilberto Báez-Yánez et al. “The impact of vessel size, orientation and intravascular contribution on the neurovascular fingerprint of BOLD bSSFP fMRI”. In: *NeuroImage* 163 (2017), pp. 13–23.

[10] Philippe Pouliot et al. “Magnetic resonance fingerprinting based on realistic vasculature in mice”. In: *Neuroimage* 149 (2017), pp. 436–445.

[11] Peter H Tomlins and Ruikang K Wang. “Theory, developments and applications of optical coherence tomography”. In: *Journal of Physics D: Applied Physics* 38.15 (2005), p. 2519.

[12] Utku Baran and Ruikang K Wang. “Review of optical coherence tomography based angiography in neuroscience”. In: *Neurophotonics* 3.1 (2016), p. 010902.

[13] Karel Svoboda and Ryohei Yasuda. “Principles of two-photon excitation microscopy and its applications to neuroscience”. In: *Neuron* 50.6 (2006), pp. 823–839.

[14] Nicholas G Horton et al. “In vivo three-photon microscopy of subcortical structures within an intact mouse brain”. In: *Nature photonics* 7.3 (2013), p. 205.

[15] Vivek J Srinivasan et al. “Quantitative cerebral blood flow with optical coherence tomography”. In: *Optics express* 18.3 (2010), pp. 2477–2494.

[16] Fritjof Helmchen and Winfried Denk. “Deep tissue two-photon microscopy”. In: *Nature methods* 2.12 (2005), pp. 932–940.

[17] Utku Baran et al. “Tail artifact removal in OCT angiography images of rodent cortex”. In: *Journal of biophotonics* 10.11 (2017), pp. 1421–1429.

[18] Philipp M Summers et al. “Functional deficits induced by cortical microinfarcts”. In: *Journal of Cerebral Blood Flow & Metabolism* 37.11 (2017), pp. 3599–3614.

[19] Andy Y Shih et al. “The smallest stroke: occlusion of one penetrating vessel leads to infarction and a cognitive deficit”. In: *Nature neuroscience* 16.1 (2013), pp. 55–63.

[20] Zachary J Taylor et al. “Microvascular basis for growth of small infarcts following occlusion of single penetrating arterioles in mouse cortex”. In: *Journal of Cerebral Blood Flow & Metabolism* 36.8 (2016), pp. 1357–1373.

[21] Eitan Anenberg et al. “Ministrokes in channelrhodopsin-2 transgenic mice reveal widespread deficits in motor output despite maintenance of cortical neuronal excitability”. In: *Journal of Neuroscience* 34.4 (2014), pp. 1094–1104.

[22] Buket Dönmez-Demir et al. “Microembolism of single cortical arterioles can induce spreading depression and ischemic injury; a potential trigger for migraine and related MRI lesions”. In: *Brain research* 1679 (2018), pp. 84–90.

[23] Monica Garcia-Alloza et al. “Cerebrovascular lesions induce transient β-amyloid deposition”. In: *Brain* 134.12 (2011), pp. 3697–3707.

[24] Jonathan Long, Evan Shelhamer, and Trevor Darrell. “Fully convolutional networks for semantic segmentation”. In: *Proceedings of the IEEE Conference on Computer Vision and Pattern Recognition*. 2015, pp. 3431–3440.

[25] Simon Jégou et al. “The one hundred layers tiramisu: Fully convolutional DenseNets for semantic segmentation”. In: *arXiv preprint arXiv:1611.09326* (2016).

[26] Andrea Tagliasacchi et al. “Mean curvature skeletons”. In: *Computer Graphics Forum*. Vol. 31. 5. Wiley Online Library. 2012, pp. 1735–1744.

[27] Rafat Damseh et al. “Automatic graph-based modeling of brain microvessels captured with two-photon microscopy”. In: *IEEE journal of biomedical and health informatics* 23.6 (2018), pp. 2551–2562.

[28] Rafat Damseh, Farida Cheriet, and Frederic Lesage. “Modeling the Topology of Cerebral Microvessels Via Geometric Graph Contraction”. In: *2020 IEEE 17th International Symposium on Biomedical Imaging (ISBI)*. IEEE. 2020, pp. 1004–1008.

[29] Christian J Schrandt et al. “Chronic monitoring of vascular progression after ischemic stroke using multiexposure speckle imaging and two-photon fluorescence microscopy”. In: *Journal of Cerebral Blood Flow & Metabolism* 35.6 (2015), pp. 933–942.

[30] Yuankang Lu et al. “Longitudinal optical coherence tomography imaging of tissue repair and microvasculature regeneration and function after targeted cerebral ischemia”. In: *Journal of Biomedical Optics* 25.4 (2020), p. 046002.

[31] Derek K Jones. *Diffusion mri*. Oxford University Press, 2010.

[32] Patrick Delafontaine-Martel et al. “Whole brain vascular imaging in a mouse model of Alzheimer’s disease with two-photon microscopy”. In: *Journal of biomedical optics* 23.7 (2018), p. 076501.

[33] Mohammad Moeini et al. “Compromised microvascular oxygen delivery increases brain tissue vulnerability with age”. In: *Scientific reports* 8.1 (2018), pp. 1–17.

[34] Xuecong Lu et al. “A pilot study investigating changes in capillary hemodynamics and its modulation by exercise in the APP-PS1 alzheimer mouse model”. In: *Frontiers in Neuroscience* 13 (2019).

[35] Patrick Delafontaine-Martel et al. “Large scale serial two-photon microscopy to investigate local vascular changes in whole rodent brain models of Alzheimer’s disease”. In: *Multiphoton Microscopy in the Biomedical Sciences XVIII*. Vol. 10498. International Society for Optics and Photonics. 2018, 104982O.

[36] OpenStax. *Anatomy of the Nervous System*. `http://cnx.org/contents/2b9420ba-0c5a-4601-bb6c-d13526fbeee3@3`. 2016.

[37] John G Nicholls and A Robert Martin. *From neuron to brain*. Vol. 271.

[38] Marco Cavaglia et al. “Regional variation in brain capillary density and vascular response to ischemia”. In: *Brain research* 910.1-2 (2001), pp. 81–93.

[39] Donald D Clarke. “Circulation and energy metabolism of the brain”. In: *Basic neurochemistry: Molecular, cellular, and medical aspects* (1999).

[40] Ravi L Rungta et al. “Vascular compartmentalization of functional hyperemia from the synapse to the pia”. In: *Neuron* 99.2 (2018), pp. 362–375.

[41] Pablo Blinder et al. “Topological basis for the robust distribution of blood to rodent neocortex”. In: *Proceedings of the National Academy of Sciences* 107.28 (2010), pp. 12670–12675.

[42] Sylvie Lorthois and Francis Cassot. “Fractal analysis of vascular networks: insights from morphogenesis”. In: *Journal of theoretical biology* 262.4 (2010), pp. 614–633.

[43] Franca Schmid et al. “Vascular density and distribution in neocortex”. In: *Neuroimage* 197 (2019), pp. 792–805.

[44] Sune N Jespersen and Leif Østergaard. “The roles of cerebral blood flow, capillary transit time heterogeneity, and oxygen tension in brain oxygenation and metabolism”. In: *Journal of cerebral blood flow & metabolism* 32.2 (2012), pp. 264–277.

[45] Leif Østergaard et al. “Capillary transit time heterogeneity and flow-metabolism coupling after traumatic brain injury”. In: *Journal of Cerebral Blood Flow & Metabolism* 34.10 (2014), pp. 1585–1598.

[46] David A Boas et al. “A vascular anatomical network model of the spatio-temporal response to brain activation”. In: *Neuroimage* 40.3 (2008), pp. 1116–1129.

[47] Louis Gagnon et al. “Quantifying the microvascular origin of BOLD-fMRI from first principles with two-photon microscopy and an oxygen-sensitive nanoprobe”. In: *Journal of Neuroscience* 35.8 (2015), pp. 3663–3675.

[48] DA Boas et al. “Can the cerebral metabolic rate of oxygen be estimated with near-infrared spectroscopy?” In: *Physics in Medicine & Biology* 48.15 (2003), p. 2405.

[49] Ying Zheng et al. “A model of the hemodynamic response and oxygen delivery to brain”. In: *Neuroimage* 16.3 (2002), pp. 617–637.

[50] Ying Zheng et al. “A three-compartment model of the hemodynamic response and oxygen delivery to brain”. In: *Neuroimage* 28.4 (2005), pp. 925–939.

[51] Theodore J Huppert et al. “A multicompartment vascular model for inferring baseline and functional changes in cerebral oxygen metabolism and arterial dilation”. In: *Journal of cerebral blood flow & metabolism* 27.6 (2007), pp. 1262–1279.

[52] Navid Safaeian, Mathieu Sellier, and Tim David. “A computational model of hemodynamic parameters in cortical capillary networks”. In: *Journal of theoretical biology* 271.1 (2011), pp. 145–156.

[53] Navid Safaeian and Tim David. “A computational model of oxygen transport in the cerebrocapillary levels for normal and pathologic brain function”. In: *Journal of Cerebral Blood Flow & Metabolism* 33.10 (2013), pp. 1633–1641.

[54] Amy F Smith et al. “Structural and hemodynamic comparison of synthetic and anatomical cerebral capillary networks”. In: (2017).

[55] AA Linninger et al. “Cerebral microcirculation and oxygen tension in the human secondary cortex”. In: *Annals of biomedical engineering* 41.11 (2013), pp. 2264–2284.

[56] Christoph Kirst et al. “Mapping the fine-scale organization and plasticity of the brain vasculature”. In: *Cell* 180.4 (2020), pp. 780–795.

[57] Romain Guibert, Caroline Fonta, and Franck Plouraboué. “Cerebral blood flow modeling in primate cortex”. In: *Journal of Cerebral Blood Flow & Metabolism* 30.11 (2010), pp. 1860–1873.

[58] Qianqian Fang et al. “Oxygen advection and diffusion in a three dimensional vascular anatomical network”. In: *Optics express* 16.22 (2008), p. 17530.

[59] Ian Gopal Gould et al. “The capillary bed offers the largest hemodynamic resistance to the cortical blood supply”. In: *Journal of Cerebral Blood Flow & Metabolism* 37.1 (2017), pp. 52–68.

[60] Franca Schmid et al. “Depth-dependent flow and pressure characteristics in cortical microvascular networks”. In: *PLoS computational biology* 13.2 (2017), e1005392.

[61] Benyi Xiong et al. “Precise cerebral vascular atlas in stereotaxic coordinates of whole mouse brain”. In: *Frontiers in neuroanatomy* 11 (2017), p. 128.

[62] Antonino Paolo Di Giovanna et al. “Whole-brain vasculature reconstruction at the single capillary level”. In: *Scientific reports* 8.1 (2018), pp. 1–11.

[63] Hana Uhlirova et al. “The roadmap for estimation of cell-type-specific neuronal activity from non-invasive measurements”. In: *Philosophical Transactions of the Royal Society B: Biological Sciences* 371.1705 (2016), p. 20150356.

[64] Michèle Desjardins et al. “Awake Mouse Imaging: From Two-Photon Microscopy to Blood Oxygen Level–Dependent Functional Magnetic Resonance Imaging”. In: *Biological Psychiatry: Cognitive Neuroscience and Neuroimaging* 4.6 (2019), pp. 533–542.

[65] Dan Ma et al. “Magnetic resonance fingerprinting”. In: *Nature* 495.7440 (2013), pp. 187–192.

[66] Thomas Christen et al. “MR vascular fingerprinting: A new approach to compute cerebral blood volume, mean vessel radius, and oxygenation maps in the human brain”. In: *Neuroimage* 89 (2014), pp. 262–270.

[67] World Health Organization et al. *Dementia: a public health priority*. World Health Organization, 2012.

[68] Helene Girouard and Costantino Iadecola. “Neurovascular coupling in the normal brain and in hypertension, stroke, and Alzheimer disease”. In: *Journal of applied physiology* 100.1 (2006), pp. 328–335.

[69] Costantino Iadecola. “Neurovascular regulation in the normal brain and in Alzheimer’s disease”. In: *Nature Reviews Neuroscience* 5.5 (2004), pp. 347–360.

[70] C Jack. “Vascular risk factor detection and control may prevent Alzheimer’s disease”. In: *Ageing research reviews* 9.3 (2010), pp. 218–225.

[71] Costantino Iadecola. “The overlap between neurodegenerative and vascular factors in the pathogenesis of dementia”. In: *Acta neuropathologica* 120.3 (2010), pp. 287–296.

[72] Sarah E Vermeer et al. “Silent brain infarcts and the risk of dementia and cognitive decline”. In: *New England Journal of Medicine* 348.13 (2003), pp. 1215–1222.

[73] Utku Baran, Yuandong Li, and Ruikang K Wang. “Vasodynamics of pial and penetrating arterioles in relation to arteriolo-arteriolar anastomosis after focal stroke”. In: *Neurophotonics* 2.2 (2015), p. 025006.

[74] Robert G Underly and Andy Y Shih. “Photothrombotic induction of capillary ischemia in the mouse cortex during in vivo two-photon imaging”. In: *Bio-protocol* 7.13 (2017).

[75] Matilde Balbi et al. “Longitudinal monitoring of mesoscopic cortical activity in a mouse model of microinfarcts reveals dissociations with behavioral and motor function”. In: *Journal of Cerebral Blood Flow & Metabolism* 39.8 (2019), pp. 1486–1500.

[76] Smrithi Sunil et al. “Awake chronic mouse model of targeted pial vessel occlusion via photothrombosis”. In: *Neurophotonics* 7.1 (2020), p. 015005.

[77] Yann LeCun, Yoshua Bengio, and Geoffrey Hinton. “Deep learning”. In: *nature* 521.7553 (2015), pp. 436–444.

[78] David E Rumelhart, Geoffrey E Hinton, and Ronald J Williams. “Learning representations by back-propagating errors”. In: *nature* 323.6088 (1986), pp. 533–536.

[79] Guillaume Bellec et al. “Biologically inspired alternatives to backpropagation through time for learning in recurrent neural nets”. In: *arXiv preprint arXiv:1901.09049* (2019).

[80] Timothy P Lillicrap et al. “Random synaptic feedback weights support error backpropagation for deep learning”. In: *Nature communications* 7.1 (2016), pp. 1–10.

[81] Ian Goodfellow, Yoshua Bengio, and Aaron Courville. *Deep learning*. MIT press, 2016.

[82] Alex Krizhevsky, Ilya Sutskever, and Geoffrey E Hinton. “Imagenet classification with deep convolutional neural networks”. In: *Advances in neural information processing systems*. 2012, pp. 1097–1105.

[83] Elie Aljalbout et al. “Clustering with deep learning: Taxonomy and new methods”. In: *arXiv preprint arXiv:1801.07648* (2018).

[84] Chong Zhou and Randy C Paffenroth. “Anomaly detection with robust deep autoencoders”. In: *Proceedings of the 23rd ACM SIGKDD International Conference on Knowledge Discovery and Data Mining*. 2017, pp. 665–674.

[85] Yoshua Bengio, Aaron Courville, and Pascal Vincent. “Representation learning: A review and new perspectives”. In: *IEEE transactions on pattern analysis and machine intelligence* 35.8 (2013), pp. 1798–1828.

[86] Xiaojin Zhu and Andrew B Goldberg. “Introduction to semi-supervised learning”. In: *Synthesis lectures on artificial intelligence and machine learning* 3.1 (2009), pp. 1–130.

[87] Jason Weston et al. “Deep learning via semi-supervised embedding”. In: *Neural networks: Tricks of the trade*. Springer, 2012, pp. 639–655.

[88] Christoph Baur, Shadi Albarqouni, and Nassir Navab. “Semi-supervised deep learning for fully convolutional networks”. In: *International Conference on Medical Image Computing and Computer-Assisted Intervention*. Springer. 2017, pp. 311–319.

[89] Hakan Bilen and Andrea Vedaldi. “Weakly supervised deep detection networks”. In: *Proceedings of the IEEE Conference on Computer Vision and Pattern Recognition*. 2016, pp. 2846–2854.

[90] Volodymyr Mnih et al. “Human-level control through deep reinforcement learning”. In: *nature* 518.7540 (2015), pp. 529–533.

[91] David Silver et al. “Mastering the game of Go with deep neural networks and tree search”. In: *nature* 529.7587 (2016), pp. 484–489.

[92] David Silver et al. “Mastering the game of go without human knowledge”. In: *nature* 550.7676 (2017), pp. 354–359.

[93] Chelsea Finn, Pieter Abbeel, and Sergey Levine. “Model-agnostic meta-learning for fast adaptation of deep networks”. In: *arXiv preprint arXiv:1703.03400* (2017).

[94] Yann LeCun et al. “Backpropagation applied to handwritten zip code recognition”. In: *Neural computation* 1.4 (1989), pp. 541–551.

[95] Yann LeCun et al. “Gradient-based learning applied to document recognition”. In: *Proceedings of the IEEE* 86.11 (1998), pp. 2278–2324.

[96] Karen Simonyan and Andrew Zisserman. “Very deep convolutional networks for large-scale image recognition”. In: *arXiv preprint arXiv:1409.1556* (2014).

[97] Christian Szegedy et al. “Going deeper with convolutions”. In: *Proceedings of the IEEE conference on computer vision and pattern recognition*. 2015, pp. 1–9.

[98] Kaiming He et al. “Deep residual learning for image recognition”. In: *Proceedings of the IEEE conference on computer vision and pattern recognition*. 2016, pp. 770–778.

[99] Gao Huang et al. “Densely connected convolutional networks”. In: *Proceedings of the IEEE conference on computer vision and pattern recognition*. 2017, pp. 4700–4708.

[100] Andrew G Howard et al. “Mobilenets: Efficient convolutional neural networks for mobile vision applications”. In: *arXiv preprint arXiv:1704.04861* (2017).

[101] Mingxing Tan and Quoc V Le. “Efficientnet: Rethinking model scaling for convolutional neural networks”. In: *arXiv preprint arXiv:1905.11946* (2019).

[102] Jonathan Long, Evan Shelhamer, and Trevor Darrell. “Fully convolutional networks for semantic segmentation”. In: *Proceedings of the IEEE conference on computer vision and pattern recognition*. 2015, pp. 3431–3440.

[103] Olaf Ronneberger, Philipp Fischer, and Thomas Brox. “U-net: Convolutional networks for biomedical image segmentation”. In: *International Conference on Medical image computing and computer-assisted intervention*. Springer. 2015, pp. 234–241.

[104] Phillip Isola et al. “Image-to-image translation with conditional adversarial networks”. In: *Proceedings of the IEEE conference on computer vision and pattern recognition*. 2017, pp. 1125–1134.

[105] Liang-Chieh Chen et al. “Deeplab: Semantic image segmentation with deep convolutional nets, atrous convolution, and fully connected crfs”. In: *IEEE transactions on pattern analysis and machine intelligence* 40.4 (2017), pp. 834–848.

[106] Simon Jégou et al. “The one hundred layers tiramisu: Fully convolutional densenets for semantic segmentation”. In: *Proceedings of the IEEE conference on computer vision and pattern recognition workshops*. 2017, pp. 11–19.

[107] Shaoqing Ren et al. “Faster r-cnn: Towards real-time object detection with region proposal networks”. In: *Advances in neural information processing systems*. 2015, pp. 91–99.

[108] Wei Liu et al. “Ssd: Single shot multibox detector”. In: *European conference on computer vision*. Springer. 2016, pp. 21–37.

[109] Kaiming He et al. “Mask r-cnn”. In: *Proceedings of the IEEE international conference on computer vision*. 2017, pp. 2961–2969.

[110] Joseph Redmon and Ali Farhadi. “YOLO9000: better, faster, stronger”. In: *Proceedings of the IEEE conference on computer vision and pattern recognition*. 2017, pp. 7263–7271.

[111] Ali Borji et al. “Salient object detection: A survey”. In: *Computational visual media* (2019), pp. 1–34.

[112] Kelvin Xu et al. “Show, attend and tell: Neural image caption generation with visual attention”. In: *International conference on machine learning*. 2015, pp. 2048–2057.

[113] Jeffrey Donahue et al. “Long-term recurrent convolutional networks for visual recognition and description”. In: *Proceedings of the IEEE conference on computer vision and pattern recognition*. 2015, pp. 2625–2634.

[114] Zichao Yang et al. “Stacked attention networks for image question answering”. In: *Proceedings of the IEEE conference on computer vision and pattern recognition*. 2016, pp. 21–29.

[115] Adam Santoro et al. “A simple neural network module for relational reasoning”. In: *Advances in neural information processing systems*. 2017, pp. 4967–4976.

[116] Peter Anderson et al. “Bottom-up and top-down attention for image captioning and visual question answering”. In: *Proceedings of the IEEE conference on computer vision and pattern recognition*. 2018, pp. 6077–6086.

[117] Xu Yang et al. “Auto-encoding scene graphs for image captioning”. In: *Proceedings of the IEEE Conference on Computer Vision and Pattern Recognition*. 2019, pp. 10685–10694.

[118] Xiang Zhang, Junbo Zhao, and Yann LeCun. “Character-level convolutional networks for text classification”. In: *Advances in neural information processing systems*. 2015, pp. 649–657.

[119] Mikael Henaff, Joan Bruna, and Yann LeCun. “Deep convolutional networks on graph-structured data”. In: *arXiv preprint arXiv:1506.05163* (2015).

[120] Jiuxiang Gu et al. “Recent advances in convolutional neural networks”. In: *Pattern Recognition* 77 (2018), pp. 354–377.

[121] Prajit Ramachandran, Barret Zoph, and Quoc V Le. “Searching for activation functions”. In: *arXiv preprint arXiv:1710.05941* (2017).

[122] Dominik Scherer, Andreas Müller, and Sven Behnke. “Evaluation of pooling operations in convolutional architectures for object recognition”. In: *International conference on artificial neural networks*. Springer. 2010, pp. 92–101.

[123] David H Hubel and Torsten N Wiesel. “Receptive fields and functional architecture of monkey striate cortex”. In: *The Journal of physiology* 195.1 (1968), pp. 215–243.

[124] Md Nasir Uddin Laskar, Luis G Sanchez Giraldo, and Odelia Schwartz. “Correspondence of deep neural networks and the brain for visual textures”. In: *arXiv preprint arXiv:1806.02888* (2018).

[125] Guohua Shen et al. “Deep image reconstruction from human brain activity”. In: *PLoS computational biology* 15.1 (2019), e1006633.

[126] Matthew D Zeiler and Rob Fergus. “Visualizing and understanding convolutional networks”. In: *European conference on computer vision*. Springer. 2014, pp. 818–833.

[127] Christian Szegedy et al. “Rethinking the inception architecture for computer vision”. In: *Proceedings of the IEEE conference on computer vision and pattern recognition*. 2016, pp. 2818–2826.

[128] Saining Xie et al. “Aggregated residual transformations for deep neural networks”. In: *Proceedings of the IEEE conference on computer vision and pattern recognition*. 2017, pp. 1492–1500.

[129] Andrej Karpathy. “Connecting images and natural language”. PhD thesis. Ph. D. thesis, Stanford University, 2016.

[130] Yoshua Bengio, Patrice Simard, and Paolo Frasconi. “Learning long-term dependencies with gradient descent is difficult”. In: *IEEE transactions on neural networks* 5.2 (1994), pp. 157–166.

[131] Ilya Sutskever, Oriol Vinyals, and Quoc V Le. “Sequence to sequence learning with neural networks”. In: *Advances in neural information processing systems*. 2014, pp. 3104–3112.

[132] Jürgen Schmidhuber. “Deep learning in neural networks: An overview”. In: *Neural networks* 61 (2015), pp. 85–117.

[133] Sepp Hochreiter and Jürgen Schmidhuber. “Long short-term memory”. In: *Neural computation* 9.8 (1997), pp. 1735–1780.

[134] Kyunghyun Cho et al. “Learning phrase representations using RNN encoder-decoder for statistical machine translation”. In: *arXiv preprint arXiv:1406.1078* (2014).

[135] Dzmitry Bahdanau, Kyunghyun Cho, and Yoshua Bengio. “Neural machine translation by jointly learning to align and translate”. In: *arXiv preprint arXiv:1409.0473* (2014).

[136] Jacob Devlin et al. “Bert: Pre-training of deep bidirectional transformers for language understanding”. In: *arXiv preprint arXiv:1810.04805* (2018).

[137] Ashish Vaswani et al. “Attention is all you need”. In: *Advances in neural information processing systems*. 2017, pp. 5998–6008.

[138] Jinhyuk Lee et al. “BioBERT: a pre-trained biomedical language representation model for biomedical text mining”. In: *Bioinformatics* 36.4 (2020), pp. 1234–1240.

[139] Michael M Bronstein et al. “Geometric deep learning: going beyond euclidean data”. In: *IEEE Signal Processing Magazine* 34.4 (2017), pp. 18–42.

[140] Thomas N Kipf and Max Welling. “Semi-supervised classification with graph convolutional networks”. In: *arXiv preprint arXiv:1609.02907* (2016).

[141] Sofia Ira Ktena et al. “Distance metric learning using graph convolutional networks: Application to functional brain networks”. In: *International Conference on Medical Image Computing and Computer-Assisted Intervention*. Springer. 2017, pp. 469–477.

[142] Marinka Zitnik, Monica Agrawal, and Jure Leskovec. “Modeling polypharmacy side effects with graph convolutional networks”. In: *Bioinformatics* 34.13 (2018), pp. i457–i466.

[143] William L Hamilton, Rex Ying, and Jure Leskovec. “Representation learning on graphs: Methods and applications”. In: *arXiv preprint arXiv:1709.05584* (2017).

[144] Shirui Pan et al. “Adversarially regularized graph autoencoder for graph embedding”. In: *arXiv preprint arXiv:1802.04407* (2018).

[145] Petar Veličković et al. “Graph attention networks”. In: *arXiv preprint arXiv:1710.10903* (2017).

[146] Yue Wang et al. “Dynamic graph cnn for learning on point clouds”. In: *Acm Transactions On Graphics (tog)* 38.5 (2019), pp. 1–12.

[147] Deisy Morselli Gysi et al. “Network medicine framework for identifying drug repurposing opportunities for covid-19”. In: *arXiv preprint arXiv:2004.07229* (2020).

[148] Ian Goodfellow et al. “Generative adversarial nets”. In: *Advances in neural information processing systems*. 2014, pp. 2672–2680.

[149] Diederik P Kingma and Max Welling. “Auto-encoding variational bayes”. In: *arXiv preprint arXiv:1312.6114* (2013).

[150] Han Zhang et al. “Self-attention generative adversarial networks”. In: *International Conference on Machine Learning*. 2019, pp. 7354–7363.

[151] Tero Karras, Samuli Laine, and Timo Aila. “A style-based generator architecture for generative adversarial networks”. In: *Proceedings of the IEEE conference on computer vision and pattern recognition*. 2019, pp. 4401–4410.

[152] Nitish Srivastava et al. “Dropout: a simple way to prevent neural networks from overfitting”. In: *The journal of machine learning research* 15.1 (2014), pp. 1929–1958.

[153] Saeid Asgari Taghanaki et al. “Deep semantic segmentation of natural and medical images: A review”. In: *Artificial Intelligence Review* (2020), pp. 1–42.

[154] Fausto Milletari, Nassir Navab, and Seyed-Ahmad Ahmadi. “V-net: Fully convolutional neural networks for volumetric medical image segmentation”. In: *2016 fourth international conference on 3D vision (3DV)*. IEEE. 2016, pp. 565–571.

[155] Petteri Teikari et al. “Deep learning convolutional networks for multiphoton microscopy vasculature segmentation”. In: *arXiv preprint arXiv:1606.02382* (2016).

[156] Rafat Damseh, Farida Cheriet, and Frederic Lesage. “Fully convolutional DenseNets for segmentation of microvessels in two-photon microscopy”. In: *2018 40th Annual International Conference of the IEEE Engineering in Medicine and Biology Society (EMBC)*. IEEE. 2018, pp. 661–665.

[157] Liang-Chieh Chen et al. “Encoder-decoder with atrous separable convolution for semantic image segmentation”. In: *Proceedings of the European conference on computer vision (ECCV)*. 2018, pp. 801–818.

[158] Hengshuang Zhao et al. “Pyramid scene parsing network”. In: *Proceedings of the IEEE conference on computer vision and pattern recognition*. 2017, pp. 2881–2890.

[159] Michal Drozdzal et al. “Learning normalized inputs for iterative estimation in medical image segmentation”. In: *Medical image analysis* 44 (2018), pp. 1–13.

[160] Zaiwang Gu et al. “Ce-net: Context encoder network for 2d medical image segmentation”. In: *IEEE transactions on medical imaging* 38.10 (2019), pp. 2281–2292.

[161] Zongwei Zhou et al. “Unet++: A nested u-net architecture for medical image segmentation”. In: *Deep Learning in Medical Image Analysis and Multimodal Learning for Clinical Decision Support*. Springer, 2018, pp. 3–11.

[162] Yu Weng et al. “Nas-unet: Neural architecture search for medical image segmentation”. In: *IEEE Access* 7 (2019), pp. 44247–44257.

[163] Robin Brügger, Christian F Baumgartner, and Ender Konukoglu. "A partially reversible U-Net for memory-efficient volumetric image segmentation". In: *International Conference on Medical Image Computing and Computer-Assisted Intervention*. Springer. 2019, pp. 429–437.

[164] Dong Nie et al. "ASDNet: Attention based semi-supervised deep networks for medical image segmentation". In: *International Conference on Medical Image Computing and Computer-Assisted Intervention*. Springer. 2018, pp. 370–378.

[165] Jo Schlemper et al. "Attention gated networks: Learning to leverage salient regions in medical images". In: *Medical image analysis* 53 (2019), pp. 197–207.

[166] Naji Khosravan et al. "Pan: Projective adversarial network for medical image segmentation". In: *International Conference on Medical Image Computing and Computer-Assisted Intervention*. Springer. 2019, pp. 68–76.

[167] Arunava Chakravarty and Jayanthi Sivaswamy. "RACE-net: a recurrent neural network for biomedical image segmentation". In: *IEEE journal of biomedical and health informatics* 23.3 (2018), pp. 1151–1162.

[168] David Lesage et al. "A review of 3D vessel lumen segmentation techniques: Models, features and extraction schemes". In: *Medical image analysis* 13.6 (2009), pp. 819–845.

[169] Muhammad Moazam Fraz et al. "Blood vessel segmentation methodologies in retinal images–a survey". In: *Computer methods and programs in biomedicine* 108.1 (2012), pp. 407–433.

[170] Alejandro F Frangi et al. "Multiscale vessel enhancement filtering". In: *International conference on medical image computing and computer-assisted intervention*. Springer. 1998, pp. 130–137.

[171] Marcela Hernández Hoyos et al. "Vascular centerline extraction in 3D MR angiograms for phase contrast MRI blood flow measurement". In: *International Journal of Computer Assisted Radiology and Surgery* 1.1 (2006), pp. 51–61.

[172] Christian Bauer and Horst Bischof. "A novel approach for detection of tubular objects and its application to medical image analysis". In: *Joint pattern recognition symposium*. Springer. 2008, pp. 163–172.

[173] Alexander Vasilevskiy and Kaleem Siddiqi. "Flux maximizing geometric flows". In: *IEEE transactions on pattern analysis and machine intelligence* 24.12 (2002), pp. 1565–1578.

[174] Carmen Alina Lupascu, Domenico Tegolo, and Emanuele Trucco. "FABC: retinal vessel segmentation using AdaBoost". In: *IEEE Transactions on Information Technology in Biomedicine* 14.5 (2010), pp. 1267–1274.

[175] Muhammad Moazam Fraz et al. “An approach to localize the retinal blood vessels using bit planes and centerline detection”. In: *Computer methods and programs in biomedicine* 108.2 (2012), pp. 600–616.

[176] Kelvin Poon, Ghassan Hamarneh, and Rafeef Abugharbieh. “Live-vessel: Extending livewire for simultaneous extraction of optimal medial and boundary paths in vascular images”. In: *International Conference on Medical Image Computing and Computer-Assisted Intervention*. Springer. 2007, pp. 444–451.

[177] Sara Moccia et al. “Blood vessel segmentation algorithms—review of methods, datasets and evaluation metrics”. In: *Computer methods and programs in biomedicine* 158 (2018), pp. 71–91.

[178] Jameson Merkow et al. “Dense volume-to-volume vascular boundary detection”. In: *International conference on medical image computing and computer-assisted intervention*. Springer. 2016, pp. 371–379.

[179] Michelle Livne et al. “A U-Net deep learning framework for high performance vessel segmentation in patients with cerebrovascular disease”. In: *Frontiers in neuroscience* 13 (2019), p. 97.

[180] Dongdong Hao et al. “Sequential vessel segmentation via deep channel attention network”. In: *Neural Networks* (2020).

[181] Qiaoliang Li et al. “A cross-modality learning approach for vessel segmentation in retinal images”. In: *IEEE transactions on medical imaging* 35.1 (2015), pp. 109–118.

[182] Y. M. Kassim et al. “Microvasculature segmentation of arterioles using deep CNN”. In: *2017 IEEE International Conference on Image Processing (ICIP)*. 2017, pp. 580–584.

[183] Seung Yeon Shin et al. “Deep vessel segmentation by learning graphical connectivity”. In: *Medical image analysis* 58 (2019), p. 101556.

[184] L. Mou et al. “Dense Dilated Network With Probability Regularized Walk for Vessel Detection”. In: *IEEE Transactions on Medical Imaging* 39.5 (2020), pp. 1392–1403.

[185] Qiangguo Jin et al. “DUNet: A deformable network for retinal vessel segmentation”. In: *Knowledge-Based Systems* 178 (2019), pp. 149–162.

[186] Mohammad Haft-Javaherian et al. “Deep convolutional neural networks for segmenting 3D in vivo multiphoton images of vasculature in Alzheimer disease mouse models”. In: *PloS one* 14.3 (2019), e0213539.

[187] Rafat Damseh et al. “Automated Analysis of Brain Microvasculature: From Segmentation to Anatomical Modeling”. In: *2020 42th Annual International Conference of the IEEE Engineering in Medicine and Biology Society (EMBC)*. IEEE. 2020.

[188] Waleed Tahir et al. “A generalizable deep-learning approach to anatomical modeling of brain vasculature (Conference Presentation)”. In: *Neural Imaging and Sensing 2020*. Ed. by Qingming Luo, Jun Ding, and Ling Fu. Vol. 11226. International Society for Optics and Photonics. SPIE, 2020. DOI: 10.1117/12.2543864. URL: https://doi.org/10.1117/12.2543864.

[189] Shir Gur et al. “Unsupervised microvascular image segmentation using an active contours mimicking neural network”. In: *Proceedings of the IEEE International Conference on Computer Vision*. 2019, pp. 10722–10731.

[190] Mihail Ivilinov Todorov et al. “Machine learning analysis of whole mouse brain vasculature”. In: *Nature Methods* 17.4 (2020), pp. 442–449.

[191] Yefeng Zheng et al. “3D deep learning for efficient and robust landmark detection in volumetric data”. In: *International Conference on Medical Image Computing and Computer-Assisted Intervention*. Springer. 2015, pp. 565–572.

[192] Haben Berhane et al. “Fully automated 3D aortic segmentation of 4D flow MRI for hemodynamic analysis using deep learning”. In: *Magnetic resonance in medicine* (2020).

[193] P. Liskowski and K. Krawiec. “Segmenting Retinal Blood Vessels With Deep Neural Networks”. In: *IEEE Transactions on Medical Imaging* 35.11 (2016), pp. 2369–2380.

[194] Andrew Nealen et al. “Laplacian mesh optimization”. In: *Proceedings of the 4th international conference on Computer graphics and interactive techniques in Australasia and Southeast Asia*. 2006, pp. 381–389.

[195] Olga Sorkine, Daniel Cohen-Or, and Sivan Toledo. “High-pass quantization for mesh encoding.” In: *Symposium on Geometry Processing*. Vol. 42. 2003.

[196] Hao Zhang, Oliver Van Kaick, and Ramsay Dyer. “Spectral mesh processing”. In: *Computer graphics forum*. Vol. 29. 6. Wiley Online Library. 2010, pp. 1865–1894.

[197] Ulrike Von Luxburg. “A tutorial on spectral clustering”. In: *Statistics and computing* 17.4 (2007), pp. 395–416.

[198] Thomas Bühler and Matthias Hein. “Spectral clustering based on the graph p-Laplacian”. In: *Proceedings of the 26th Annual International Conference on Machine Learning*. 2009, pp. 81–88.

[199] J. Pang and G. Cheung. “Graph Laplacian Regularization for Image Denoising: Analysis in the Continuous Domain”. In: *IEEE Transactions on Image Processing* 26.4 (2017), pp. 1770–1785.

[200] Oscar Kin-Chung Au et al. “Skeleton extraction by mesh contraction”. In: *ACM transactions on graphics (TOG)* 27.3 (2008), pp. 1–10.

[201] Andrea Tagliasacchi et al. “Mean curvature skeletons”. In: *Computer Graphics Forum*. Vol. 31. 5. Wiley Online Library. 2012, pp. 1735–1744.

[202] Andrea Tagliasacchi et al. “3D skeletons: A state-of-the-art report”. In: *Computer Graphics Forum*. Vol. 35. 2. Wiley Online Library. 2016, pp. 573–597.

[203] Gabriel Taubin. “A signal processing approach to fair surface design”. In: *Proceedings of the 22nd annual conference on Computer graphics and interactive techniques*. 1995, pp. 351–358.

[204] Mark Meyer et al. “Discrete differential-geometry operators for triangulated 2-manifolds”. In: *Visualization and mathematics III*. Springer, 2003, pp. 35–57.

[205] Bruno Vallet and Bruno Lévy. “Spectral geometry processing with manifold harmonics”. In: *Computer Graphics Forum*. Vol. 27. 2. Wiley Online Library. 2008, pp. 251–260.

[206] Kaleem Siddiqi and Stephen Pizer. *Medial representations: mathematics, algorithms and applications*. Vol. 37. Springer Science & Business Media, 2008.

[207] Punam K Saha, Gunilla Borgefors, and Gabriella Sanniti di Baja. “A survey on skeletonization algorithms and their applications”. In: *Pattern recognition letters* 76 (2016), pp. 3–12.

[208] André Sobiecki, Andrei Jalba, and Alexandru Telea. “Comparison of curve and surface skeletonization methods for voxel shapes”. In: *Pattern Recognition Letters* 47 (2014), pp. 147–156.

[209] Hari Sundar et al. “Skeleton based shape matching and retrieval”. In: *2003 Shape Modeling International.* IEEE. 2003, pp. 130–139.

[210] Ilya Baran and Jovan Popović. “Automatic rigging and animation of 3d characters”. In: *ACM Transactions on graphics (TOG)* 26.3 (2007), 72–es.

[211] Stefano Moriconi et al. “Inference of cerebrovascular topology with geodesic minimum spanning trees”. In: *IEEE transactions on medical imaging* 38.1 (2018), pp. 225–239.

[212] Ashirwad Chowriappa et al. “3-d vascular skeleton extraction and decomposition”. In: *IEEE journal of biomedical and health informatics* 18.1 (2013), pp. 139–147.

[213] Jean-Paul Charbonnier et al. “Automatic pulmonary artery-vein separation and classification in computed tomography using tree partitioning and peripheral vessel matching”. In: *IEEE transactions on medical imaging* 35.3 (2015), pp. 882–892.

[214] Rubén Cárdenes et al. “Automatic aneurysm neck detection using surface Voronoi diagrams”. In: *IEEE transactions on medical imaging* 30.10 (2011), pp. 1863–1876.

[215] Hrvoje Bogunović et al. “Anatomical labeling of the circle of willis using maximum a posteriori probability estimation”. In: *IEEE transactions on medical imaging* 32.9 (2013), pp. 1587–1599.

[216] Uyen TV Nguyen et al. “An automated method for retinal arteriovenous nicking quantification from color fundus images”. In: *IEEE Transactions on Biomedical Engineering* 60.11 (2013), pp. 3194–3203.

[217] Tamal K Dey and Jian Sun. “Defining and computing curve-skeletons with medial geodesic function”. In: *Symposium on geometry processing*. Vol. 6. 2006, pp. 143–152.

[218] Hui Huang et al. “L1-medial skeleton of point cloud.” In: *ACM Trans. Graph.* 32.4 (2013), pp. 65–1.

[219] Andrei C Jalba, Jacek Kustra, and Alexandru C Telea. “Surface and curve skeletonization of large 3D models on the GPU”. In: *IEEE transactions on pattern analysis and machine intelligence* 35.6 (2012), pp. 1495–1508.

[220] Kaleem Siddiqi et al. “Hamilton-jacobi skeletons”. In: *International Journal of Computer Vision* 48.3 (2002), pp. 215–231.

[221] Mohamed Sabry Hassouna and Aly A Farag. “Variational curve skeletons using gradient vector flow”. In: *IEEE Transactions on Pattern Analysis and Machine Intelligence* 31.12 (2008), pp. 2257–2274.

[222] Tao Ju, Matthew L Baker, and Wah Chiu. “Computing a family of skeletons of volumetric models for shape description”. In: *Computer-Aided Design* 39.5 (2007), pp. 352–360.

[223] Carlo Arcelli, Gabriella Sanniti di Baja, and Luca Serino. “Distance-driven skeletonization in voxel images”. In: *IEEE Transactions on Pattern Analysis and Machine Intelligence* 33.4 (2010), pp. 709–720.

[224] Judson P Jones and Larry A Palmer. “An evaluation of the two-dimensional Gabor filter model of simple receptive fields in cat striate cortex”. In: *Journal of neurophysiology* 58.6 (1987), pp. 1233–1258.

[225] Haiqing Li, Qi Zhang, and Zhenan Sun. “Iris recognition on mobile devices using near-infrared images”. In: *Human Recognition in Unconstrained Environments*. Elsevier, 2017, pp. 103–117.

[226] Kevin P Murphy. *Machine learning: a probabilistic perspective*. MIT press, 2012.

[227] Claude Sammut and Geoffrey I Webb. *Encyclopedia of machine learning*. Springer Science & Business Media, 2011.

[228] Leo Breiman. “Random forests”. In: *Machine learning* 45.1 (2001), pp. 5–32.

[229] Tin Kam Ho. “The random subspace method for constructing decision forests”. In: *IEEE transactions on pattern analysis and machine intelligence* 20.8 (1998), pp. 832–844.

[230] Yoav Freund, Robert E Schapire, et al. “Experiments with a new boosting algorithm”. In: *icml*. Vol. 96. Citeseer. 1996, pp. 148–156.

[231] Pierre Geurts, Damien Ernst, and Louis Wehenkel. “Extremely randomized trees”. In: *Machine learning* 63.1 (2006), pp. 3–42.

[232] Juan José Rodriguez, Ludmila I Kuncheva, and Carlos J Alonso. “Rotation forest: A new classifier ensemble method”. In: *IEEE transactions on pattern analysis and machine intelligence* 28.10 (2006), pp. 1619–1630.

[233] Vivek J Srinivasan et al. “Quantitative cerebral blood flow with optical coherence tomography”. In: *Optics express* 18.3 (2010), pp. 2477–2494.

[234] Wolfgang Drexler et al. “In vivo ultrahigh-resolution optical coherence tomography”. In: *Optics letters* 24.17 (1999), pp. 1221–1223.

[235] Maciej Wojtkowski et al. “Ultrahigh-resolution, high-speed, Fourier domain optical coherence tomography and methods for dispersion compensation”. In: *Optics express* 12.11 (2004), pp. 2404–2422.

[236] R Leitgeb, CK Hitzenberger, and Adolf F Fercher. “Performance of fourier domain vs. time domain optical coherence tomography”. In: *Optics express* 11.8 (2003), pp. 889–894.

[237] Benjamin J Vakoc et al. “Three-dimensional microscopy of the tumor microenvironment in vivo using optical frequency domain imaging”. In: *Nature medicine* 15.10 (2009), pp. 1219–1223.

[238] Zhongping Chen et al. “Noninvasive imaging of in vivo blood flow velocity using optical Doppler tomography”. In: *Optics letters* 22.14 (1997), pp. 1119–1121.

[239] Enock Jonathan, Joey Enfield, and Martin J Leahy. “Correlation mapping method for generating microcirculation morphology from optical coherence tomography (OCT) intensity images”. In: *Journal of biophotonics* 4.9 (2011), pp. 583–587.

[240] Ahhyun S Nam, Isabel Chico-Calero, and Benjamin J Vakoc. “Complex differential variance algorithm for optical coherence tomography angiography”. In: *Biomedical optics express* 5.11 (2014), pp. 3822–3832.

[241] Jonghwan Lee et al. “Multiple-capillary measurement of RBC speed, flux, and density with optical coherence tomography”. In: *Journal of Cerebral Blood Flow & Metabolism* 33.11 (2013), pp. 1707–1710.

[242] LaVision Biotech. *2-Photon Microscopy Systems*. `https://www.lavisionbiotec.com/products/trim-scope.html`. 2020.

[243] Winfried Denk, James H Strickler, and Watt W Webb. “Two-photon laser scanning fluorescence microscopy”. In: *Science* 248.4951 (1990), pp. 73–76.

[244] Fritjof Helmchen and Winfried Denk. “Deep tissue two-photon microscopy”. In: *Nature methods* 2.12 (2005), pp. 932–940.

[245] Andreas Ibraheem and Robert E Campbell. “Designs and applications of fluorescent protein-based biosensors”. In: *Current opinion in chemical biology* 14.1 (2010), pp. 30–36.

[246] James T Russell. “Imaging calcium signals in vivo: a powerful tool in physiology and pharmacology”. In: *British journal of pharmacology* 163.8 (2011), pp. 1605–1625.

[247] Sarah Kretschmer et al. “Autofluorescence multiphoton microscopy for visualization of tissue morphology and cellular dynamics in murine and human airways”. In: *Laboratory investigation* 96.8 (2016), pp. 918–931.

[248] Nathalie L Rochefort and Arthur Konnerth. “Dendritic spines: from structure to in vivo function”. In: *EMBO reports* 13.8 (2012), pp. 699–708.

[249] Sava Sakadžić et al. “Two-photon high-resolution measurement of partial pressure of oxygen in cerebral vasculature and tissue”. In: *Nature methods* 7.9 (2010), pp. 755–759.

[250] Andy Y Shih et al. “Two-photon microscopy as a tool to study blood flow and neurovascular coupling in the rodent brain”. In: *Journal of Cerebral Blood Flow & Metabolism* 32.7 (2012), pp. 1277–1309.

[251] Felix Bloch. “Nuclear induction”. In: *Physical review* 70.7-8 (1946), p. 460.

[252] Edward M Purcell, Henry Cutler Torrey, and Robert V Pound. “Resonance absorption by nuclear magnetic moments in a solid”. In: *Physical review* 69.1-2 (1946), p. 37.

[253] Paul C Lauterbur. “Image formation by induced local interactions: examples employing nuclear magnetic resonance”. In: *nature* 242.5394 (1973), pp. 190–191.

[254] Peter Mansfield. “Multi-planar image formation using NMR spin echoes”. In: *Journal of Physics C: Solid State Physics* 10.3 (1977), p. L55.

[255] Erwin L Hahn. “Spin echoes”. In: *Physical review* 80.4 (1950), p. 580.

[256] Marco Pizzolato. “Computational diffusion & perfusion MRI in brain imaging”. PhD thesis. Université Côte d’Azur, 2017.

[257] Edward O Stejskal and John E Tanner. “Spin diffusion measurements: spin echoes in the presence of a time-dependent field gradient”. In: *The journal of chemical physics* 42.1 (1965), pp. 288–292.

[258] Peter Hänggi and Fabio Marchesoni. *Introduction: 100 years of Brownian motion*. 2005.

[259] Denis Le Bihan and E Breton. “Imagerie de diffusion in vivo par résonance magnétique nucléaire”. In: *Comptes rendus de l’Académie des sciences. Série 2, Mécanique, Physique, Chimie, Sciences de l’univers, Sciences de la Terre* 301.15 (1985), pp. 1109–1112.

[260] Denis Le Bihan. “Diffusion MRI: what water tells us about the brain”. In: *EMBO molecular medicine* 6.5 (2014), pp. 569–573.

[261] Christopher G Filippi et al. “Diffusion tensor imaging of patients with HIV and normal-appearing white matter on MR images of the brain”. In: *American Journal of Neuroradiology* 22.2 (2001), pp. 277–283.

[262] Adolf Pfefferbaum et al. “Age-related decline in brain white matter anisotropy measured with spatially corrected echo-planar diffusion tensor imaging”. In: *Magnetic Resonance in Medicine: An Official Journal of the International Society for Magnetic Resonance in Medicine* 44.2 (2000), pp. 259–268.

[263] Michael E Moseley et al. “Early detection of regional cerebral ischemia in cats: comparison of diffusion-and T2-weighted MRI and spectroscopy”. In: *Magnetic resonance in medicine* 14.2 (1990), pp. 330–346.

[264] Philippe Douek et al. “MR color mapping of myelin fiber orientation”. In: *J Comput Assist Tomogr* 15.6 (1991), pp. 923–929.

[265] Peter J Basser et al. “In vivo fiber tractography using DT-MRI data”. In: *Magnetic resonance in medicine* 44.4 (2000), pp. 625–632.

[266] Julio A Chalela et al. “Magnetic resonance imaging and computed tomography in emergency assessment of patients with suspected acute stroke: a prospective comparison”. In: *The Lancet* 369.9558 (2007), pp. 293–298.

[267] Marco Essig et al. “Perfusion MRI: the five most frequently asked technical questions”. In: *American Journal of Roentgenology* 200.1 (2013), pp. 24–34.

[268] Michael J Paldino and Daniel P Barboriak. “Fundamentals of quantitative dynamic contrast-enhanced MR imaging”. In: *Magnetic resonance imaging clinics of North America* 17.2 (2009), pp. 277–289.

[269] Aghogho Odudu et al. “Arterial spin labelling MRI to measure renal perfusion: a systematic review and statement paper”. In: *Nephrology Dialysis Transplantation* 33.suppl_2 (2018), pp. ii15–ii21.

[270] Denis Le Bihan et al. “Separation of diffusion and perfusion in intravoxel incoherent motion MR imaging.” In: *Radiology* 168.2 (1988), pp. 497–505.

[271] Christian Federau. “Intravoxel incoherent motion MRI as a means to measure in vivo perfusion: A review of the evidence”. In: *NMR in Biomedicine* 30.11 (2017), e3780.

[272] Stefano Moriconi et al. “Towards Quantifying Neurovascular Resilience”. In: *Machine Learning and Medical Engineering for Cardiovascular Health and Intravascular Imaging and Computer Assisted Stenting*. Springer, 2019, pp. 149–157.

[273] Stefano Moriconi. “Inferring geodesic cerebrovascular graphs: image processing, topological alignment and biomarkers extraction”. PhD thesis. UCL (University College London), 2020.

[274] Yan Wang et al. “Deep distance transform for tubular structure segmentation in ct scans”. In: *Proceedings of the IEEE/CVF Conference on Computer Vision and Pattern Recognition*. 2020, pp. 3833–3842.

[275] Waleed Tahir et al. “A generalizable deep-learning approach to anatomical modeling of brain vasculature (Conference Presentation)”. In: *Neural Imaging and Sensing 2020*. Vol. 11226. International Society for Optics and Photonics. 2020, p. 1122611.

[276] Juntang Zhuang. “Laddernet: Multi-path networks based on u-net for medical image segmentation”. In: *arXiv preprint arXiv:1810.07810* (2018).

[277] Kai Lawonn et al. “A Geometric Optimization Approach for the Detection and Segmentation of Multiple Aneurysms”. In: *Computer Graphics Forum*. Vol. 38. 3. Wiley Online Library. 2019, pp. 413–425.

[278] Philbert S Tsai et al. “Correlations of neuronal and microvascular densities in murine cortex revealed by direct counting and colocalization of nuclei and vessels”. In: *Journal of Neuroscience* 29.46 (2009), pp. 14553–14570.

[279] Yang Wang et al. “Regional reproducibility of pulsed arterial spin labeling perfusion imaging at 3T”. In: *Neuroimage* 54.2 (2011), pp. 1188–1195.

[280] Nicholas A Telischak, John A Detre, and Greg Zaharchuk. "Arterial spin labeling MRI: clinical applications in the brain". In: *Journal of Magnetic Resonance Imaging* 41.5 (2015), pp. 1165–1180.

[281] Pan Su et al. "Multiparametric estimation of brain hemodynamics with MR fingerprinting ASL". In: *Magnetic resonance in medicine* 78.5 (2017), pp. 1812–1823.

[282] Greg Zaharchuk et al. "Arterial spin-labeling MRI can identify the presence and intensity of collateral perfusion in patients with moyamoya disease". In: *Stroke* 42.9 (2011), pp. 2485–2491.

[283] Jeroen Hendrikse, Esben Thade Petersen, and Xavier Golay. "Vascular disorders: insights from arterial spin labeling". In: *Neuroimaging Clinics* 22.2 (2012), pp. 259–269.

[284] JA Wells et al. "MRI of cerebral micro-vascular flow patterns: A multi-direction diffusion-weighted ASL approach". In: *Journal of Cerebral Blood Flow & Metabolism* 37.6 (2017), pp. 2076–2083.

[285] Seongjin Choi et al. "DTI at 7 and 3 T: systematic comparison of SNR and its influence on quantitative metrics". In: *Magnetic resonance imaging* 29.6 (2011), pp. 739–751.

[286] Cornelius von Morze et al. "Reduced field-of-view diffusion-weighted imaging of the brain at 7 T". In: *Magnetic resonance imaging* 28.10 (2010), pp. 1541–1545.

[287] Liang Zhan et al. "Magnetic resonance field strength effects on diffusion measures and brain connectivity networks". In: *Brain connectivity* 3.1 (2013), pp. 72–86.

[288] Daniel Gallichan. "Diffusion MRI of the human brain at ultra-high field (UHF): A review". In: *NeuroImage* 168 (2018), pp. 172–180.

[289] Nicolas Adrien Pannetier et al. "A simulation tool for dynamic contrast enhanced MRI". In: *PloS one* 8.3 (2013), e57636.